Design and Implementation of Smart Voltage Source Inverter (SVSI) with Renewable Energy Source (RES)

by

Fida Hasan Md Rafi

Dissertation submitted in fulfilment of the requirements for the degree of

DOCTOR OF PHILOSOPHY

Department of Engineering

Faculty of Science and Engineering

Macquarie University

Sydney, Australia

July 2017

Statement of Originality

"This work has not previously been submitted for a degree or diploma in any university. To the best of my knowledge and belief, the PhD thesis contains no material previously published or written by another person except where due reference is made in the report itself."

Fida Hasan Md Rafi

Macquarie University

Acknowledgements

This dissertation would not have been possible without the continuous support and guidance of several individuals, especially my principal supervisor Associate Professor Jahangir Hossain. I would like to express my sincere gratitude to him for his support, patience, and encouragement throughout my PhD study. He is a hardworking person himself and always suggests that his students spend enough time for studies, and on numerous occasions I found his insightful suggestions really encouraging and helpful which has helped with the completion of this PhD thesis. He has always managed time for our weekly group meetings and individual meetings despite his tight working schedule. His technical knowledge is vast and quite diverse which has made it possible for me to formulate new ideas and apply them in real-life scenarios related to my research field. In reviewing my writings, he provides many critical and informative comments within a short period of time and this has helped me to publish several top-tier journal and conference papers in my PhD study. He is also friendly with his students and I have received very fruitful support from him regarding my personal problems. Many thanks also go to his open-mindedness and academic and personal support.

I am lucky to have two knowledgeable co-supervisors, Professor Graham Town and Professor Junwei Lu from Griffith University. Although they are mentioned as co-supervisors in my admission documents, their continuous support was just as good as that of my main supervisor. I am really thankful to them for their time to read my manuscripts and provide valuable suggestions for my research, especially with my experimental work.

I would like to express my special gratitude to Dr Douglas Carter from Denkinetic Pty Ltd for his invaluable support with my experimental work. He helped me with the application of the smart voltage source inverter controller and let me use his switchgear controller unit. It was a great favour from him and his support is gratefully acknowledged.

I am also thankful to Dr Keith Imrie, Honorary Associate at Macquarie University, for proof-reading my thesis within a very short period of time.

My appreciation goes to fellow postgraduate students, especially Md Shamiur Rahman from my research group, for making my journey a memorable experience and sharing friendship during the

past few years. My sincere thanks go to those who, either close at hand or at a distance, were concerned about me and my studies. I also wish to extend my warmest thanks to my friends in the university and wider community who have made my stay in Australia fruitful and enjoyable.

Moreover, I am grateful for the enormous support and understanding of my family in Bangladesh and relatives in Australia, especially my aunt Dr. Nazma Alam and uncle Dr. Shamsul Alam.

Last, but certainly not least, I am indebted to the Queensland Micro and Nanotechnology Centre (QMNC), Griffith University and the Department of Engineering, Faculty of Science and Engineering, Macquarie University for their financial support and the opportunity to embark on this PhD journey.

Abstract

Renewable energy sources (RES), such as photovoltaic (PV) and battery energy storage (BES) systems, are becoming popular due to their ease of installation, reduction in greenhouse gas emissions and economic benefits from electricity bill reduction. However, the increasing amount of RES penetration into the low-voltage (LV) network is making the existing passive distribution network face many challenging issues such as voltage rise at the point of common coupling (PCC), voltage unbalances, power quality degradation etc. Additionally, the unbalanced distribution of linear and nonlinear single-phase loads and RES installations are causing high neutral current generation along with neutral to ground voltage rise at the PCC in three-phase four-wire LV networks. Therefore, in this dissertation, a multifunctional smart voltage source inverter (SVSI) is designed with a PV system to provide optimised and coordinated voltage regulation and improved neutral current compensation performance at customer installation points.

The first contribution of this research is the development of a hierarchical control selection method to mitigate the voltage-rise associated with increasing PV penetration in a balanced three-phase three-wire Australian LV network. The proposed method utilises five control modes based on the PV penetration level in the LV network. The voltage regulation method provides a step-by-step requirement of different voltage regulation devices such as a distributed static synchronous compensator (D-STATCOM), D-STATCOM/BES, residential SVSI, BES and power sharing among neighbouring RES units for critically voltage-sensitive areas in the LV network. The developed control selection method provides an optimised and economical way to achieve 100% penetration of RESs into the LV network without any voltage constraints.

The second contribution of this research is the design and application of a multi-functional three-phase (3P) four-leg (4L) PV-SVSI with a novel neutral current control which can significantly compensate for the load-generated current at different network locations. The relationship between the load-generated neutral current and the zero sequence R/X ratio (R_0/X_0) of the transmission-line neutral conductor is developed. The 3P-4L PV-SVSI is designed to operate robustly with variable R_0/X_0 ratios and system fault conditions. Comparisons of neutral current compensation operation with existing passive and active neutral compensation methods are presented to verify the efficacy and novelty of the proposed system.

The third contribution of this dissertation is the development of a novel dynamic capacity distribution (DCD) method to improve the neutral current compensation from the 3P-4L PV-SVSI. The DCD method distributes the available capacity after active and reactive power regulation operations from the SVSI to the neutral current controller for higher capacity neutral current compensation. Traditional current limiters with dynamic value assigning function are used to utilise the DCD method in the four-leg inverter to achieve better unbalanced compensation than that provided by existing methods.

The final contribution of this research is the construction and application of a 3P-4L SVSI hardware prototype for experimental results verification. The four-leg VSI system is constructed by modifying the Semiteach three-leg teaching module, and the fourth leg is controlled independently in the system. The same inverter system is operated in three- and four-leg inverter configurations with a real-time digital signal processor (DSP) controller module provided by Denkinetic Pty Ltd and using Code Composer Studio (CCS) software.

Different case studies are conducted with both inverter configurations in the power system computer aided design/ electromagnetic transient DC (PSCAD/EMTDC) software platform and in an experimental setup to verify the efficacy of the proposed methodologies. Proper electrical connection standards are also ensured in the designed PV-SVSI system, such as total harmonic distortion less than 5%, voltage unbalance factor less than 2%, and neutral to ground voltage less than 1 V. The case studies' results show that the designed multifunctional PV-SVSI can provide stabilised performance with the proposed methods in voltage regulation and neutral current compensation, despite the variations in sun irradiance, customer load profiles, network parameters, and different fault conditions.

Table of Contents

List of Tables

List of Figures

List of Symbols

R/X	Resistance by reactance ratio of transmission line
R_+/X_+	Positive sequence resistance by reactance ratio of transmission conductor
R_0/X_0	Zero sequence resistance by reactance ratio of neutral conductor
V_g	Grid-side voltage at PCC
I_g	Grid-side current
L_g	Grid-side inductance of transmission line
R_g	Grid-side resistance of transmission line
I_L	Load current
I_{Ln}	Load-generated neutral current
I_B	Battery current
C_{DC}	DC-link capacitor
C_n	DC-link to neutral conductor capacitor
I_{DC}	DC current
V_{DC}	DC voltage
G	Arbitrary constant to represent voltage or current quantity
$G_{neg.seq}$	Negative sequence component of G
$G_{pos.seq.}$	Positive sequence component of G
$G_{zero.seq.}$	Zero sequence component of G
ΔV	Voltage difference
I_{Ls}	Current corresponding to sunlight
I_s	Reverse saturation current
N_s	Number of PV cells in series
N_p	Number of PV modules in parallel
R_s	Series resistances of the PV array
R_{sh}	Shunt resistances of the PV array
I_{pv}	Current flowing through the PV array
V_{pv}	Output voltage of the PV array
k	Boltzmann constant
q	Charge of an electron
A	Ideality factor of p-n junction

T_r	Cell reference temperature
P_{PV}	PV-generated power
i_f	Inverter-side phase current
S	Phase modulating signal
L_f	Inverter-side filter inductor value
r_f	Inverter-side line resistance
C_f	Filter capacitor A phase
V_{cf}	Voltage at filter capacitor
R_d	Damping resistor
ω_{PCC}	Angular frequency
I_{fd}	Direct-axis current of inverter side
I_{fq}	Quadrature-axis current of inverter side
I_{f0}	Zero-axis current of inverter side
I_{fn}	Inverter-side neutral current
I_{gd}	Direct-axis current of grid side
I_{gq}	Quadrature-axis current of grid side
I_{g0}	Zero-axis current of grid side
I_{gn}	Grid-side neutral current
S_d	Direct-axis modulation signal of VSI
S_q	Quadrature-axis modulation signal of VSI
S_0	Zero-axis modulation signal of VSI
S_N	Neutral component modulation signal of VSI
P_{PCC}	PCC active power
Q_{PCC}	PCC reactive power
V_{gd}	Direct-axis voltage of grid side
V_{gq}	Quadrature-axis voltage of grid side
V_{g0}	Zero-axis current of grid side
V_n	Neutral to ground voltage at PCC
d	Duty ratio
Z_0	Transmission-line zero sequence impedance

Abbreviations and Acronyms

1P	Single-phase
2C	Split-DC capacitor
3D-VSM	Three-dimensional space vector modulation
3-HB	Three half bridge
3P-3L	Three-phase three-leg
3P-3W	Three-phase three-wire
3P-4L	Three-phase four-leg
3P-4W	Three-phase four-wire
3P-G	Three-phase to ground
AC	Alternating current
ANCC	Active neutral current compensation
ANSI	American National Standards Institute
APF	Active power filter
AS	Australian Standard
AVC	Automatic voltage compensator
BES	Battery energy storage
BMMS	Battery monitoring and management system
CAD	Computer aided design
CB	Circuit breaker
CC	Constant current
CCS	Code Composer Studio
CMV	Common mode voltage
CP	Constant power
CSI	Current source inverter
CUF	Current unbalance factor
CV	Constant voltage
CZ	Constant impedance
DC	Direct current
DCC	Decoupled current controller
DCD	Dynamic capacity distribution
DG	Distributed generation
DIMM	Dual-in-line memory module
DN	Distribution network
DNO	Distribution network operator
DOC	Depth of charge
DOD	Depth of discharge

DP	Dominant pole
DSP	Digital signal processor
D-STATCOM	Distributed static synchronous compensator
DT	Distribution transformer
DVR	Dynamic voltage restorer
EHV	Extra-high-voltage
EV	Electric vehicle
FACTS	Flexible AC transmission system
FIT	Feed-in tariff
FRT	Fault ride through
HV	High-voltage
IEC	International Electrotechnical Commission
IGBT	Insulated gate bipolar transistor
IT	Information Technology
JTAG	Joint test action group
LED	Light emitting diode
L-G (1L-G)	Line to ground
L-L-G (2L-G)	Double lines to ground
LV	Low-voltage
MCU	Micro-controller unit
MF	Module front
MPPT	Maximum power point tracking
MR	Module rear
MT	Matching transformer
MV	Medium-voltage
NECA	National Electricity Code Australia
NEMA	National Electrical Manufacturers Association
NER	National Electricity Regulator
NGV	Neutral to ground voltage
NN	Neutral network
NZS	New Zealand standard
OLT	On/off load tap changing
p.u.	Per unit
PCC	Point of common coupling
pf	Power factor
PHEV	Plug-in hybrid electric vehicle
PI	Proportional-integral
PLL	Phase locked loop
PMSM	Permanent magnet synchronous machine
P-P	Peak to peak

PSCAD/EMTDC	Power system computer aided design/ electromagnetic transient DC
PV	Photovoltaic
PWM	Pulse width modulation
RCCB	Residual current circuit breaker
RES	Renewable energy source
Rms	Root mean square
SNI	Current sensor module
SNV	Voltage sensor module
SOC	State of charge
SPETS	Semiteach power electronic teaching system
SPWM	Sinusoidal pulse width modulation
SRF	Synchronously rotating frame
STATCOM	Static synchronous compensator
STC	Standard test condition
SVSI	Smart voltage source inverter
THD	Total harmonic distortion
TI	Texas Instrument
Tx	Transformer
UF	Unbalance factor
UPS	Uninterruptible power supply
VAR	Volt-ampere reactive
VSC	Voltage source converter
VSI	Voltage source inverter
VUF	Voltage unbalance factor
ZT	Zig-zag transformer

Publication Overview

Refereed Journal Papers

1. **Fida Hasan Md Rafi**, and M. J. Hossain, "Trends in Neutral Compensation Techniques using Power Electronic Converters for Unbalanced Three-Phase Four-Wire Distribution System: An Overview," Applied Energy, 2017 (*under review*). (Chapter 1 & 2)
2. **Fida Hasan Md Rafi,** M. J. Hossain, and J. Lu, "Hierarchical controls selection based on PV penetrations for voltage rise mitigation in a LV distribution network," International Journal of Electrical Power & Energy Systems, vol. 81, pp. 123–139, 2016. (Chapter 3)
3. **Fida Hasan Md Rafi**, M. J. Hossain, and J. Lu, "Improved neutral current compensation with a four-leg PV smart VSI in a LV residential network," IEEE Transaction on Power Delivery, 2016 (early access online). (Chapter 4)
4. **Fida Hasan Md Rafi**, M. J. Hossain, G.Town, and J. Lu, "Dynamic capacity allocation operations of a four leg PV-SVSI in a residential area," IEEE Transaction on Industrial Informatics, 2016 (*under review*). (Chapter 5)
5. **Fida Hasan Md Rafi**, and M. J. Hossain, "Hardware implementation of a four leg inverter with novel neutral current compensation operation and commercial loads," IEEE Transaction on Industrial Electronics, 2017 (*under review*). (Chapter 6)

Scholarly Book Chapter

6. M. S. Rahman, **Fida Hasan Md Rafi**, M. J. Hossain, and J. Lu, "Power Control and Monitoring of the Smart Grid with EVs," in Vehicle-to-Grid: Linking Electric Vehicles to the Smart Grid, IET publisher, 2015.

Refereed Conference Papers

7. **Fida Hasan Md Rafi**, M. J. Hossain, M. S. Rahman, and J. Lu, "Impact of controlling zero sequence current in a three phase four wire LV network with PV," Power and Energy General Meeting, Boston, USA, 2016.
8. **Fida Hasan Md Rafi**, M. J. Hossain, M. S. Rahman, and J. Lu, "Implementation of Independent Improved Neutral Current Controller Using Four Leg PV-VSI," Australasian Universities Power Engineering Conference, 2016.
9. **Fida Hasan Md Rafi**, M. J. Hossain, D. Leskarac, and J. Lu, "Reactive power management of a AC/DC microgrid system using a smart PV inverter," Power and Energy General Meeting, Denver, USA, 2015.

10. **Fida Hasan Md Rafi**, M. J. Hossain, and J. Lu, "Design of a single stage transformerless VSI in a smart microgrid for PV-STATCOM/ESS operations," Australasian Universities Power Engineering Conference, pp. 1-6, 2014.
11. **Fida Hasan Md Rafi**, M. J. Hossain, and J. Lu, " PV microgrid islanded operation analysis with the designed smart VSI," IEEE Conference on Industrial Electronics and Applications, Auckland, New Zealand, 2015.

Chapter 1
Introduction

1.1 General Overview

The relationship between energy demand and availability of energy resources is quite complex. Our demand for energy is increasing everyday and, to keep up with the required demand, different energy resources, such as fossil fuels, natural gas, oil, nuclear power plants, hydro plants etc., are used extensively to generate power. The excessive use of fossil-fuel energy sources raises global warming concerns by increasing the amount of greenhouse gas emissions. The desire for new energy sources became evident during the early 1990s, which were arrived at following the first solar power technology application in satellite stations in the early 1950s [1]. Since the early 21st century, the penetration of different renewable energy sources (RES), such as photovoltaic (PV), wind energy etc., has increased tremendously, exceeding all predictions as is evident from Table 1.1 where the total RES installations from 2004 to the end of 2015 are presented. Solar PV and wind power utilisation has increased by nearly 100% in the past decade. Rooftop PV installation is one of the most popular RESs among residential and commercial customers due to its ease of installation and feed-in-tariff (FIT) offers. Both large- and small-scale RES installations are becoming popular in power generation and distribution networks. The RES installations roadmap with the existing power system networks is depicted in Fig. 1.1.

Table 1.1 Total renewable energy levels throughout the world [2-3]

Energy source	Start of 2004 (GW)	End 2012 (GW)	End 2015 (GW)
Hydro power	715	960	1,064
Bio Power	<36	83	106.4
Geothermal power	8.9	11.5	13.2
Solar PV	2.6	100	227
Solar thermal power	0.4	2.5	4.8
Wind power	48	283	433

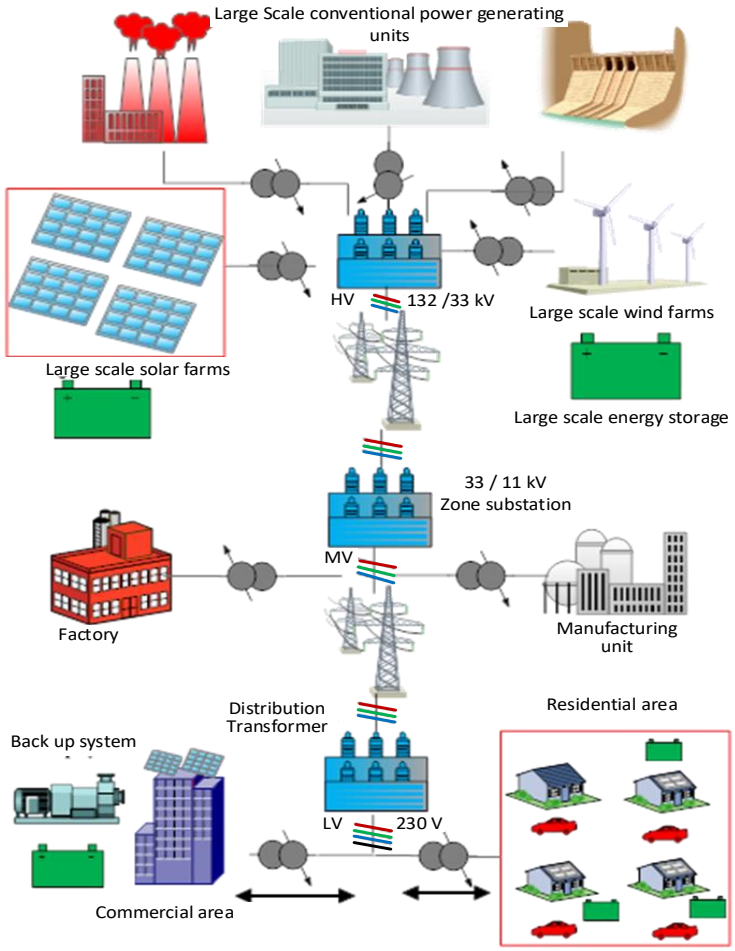

Figure 1.1. RES application in power system network

The solar PV market throughout the world had a record increase in 2015 of over 50 GW, increasing the global capacity to a total of 227 GW [3]. The top ten countries with the highest solar PV installations at the end of 2015 are shown in Fig. 1.2.

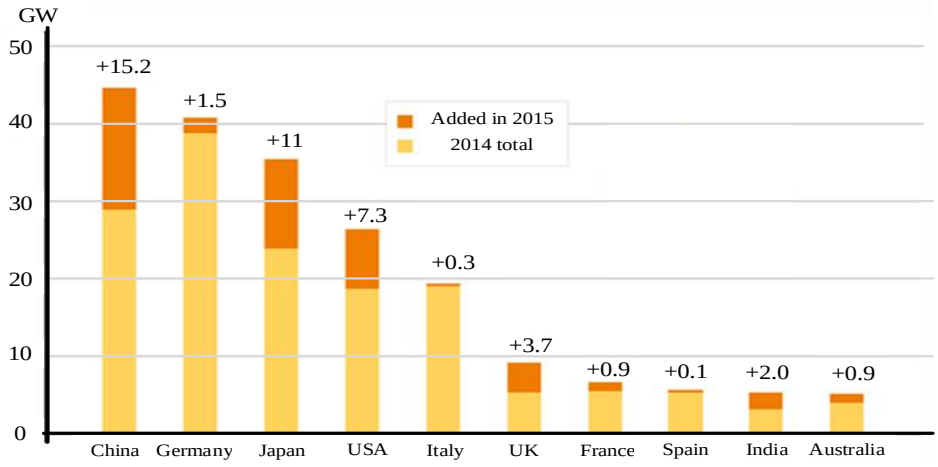

Figure 1.2. Top ten countries for solar PV installation at the end of 2015 [2]

It can be seen from Fig. 1.2 that Australia is one of the top ten countries with the highest PV installations and had nearly 1 GW of solar PV installed in 2015. The increasing number of solar PV units, especially small-scale units, into the LV network has generated a new way of utilising the bidirectional power flow in the distribution network. The low load demand and high power generation during daytime from residential areas can allow feedback of the PV-generated excess power to the main grid and obtain benefits by utilising the feed-in-tariff (FIT) and small-scale technology certificate schemes [4]. Excessive back feeding of PV-generated power may benefit consumers economically but this puts pressure on the low-voltage (LV) distribution network, causing voltage-rise at the point of common coupling (PCC), unbalanced current generation and stability issue in the network. Therefore, many distribution network operators put restrictions on allowable PV installation numbers, reduce the FIT offer and apply expensive solutions to mitigate the instability. One local power distribution company in Australia, Energex, which is located in Brisbane, has presented different network solutions based on different PV penetration numbers to provide voltage-rise compensation in its network as shown in Table 1.2.

Table 1.2 Increasing PV penetrations solutions from Energex, Australia [5]

PV penetration level	Network solutions
From 30-70%	1. Balance of PV load 2. Change of transformer tap
From 40-100%	3. First two steps 4. Upgrade transformer 5. New transformer 6. Re-conductor mains
From 100-200%	7. Above steps 8. New technology (on-load tap transformer, LV regulator, static synchronous compensator (STATCOM)

It is evident from Table 1.2 that the distribution network can sustain a PV penetration of upto 30% but needs to provide additional solutions to manage the challenging issues after a certain penetration level. Based on the increasing PV installations and unbalances in the LV network, the associated problems are stated in the next section, and the motivation of the research study is presented.

1.2 Problem Statement and Research Motivation

Most customer loads and PV installations, such as rooftop PV, in the LV network are single-phase type which are commonly supplied by a three-phase four-wire LV distribution network to residential and commercial areas. Many challenging issues arise with the increase in PV installations and the usage of single-phase loads, such as personal computers, air conditioning devices etc., which are described below:

- **Maximum resource utilisation:** One of the main challenges with RES installations is how to get the maximum benefits from installed resources. The variation in sun irradiance and temperature has a direct effect on the power production from PV units. Low or no irradiance, such as during cloudy days and night time, can result in inactive operation of a PV installation. Therefore, whole-day resource utilisation from PV installations needs to be ensured, either using additional battery energy storage (BES) and/or utilising both active and reactive power from the inverter unit. Instead of installing several devices to mitigate the problems in the network, efficient methodologies need to be developed to get the expected outcomes with minimal resource requirements.
- **High PCC voltage:** Low customer load demand and high power generation from PV units (worst-case scenario) can raise the PCC voltage beyond the allowable limits (generally ±6%) causing unnecessary tripping of the customer load or the PV unit. An efficient technique must be devised and implemented to keep the customer unit connected even during the worst case scenario. In addition, many distribution network operators (DNOs) restrict installation of PV units after a certain PV penetration level. This provides an indirect solution to the voltage-rise problem, however, it creates a direct issue with more RES integration into the network. To solve the voltage-rise and PV penetration issues, different traditional methods can be applied, such as increasing conductor size, transformer tap changing, installing static capacitor banks, dynamic VAR support devices, such as distributed static synchronous compensator (D-STATCOM) etc. However, an economic justification for the applied/proposed solution needs to be provided to achieve the best cost-benefit results.

- **Load intermittency:** The peak load demand is different for residential and commercial areas. Even the daily load usage pattern is different due to the continuously changing load demands from hour to hour, day to day, weekdays to weekends, and season to season. A robust system needs to be utilised to provide appropriate functions irrespective of load usage patterns.
- **High neutral current, and neutral to ground voltage:** Three-phase four-wire power distribution systems are more vulnerable to unbalance problems due to the neutral wire connections. Unbalanced loads and unplanned PV allocations can cause a high neutral current at the PCC, resulting in a high neutral to ground voltage and more losses in the system. An efficient method needs to be devised to reduce the stress on the neutral line irrespective of load and PV usage status.
- **Power quality issue and phase balancing:** Increasing application of non-linear loads, such as adjustable speed drive (ASD) devices, personal computers etc., pollute the interconnected system, causing sensitive equipment to function abnormally and voltage unbalance at the PCC.
- **Network diversity:** Different customer installation points have different network characteristics, such as variations in the R/X ratio. The network parameters play a vital role in providing different solutions to arising problems. A robust inverter system should be developed to provide stable operation irrespective of network parameter variations.

The research motivations for this thesis are based on finding new and practical solutions for some of the aforementioned challenging issues.

1.3 Objectives and Contribution of This Research

The research objectives of this thesis are focused on finding solutions to the challenging issues as mentioned in the preceding subsection. The objectives are as follows:

i. finding novel and innovative methods for voltage-rise and neutral current mitigation;
ii. design and development of cost-efficient control methodologies with RES installations to achieve maximum resource utilisation;

iii. develop robust inverter controls to mitigate high neutral current from continuously changing load profiles at different network locations;
iv. application of an effective control methodology to achieve higher neutral current compensation performance without disturbing other control operations, i.e. active and reactive controls; and
v. develop an experimental prototype of a smart inverter with multifunctional capabilities.

The broader view of the research objective is to design and develop a PV multifunctional smart voltage source inverter (SVSI) with independent active, reactive and neutral current compensation controls.

The contributions of this thesis are as follows:

i. development of a novel voltage-rise mitigation method utilising available resources and focusing on increasing PV penetration levels on the LV network;
ii. design and development of a three-phase four-leg single-stage transformerless PV-SVSI with independent and robust neutral current compensation with continuously changing sun irradiance, temperature, residential and commercial load data;
iii. development of the relationship between the neutral conductor zero sequence R/X ratio and the load-generated neutral current to evaluate the robustness of the neutral current controller;
iv. construction of a novel capacity management method to dynamically allocate SVSI capacity for active, reactive and neutral current compensation; and
v. construction of a hardware prototype of the four-leg inverter with independent neutral current control capability using a digital signal processor (DSP)-based switchgear controller.

1.4 Thesis Organisation

This thesis is organised as follows:

- **Chapter 2** presents an extensive literature review and mathematical modelling of the dynamic devices, such as PV, battery energy storage (BES), three-leg inverter, D-STATCOM, four-leg inverter and the LV power system network. The literature review is

focused on the voltage-rise regulation and neutral current compensation methods in a three-phase four-wire LV network. The literature review helps to find an appropriate compensation device and a methodology to accomplish the research objectives;

- **Chapter 3** presents a novel methodology to mitigate the voltage-rise issue with increasing PV penetration into an LV network. Different traditional and dynamic solutions are incorporated with PV and BES to achieve a higher percentage of RES penetration into the LV network;
- **Chapter 4** analyses the unbalance trend and the corresponding neutral current generation effects from real load profiles of residential customers. The effects of different R/X ratios at different network locations are monitored and a relationship between the neutral conductor zero sequence R/X ratio and load side neutral current generation is developed. A robust four-leg PV-SVSI is designed to provide improved neutral current compensation with variations in network and load parameters;
- **Chapter 5** presents a new capacity utilisation method from the four-leg PV-SVSI to provide higher neutral current compensation. The method is incorporated with a traditional four-leg inverter with PI controller, and results are compared with a fixed-capacity active neutral compensator described in Chapter 4. Improved neutral current compensation, better phase balancing, improved unbalance factor and correction of the neutral shift voltage is presented for the proposed method;
- **Chapter 6** presents the experimental setup and discusses the results from the four-leg hardware prototype. The construction of the four-leg hardware prototype from a Semiteach three-leg inverter teaching system is presented and a DSP-based switchgear controller is used to apply the control methods to the four-leg SVSI with different load values; and
- **Chapter 7** concludes the thesis by summarising the findings of this study and suggesting future research directions on this topic.

Chapter 2

Literature Review and System Modelling

2.1 Introduction

In many residential and commercial low-voltage (LV) networks, a three-phase four-wire (3P-4W) distribution system is used to accommodate single- and three-phase customer loads and renewable energy source (RES) installations, such as photovoltaic (PV), wind energy system etc. The increase in the number of RES installations raises the concern of a voltage-rise at the customer connection point due to excess reverse power flow to the supply network. Additionally, the unequal distribution of loads, both linear and nonlinear types, and RES installations can cause severe neutral current generation and associated voltage unbalance problems, such as neutral to ground voltage-rise, neutral voltage shift, harmonics generation etc. at the point of common coupling (PCC). A high PCC voltage can cause unnecessary tripping of customer installation units and a high neutral current can cause electrical safety concerns for customers. To find novel and effective solutions to the aforementioned issues, this chapter presents a literature review of different voltage regulation devices and active neutral current compensation methods. Based on the findings from the literature review, the modelling of different RES and power electronic converter units is also presented in this chapter. Different electricity connection standards are summarised in the literature review section to provide a guideline for appropriate voltage regulation and unbalance compensation.

2.2 Review on Voltage-Rise Regulation Methods

The requirement to regulate voltage is common in power system networks especially with high load demand and sudden electrical faults. High load demand and electrical faults cause a voltage-sag at the particular connection point and require the system voltage to be regulated to the nominal voltage value (1 per unit (p.u.)). However, with a PV system, especially in residential areas, the voltage-rise occurs due to excess feedback power from PV installations. The time mismatch in the peak PV generation and customer load demand time makes the situation much worse for low-

voltage (LV) networks. Different compensation devices, such as capacitor banks, flexible AC transmission system (FACTS) devices, on/off load tap-changing transformers (OLT), and automatic voltage compensators (AVC), have already been applied to restore stability on high-voltage (HV) and medium-voltage (MV) networks [6]. Similar devices in a comparatively low power range are also applicable to the LV network. Generally, absorbing certain levels of reactive power, i.e. lagging power factor (pf), from highly PV-penetrated networks can prevent unnecessary tripping and instability in a voltage-rise scenario [7]. Voltage regulation controls are commonly applied using distributed static compensation devices (D-STATCOM), mechanically switched capacitor banks and OLTs in the LV networks. The voltage regulation methods in the LV network can be classified into two categories:

i. Centralised regulation method: This type of compensation method is generally operated by the DNOs and is effective for comparatively small areas, for example, tap changing transformers, capacitor banks, STATCOM/BES, DVR etc.

ii. Decentralised regulation method: It can be applied by both DNOs and customers themselves with appropriate devices. The decentralised compensation method focuses voltage regulation at a particular connection point using dynamic devices, such as D-STATCOM, smart voltage source inverters (SVSI) etc.

The traditional LV distribution network exhibits a high resistance to reactance (R/X) ratio on transmission-lines (higher than 1), i.e. it has a resistive nature. Therefore, in some situations, voltage regulation utilising active power devices, such as BES charging during peak PV generation time, proves more effective than reactive power compensation [8], [9]. There are also some indirect voltage regulation methods available during a peak PV generation period, such as operating the PV units at a lower maximum power point (MPP) than the rated one (active power curtailment) [10], a load scheduling operation with thermal storage heaters [11] and hot water storage systems [12], and demand shifting [13].

Depending on specific requirements and network locations, different voltage-rise mitigation methods have proved to be more effective than others. Therefore, in this thesis, a coordinated voltage regulation method is proposed to utilise different voltage regulation devices at different PV penetration levels to permit more installation of PV units into the LV network. A more constructive review on the specific voltage-rise mitigation methods is presented in Chapter 3.

2.3 Review of Neutral Current Compensation Methods

Advances in information technology (IT) are making the world much more digitised with computer technology and electronic devices dominating in almost every aspect of people's lives. Commonly used single-phase loads are the adjustable speed drive motors in air conditioners, switch mode power supplies, LED lights, electronic ballasts, photocopy machines etc. These loads are generally supplied by the three-phase four-wire LV network utilising a delta-wye configured distribution transformer (DT) as shown in Fig. 2.1.

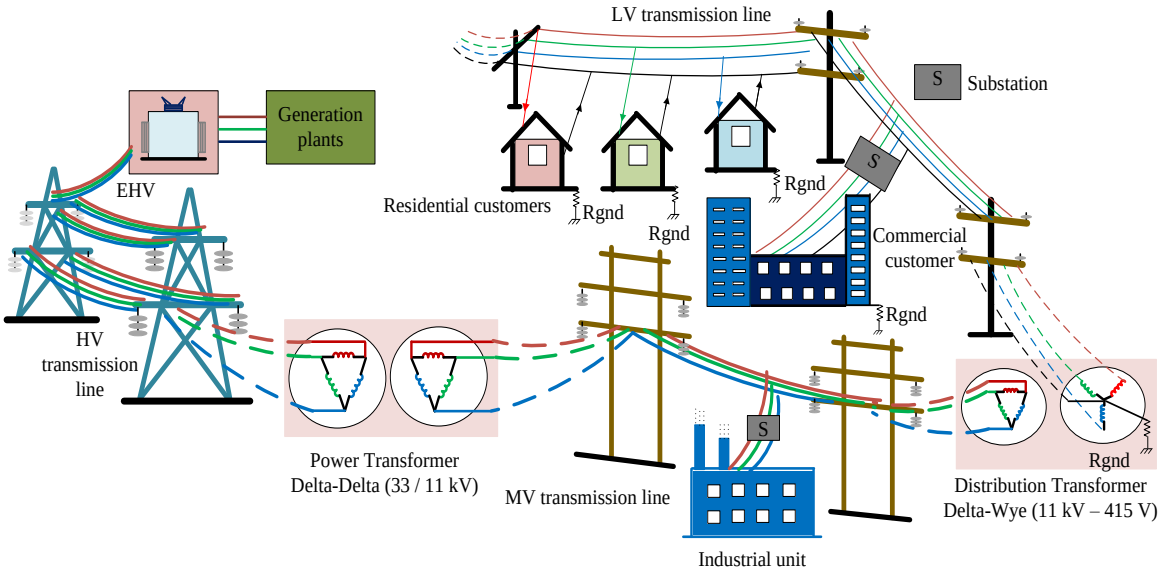

Figure 2.1. Traditional power system network

The neutral line from the wye common terminal of the DT is used to represent a reference point for the connected loads. The neutral conductor is mainly designed to carry currents generated from system abnormalities, such as a single-line to ground fault. However, the commonly used power electronic loads have nonlinear characteristics which generate a high amount of harmonic content, especially third harmonic content, and pollute the supply connection voltage [14]. The single-phase supply to the unfiltered nonlinear loads requires a low current and causes very narrow non-overlapping current pulses on the three-phase. With this type of load connection, only one-phase carries current at any instant and all the narrow pulses from the three-phases are accumulated in the neutral line, which acts as the return path. This generally causes the neutral conductor to have three times as many current pulses compared to the phase lines [15]. Additionally, the generation of a fundamental zero sequence current component is related to the unbalanced distribution of the

continuously changing single-phase linear loads which also flow through the neutral transmission-lines, and can cause overloading in the neutral conductor. Even with a balanced load distribution in three phases, excessive neutral current can be generated with computer or switch-mode power regulator type loads in a 3P-4W network [16]. The neutral overloading condition becomes worse with the unplanned allocation of single-phase PV installations [17]. There are many issues arising from the unbalanced distribution network, for example:

i. overloading the neutral conductor since generally, the neutral conductor is designed with the same capacity as the phase conductors; however, during unbalance situations, as much as three times the phase current can flow via the neutral conductor, causing a severe overloading issue [18];
ii. over-sizing the three-phase generator due to the higher current requirement from the three phases [19];
iii. over-heating of the distribution transformer, increased losses and reduced overall system efficiency as the zero sequence harmonic current flows via the fuel tank wall and the steel component of the distribution transformer which can generate heat, cause winding insulation failure and reduce equipment lifetime [20-21];
iv. poor voltage quality at the supply side and harmonic generation [14];
v. fire and electrical safety concerns for customers [22];
vi. power-line communication interference [23];
vii. prolonged and abnormal vibrations in rotary machines, such as in induction motors;
viii. malfunctioning of sensitive equipment, for example, medical appliances, process control plants, telecommunications etc.;
ix. mal-operation of protective relays;
x. unstable control operation from power electronic converters;
xi. neutral to ground voltage (NGV) rises above the standard limit which can occur in ineffectively grounded power systems because of the asymmetry in distributed parameters and resonance between the Petersen coil and distributed capacitances; this can act as common mode noise to sensitive electronics equipment [24-25];
xii. neutral shift voltage is the product of neutral impedance and the neutral current flowing in the neutral conductor which can cause a premature failure of the adjustable speed control induction motors and synchronous motors [26-27];

xiii. common mode voltage, which can cause electromagnetic interference and induced voltage problems can reduce the leakage current at customer installation points;

xiv. phase unbalance causes lower order torque pulsations in electro-mechanical systems, for example, generators leading to increased mechanical losses and instability; and

xv. high neutral current can cause high losses in the transmission-line ($I_N^2R_{line}$). In South Korea, the neutral current is restricted to less than 20% of the normal phase currents for overhead transmission-lines in order to reduce losses [23].

Different countries throughout the world use different grounding systems to compensate for sudden imbalances in the network, such as an isolated neutral in Italy, Switzerland, and Finland; multiple grounding of the neutral and connection to the utility neutral with customer grounding in the USA, Australia, and Greece; solid neutral grounding in the UK, resistance neutral grounding in France and the UK, reactance grounding in Belgium, Spain, Portugal, and the Netherlands; and via a 'Petersen' coil in Germany [28]. Because of the unbalances in the power system network, the existing grounding system is facing new challenges which are more focused about the proper operation of electrical equipment and providing safety to customers.

Compensation of the unbalance and zero sequence quantities can be possible with additional compensation devices installed only on the secondary side of the transformer, and the load-generated neutral current needs to be compensated at the PCC to make sure the transformer neutral point remains at virtually zero potential [20]. Increasing the neutral conductor capacity is the simplest solution, however, it is not an economical and robust solution [18]. The network unbalance can also be mitigated using phase balancing [29] and phase swapping techniques [30]; however, this requires additional device installation and is more suitable for three-phase three-wire networks. There are two main types of neutral current, voltage unbalance and harmonic compensation methods available for 3P-4W networks:

(i) Passive compensation

(ii) Active compensation

The working principle of passive compensation methods is to absorb the zero sequence current flowing through the neutral conductor and improve the output current harmonics. Popularly used passive unbalanced compensation devices consist in the application of passive filter combinations [31-33], synchronous machines [21], magnetic transformer configurations, such as zig-zag, delta-

wye, T-connected etc. [34], and the combination of transformer and three-phase voltage source converters [35-37]. Installing passive compensation devices is quite simple, however, they need to be installed close to customer connection points to provide better performance. Additionally, they are quite bulky in size, expensive, and only provide indirect control over the unbalanced quantities.

Active neutral compensation is done by the power electronic converter which is a mandatory requirement for RES, uninterruptible power supplies (UPS) and active power filter (APF) topologies that need to be integrated into the three-phase four-wire distribution network. Therefore, in this thesis, neutral current compensation and unbalanced mitigation is focused primarily on the active neutral current compensation (ANCC) method. The available ANCC methods are described below.

2.3.1 Single-phase active power filter (APF) configurations

The installation of transformers close to the customer connection point provides passive neutral current compensation, but it suffers from unreliable performance during unbalance in the supply side. Therefore, single-phase converters are generally installed in series and shunt connection at the fourth wire to provide a hybrid solution for neutral current compensation. Single-phase converter connections with different transformer configurations are shown in Figs. 2.2 (a)-(d) [38-41]. The transformer, such as zig-zag and delta-wye, is connected in parallel with the loads, and the single-phase converter is connected in series with the neutral line with an additional bypass switch which will operate in case of converter failure as shown in Fig. 2.2 (a) [38]. The capacity reduction of the transformer for neutral current compensation is presented in [39], where an additional three-leg converter is used with the delta side of the zig-zag transformer as illustrated in Fig. 2.2 (b). The presented filter topology provides a six-fold lower capacity requirement the neutral current compensation from the ZT. The neutral current generated from voltage (capacitive) and current (inductive) source loads are compensated using a single-phase inverter and ZT application in [40]. The rectifier at the DC-side of the single-phase APF from the previously mentioned methods is removed using an additional control loop for the DC bus voltage regulation as indicated in Fig. 2.2 (c). This permits a lower volt-ampere requirement from the total installation unit and provides superior neutral current harmonic compensation performance. A single-phase series APF coupled with a matching transformer is utilised with the neutral conductor to mitigate either the third harmonic voltage contents or the neutral current as shown in Fig. 2.2 (d) [41]. The

APF is designed to behave as an inductor for the neutral current components. The sensed neutral current is transformed into synchronously rotating frame (SRF) *dq* components utilising the third harmonic phase angle from the neutral point voltage, and normalised to compensate for the output neutral current in addition to the DC bus voltage regulation.

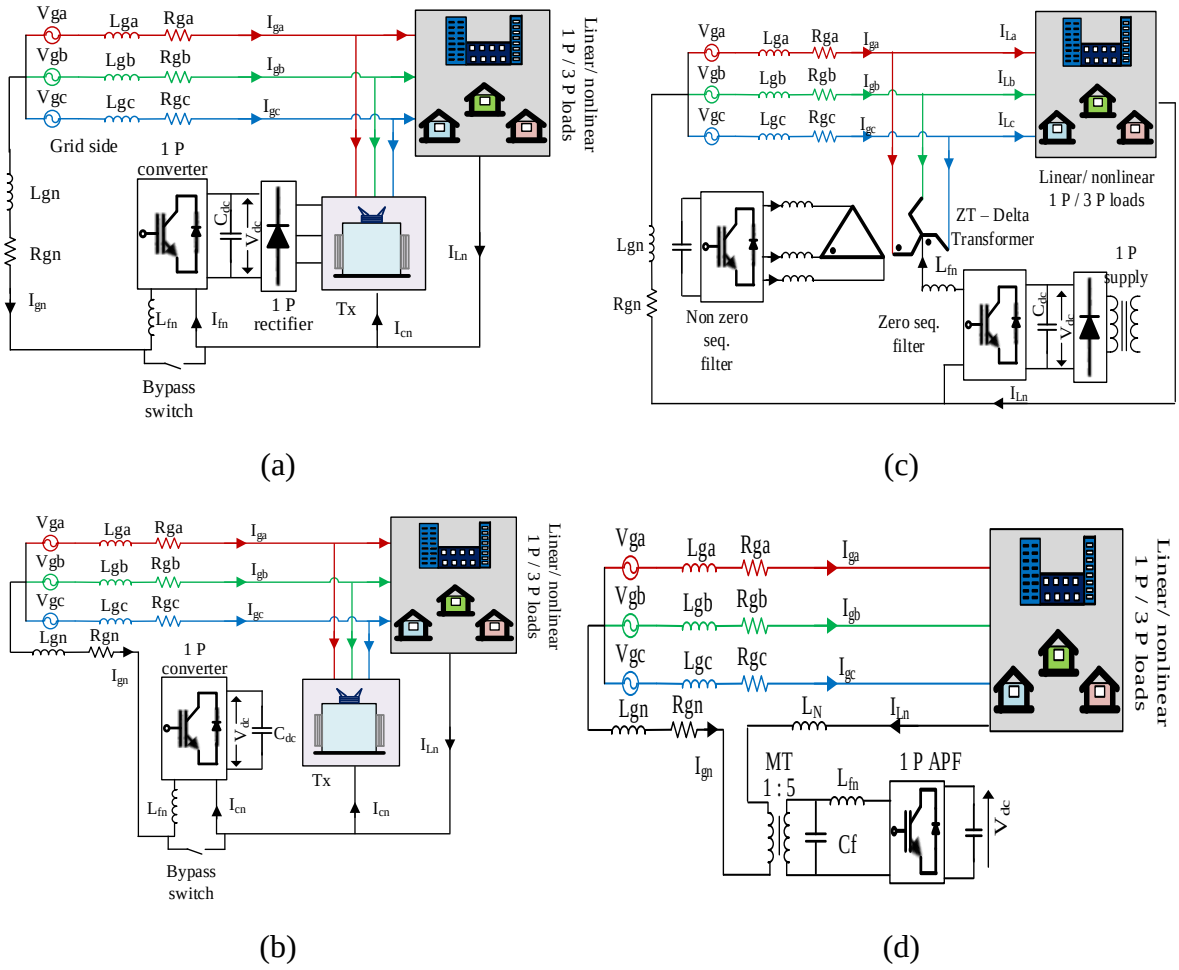

Figure 2.2. Singe-phase converter configurations from (a) [38], (b) [39], (c) [40], and (d) [41]

2.3.2 Three-phase four-wire APF configurations

One of the common three-phase four-wire APF devices is the split DC-link capacitor inverter. The fourth wire from the 3P-4W distribution system is connected at the middle point of the DC-link capacitors as depicted in Fig. 2.3 (a). The harmonic currents can flow via either of the capacitors and be absorbed. While this offers indirect control over the neutral current, it also provides a simple solution for the four-wire system with minimum switching device requirement. The shunt split-DC APF is presented for the compensation of current harmonics and zero sequence components using constant-power and sinusoidal current supply methods in [42]. The 3P-4W APF

does not require any extra DC power supply, and an additional DC voltage control loop serves to regulate the DC bus voltage difference between the two capacitors to become zero.

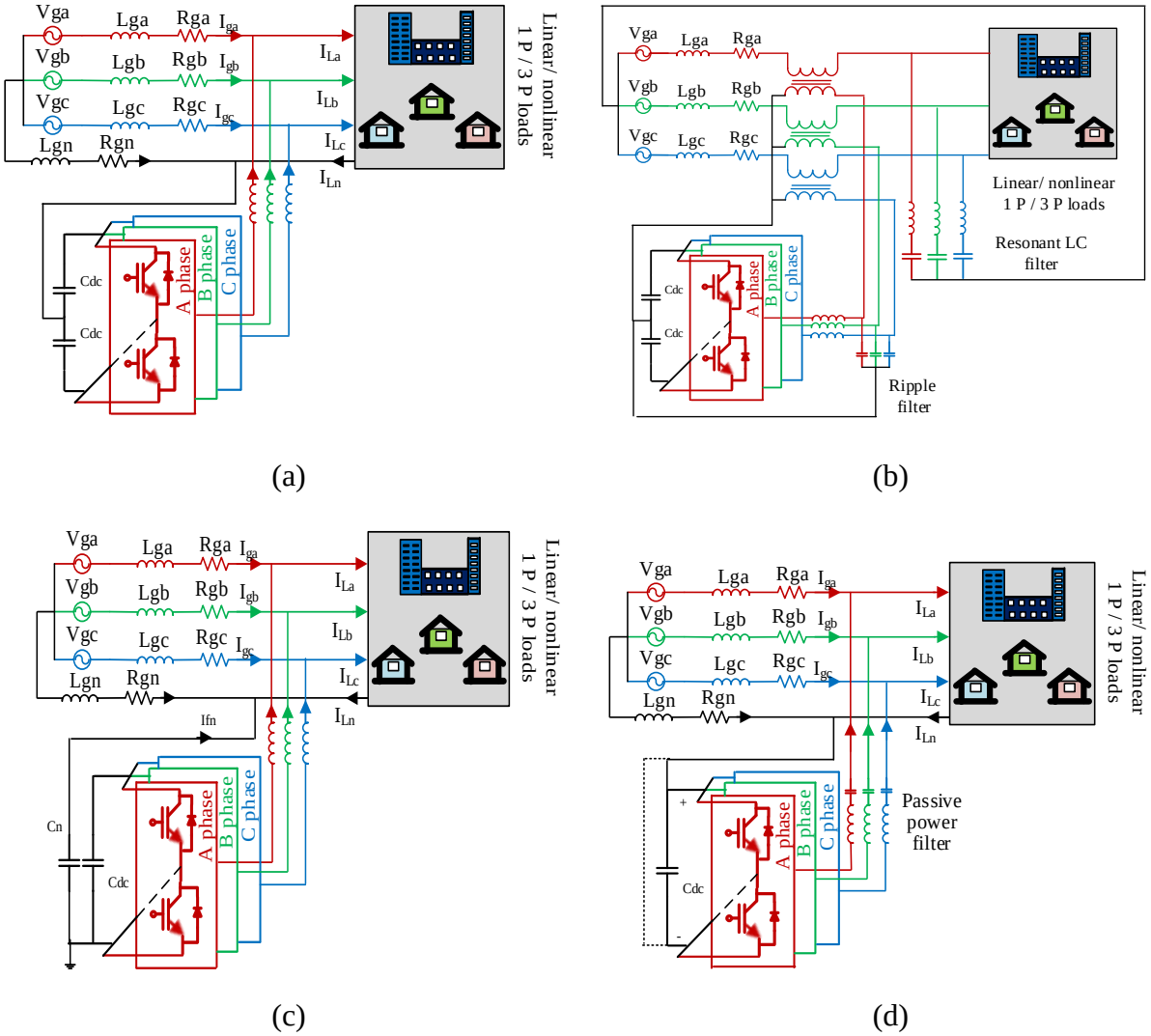

Figure 2.3. 3P-4W converter configurations from (a) [42], (b) [44], (c) [45], and (d) [46]

Utilising the symmetrical components of the PCC voltage, a three-dimensional space vector modulation (3D-SVM) method is presented with grid feeding operation in [43]. Series APF application with a capacitor midpoint converter is employed to compensate for voltage unbalances, such as sag and swell. It requires, however, additional zero sequence harmonic filtering as shown in Fig. 2.3 (b) [44].

Instead of using two DC-link capacitors, a hybrid combination of a single DC-link and a small AC capacitor is utilised in [45] to provide similar APF performance in a 3P-4W system using

instantaneous symmetrical compensation theory with a hysteresis-band controller as shown in Fig. 2.3 (c). The small AC capacitor is connected between the negative DC bus and the grid neutral connection. The proposed system eliminates the complexity of DC bus voltage regulation from the split DC converter topology. The authors in [46] proposed using a hybrid power filter combination by connecting the utility-side neutral directly to the positive or negative terminal of the DC bus as shown in Fig. 2.3 (d). This topology improves the performance of the passive filter section and reduces manufacturing costs. Additionally, due to the application of the passive filter in series at the AC side, the grid-side voltage drops across the AC capacitor and permits a less DC voltage required at the DC side.

2.3.3 Three-phase four-leg converter configurations

An established way to provide the neutral point for a three-phase four-wire network is to add an additional fourth leg, called a neutral leg, to the conventional three-leg inverter. The three-phase four-leg topology provides an additional degree of freedom for controlling the neutral current in addition to the active and reactive power compensation from the converter system. The configuration of the four-leg inverter is shown in Fig. 2.4 (a). The four-leg APF topology was introduced in the early 1980s and since then it has been attracting attention in many practical application sectors, for example, aircraft variable power supply [47], power supply for data and IT centres [48], electric vehicle applications [49], multiple AC induction motors control [50], permanent-magnet synchronous machine (PMSM) improved fault tolerance capability [51], APF operation [52-54], STATCOM operation [55-56], dynamic voltage restorer (DVR) to provide voltage support to sensitive loads during voltage imbalances [57], RES installation with grid [58-62], standalone operation with RES units [63], leakage-current elimination from PV installations [64], unified power quality conditioning operation [65], in matrix converters which can operate under high temperature and pressure [66], medical equipment etc.

A Shunt APF operation with two-level four-leg inverter is proposed in [58] which performs compensation of voltage unbalance and current harmonics while supplying power from the RES to the grid. The authors used a digital controller, applying instantaneous reactive power theory to control the inverter and a periodic sampling technique for generating the switching states. Using the hysteresis controller, similar APF functionality is included with RES installations with a four-leg inverter to enhance the PQ performance in [59]. Different power-generation and load-demand

scenarios are presented to evaluate the proposed system's performance. With traditional PI controllers, the authors in [60] proposed a dual stage topology with a PV system and two parallel-connected four-leg inverters. A novel zero sequence circulating current compensation method is proposed in addition to the APF operations. Similar APF operation from an RES integrated four-leg inverter is presented with a neutral network (NN) control algorithm based on least mean square Adaline (adaptive linear element) in [61] and a model predictive current scheme in [62] to estimate the control reference signals robustly.

A similar four-leg topology can also be applied to the current source inverter (CSI), which utilises a larger DC-link inductor connected in series with the DC current source at the DC-side of the inverter as shown in Fig. 2.4 (b). The CSI topology provides a higher AC output voltage than the VSI topology along with other traditional operations similar to VSI [67]. The combination of four-leg and split DC-link capacitor topologies is used to eliminate the common mode voltage (CMV) created by the modulation operation of the inverter. The configuration is known as an active split DC-link converter topology and is shown in Fig. 2.4 (c). Common mode current can cause malfunctioning of sensitive electronic devices, for instance in aircraft, industrial appliances, and motor drives. The active split DC-link combination is utilised to force the common mode to ground voltage zero. Adding the fourth leg with the split DC-link method reduces the switching frequency component in the common mode voltage and actively regulates the CMV to zero [68]. The authors in [69] developed a relationship that represents the load neutral point voltage (LPNV) effects with the inverter switching states and the ratio of the neutral inductor to the phase inductors (k). They applied a modified switching strategy to coordinate the 16 switching states from the inverter into four switching groups, utilised to eliminate the LPNV based on different values of k. However, the introduction of the split DC capacitors generates an oscillation in the output voltage with discontinuous modulating signals from the inverter. Therefore, the single DC-link three-phase four-leg multifunctional inverter topology is utilised in this thesis with the grid-tied PV system.

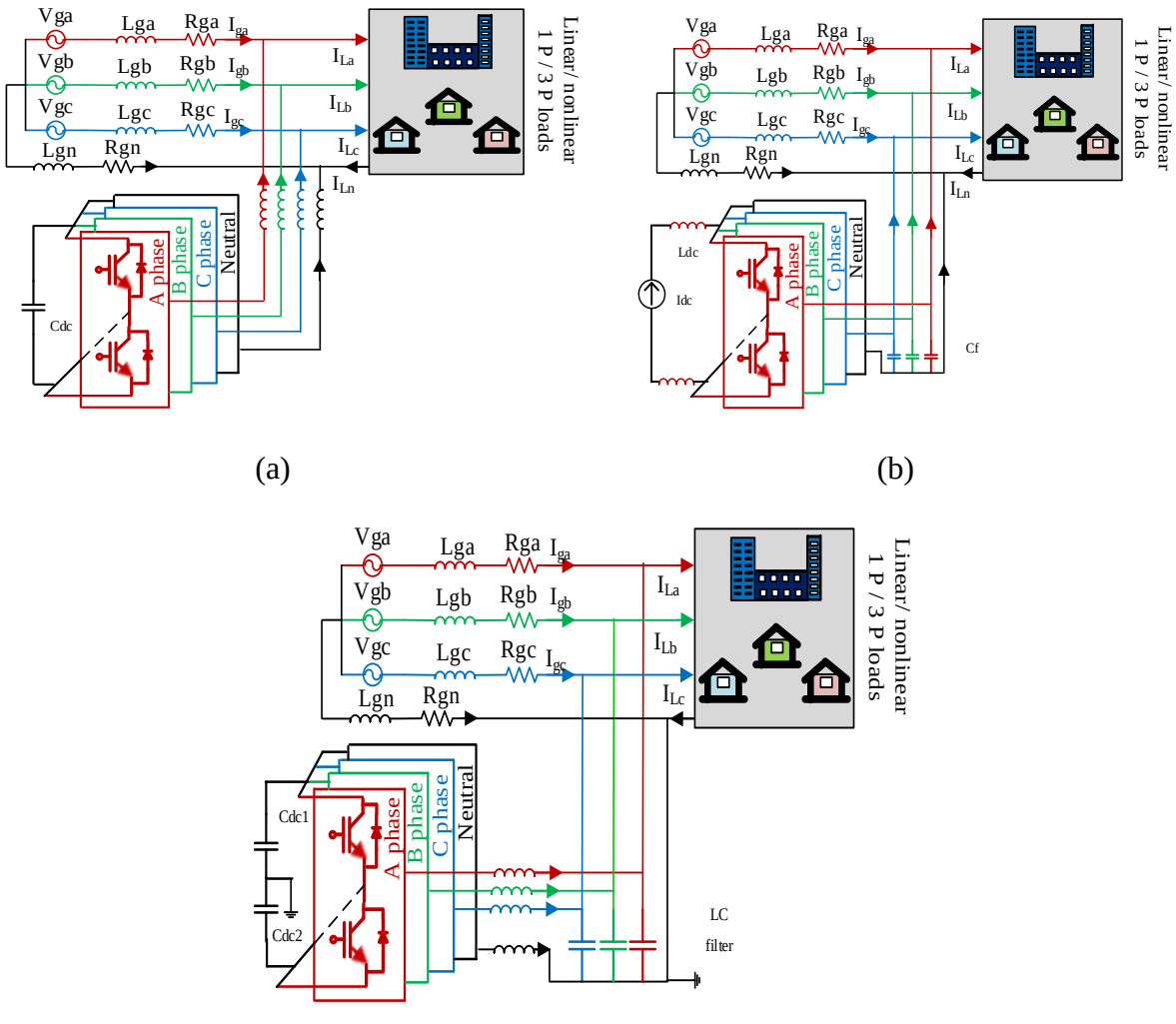

Figure 2.4. Three-phase four-leg converter configurations: (a) VSI, (b) CSI, and (c) active split DC-link

2.3.4 Three half-bridge configuration

The three half-bridge (3-HB) connection with a single DC-link capacitor allows the APF topology to have independent control over all three phases. Traditional APF operations in a 3P-4W system, such as regulation of reactive power, elimination of harmonic currents, correction of phase unbalance, and compensation of neutral current, can also be performed with the 3-HB configuration. Control over each phase quantity is possible utilising each half-bridge to operate similarly as a single-phase APF as shown in Fig. 2.5. Therefore, even with single-phase or double-phase disconnection conditions, it is possible to keep the other phase/s operation running without affecting the DC-link capacitor. This configuration provides indirect control over the neutral

current and, due to higher switching device requirements, it is mainly suitable for high-power applications [70-71].

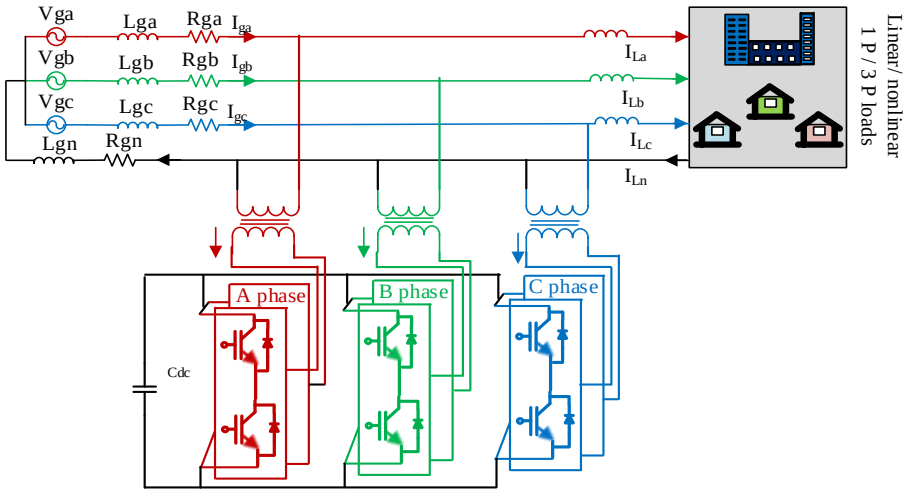

Figure 2.5. Three half-bridge (3HB) converter topology

Many significant studies have been done on voltage regulation [7-13] and unbalanced compensation [14-71]. To achieve independent control over active, reactive and unbalanced compensation, active compensation devices, for example split DC-link (2C), four-leg inverter (4L) configuration, and three half-bridge (3-HB) configurations, are found to have the most versatile control options, especially considering the integrated operation with RES. The technical requirements and comparing the performance of the capacitor midpoint (2C), 4L-VSI, and 3-HB configurations are shown in Table 2.1. From Table 2.1, it can be seen that the 2C configuration provides the simplest way of controlling active, reactive and unbalance compensation, however, it suffers from DC bus voltage imbalance and requires a high value of DC capacitors. The 3-HB configuration provides flexible control on each phase quantity and controls the neutral current indirectly by balancing the three phases. However, it requires a higher number of switches which can increase switching losses for low-power applications. While the four-leg topology lacks the control over each phase quantity (independent control over A, B, and C phases), it does provide superior performance in the three-phase range, and it is most suitable for low to medium power applications. The majority of residential and commercial users are situated in the LV network, and therefore considering the application of RES and unified control of active, reactive and neutral current regulations, the four-leg converter topology is considered in this research to evaluate the performance improvement with the proposed control methodologies.

Table 2.1 Comparison of different four-wire converter configurations [72-73]

Parameter	Capacitor mid-point (2C)	Four-leg (4L)	3-HB
V_{DC}	Highest (2.8 * Vrms)	Medium (2.4 * Vrms)	Lowest (1.4 * Vrms)
DC capacitor requirement and quantity	Highest 2 C_{DC}	medium 1 C_{DC}	Low 1 C_{DC}
I_{rms} through C_{DC}	Highest	Medium	Lowest
Energy stored (C_{DC})	Highest	Low	Lowest
Neutral current	Full neutral current through C_{DC}	Direct control by fourth leg	Indirect control by phase balancing/ harmonic compensation
Additional sensor	Extra dc bus voltage	Extra neutral current sensor for the fourth leg	None
No. of switches	6	8	12
Switching device power	Low	Highest	Low
Switching device rating	High voltage	Unequal rating for the fourth leg	Equal rating
Isolation transformer	No	No	Yes
Modulation	Sine PWM	3D-SVM and/or *dq0*	Single-phase
Size/weight	Medium	Low	High
APF control	Indirect	Direct	Indirect
Current unbalance factor	Highest	Lowest	Low
Neutral current mitigation	Degraded performance with unbalanced dc voltage	Better than 2C and 3HB	Better than 2C
Cost	Lowest	Higher than 2C	Highest
Application sector	Low or medium power application	Low or medium power application	Medium to high power application
RES integration	Not common	Common	Not common

2.4 Different Electrical Connection Standards

Most countries have their own electricity connection standards which are generally provided by local distribution network operators (DNO) for particular areas. In general, the voltage regulation requires DNOs to maintain the PCC voltage at ± 6%. However, some DNOs prefer the voltage range to be within the range of + 10% and - 6% to accommodate more RESs into their system [74]. Any electrical equipment connected to the distribution network needs to follow specific power quality standards. The electrical equipment can be any consumer loads or RES units which are generally connected via a power electronic converter to the grid. Nonlinear loads typically draw non-sinusoidal currents from a sinusoidal supply voltage, causing poor power quality at the supply side. European Union Industry and Commerce pays approximately 10 billion euros each year due to losses resulting from poor power quality in their distribution network [75]. To interact with the power quality issues, two types of voltages are defined in the IEC 038 standard [76]:

i. Supply voltage (Line to line (L-L) / line to neutral (L-N) at PCC
ii. Utility voltage at the plug/ terminal of electrical equipment

It is the responsibility of customers to maintain good power quality at their utility voltage connection point and the DNOs are responsible for the supply voltage side. Degradation in the customer end voltage can happen because of disturbances on the supply side or by any other equipment operated by different users connected at the utility side. Therefore, a specific unbalance factor for voltage is maintained at the customer connection point. There are many definitions available for the voltage unbalance factor [16]. Considering the positive and negative sequence components of the voltage and current at the PCC, the unbalance factor (UF) can be expressed as:

$$UF = \frac{|G_{neg.seq.}|}{|G_{pos.seq.}|} \tag{2.1}$$

where G can be voltage or current. Most of the international standards use the above expression to define the UF in their network. However, for a 3P-4W network, the UF should be expressed considering additional zero sequence components as considered in (2.2) below [24], [27]:

$$UF = \frac{\sqrt{|G_{neg.seq.}^2|+|G_{zero.seq.}^2|}}{|G_{pos.seq.}|} \tag{2.2}$$

The VUF requirements from different countries are shown in Table 2.2 [77].

Table 2.2 Voltage unbalance factor standards for different countries

Country	VUF (%)	Code
USA	< 3 2 1	ANSI C84.1 IEC [78] NEMA-MG-1[79]
England and Wales	1 (under planned outage)	CIGRE working group C4.07 recommends 2 % for HV, MV, and LV 1.5 % for EHV 3% for predominantly single-phase load connections
Scotland	2	GB grid code
Germany	2	At transmission and distribution levels
Australia	2	For short duration 3% [80]
France	2	RTE at transmission level
South Africa	2	For HV, MV and LV. Increase to 3% is considered
Canada, Hydro Quebec	1	Transmission level based on 2 hrs avg. (2% for MV and LV network)
New Zealand	1	Electricity Governance Rules 2003, Part C Common Quality
Brazil	2	At all voltage levels

ANSI C84.1 recommends the maximum VUF to be less than 3%, however, in most of the states in the USA, the VUF is restricted to max 2.5% [81]. The ANSI/IEEE std. 141-1993 and 241-1990 state that computer loads behave abnormally if the VUF is higher than 2.5%. A few motor manufacturers require the current unbalance factor (CUF) to be 5% to validate their warranty claims, whereas NEMA MG1 requires VUF to be 1% which generates around 6-10% CUF into the connected system [78]. Details about the effects of voltage unbalance on certain types of motor can be found in Australian Standard AS 1359.31.

The National Electricity Code of Australia (NECA) and National Electricity Regulator (NER) mainly set the voltage and current unbalance limits within Australia's electricity network. The permissible VUF and different electrical connection standards in Australia are shown in Tables 2.3 and 2.4.

Table 2.3 VUF at specific voltage levels in Australia [80]

Voltage level	Unbalanced factor $_{Neg. seq.}$			
	No contingency %	Credible contingency event	General	Once per hr
>100 kV	0.5	0.7	1	2
10 kV to 100 kV	1.3	1.3	2	2.5
< 10 kV	2	2	2.5	3

Table 2.4 Australian Standards (AS) and New Zealand Standards (NZS) specifications [74]

Standard	Purpose	
AS 4777	Energy system connection to grid via inverters	ΔV + 10%, -6% pf 0.8 lead to 0.95 lag THD till 50^{th} < 5% DC output current at Ac terminal < 0.5%, i.e. 5 mA In three-phase systems, the phase imbalance between the phases must be less than 20 A, VUF 2%
AS 3000	Electrical installation wiring rules	

AS/NZS 61000.3.100	Steady state voltage limit in public electricity systems	Nominal 230 V, Maximum 253 V, Preferred 244 V Minimum 216 V Preferred 225 V
AS 61000.3	Electromagnetic compatibility limits EMC	
AS 61000.3.2	Limits for harmonic current emissions	
AS/NZ TR IEC 61000.3.14	Assessment of emission limits for harmonics, inter-harmonics, voltage fluctuations and unbalance for the connection of disturbing installation to LV power system	VUF less than 2%

According to one of largest local DNOs in Australia, Ausgrid, NSW, the customer should use special relay circuits to trip the equipment generating an unbalanced current. Additionally, customers should ensure that their load is balanced and the neutral to ground voltage is less than 10 V [74]. The neutral to ground voltage can rise during phase to ground faults in a situation where the neutral wires are connected to metallic water pipes. Special neutral displacement protection relays can also be installed to prevent the NGV rise [78].

From Table 2.1, it can be seen that the requirement of dynamic solutions, such as the application of STATCOM, is considered after the PV penetration is higher than 100%. This is to maintain the PCC voltage within range, however, the situation can get worsen with network unbalance issues as described in the above sections. Energex, the local DNO for Brisbane, Queensland, recommends that PV installations higher than 3 kVA units should provide any required leading or lagging pf operation to regulate the PCC voltage at the customer installation point [5].

Based on the literature review and electricity connection standards, it is evident that RESs and power electronic converters installed in the LV network need to reflect proper dynamic characteristics in simulation and hardware platforms. This is necessary to verify the requirements from the electricity connection standards. Therefore, in the next section, a detailed modelling of the RES and inverter units is described. The construction and description of the considered low-voltage power system network as it operates in Brisbane is presented at the end of this chapter.

2.5 Modelling of RESs and Power Electronic Converters

To evaluate the effect of PV penetration, a single-stage transformerless three-phase three-leg (3P-3L) inverter topology is designed with a dynamic PV module and battery energy storage (BES) system. The D-STATCOM and smart VSI units are designed in similar configurations but with different current and voltage ratings. For analysing the unbalance effects in the three-phase four-wire (3P-4W) LV network, a three-phase four-leg (3P-4L) inverter is designed with the PV system. Both the three-leg and four-leg inverters are designed to have independent control over active and reactive powers. The modelling of the considered RES units and the power electronic converters is described below:

i. PV system
ii. BES system
iii. Three-leg STATCOM and smart VSI
iv. Four-leg smart VSI

2.5.1 PV system

A real-life PV system exhibits nonlinear characteristics due to the variations in sun irradiance, temperature, cloud-passing etc. To avoid complexity and reduce the simulation time, a constant DC voltage source is generally used to model for the PV units. However, to capture most of the nonlinear characteristics and to provide approximate real-life performance from the designed system, a dynamic PV module is utilised consisting of several series and parallel connected arrays, which are further subdivided into series-parallel PV cell combinations.

Generally, a PV installation unit consists of two sections:

i) PV modules with/without DC-DC converter, and
ii) Interlinking power electronics interface voltage source converter (VSC) between the DC and AC side

The maximum power point tracking (MPPT) operation is commonly integrated with the DC-DC boost converter section and this topology is considered as a double-stage PV-VSI installation. Instead of a double-stage design, a single-stage PV system is focused on in this research study, i.e. without the DC-DC converter stage. Although single-stage PV operation requires a higher DC bus

voltage for independent active and reactive power control operations from the VSC, the energy losses associated with a multistage energy converter can be avoided. This also provides a faster dynamic response due to the absence of DC-DC converter execution time delay. The current from the PV array can be expressed as [82-83]:

$$i_{pv} = N_p I_{Ls} - N_p I_s \left[\exp\left[\alpha_p \left(\frac{V_p}{N_s} + \frac{R_s i_{pv}}{N_p}\right)\right] - 1\right] - \frac{N_p}{R_{sh}}\left(\frac{v_{pv}}{N_s} + \frac{R_s i_{pv}}{N_p}\right) \quad (2.3)$$

where I_{Ls} is the current corresponding to sunlight

I_s is reverse saturation current chosen as 9×10^{-11} A

N_s is the number of cells in series

N_p is the number of modules in parallel

R_s and R_{sh} are the series and shunt resistances of the array

i_{pv} is the current flowing through the array

v_{pv} is the output voltage of the array

The constant $\alpha_p = \frac{q}{AkT_r}$

where $k = 1.3807 \times 10^{-23}$ J K^{-1} is the Boltzmann constant

$q = 1.6022 \times 10^{-19}$ C is the charge of an electron

A is the p-n junction ideality factor with a value between 1 and 5,

and T_r is the cell reference temperature, generally 25°C or 298 K.

The power delivered by the solar cell can be expressed as a function of solar irradiance, temperature, and the corresponding voltage and can be expressed as:

$$P_{pv} = f(v_{dc}, S, T) = i_{pv} v_{pv} \quad (2.4)$$

The characteristics of the PV unit (maximum 20 kW at standard test condition) with variation in solar irradiance are shown in Figs. 2.6 and 2.7.

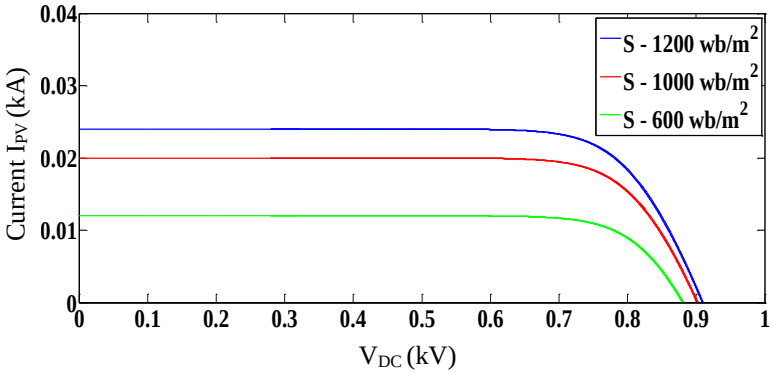

Figure 2.6. PV-generated current vs V_{DC} characteristics with variable solar irradiance

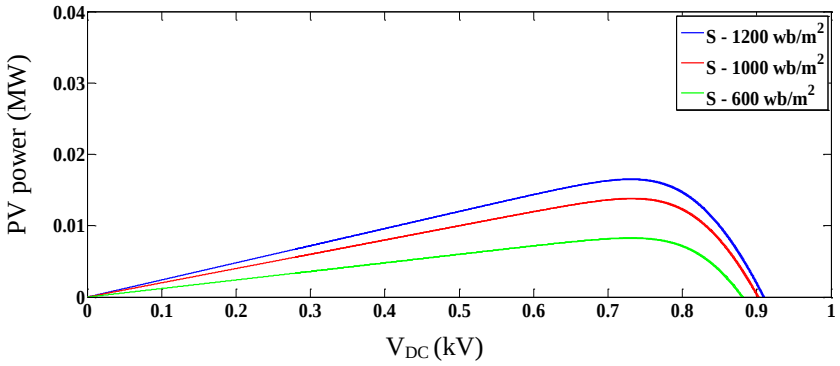

Figure 2.7. PV-generated power vs V_{DC} characteristics with variable solar irradiance

The single-stage DC voltage regulation can be written as

$$\dot{v}_{DC} = \frac{1}{C_{DC}}(i_{PV} - i_{DC}) \tag{2.5}$$

The PV generated DC current and inverter output AC current can be related using the three modulating signals (S_a, S_b, S_c) from the voltage source inverter (VSI) as

$$i_{DC} = i_{fa}S_a + I_{fb}S_b + i_{fc}S_c \tag{2.6}$$

where a, b, c signify the parameters corresponding to the three-phases.

Inserting (2.5) into (2.6) results in:

$$\dot{v}_{DC} = \frac{1}{C_{DC}} i_{PV} - \frac{1}{C_{DC}}(i_{fa}S_a + I_{fb}S_b + i_{fc}S_c) \tag{2.7}$$

The PV-generated DC current is converted to an AC current with the VSI modulation technique which uses a high-frequency switching with the power electronic switches. Therefore, the VSI

output current contains a great amount of lower- and higher-order harmonics. Generally, a filter combination is used to smooth out the harmonic contents before supplying the current to the loads. Commonly used filters are L, LC, and LCL combinations. Selecting the filters depends on several parameters, such as ripple current percentage, reactive power requirement, switching frequency, ripple attenuation factor etc. In some cases, active filtering is also performed by compensating the harmonic currents utilising the VSI current injection method. Among the passive filters, the LCL filter provides a higher noise attenuation at 60 dB/decade than the L (20 dB/decade) or LC (40 dB/decade) filters. Therefore, for the simulation analysis, an LCL filter is utilised with the 3P-3L PV-VSI. Considering the same value for the three-phase filter inductor as (L_f), the mathematical modelling of the PV-VSI with the LCL filter from Fig. 2.8 can be written as [82-84]:

$$\begin{aligned}
\dot{i}_{fa} &= -\frac{R_{fa}}{L_{fa}} i_{fa} - \frac{1}{L_{fa}} v_{cfa} + \frac{v_{DC}}{3L_f}(2S_a - S_b - S_c) \\
\dot{i}_{fb} &= -\frac{R_{fb}}{L_{fb}} i_{fb} - \frac{1}{L_{fb}} v_{cfb} + \frac{v_{DC}}{3L_f}(-S_a + 2S_b - S_c) \\
\dot{i}_{fc} &= -\frac{R_{fc}}{L_{fc}} i_{fc} - \frac{1}{L_{fc}} v_{cfc} + \frac{v_{DC}}{3L_f}(-S_a - S_b + 2S_c)
\end{aligned} \tag{2.8}$$

$$\begin{aligned}
\dot{v}_{cfa} &= \tfrac{1}{C_{fa}}\left(i_{fa} - i_{ga}\right) & \dot{i}_{ga} &= \tfrac{1}{L_{ga}}\left(v_{cfa} - v_{ga}\right) \\
\dot{v}_{cfb} &= \tfrac{1}{C_{fb}}\left(i_{fb} - i_{gb}\right) & \dot{i}_{gb} &= \tfrac{1}{L_{gb}}\left(v_{cfb} - v_{gb}\right) \\
\dot{v}_{cfc} &= \tfrac{1}{C_{fc}}\left(i_{fc} - i_{gc}\right) & \dot{i}_{gc} &= \tfrac{1}{L_{gc}}\left(v_{cfc} - v_{gc}\right)
\end{aligned} \tag{2.9}$$

where $\dot{x} = \frac{dx}{dt}$; x can be current or voltage, and the remaining symbols have the standard meanings.

Since, controlling DC quantities is faster and easier than controlling AC quantities, the synchronous rotating frame transformation (*abc-dq*) is applied to (2.7)-(2.9). A phase locked loop (PLL) is used to extract the synchronous angle ω_{pcc} from the grid. It is considered that the inverter side line resistance (R_f) and filter capacitors (C_f) in three phases have same value. The *abc-dq* transformed quantities are as follows:

$$\begin{aligned}
C_{DC}\dot{v}_{DC} &= i_{PV} - i_{fd}S_d - i_{fq}S_q \\
L_f\dot{i}_{fd} &= -R_f i_{fd} + \omega_{pcc}L_f i_{fq} - v_{cfd} + S_d\, v_{DC}
\end{aligned}$$

$$
\begin{aligned}
L_f \dot{i}_{fq} &= -R_f i_{fq} - \omega_{pcc} L_f i_{fd} - v_{cfq} + S_q \, v_{DC} \\
C_f \dot{v}_{cfd} &= \omega_{pcc} C_f v_{cfq\_} C_f (i_{fd} - i_{gd}) \\
C_f \dot{v}_{cfq} &= -\omega_{pcc} C_f v_{cfd\_} C_f (i_{fq} - i_{gq}) \\
L_g \dot{i}_{gd} &= +\omega_{pcc} L_g i_{gq} + v_{cfd} - v_{gd} \\
L_g \dot{i}_{gq} &= -\omega_{pcc} L_g i_{gd} + v_{cfq} - v_{gq}
\end{aligned}
\tag{2.10}
$$

From the transformed quantities, the instantaneous active and reactive powers can be written as:

$$
\begin{aligned}
P_{PCC} &= \frac{3}{2}(v_{gd} i_{gd} + v_{gq} i_{gq}) \\
Q_{PCC} &= \frac{3}{2}(v_{gq} i_{gd} - v_{gd} i_{gq})
\end{aligned}
\tag{2.11}
$$

The phase locked loop (PLL) angle from the supply voltage is utilised which makes the *q*-axis voltage component vector, v_{gq}, align with the grid voltage vector, resulting in $v_{gq}=0$, and the instantaneous powers can be written as:

$$
\begin{aligned}
P_{PCC} &= \tfrac{3}{2} v_{gd} i_{gd} \\
Q_{PCC} &= -\tfrac{3}{2} v_{gd} i_{gq}
\end{aligned}
\tag{2.12}
$$

It can be seen from (2.12) that the active and reactive powers can be controlled independently by controlling the i_{gd} and i_{gq} currents.

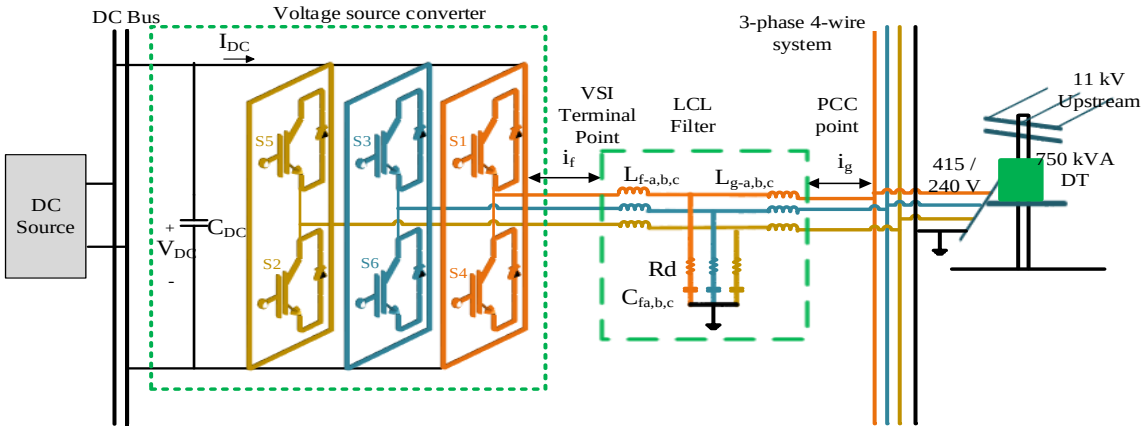

Figure 2.8. Three-phase three-leg VSI connection diagram

2.5.2 BES system

Two types of BES installations are considered for the PV penetration analysis in Chapter 3:

i) BES with D-STATCOM, and

ii) Residential BES with three-phase PV units.

The battery model available in the power system computer aided design (PSCAD) software master library is utilised in this thesis and is chosen because of its dynamic characteristics, namely a state of charge (SOC) dependent battery terminal voltage [85-86]. The battery parameters can be calculated from the BES discharge curve provided by the manufacturers. A separate battery monitoring and management system (BMMS) is designed using a bidirectional DC-DC converter as shown in Fig. 2.9 (a), and connected to the DC bus. The BMMS reduces the BES terminal voltage requirement by one half compared to the direct connection of the BES to the DC bus.

Depending on the battery size, maximum and minimum I_d current limits are chosen for the BES charging and discharging operations as shown in Fig. 2.10. The BMMS utilises the switch S_{buck} for the charging operation (voltage buck) and switch S_{boost} for the discharging operation (voltage boost). To prevent overloading in the VSC current controllers, the constant-current charge and discharge methods are used in this research. The charging/discharging command is initiated after monitoring the battery SOC, PV generation status, load demand requirement, and power-sharing requirement. A uniform rates of charge and discharge is used with the BMMS, however, non-uniform techniques can also be incorporated with the designed BMMS system for diverse BES operations.

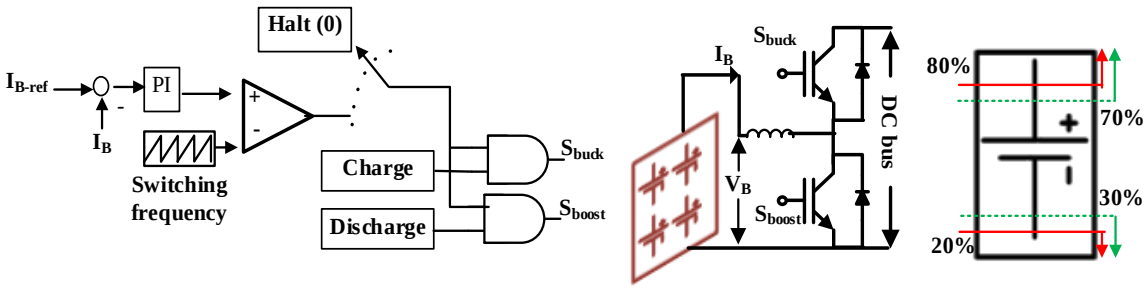

(a) (b) (c)

Figure 2.9. (a) BMMS control diagram, (b) connection with DC bus, and (c) SOC limits

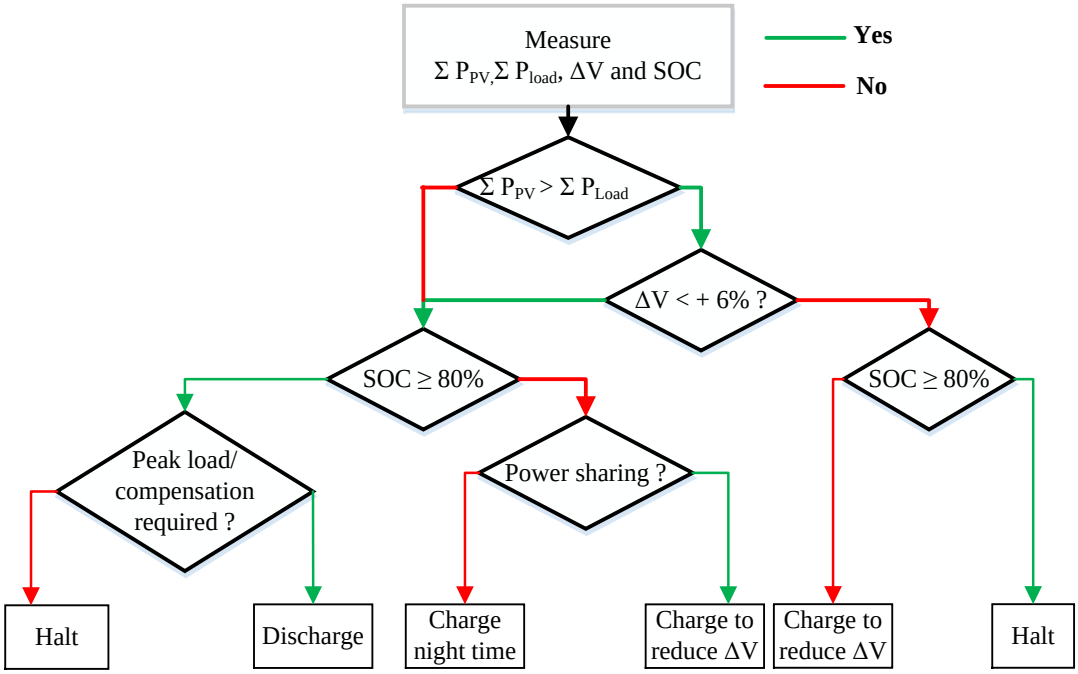

Figure 2.10. BES charge, discharge, and halt operations flow chart

The BMMS system controls the DC-DC controller for three operating modes:

i. Charge

ii. Discharge, and

iii. Halt

Deep charge and discharge operations are avoided in the BMMS design. This restricts the depth of charge (DOC) and depth of discharge (DOD) levels to a maximum 80% and minimum 20% level. For daytime charging, another 10% SOC limit can be considered, making the DOC and DOD a maximum 70% and minimum 30% as shown in Fig. 2.9 (c).

2.5.3 Three-leg D-STATCOM and smart VSI

D-STATCOM is a shunt-connected VSC which is mainly used for dynamic voltage restoration, flicker mitigation, and utility power factor (pf) correction by controlling the angle between the converter output current and grid voltage. Depending on the system requirement, it can inject reactive power, i.e. inject capacitive current, or can absorb reactive power, i.e. absorb inductive current, to/from the connected system. One of the main reasons for the wide application of D-STATCOM in a dynamic analysis is its characteristic of having control over its rated current, despite reductions in the connection point voltage [87]. The dynamic models of the PV-VSI and

STATCOM-VSC are similar in configuration as shown in Fig. 2.8. The VSCs in both devices can be controlled using the voltage magnitude and phase angle. The traditional D-STATCOM is capable of working in two quadrant modes, i.e. inductive (lagging) and capacitive (leading) modes. The DC capacitor of the VSC plays an imperative role for individual controls over active and reactive power components. The charging of the DC capacitor is generally controlled via the anti-parallel diode with each IGBT switches in the VSC. Installing a separate storage medium, such as BES, with D-STATCOM can control the system in four quadrant operating modes which results in additional BES charging and discharging modes.

A similar control concept can be applied for the PV smart VSI with reactive compensation capability. As the total capacity of the VSI is designed to handle maximum PV output during peak PV generation, except around mid-day, the PV-VSI cannot use its full capacity. For example, for a standard test condition (STC), a 5 kVA PV unit can supply around 4.3-4.5 kW after compensating for the line and switching losses. If the sun irradiation becomes less than the STC, the VSC will only supply reduced active power and will have some unused capacity available during the day and almost full capacity during the night. It can be calculated as:

$$Q_{vsc} = \sqrt{S_{vsc}^2 - P_{vsc}^2} \tag{2.13}$$

where S_{vsc}, P_{vsc} and Q_{vsc} are the apparent, instantaneous active, and reactive powers of the VSC. For unity pf VSI operation, Q_{VSC}, and for D-STATCOM P_{VSC}, is generally set to zero. Therefore, a unity pf VSI cannot utilise the unused capacity from the PV installations. For smart VSI operations, Q_{VSC} is set to fixed pf 0.95 lagging control following the Australian connecting standards. In addition, the unused Q_{VSC} can also be utilised for power-sharing among neighbouring RES units if required. The current references for active and reactive current controllers can be written from (2.12) as [87]:

$$\begin{aligned} i_{dref} &= \frac{\frac{2}{3}P_{pcc}}{v_{gd}} \\ i_{qref} &= -\frac{\frac{2}{3}Q_{pcc}}{v_{gd}} \end{aligned} \tag{2.14}$$

The $Q_{pcc\text{-}ref}$ can be set either as a fixed reference or be generated via additional external control loops, such as PCC voltage regulation, pf correction, VAR compensation etc. In this thesis, the PCC voltage regulation is mainly focused on both D-STATCOM and smart VSI operation. The PCC voltage can be regulated by controlling the v_{gd} voltage component as seen from (2.14).

For D-STATCOM and smart VSI operation, two external control loops, one for DC bus voltage and one for PCC rms voltage regulation, are designed. Both leading and lagging pf control operations are considered for D-STATCOM, whereas only the lagging pf operation is considered for PV- SVSI. The internal decoupled current control loop is designed from (2.10). The output from the external control loops are utilised as the reference inputs for the decoupled current controller and used to generate the modulating signals for the VSC switching operation. The traditional pulse-width modulation (PWM) switching technique is applied to generate the switching signals for the six switches for the D-STATCOM and PV inverters (both unity pf and SVSI). The detailed VSI control structures are shown in Fig. 2.11.

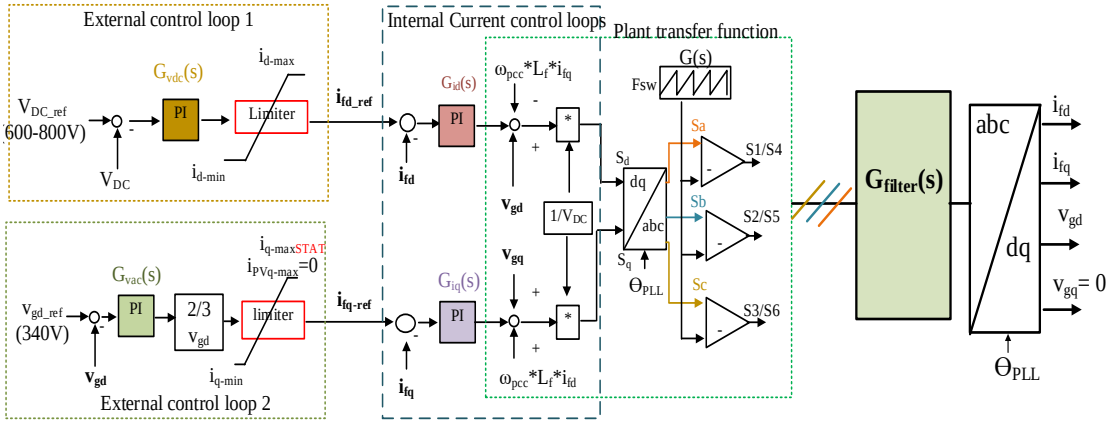

Figure 2.11. Control diagram of 3P-3L D-STATCOM and smart VSI

The controllers are tuned to maintain the modulation signals within the linear operation region (± 1). The single-phase PWM signal is shown in Fig. 2.12. The individual control loops and the plant transfer functions are linearised using a small perturbation around the DC operating point [83], and the PI gain values are initially set using the symmetrical optimum tuning method. To reduce the harmonic content generated by the switching signals and external noise, the LCL filter is designed and implemented with the SVSI and D-STATCOM units [84].

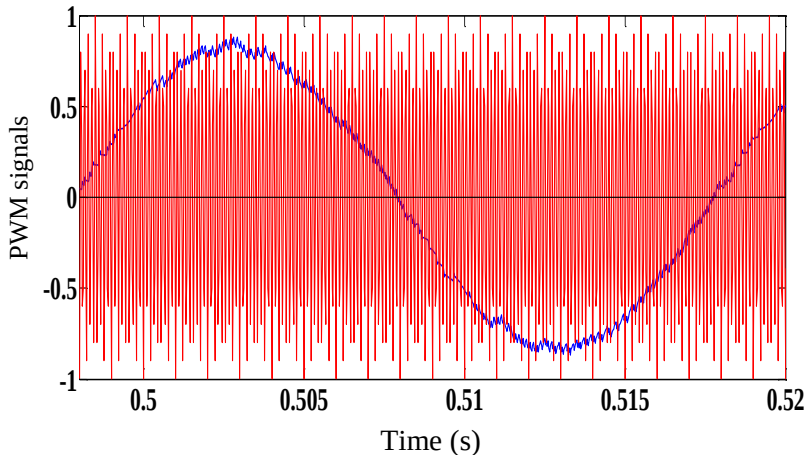

Figure 2.12. SPWM signals

2.5.4 Three-phase four-leg smart VSI (SVSI)

The three-phase four-leg SVSI is designed to operate with the 3P-4W LV network as shown in Fig. 2.13. The additional fourth leg is utilised to apply independent neutral current control and the other three legs are used to control active and reactive powers from the system.

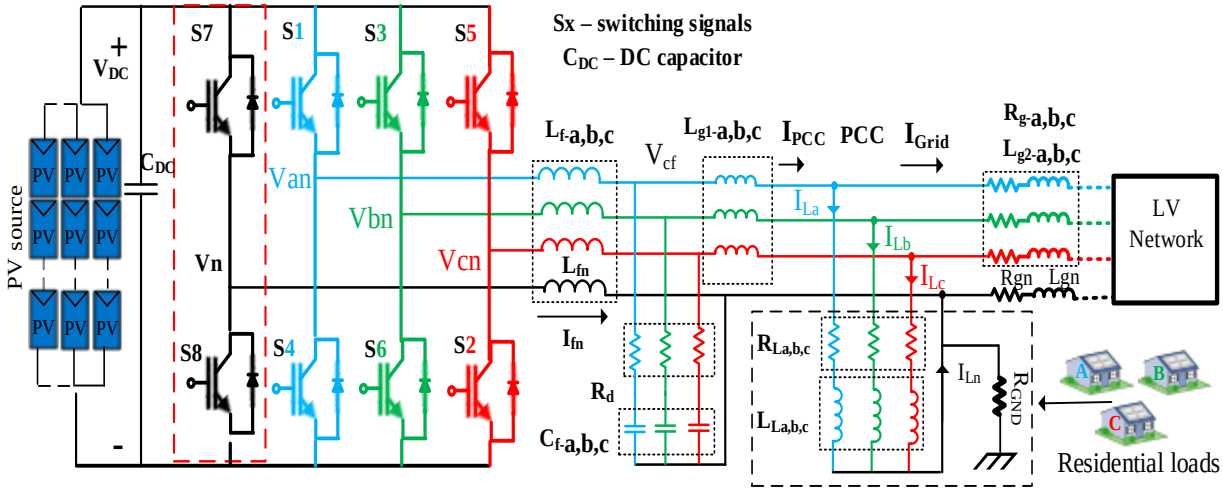

Figure 2.13. PV with four-leg SVSI connection

The single-phase average equivalent-circuit representation of the designed 3P-4L PV-SVSI system is shown in Fig. 2.14. Due to the switching frequency being higher than the fundamental frequency, voltage and current ripples are ignored in the average equivalent-circuit modelling [60].

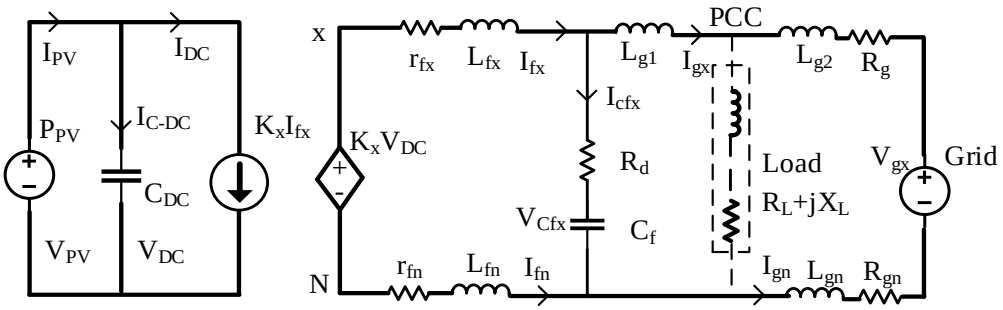

Figure 2.14. Average equivalent circuit model of single-phase unit

Considering the resistive line losses and applying a passive damping resistor R_d in series with the filter capacitor C_f, the dynamics of the four-leg PV-VSI system can be written as:

$$L_{f_x}\frac{d}{dt}I_{fx} = V_{DC}K_x - r_{fx}I_{fx} - R_d\left(I_{fx} - I_{gx}\right) - V_{cfx} + L_{fn}\frac{d}{dt}I_{fn} + r_{fn}I_{fn} \tag{2.15}$$

$$L_{gx}\frac{d}{dt}I_{gx} = V_{cfx} - R_{gx}I_{gx} + R_d\left(I_{fx} - I_{gx}\right) - V_{gx} + L_{gn}\frac{d}{dt}I_{gn} + R_{gn}I_{gn} \tag{2.16}$$

$$C_f\frac{d}{dt}V_{cfx} = I_{fx} - I_{gx} \tag{2.17}$$

$$C_{DC}\frac{d}{dt}V_{DC} = I_{PV} - I_{DC} = I_{PV} - K_x^T I_{fx} \tag{2.18}$$

$$I_{fn} = -\sum I_{f(a,b,c)} \tag{2.19}$$

where K denotes the duty-ratio vector of the VSI, *x* represents the phase *a, b, c,*

$I_{fx} = [I_{fa} \quad I_{fb} \quad I_{fc}]^T$, $I_{gx} = [I_{ga} \quad I_{gb} \quad I_{gc}]^T$, $V_{cfx} = [V_{cfa} \quad V_{cfb} \quad V_{cfc}]^T$,

$r_{fx} = [r_{fa} \quad r_{fb} \quad r_{fc}]^T$, $V_{gx} = [V_{ga} \quad V_{gb} \quad V_{gc}]^T$, and $K_x = [k_a \quad k_b \quad k_c]^T$.

Based on the expressions (2.15) to (2.18), the equivalent average circuit model of the 4L-SVSI is shown in Fig. 2.14. The small signal average circuit model is shown in Fig. 2.15. The grid-side neutral inductance and resistance are included in the zero sequence equivalent circuit model as new terms to analyse the effect of load-generated neutral current with different transmission line conductors and network locations. The load connection is shown at the PCC in Fig. 2.14; however, the load interactions with the controllers are not considered in the modelling, in order to design

the controllers as independent from external disturbances. The designed controller can work irrespective of the load types. A grid-side filter inductance (L_{g1}) is combined with the corresponding grid transmission-line inductance (L_{g2}). The grid-side neutral-conductor inductance (L_{gn}) and resistance (R_{gn}) are newly added to the dynamic equations to reflect the controller performance variation with a variable R_0/X_0 ratio of the LV network. Applying Park transformation utilising the synchronous angle of the PCC voltage on expressions (2.15) - (2.19), the *d-q-0* reference-frame dynamic equations can be written as:

$$\frac{d}{dt}I_{fz} = G_{Lf}V_{DC}K_z - G_{Rf}I_{fz} - G_L R_d\left(I_{fz} - I_{gz}\right) - G_{Lf}V_{cfz} + \omega I'_{fz} \tag{2.20}$$

$$\frac{d}{dt}I_{gz} = G_{Lg}V_{cfz} - G_{Rg}I_{gz} + G_{Lg}R_d\left(I_{fz} - I_{gz}\right) - G_{Lg}V_{gz} + \omega I'_{gz} \tag{2.21}$$

$$\frac{d}{dt}V_{cfz} = \frac{I_{fz}}{C_f} - \frac{I_{gz}}{C_f} + \omega V'_{cfz} \tag{2.22}$$

$$\frac{d}{dt}V_{DC} = \frac{I_{PV}}{C_{DC}} - \frac{K_z^T I_{fz}}{C_{DC}} \tag{2.23}$$

$$I_{fn} = -3I_{f0} \tag{2.24}$$

where *z* represents *d*, *q*, *0* components,

$I_{fz} = [I_{fd} \quad I_{fq} \quad I_{f0}]^T$, $I'_{fz} = [I_{fq} \quad -I_{fd} \quad 0]^T$, $I_{gz} = [I_{gd} \quad I_{gq} \quad I_{g0}]^T$,

$I'_{gz} = [I_{gq} \quad -I_{gd} \quad 0]^T$, $V_{cfz} = [V_{cfd} \quad V_{cfq} \quad V_{cf0}]^T$, $V'_{cfz} = [V_{cfq} \quad -V_{cfd} \quad 0]^T$,

$V_{gz} = [V_{gd} \quad V_{gq} \quad V_{g0}]^T$, $I_{gz} = [I_{gd} \quad I_{gq} \quad I_{g0}]^T$, $K_z = [k_d \quad k_q \quad k_0]^T$,

$G_{Lf} = \begin{bmatrix} \frac{1}{L_f} & 0 & 0 \\ 0 & \frac{1}{L_f} & 0 \\ 0 & 0 & \frac{1}{L_f+3L_{fn}} \end{bmatrix}$, $G_{Rf} = \begin{bmatrix} \frac{r_f}{L_f} & 0 & 0 \\ 0 & \frac{r_f}{L_f} & 0 \\ 0 & 0 & \frac{r_f+3r_{fn}}{L_f+3L_{fn}} \end{bmatrix}$, $G_{Lg} = \begin{bmatrix} \frac{1}{L_g} & 0 & 0 \\ 0 & \frac{1}{L_g} & 0 \\ 0 & 0 & \frac{1}{L_g+3L_{gn}} \end{bmatrix}$, and

$$G_{Rg} = \begin{bmatrix} \frac{R_g}{L_g} & 0 & 0 \\ 0 & \frac{R_g}{L_g} & 0 \\ 0 & 0 & \frac{R_g+3R_{gn}}{L_g+3L_{gn}} \end{bmatrix}$$

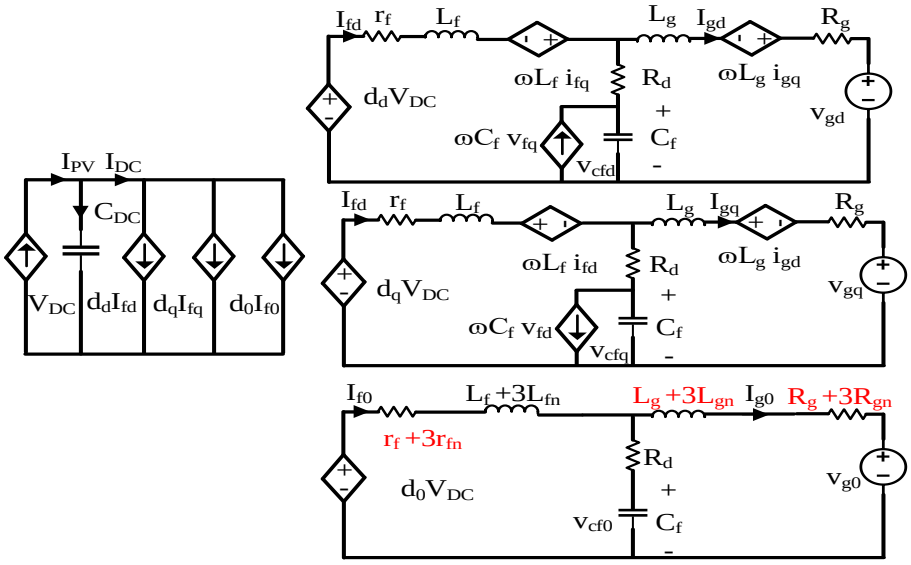

Figure 2.15. Three-phase equivalent circuit model of the PV-SVSI

Utilising the expressions (2.20) - (2.23), a decoupled current controller is designed for the *d* and *q* current components to control the active and reactive powers independently. It can be seen from (2.24) that the zero sequence and correspondingly the neutral current components do not have any coupling terms with other reference frames, i.e. *d* and *q* components, making them inherently independent control variables. The output of the external DC voltage regulator is used as the reference to the *d* component current controller to retain constant DC bus voltage and a seamless transition between PV active and inactive operation periods. The $I_{q\text{-}ref}$ is set dynamically as follows:

$$I_{q_{ref}(\pm)} = \pm \frac{\sqrt{S^2 - P^2}}{\frac{3}{2} V_{gd}} \qquad (2.25)$$

where S represents the inverter total allocated capacity for active (P) and reactive (Q) operations. The external PCC voltage controller utilised with the 3P-3L SVSI is applied with the four-leg inverter with dynamic reactive power control operation. The additional degree of freedom from the fourth leg control is utilised for the neutral current compensation. Monitoring the load neutral current from customer installation point, a single reference is used as the reference for the neutral

current controller. The traditional sinusoidal pulse width modulation (SPWM) technique is applied with the transformed modulating signals (S_d, S_q, S_0) to S_A, S_B, S_C, S_N, and compared with the carrier-frequency generator to generate switching signals (2^4) for the four-leg SVSI switches (S_{1-8}). Proper saturation limits are maintained for the active, reactive, and neutral current controllers to ensure robust linear-region operation from the designed controllers. The detailed control block diagram of the 3P-4L PV-SVSI is presented in Chapter 4 and 5.

2.6 Low-Voltage Distribution Network Design

The performance of the designed three-leg and four-leg PV-SVSI is analysed in the context of the Australian 3P-4W LV distribution network as shown in Fig. 2.16 using the PSCAD/EMTDC software environment with real customer loads, sun irradiance, and temperature data.

Figure 2.16. LV residential network in Brisbane, Australia

The LV network (11 kV/ 415 V) is designed from the 33 / 11 kV upstream network using a distribution transformer (DT) and transmission-pole data from an inner northern residential suburb of Brisbane and provided by Energex, one of the largest DNOs in Queensland, Australia. The Newmarket zone 11 kV substation comprises around 2,373 customers with 8,495 kVA of installed load. The feeder minimum load is around 70 A, and at midday is around 100 A. Maximum summer and winter load currents are 150 A and 250 A, respectively. An individual customer loading has been designed with a maximum 3.3 kW and a minimum 0.55 kVA with 0.95 pf lagging. The base loading of the network is around 230 kW and 60 kVAR. The LV network consists mainly of three-phase four-wire overhead distribution lines, supplied from one 500 kVA DT. One-year-average

loading data for individual customers is used as the base LV feeder network. The total span of the considered LV distribution system is approximately 1.8 km long with two ring networks. The overhead transmission-line conductor specifications are provided in Table A1 in the Appendix.

2.7 Chapter Summary

A literature review of different voltage regulation devices and active neutral current compensation devices along with electricity connection standards from different countries are presented in this chapter. Based on the knowledge from the literature review, three-phase three-leg and four-leg inverter topologies are utilised with the PV system for active, reactive and neutral compensation operations in a three-phase four-wire distribution network. A mathematical modelling of the RES and power electronic converter units is developed and different current control loops are designed for different control operations. Three-phase three-leg and three-phase four-leg SVSI controllers are utilised for voltage-rise mitigation in Chapter 3 and for active neutral current compensation operation in Chapters 4 and 5, respectively.

The next chapter describes the proposed voltage-rise mitigation method and presents results of applying the proposed method with PV, BES, 3P-3L SVSI and the D-STATCOM system in the three-phase three-wire balanced LV network.

Chapter 3

Penetration of Renewable Energy Sources into LV Network

The proliferation of renewable energy sources (RES) integration into traditional distribution networks is conspicuous, especially in low-voltage (LV) networks. Increasing PV penetration in the LV network is changing the distribution network (DN) from passive to active, i.e. power flow is not only unidirectional from generators to loads, it is now bidirectional, which causes dramatic effects, such as voltage-rise and poor power quality [88].To mitigate the issues arising with RES gradual integration into LV network, in this chapter a novel hierarchical control selection methodology is developed based on the number of PV penetrations into the LV network. Different RES, such as PV and battery, and smart autonomous devices, for example smart voltage source inverter (SVSI) and distributed static synchronous compensator (D-STATCOM) are utilised to evaluate the effect of gradual PV penetration. Furthermore corresponding control mechanisms are proposed to mitigate the effects, for instance voltage-rise.

This chapter is organised as follows. Section 3.1 introduces the problems associated with increasing RES penetration into the LV network and corresponding background reviews. In Section 3.2 the system configuration and description is presented, while in Section 3.3 the proposed novel hierarchical control methodology is discussed. Different case study results conducted in the Australian LV network are presented in Section 3.5, and a comparative economical analysis is conducted in Section 3.6. Finally, Section 3.7 is the summary of the main themes covered here.

3.1 Introduction

The PV system installation is becoming more popular in all power-using sectors, such as residential and commercial areas, and industrial power plants. Increasing RESs, such as PV system and its integration, into the LV networks can cause severe voltage-rise at the customer installation point due to high PV generation and low consumer demand. Rooftop PV units in the LV networks contribute 43% to the total installations; Queensland's installations alone cover one-third of the total PV capacity [89]. Energex, the local distribution network operator (DNO) in Queensland,

supports approximately 570 MW of PV installations in its DNs [90-91]. Despite the increasing number of PV installations, local DNOs do not allow voltage regulation at the customer's end in most Australian LV networks. Given the stringent PV connecting standards, voltage compensation devices are becoming more popular in LV networks. The countries with a high number of PV installations, such as Germany and Italy, have already started applying local voltage support at PV installations, due to the fact that local regulations provide better network stability than traditional centralised solutions [92-94]. The widely installed local dynamic compensation device in the LV network is the D-STATCOM, especially in places where a smart voltage source inverter (SVSI) operation is not permitted. The combined operation of battery energy storage (BES) with D-STATCOM can provide an additional degree of freedom for the independent control over active and reactive powers, which has resulted in more demand for centralised BES installations in the LV networks [95]. During peak PV generation periods, the total PV power, after load compensation, is directly fed back to the distribution grid. After reaching a certain level of PV penetration, namely, when it exceeds the maximum limit of existing DNs, the reverse power flow causes voltage violations at the point of common coupling (PCC), i.e. it exceeds +6% of the voltage level, resulting in unwanted tripping of PV installation units.

Authors in [86] propose power-sharing controls among residential BES during peak PV generation periods for voltage regulation purposes. However, with the current price of BES installations, the required regulated operations will leave customers with additional costs. Similarly, the emerging plug-in hybrid vehicle (PHEV) is utilised for peak PV charging operation to reduce electricity bills and voltage regulation in [96]; however, this requires stringent charging scheduling to obtain effective results. With the aim of reactive power loss reduction, due to penetration of distributed generation (DG), authors in [98] propose a coordinated reactive power management method designing load flow models; however, applicability in the actual LV network is not presented. Alternatively, regulating specific loads, such as thermal storage heaters and hot water storage systems, will effectively reduce voltage-rise during peak DG generations [98-99]. Nevertheless, this requires higher installation costs and exhibits slower voltage restoration operation. Utilising fast artificial dynamic systems with the sensitivity theory, authors in [100] propose a centralised real-time control of reactive power from PV inverters for voltage regulation, but this is only applied to the MV distribution networks whereas the main voltage disturbances occur in LV networks.

Due to the active nature and highly resistive line characteristic of the rural and most urban DNs, centralised controls have less impact on far-end users experiencing voltage-rise problems. Therefore, decentralised controls are becoming imperative and much significant research has been undertaken utilising reactive power support from modified PV-VSI [101]-[103]. Authors in [104] present the comparison between the centralised and distributed controls based on optimal power-flow (OPF) methods, while the benefits of decentralised controls with minimum communication requirements are exploited in [105]. Utilising demand-shifting operations to achieve higher renewable energy penetration in the European LV networks, the Monte Carlo sensitivity analysis is applied to consider the flexible demand topology for end customers in [106]. However, the impacts of compensation devices as well as future PV penetrations are not considered. Decentralised active power curtailment and local reactive-power support with minimum communication support is proposed [107]. Despite the improved voltage profile, the curtailed power causes energy to be wasted, and challenges about how the power-sharing will be utilised with unity pf VSI are not mentioned [107]. Considering actual Australian LV networks, [108] and [109] propose a local reactive power and residential BES control operations to regulate voltage. However, as the grid connection standard is still stringent about local reactive-power support, determining at what conditions the local compensation controls will be imperative rather than optional is not addressed properly. Also needing consideration is that traditional DNs can sustain a certain amount of PV penetration without any voltage constraint issues as shown in Table 1.2 in Chapter 1. Therefore, advanced compensation devices are not necessarily required for voltage mitigation unless certain PV penetration levels are exceeded.

One of the main objectives of this research study is to develop a hierarchical control selection method for voltage-rise mitigation based on PV penetration levels in the LV network. Unlike [104] and [108], the DN is considered as the primary voltage regulator, and upon failure of the DN regulation operation a decentralised dynamic voltage regulation device, D-STATCOM/BES, is considered. Finally, emerging local regulation solutions, such as smart PV-VSI with fixed reactive power capability [110], residential BES installation, and power-sharing among neighbouring RES units, are considered. The control selection methodology is dominated by many factors, such as the cost effectiveness of the present situation, connecting standards, and device availability. Local support from the customers' installations are considered only after the failure of centralised regulation operations. The combined operation of unity pf and smart VSI with fixed lagging pf

operation is included for the voltage regulation controls in the proposed method. Unlike [86], the requirement of residential BES installation is considered only for specific customers in critically voltage-sensitive areas. Therefore, customers do not necessarily need to install BES as a pre-requirement of PV interconnection to the already PV-saturated local grid. Power-sharing among neighbouring RES units is considered as the last regulation solution and has proved to be effective in achieving 100% renewable-energy integration.

3.2 System Configurations

The connection of the residential DC renewable sources, such as PV and BES, with the designed three-phase three-leg SVSI to the utility grid is shown in Fig. 3.1. Each of the RES sources and residential customer loads is connected to the grid via over-current protection circuit breakers. The same inverter configuration is utilised at different customer installation points with the proposed voltage regulation method in the LV network. The proposed voltage regulation method is described in detail in the next section.

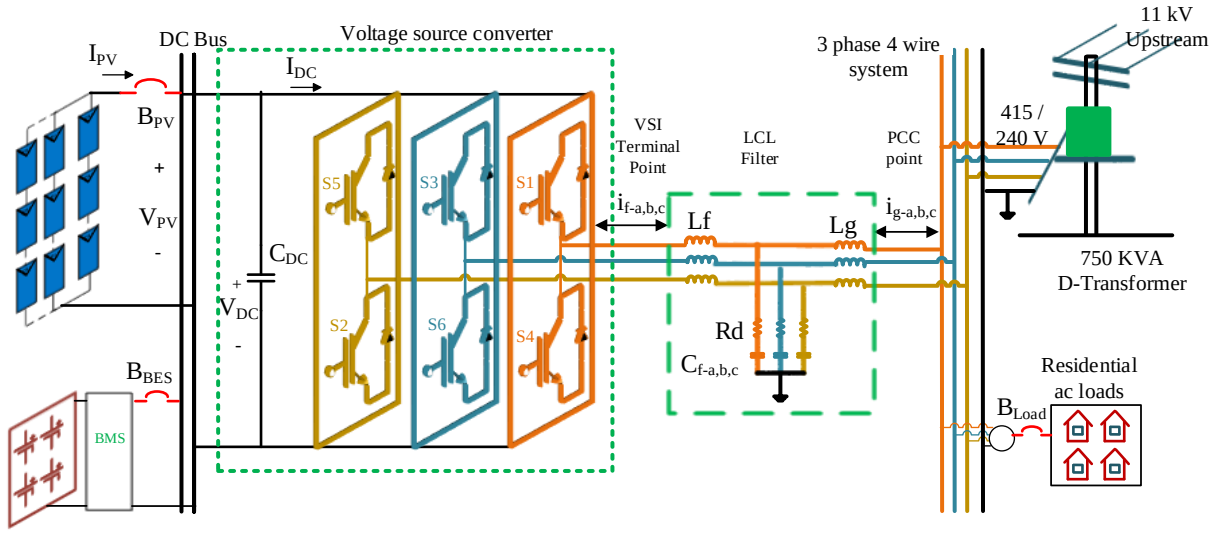

Figure 3.1. PV unit and BES detailed connection diagram

3.3 Developed Novel Control selection Methodology

Traditional LV networks are capable of accommodating certain levels of PV penetration without any major issues, even with unity pf inverters in the PV system. Energex, the local DNO for Queensland, Australia, permits around 30% PV penetration in the LV network considered in this study [110]. With the increasing number of PV installations in Australia (rising from 8000 to 1.4 million within the last 7 years [111]), the allowable PV penetration level is expected to be exceeded in the very near future. The threshold point, i.e. when additional compensation devices will become more practical to implement rather than optional, needs to be identified. Therefore, this research work proposes a gradual requirement of device installation for voltage-rise mitigation within the LV network. The voltage-rise is considered to occur as a result of the high PV generation with the standard load demand occurring during the daytime in residential areas. The main focus for the control selection method is given to the condition whether the total PV generation (ΣP_{pv}) is higher than the total load demand ($\Sigma P_{demand)}$ or not. Based on the previous condition, five control selection modes are developed and shown in Fig. 3.2.

Mode A. Normal network
Mode B. D-STACOM/BES with BES charging
Mode C. D-STATCOM/BES with PV- SVSI
Mode D. D-STATCOM/BES with PV-SVSI and residential BES
Mode E. D-STATCOM/BES with PV-SVSI and BES power-sharing

} $\Delta V > +6\%$

3.3.1 Mode A. Normal network ($\Sigma P_{pv} < \Sigma P_{demand}$)

If the total PV generation (ΣP_{PV}) in a particular area is less than the load demand (ΣP_{demand}), the system will continue its operation in the normal mode, monitoring system faults, voltage regulation during high load demand, frequency regulation etc. D-STATCOM/BES is considered to be available from the normal operating mode and can provide both voltage-sag and swell regulation. The power flow in the considered mesh/loop network exhibits more complicated control characteristics than traditional radial networks, due to the presence of multiple paths for the controlled current to flow. In complex network configurations, D-STATCOM/BES helps to restore the system's normal operation more robustly than D-STATCOM's operation alone. In the considered LV network, if the PV penetration remains less than 30%, say 5 customers each having

5 kVA units in individual installation locations, and total PV installations around 200 kVA at eight test points in the span of an approximately 2 km long LV network (ring), it is considered to be a normal operating mode. Furthermore traditional D-STATCOM/BES operations along with grid support are considered enough to stabilise the overall network, even in the case of system faults and sudden load changes for a full day operation period.

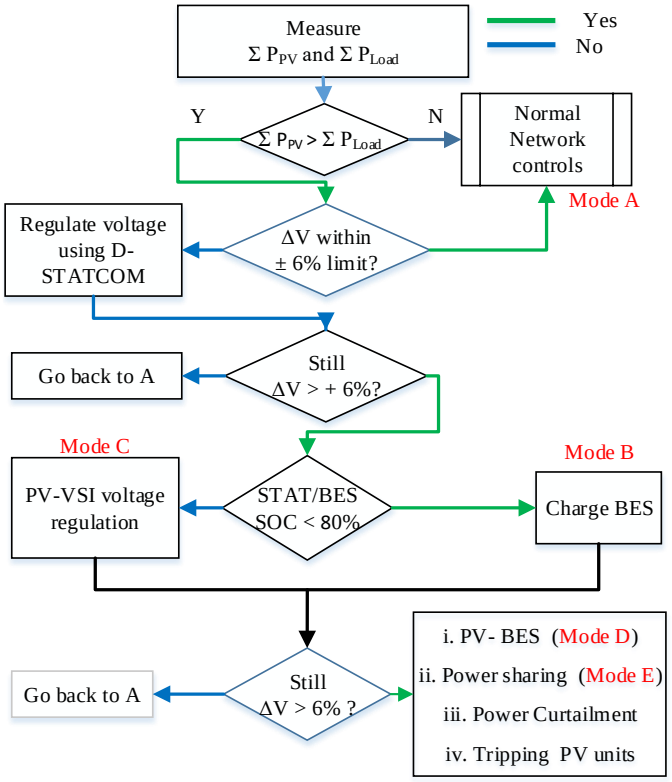

Figure 3.2. Hierarchical control selection methodology

3.3.2 Mode B. D-STATCOM/BES with BES charging ($\Sigma P_{pv} > \Sigma P_{demand}$)

If the PV penetration rises higher than 30%, $\Sigma P_{pv} > \Sigma P_{demand}$ and the PCC voltage is higher than 1.06 per unit (p.u.), then initially D-STATCOM will try to regulate the terminal voltage with its full-capacity reactive power support. If the voltage difference (ΔV) remains higher than + 6% then the control will initiate the BES charging operation; otherwise, it will return to control mode A as shown in Fig. 3.2. Generally, the BES associated with D-STATCOM is considered for specific operations like RES intermittency impact reduction and oscillation smoothing. BES charging during PV peak generation can also be considered an effective solution for voltage regulation purposes [112]. The BES is commonly charged during late-night periods due to low tariff rates. If daytime charging is required, the BES charging schedule needs to be maintained at the upper

minimum level (state of charge (SOC) of 60%) during the night time, and the remaining BES capacity (SOC of 20%) should be used for daytime charging. The deep charging operation is avoided in this research so that the BES life cycle increases. If the control mode B improves the voltage profile, the BES charging will be switched to the halt mode, while D-STATCOM will continue to regulate the terminal voltage in the normal operating mode.

If the PV penetration exceeds 50%, additional supporting devices besides D-STATCOM/BES are required to keep the PV-installed customers connected to the network without causing any major voltage problems. From the literature, widely suggested additional voltage-processing decentralised controls are:

i. PV system with smart VSI having reactive power regulation control
ii. PV peak generation charging from customer BES installations
iii. Power-sharing among neighbouring DG units
iv. Active power curtailment, and
v. Tripping of a particular PV installation section.

The last two solutions (iv) and (v) are not considered in the proposed control selection method due to their low efficiency and less reliable operations.

3.3.3 Mode C. D-STATCOM/BES with PV- SVSI ($\Sigma P_{PV} > \Sigma P_{demand}$, Q_{STAT}, BES_{STAT} max. lim.)

Among the existing control options mentioned above, the PV with smart VSI having reactive power capability is one of the most researched topics; in some countries, such as Germany and Italy, this control has already been applied for local voltage regulation. Due to the additional cost of BES installation and communication link requirements for power-sharing controls, the smart VSI strategy is considered as more cost effective than other solutions at a PV penetration higher than 50%. The theory behind smart VSI is the principle of de-rating power controls. The de-rated controls select a new active power limit ($P_{modified}$) from the standard rated power (P_{rated}) creating some capacity available for reactive power operation as shown in Fig. 3.3. Generally, the reactive-power capability curve is provided by the local DNOs to restrict the over-use of smart VSI operation [108]. Recently in Australia, a few DNOs now allow a smart VSI installation with a fixed 0.95/0.90 pf lagging operations [110], [113]. Therefore, if the operating mode B fails to regulate the terminal voltage at a specific area, depending on the size of the PV installations, fixed 0.95/0.90 pf lagging support has been applied. In the proposed method, rather than following a specific capability curve, either a fixed lagging or unity pf operation is considered. The smart VSI

operation can also be considered as a form of distributed local control, and consequently minimum communication is required. The important consideration here is that, up to a certain PV penetration, unity pf VSI will be installed in the network. After the failure of available supporting devices, the requirement for a PV system with smart VSI installation becomes critical. In that kind of scenario, customers and DNOs can easily come to mutual agreements for local VAR support for mutual benefits.

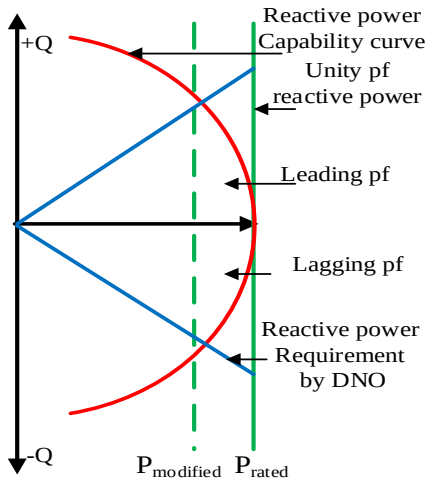

Figure 3.3. De rated PV-VSI operating curve

If the combined operation of D-STATCOM/BES and the local VAR support fails to regulate the voltage-rise, a residential BES installation is chosen as the next control to be included for voltage regulation purposes. After exceeding 65% PV penetration, which is around 100 customers with 5 kVA units, a residential BES installation with peak PV charging becomes most cost effective and an imperative control technique for voltage-rise mitigation.

3.3.4 Mode D. D-STATCOM/BES with PV- SVSI and residential BES ($\Sigma P_{PV} > \Sigma P_{demand}$, $Q_{STAT.}$, $BES_{STAT.}$, PV-VSI_Q max. limit)

The reduction in the installation costs of BES is making it more popular in both commercial and residential areas, especially among customers having PV installed in their premises. Residential BES installations can be used for load balancing, peak load reduction and help reduce customers' electricity bills. The application of BES as an uninterruptable power supply (UPS) in rural areas is quite popular. However, in urban areas, the installation of BES is optional rather than imperative, resulting in less motivation towards the wide installation of BES units. Also, the excess PV power can easily be supplied back to the grid for feed-in tariff (FIT) offers. However, it is found that even

when having FIT offers, customers with BES installation with PV units would get more economical benefit in terms of electricity bill reductions. Furthermore in the near future, the PV and BES installation would be considered as a bundled unit to reduce the excess feedback power to the grid as well as to compensate for voltage-rise occurrences. If the PV penetration exceeds that limit where the combined operation from control selection mode C fails to regulate the voltage-rise, the residential BES charging operation in specific areas along with D-STATCOM/BES and smart VSI operation would be the most effective and economical control selection technique.

In the event that all the above-mentioned solutions fail to regulate the voltage within the limits, active and reactive power-sharing among neighbouring RES installation units is considered the best possible solution to accommodate more PV installations. Theoretically, power-sharing methods can serve as an effective solution for all PV penetration conditions, however, it requires the availability of advanced devices, such as smart VSI, residential BES etc. Communication among the neighbouring units and the permission of local power-sharing in the LV grid from the local DNOs plays an important role in the implementation of the proposed power-sharing technique. If control mode D along with other voltage regulation operations from A - C fail to regulate the voltage within the standard limits, active and reactive power-sharing among neighbouring DG units is applied in the LV network. For the considered LV network, it is found that if the PV penetration exceeds 85%, say 125 customers with 5 kVA PV units each, power-sharing becomes mandatory to maintain healthy electrical characteristics of the LV network.

3.3.5 Mode E. D-STATCOM/BES with PV-SVSI and BES power-sharing ($\Sigma P_{pv} > \Sigma P_{demand}$, Q_{STAT}, BES_{STAT}, $PV\text{-}VSI_{Q}$, BES_{PV}, max. limit)

Power-sharing among different DG units in the microgrid, either grid-connected or islanded, is a challenging research topic for the smart-grid network. Many autonomous power-sharing methods, such as fixed and variable droop controls, are available with minimal communication requirements, as discussed in the Introduction. However, power-sharing among DG units in the mesh/loop LV network is more challenging than in the simpler radial distribution networks. This is due to the controlled current division characteristic in multipath networks. To make power-sharing control simpler with minimum communication requirements, control mode E is proposed only when all the other combined operations, stated above, fail to regulate the voltage profile and the power quality degrades. The output power oscillation created from poor power quality can also

be improved utilising power-sharing as shown in the performance analysis section. The PCC terminal voltages, smart VSI reactive current limit, SOC of the residential BES, and PV generation are considered as the decision-making factors related to the power-sharing controls. If all the parameters exceed their maximum allowable set limits, only then will power-sharing for specific areas experiencing voltage-rise be enabled. The power-sharing control-signal generation method is illustrated in Fig. 3.4.

The proposed control selection methodology based on PV penetration level is shown in Fig. 3.5 and a corresponding number of customers is shown in Table 3.1.

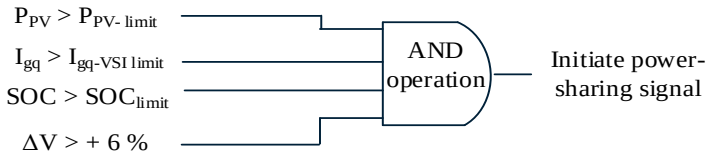

Figure 3.4. Control management diagram for the proposed power-sharing method

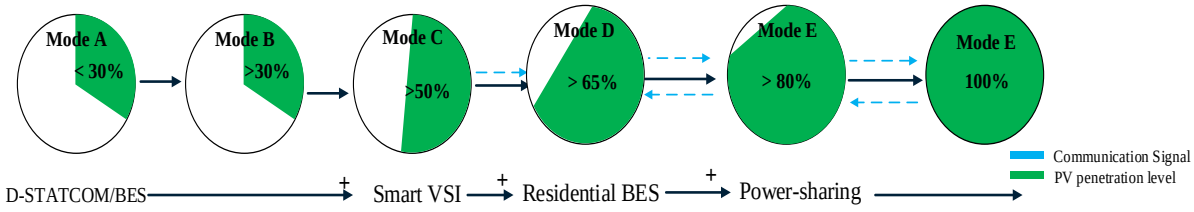

Figure 3.5. Graphical presentation of hierarchical control selection method

Table 3.1. Novel control selection methodology based on Australian LV network

PV penetration level ($PV_{pen.}$)	No of customers each with 5 kVA PV installation in the LV network	Control selection mode
$PV_{pen.} \leq 30\%$	0 - 40 customers (max. ~ 200 kVA)	A
$31\% < PV_{pen.} < 50\%$	41 - 70 customers (max. ~ 350 kVA)	B
$51\% < PV_{pen.} < 65\%$	71 - 99 customers (max. ~ 500 kVA)	C
$66\% < PV_{pen.} < 85\%$	100 - 125 customers (max. ~ 625 kVA)	D
$PV_{pen.} > 85\%$	126 - 150 customers (max. ~ 750 kVA)	E

3.4 PV Penetration Analysis with Proposed Method

A description of the LV network is presented in Chapter 2. The transmission-line R/X ratio is assumed to be unity in this chapter to represent urban-area characteristics. However, the R/X ratio is not a fixed integer quantity and varies with different transmission-line conductor values. To reduce the simulation time, clustered PV installations are considered rather than individual customer PV installations for the PV penetration analysis with the considered LV network. For example, a single 50 kW PV is assumed for 10 customers with 5 kVA PV installation capacity. Similarly, local reactive power support is considered utilising the accumulated kVAR rating from 10 customers having 0.95 pf lagging characteristics. A 5 kVA PV unit with 0.95 pf lagging operation should support around 2 kVAR. Therefore, a total 20 kVAR rating is considered from the ten PV installations at each test point. The PV units and other inverter parameters are shown in Table 3.3 at the end of this chapter. It is estimated that, under a standard test condition (STC), a PV module from the PSCAD/EMTDC master library generates around 650 W. The peak voltage and current of a single PV module are around 81 V and 8.125 A for 108 cells in series and 4 cells in parallel connections. The open-circuit PV array voltage is around 900 V [114]. The BES voltage is assumed to approximately 320 V with a maximum charge/discharge current of around 40 A for the 20 kWh clustered residential units (2 kWh for each customer) and around 60 A for the 30 kWh D-STATCOM unit. The D-STATCOM capacity is set around 30 kVA with the maximum current limiter set at ± 60 A. As the voltage-dip scenario is not correlated with increasing PV penetration levels, the voltage-sag scenario is analysed with the D-STATCOM/BES operations alone, with different faults, such as symmetrical and asymmetrical. The 44-bus LV network with the chosen test points and D-STATCOM/BES location are shown in Fig. 3.6. The distances between the distribution transformer (DT) and the test points are given in Table 3.2. The worst-case scenario with a high PV generation and low load demand is considered for both summer and winter seasons, and the PV penetration analysis in the LV network is simulated with consecutive three days data without utilising data from night time, i.e. from 6 am to 5 pm (11 hr data from each day).

Table 3.2 Distance of test points from distribution transformer (DT)

Points	Distance
Upstream to T_{dx}	1.5 km
T_{dx} to P1	260 m
P2	420 m
P3	90 m
P4	180 m
P5	220 m
P6	360 m
D-STATCOM/BES	355 m
P8	160 m
P9	100 m

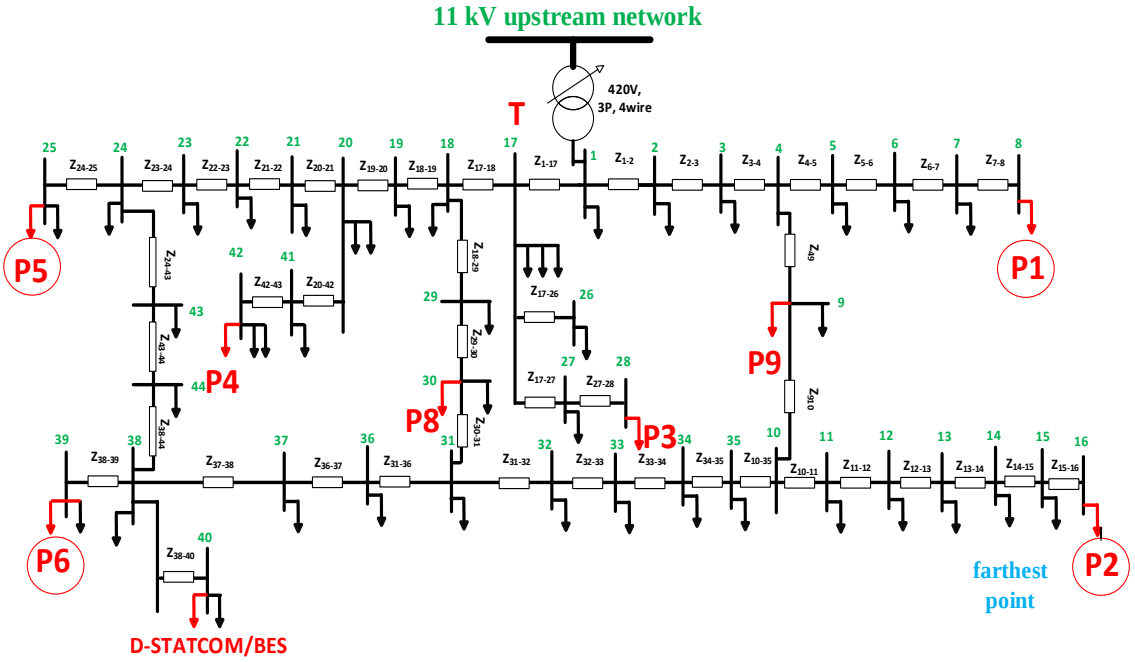

Figure 3.6. LV residential network one-line diagram (44-bus) with the test points

3.4.1 Residential load profiles during summer and winter

The load requirement varies in different seasons. In addition to the normal household loads, the active power demand is quite high during winter, due to the application of resistive-type heaters, whereas reactive power demand is higher in summer because air conditioners are being run. Similarly, the power generation from rooftop PV units is higher during summer than winter due to weather characteristics. Therefore, the PV penetration analysis focuses mainly the sun irradiance profile from the summer season. Typical residential load profiles with a 10 kVA PV unit during summer and winter are presented in Figs. 3.7 to 3.9.

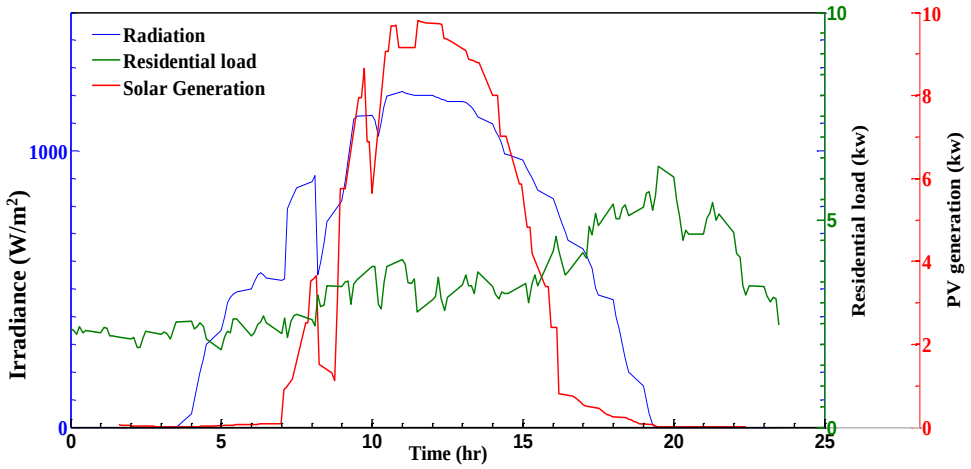

Figure 3.7. Solar irradiance, PV generation, and residential loads during summer

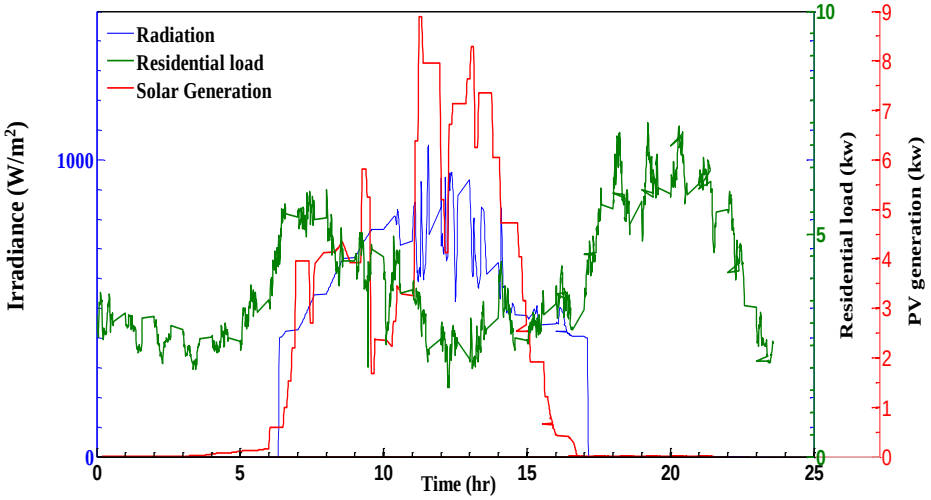

Figure 3.8. Solar irradiance, PV generation, and residential load profiles during winter

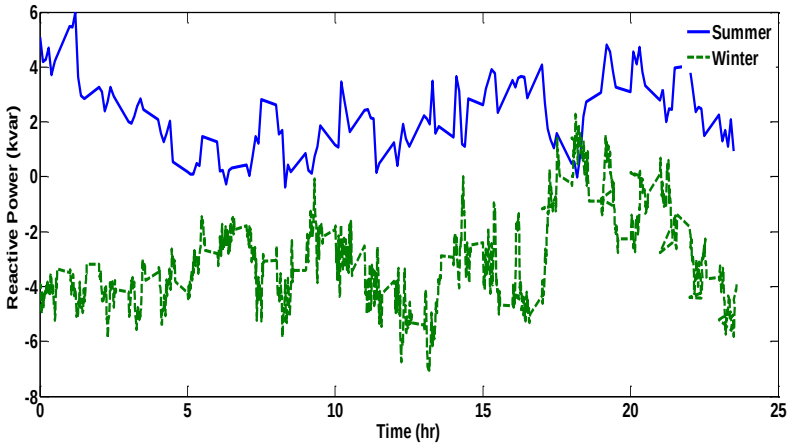

Figure 3.9. Reactive power consumption comparison between summer and winter

3.4.2 PV penetration and different voltage regulation methods

An initial analysis is conducted in the considered LV network by increasing the PV penetration gradually to monitor the voltage-rise at the STC. Generally, 25°C temperature and 1000 W/m^2 sun irradiance are considered as STC conditions for a PV unit. Based on the initial analysis, it is found that till 30% PV penetration, say 5 customers each having 5 kVA units at each test point (total 8 points), the LV network supports the reverse power from the PV units without causing voltage constraints and the D-STATCOM/BES unit is able to regulate the voltage to be close to unity, if required. When the PV penetration is increased to 50%, for instance 9 customers each having 5 kVA units at all the 8 points, the terminal voltages at the farthest points start increasing, but do not exceed the +6% limit. Finally, if the PV penetration is increased to 70%, where 15 customers each have 5 kVA units at all 8 points, this results in the terminal voltages exceeding the limit at all the farthest points; however, the point (P3) close to the distribution transformer remains within the standard limit. The results are shown in Fig. 3.10 and it can be seen that the most critical voltage-rise points are point 2 (P2), point 6 (P6), point 5 (P5) and point 1 (P1). As P2 (420 m) and P6 (360 m) are the farthest points from the distribution transformer, it is expected that increasing PV penetration will have a higher impact on these two points and neighbouring areas. The remaining test points, namely, point 4 (P4), point 8 (P8), and point 9 (P9) are not shown in Fig. 3.10, because those points are not as critically sensitive to increasing PV penetration as much as the farthest ones.

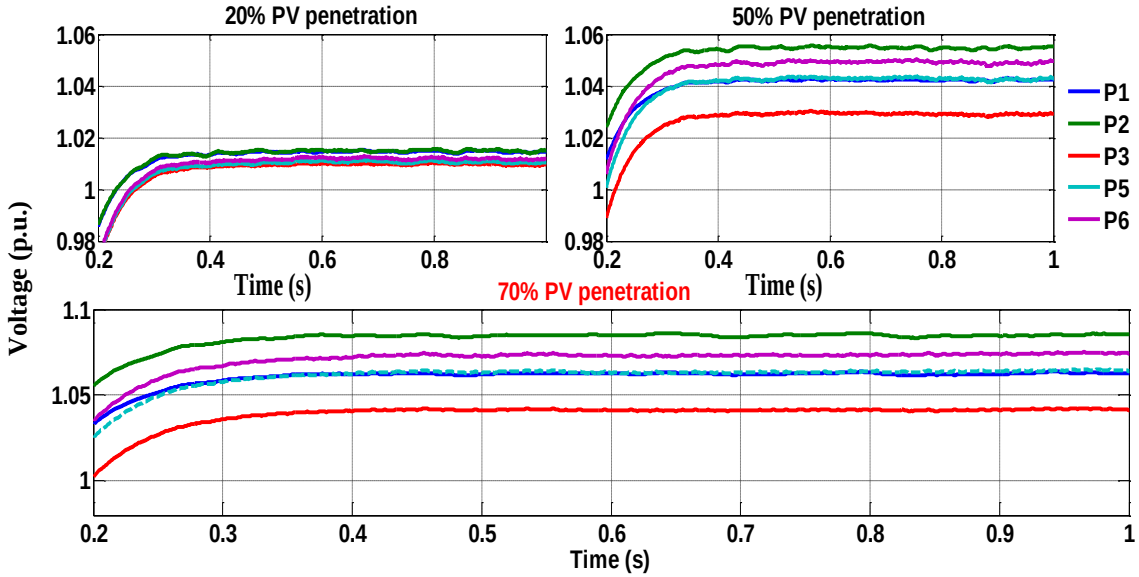

Figure 3.10. PV penetration analysis at STC

The distribution transformer in the LV network is an off-load tap-changing type. Initially, therefore a traditional solution is applied with a highly PV-penetrated network ($PV_{pen.}$ > 85%, 17 customers each with 5 kVA PV units at all 8 test points) to verify the voltage regulation effects. The tap of the distribution transformer is increased from 1 to 1.025 (2.5%) at 0.50 s and then to 1.05 (5%) at 1.0 s to reduce the voltage swell throughout the network. The results are shown in Fig. 3.11.

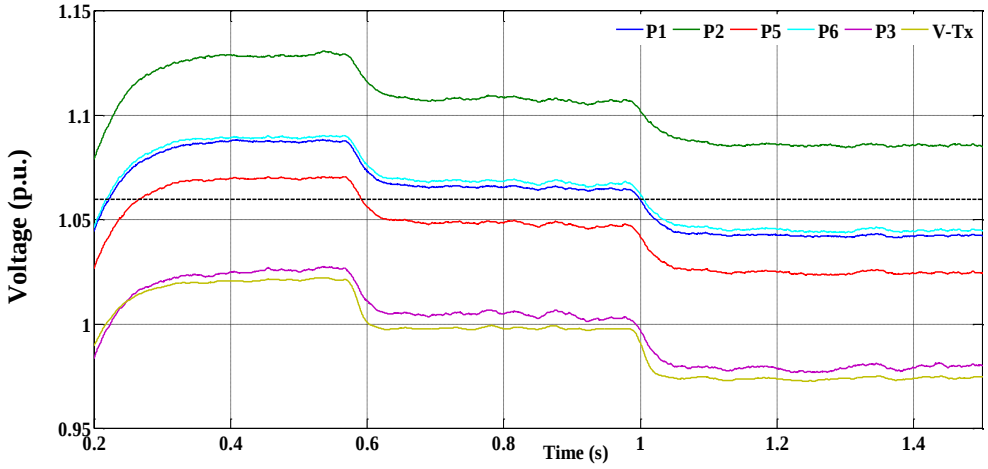

Figure 3.11. OLT operation for voltage-rise mitigation

It can be seen from Fig. 3.11 that the tap-changing improves the voltage profile significantly at the DT terminal point (V_{Tx}) and at P3, which is close to the DT. The farthest corner points within the network, such as P2, P6, P5, and P1 are also affected by the tap-changing operations and demonstrate a similar voltage-reduction effect. However, with the DT tap position at 1.05, the P2 point still remains higher than the allowable limit (1.06), and the voltage of P3 hovers around 0.96 p.u. Further tap-changing (from 1.05 to 1. 075) can move the P2 voltage within the + 6% limit; however, it will cause the P3 voltage to go below the – 6% limit. Therefore, alternative solutions are required to improve the P2 area voltage profile, while keeping other test points within the ± 6% limit.

Increasing the conductor size by replacing the existing lines can certainly increase the network capacity for more PV penetration, but this would not be an economical solution. Other traditional solutions, such as capacitor banks, can be installed at the farthest points to improve the voltage profile, and this is generally applied in industrial and residential areas. However, due to the slow response time of capacitor banks, sometimes it may cause unnecessary tripping due to the time lag and high inrush current to charge up the capacitors. Therefore a passive solution, such as a

capacitor bank installation is not considered in PV penetration improvement scenarios. Moreover, the centralised regulation controller has less impact on highly DG-penetrated networks. Therefore, in the proposed voltage-control method with increasing PV penetration, different decentralised controllers are considered after the PV penetration exceeds 50%. Various centralised and decentralised voltage regulation controllers are applied with PV penetration higher than 65%, and the results are shown in Figs. 3.12 and 3.13.

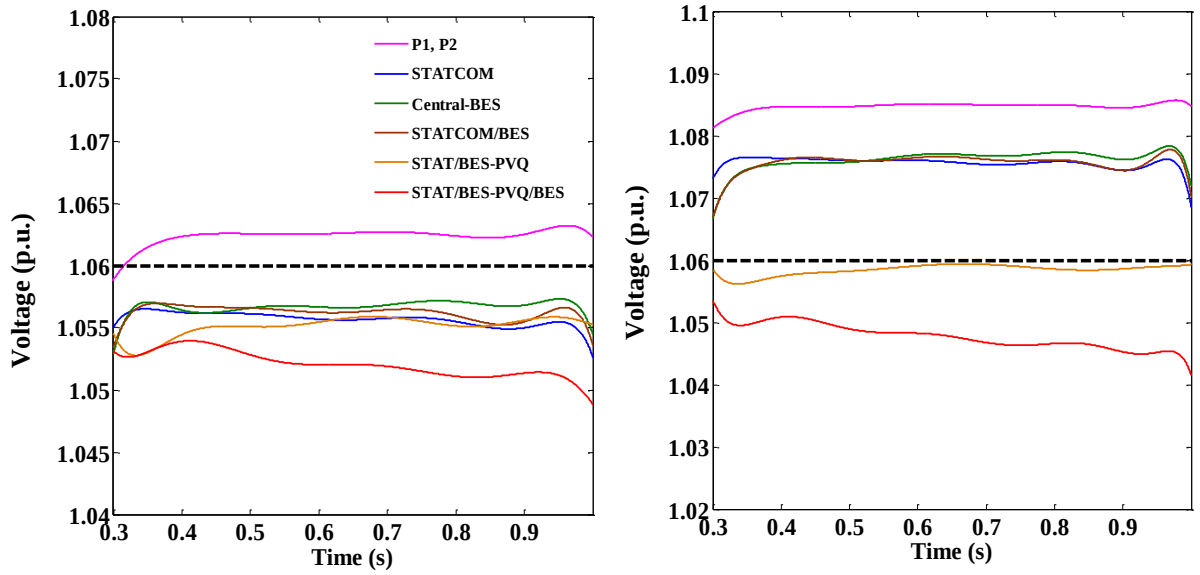

Figure 3.12. Test points P1 (left) and P2 (right) at $PV_{pen.}$ > 65%

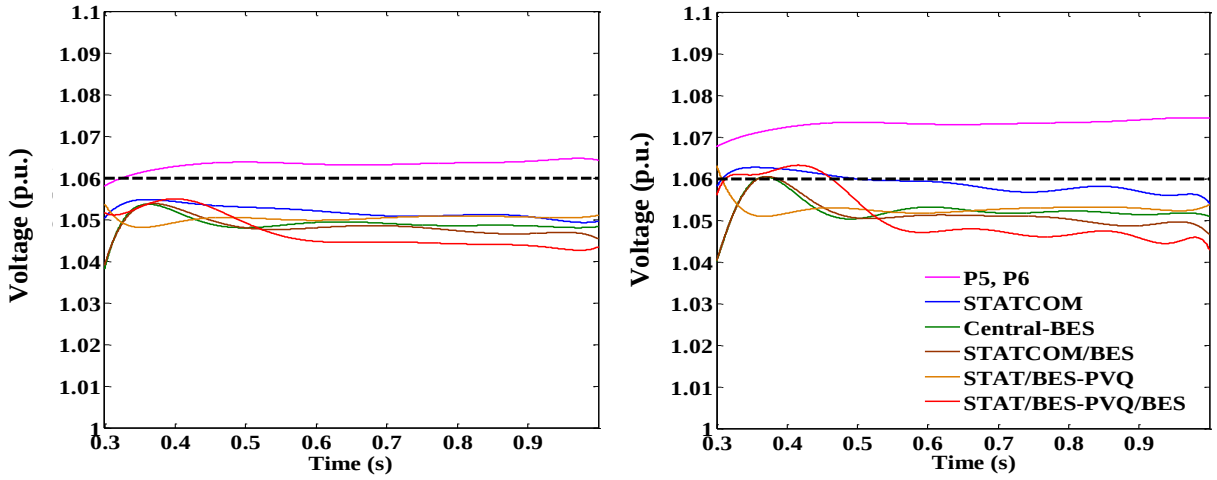

Figure 3.13. Test points P5 (left) and P6 (right) at $PV_{pen.}$ > 65%

From the initial test results as shown in Figs 3.12 and 3.13, it is evident that, at a PV penetration higher than 65%, the P2 voltage can only be controlled using control mode D; whereas at other

test points P1, P5 and P6 the voltage can easily be controlled using any controller modes from B to E. Based on these results, it can be inferred that test point P2 is the most critically sensitive area with increasing PV penetration. Consequently, the main consideration is given to P2 voltage regulation with PV penetrations higher than 50% within the LV network. Instead of installing dynamic voltage-compensation devices throughout the LV network, the proposed control selection methodology recommends the installation of specific compensation devices only at the critical voltage-sensitive points and provides an optimised economical solution with advanced dynamic solutions for voltage regulation.

3.4.3 Voltage regulation with variation in environmental parameters

In DG units, environmental parameters play a significant role in producing output power. For a PV system, stochastic irradiance and temperature variations are the main parameters. The irradiance variations in different seasons over a three-day period are shown in Fig. 3.14. The solar irradiance data is collected with a Pyranometer from the microgrid installation at Griffith University, Australia. The same irradiance data is utilised with all the eight aggregated PV units.

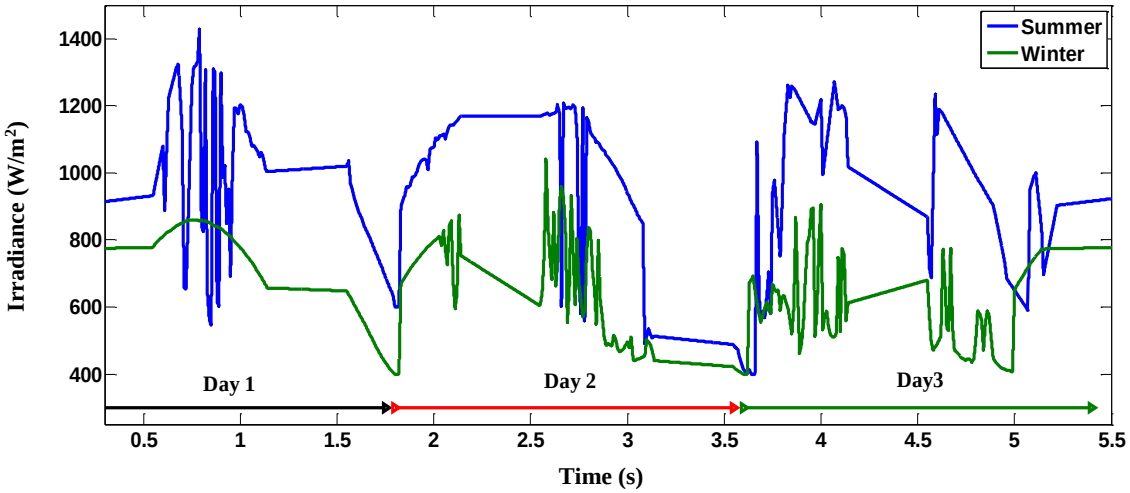

Figure 3.14. Summer (29th -31st Jan. 2015) and winter (7th -9th June 2015) irradiance

The irradiance data is collected in 2015 for a three-day period from 6 am to 5 pm at 5-minute intervals. The simulation time step is selected as 50 µs, and a 1.8 s simulation run-time is represented for one-day performance from 6 am to 5 pm (11 hr data with 5 mins intervals results in 1.8 s simulation time in PSCAD/EMTDC software). The temperature varies between 25-35°C during summer and between 10-20°C during winter.

At PV penetration levels of higher than 50%, the PV output power and terminal voltage are shown in Figs. 3.15 and 3.16. The PV-generated power is higher during summer (max. 60 kW) than winter (max. 48 kW). The designed PV-system dynamic model can easily track the stochastic irradiance, which makes the analysis results from this research study applicable to real-life scenarios. In both seasons, test point P2 remains the most critically voltage-sensitive point, whereas only during summer, along with P2, the P1, P5, and P6 test points exhibit voltage-limit constraints. This initial PV penetration test analysis is performed to evaluate the critical voltage-sensitive points throughout the network, which are the farthest corner points, and corresponding voltage regulation control modes are selected following the proposed hierarchical method.

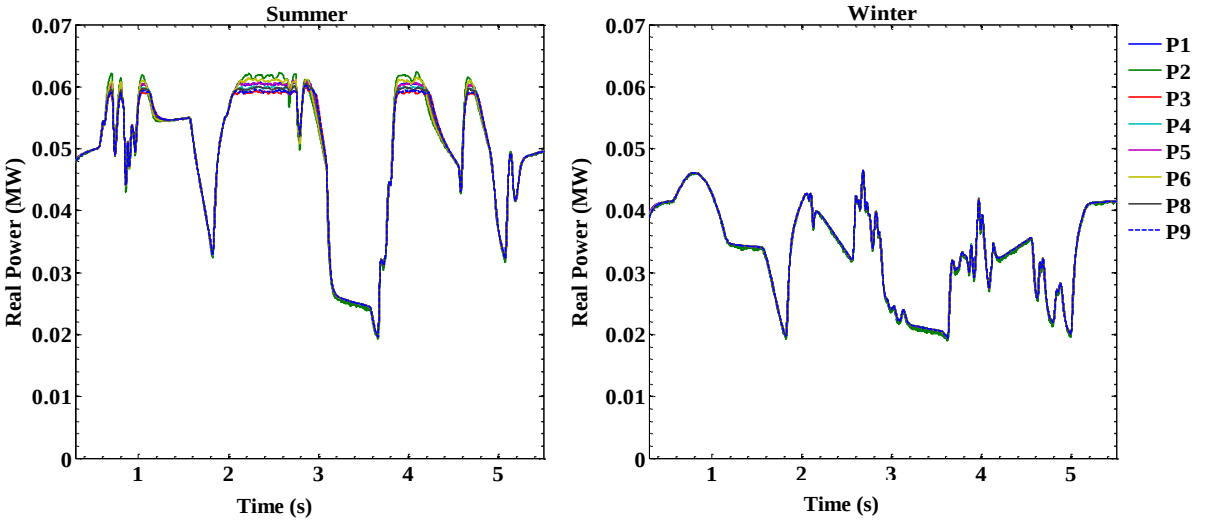

Figure 3.15. PV power generation during summer and winter with $PV_{pen.}$ > 50%

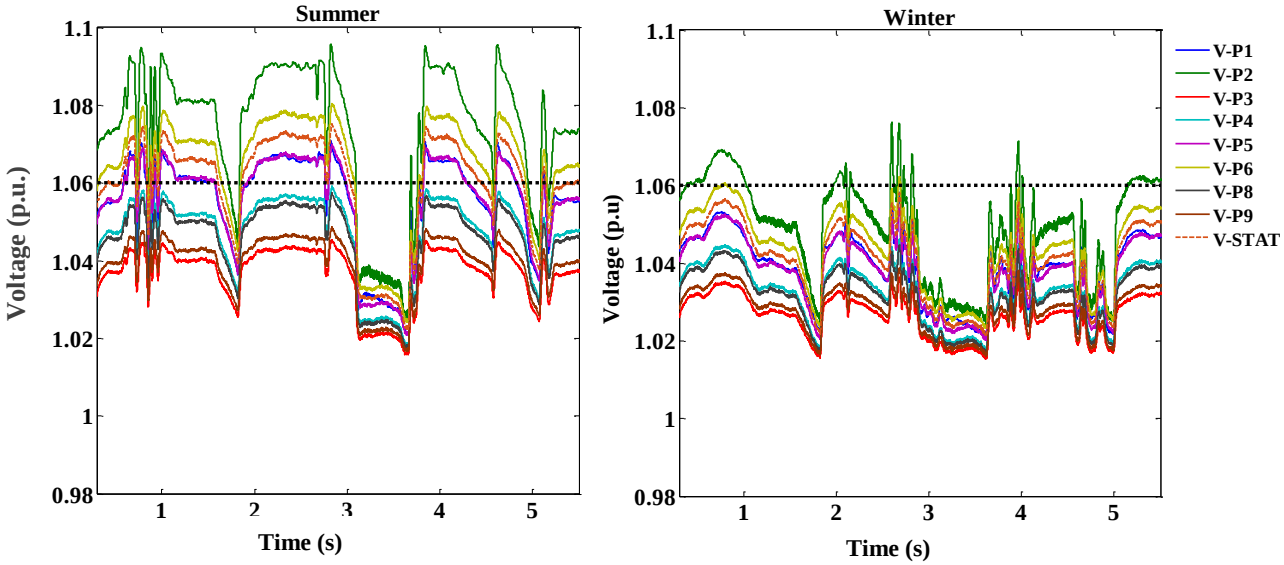

Figure 3.16. V_{PCC} at different test points during summer and winter

3.4.4 PV penetration higher than 50% during summer

This case study shows the voltage profile improvement with PV penetrations higher than 50% using the control modes C and D. As the proposed control selection method is hierarchical, initially the controller selects operating mode B with D-STATCOM regulation and BES charging operation at their maximum capacity ratings. The controller regulates the terminal voltages of P1, P5 and P6, however, the critical point P2 remains higher than 1.06 p.u. as shown in Fig. 3.17.

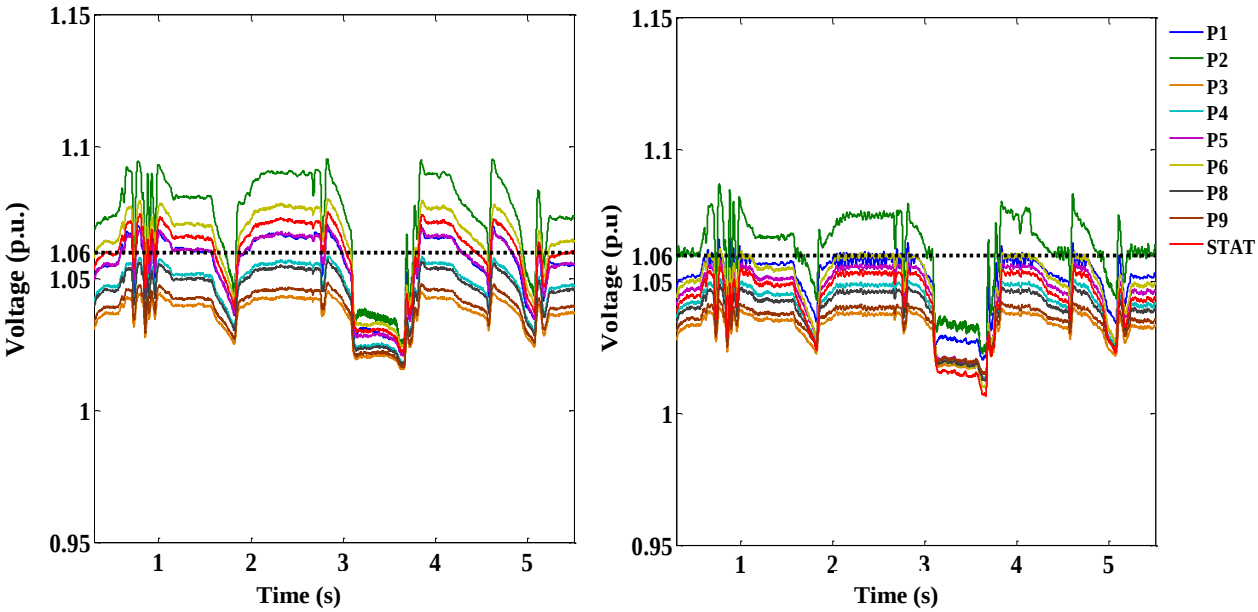

Figure 3.17. V_{PCC} with no compensation (left), and D-STATCOM/BES (right)

Therefore, the proposed method selects the controllers from control mode C and then D to improve the terminal voltage at test point P2. Each test point has 11 customers with 5 kVA PV unit installations. Therefore, during peak PV generation time, one cluster PV unit delivers around 50 kW of active power which is the aggregate of 11 customers with PV units installed at the PCC. The proposed hierarchical control selection method determines that only one (P2) out of eight test points requires the installation of the smart VSI and BES units, and this provides the most economical solution with the existing PV penetration scenario. Despite the marginal voltage-profile improvement using control mode C, at some instances during the three-day operation period the P2 point exceeds the + 6% PCC voltage limit. This occurs mainly during the peak PV generation periods which consume the VSI total capacity for active power supply, making the capacity for reactive power operation almost zero. The voltage of P2 can be further improved by increasing the reactive power capacity of the VSI; however, this is not considered in the proposed method so as not to contradict the Australian connecting standards for residential or commercial

PV units. Therefore, control mode D, i.e. the PV smart VSI with residential BES charging operation, is applied and a lower than 1.06 p.u. terminal voltage at P2 is achieved as shown in Fig. 3.18. The operating mode D is only applied at P2 with a less than 6 kWh charging requirement and, at the same time, the remaining network is compensated by the D-STATCOM/BES operation.

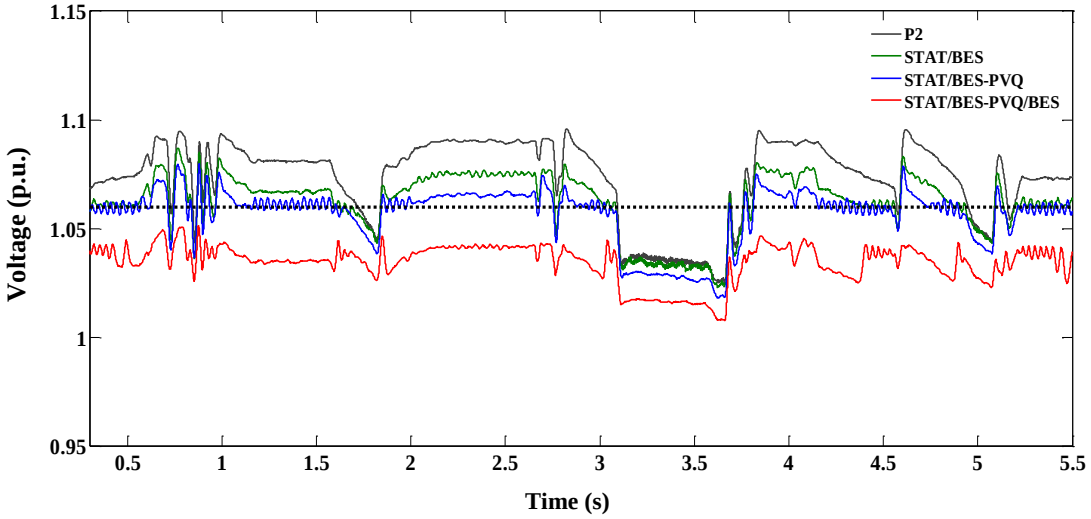

Figure 3.18. Operating modes (B, C, and D) performance comparison at P2

Three observation points (OP) are shown in Fig. 3.19 to explain the operation of different control modes. For this analysis, a 10 kVAR local voltage regulation from the smart PV-VSI and around 6 kWh charging support from the residential BES installation are selected for the P2 area. Of the 11 customers at each test point, half of the customers are assumed to have with unity pf PV-VSI and half have PV-smart VSI installations. Therefore, it is assumed that a total of 10 kVAR can be available from 11 customers. With the help of local reactive power support, operating mode C results in active power with a lower than rated generation, as shown in OP1.This is due to the de-rating operation with fixed VAR support from VSI. However, with operating mode D, the voltage-profile result from Fig. 3.18 shows improvement, with better power quality at the same OP1 as illustrated in Fig. 3.19. Similar performance improvement with control mode D can be observed in OP2 in a different time frame (3.80 - 4.30 s). To avoid overloading the PV-VSI with control mode C, the local VAR support from the smart VSI is switched to unity pf operation automatically when the PCC terminal voltage becomes less than ± 3%, as shown in OP3 in Fig. 3.19. However, with control mode D, the smart VSI continues to operate at a maximum kVA capacity despite the V_{PCC} becoming less than the - 3% ratings. This is mainly incorporated with control mode D to accommodate more PV penetration into the LV network as well as to compensate for the

oscillation in the PV output power due to the stochastic irradiance and BES charging dynamics. Although for PV penetration less than 65% control mode C is sufficient to regulate the P2 terminal voltage within the ± 6% limit, it can also be seen that with control mode D both the voltage and active power profiles indicate better performance than control mode C due to the additional BES charging operation available.

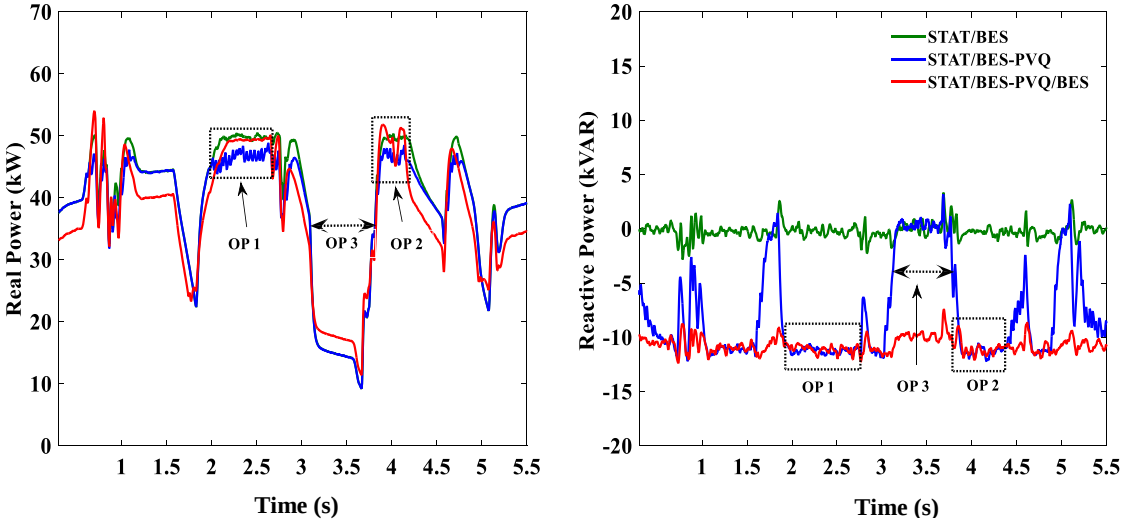

Figure 3.19. Active power (left), and reactive power (right) with different modes at P2

This case analysis has verified that, at a PV penetration of higher than 50% for the considered residential area, the network requires additional local voltage-compensating devices; however, the combined voltage regulation from local active and reactive regulation (control mode D) can perform better than individual reactive-power regulation. This is also related to the fact that, in the actual system, the R/X ratio of the P2 transmission-line section shows a more resistive line, and active-power voltage regulation controllers provide superior performance to reactive-power regulation controllers. The proposed hierarchical control selection method helps to reduce the capacity requirement from the residential BES installation compared to the installation of community energy storage.

3.4.5 PV penetration higher than 65% with various faults

The previous section has shown that even with a PV penetration of higher than 50%, control mode D provides better voltage regulation operation at the most critical voltage-sensitive point P2. Therefore, in this case study the overall performance improvement with support from D-STATCOM/BES for control mode D is evaluated. Different symmetrical and asymmetrical faults, such as three-phase to ground (3P-G) from 1.30 -1.50 s, double-lines to ground (L-L-G) from 2.30 - 2.50 s, and a single line to ground (L-G) from 4.00 - 4.20 s are applied at different locations in the LV network for a 20 s duration. The effect of different faults on the voltage and corresponding reactive powers at test points P1 and P5 are shown in Fig. 3.20. Generally, circuit breakers are used to trip the faulty section from the active system in case the fault sustains for a longer duration, however, this case considers mainly transient and intermittent faults for five cycles to evaluate the robust fault recovery operation of the designed controllers.

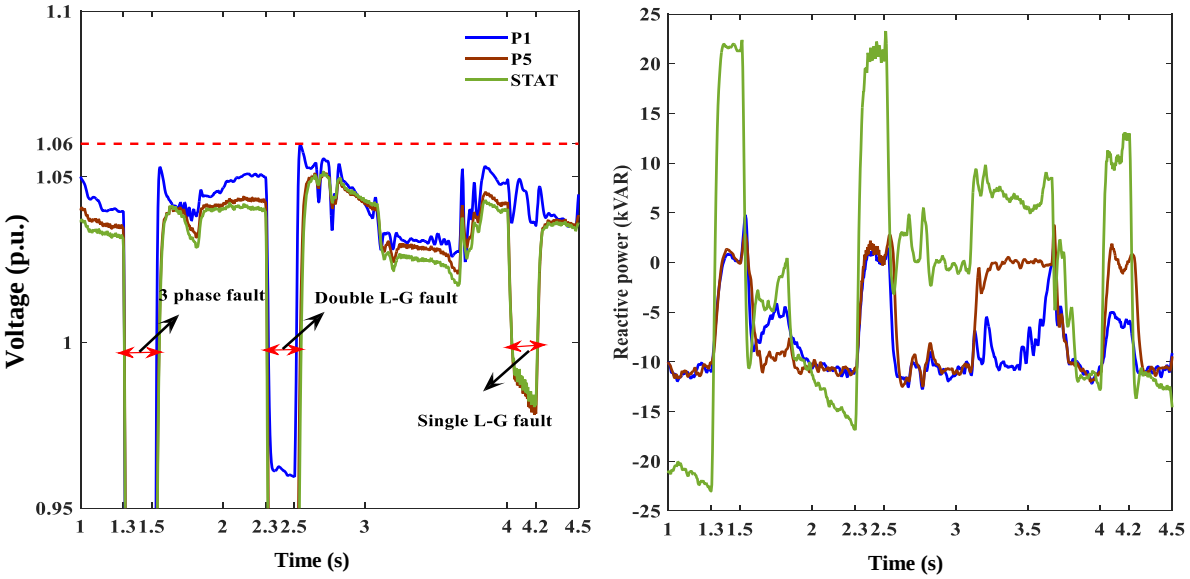

Figure 3.20. Faults' effects on voltages (left) and reactive power (right)

Considering the farthest and closest locations from the fault location, operating mode D is applied at test points P1 and P5. From the results shown in Fig. 3.20, it is evident that D-STATCOM alone is supplying the required reactive power to compensate for the fault whereas points P1 and P5 continue to provide variable VAR support to the PCC. During the fault, D-STATCOM/BES also regulates the active power for the overall LV-network stability improvement while letting the other PV areas operate with a voltage ride-through function. This can be seen

from the output powers from the PV units and the SOCs of the BES installations as shown in Fig. 3.21.

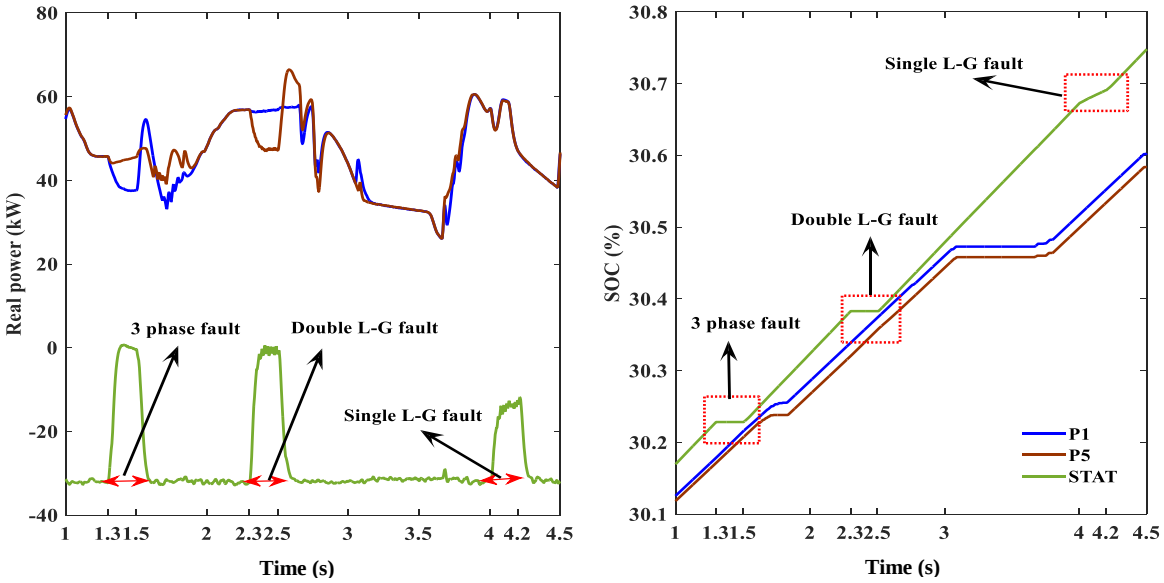

Figure 3.21. Faults' effects on active power (left) and battery SOC (right)

This explains that, although D-STATCOM/BES requires additional local support for voltage regulation at critical voltage-sensitive areas, the D-STATCOM/BES installation in the LV network itself improves the overall performance of the highly PV-penetrated residential network even in extreme disturbance scenarios such as a 3P-G fault.

3.4.6 PV penetration higher than 85% during summer

Despite the local voltage regulation operations from control mode D, if the PCC voltage remains higher than the + 6% limit due to higher PV penetration numbers, power-sharing among neighbouring DG units becomes the optimum solution. Control mode E is selected for power-sharing among neighbouring DG units with a minimum communication requirement. The communication can be performed using simple distress signalling via power-link communication [107], [115]. Being close to urban-area customers, four-quadrant smart meters can also be utilised for communication via RS485 [110]. The hierarchical control selection method utilises control mode E only at the critical test point P2, and the controller performance is compared with control mode D in Figs. 3.22 and 3.23. The solid lines in those plots represent the mode-D results, while the dotted lines (P2*) represent the results after the application of control mode E. The PCC voltage controllers are designed to operate only after the PCC voltage exceeds + 3% (p.u.). Therefore, the

P9 area continues to operate in the normal control mode (B), despite the neighbouring P2 area experiencing voltage constraints. Under the effect of control mode E, the local controller, experiencing higher voltage, initiates power-sharing signals following the proposed method which is shown in Fig. 3.4 for the neighbouring DG units. Upon receiving the signal (with a few ms delay), the P9 area starts sharing active power first and reactive power later to regulate the P2 terminal voltage as shown in Figs. 3.22 and 3.23.

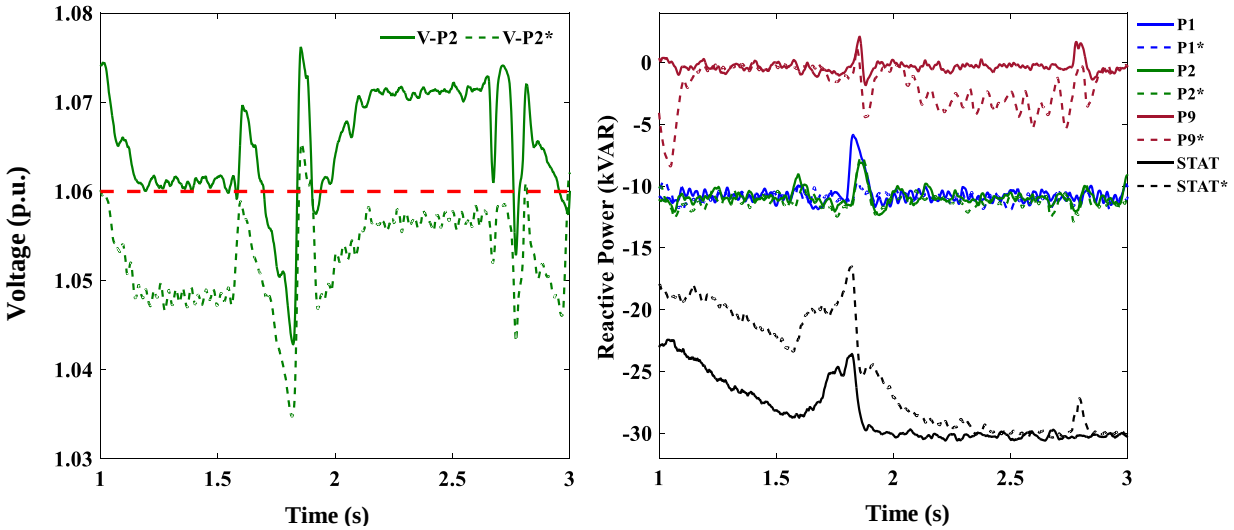

Figure 3.22. Power-sharing at P2: voltage (left) and reactive power (right)

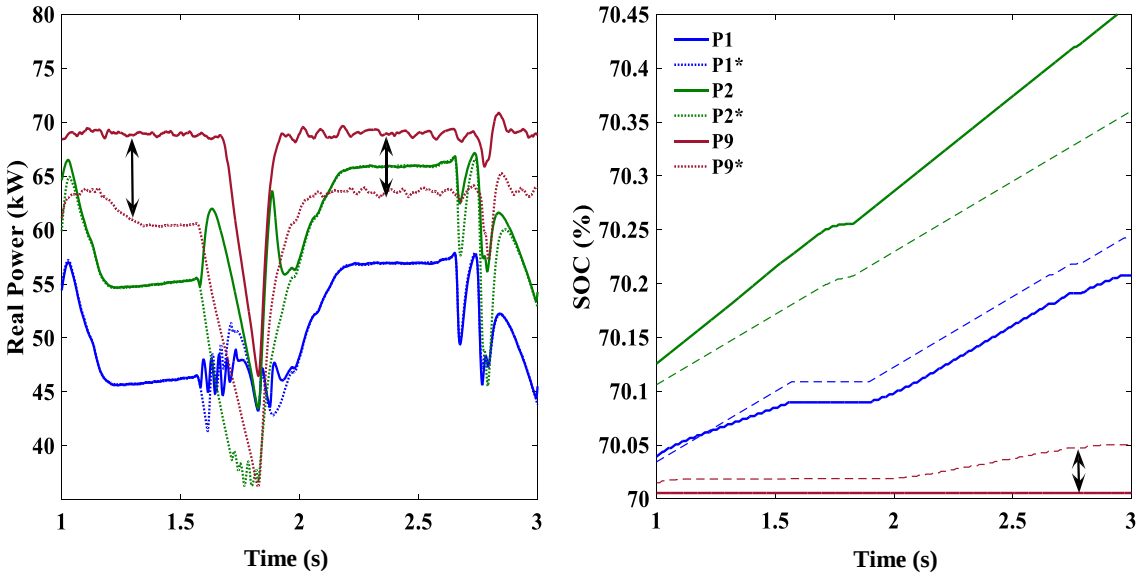

Figure 3.23. Power-sharing at P2: active power (left) and battery SOC (right)

In this case, active power-sharing is given first priority over reactive power-sharing due to the resistive nature of the transmission lines of the LV network. It can be seen at the time period from

1.80 – 2.80 s that, even with the BES charging operation, i.e. the active power-sharing operation from the P9 area, P2 requires additional support to maintain the voltage limit and further initiates the power-sharing signal. Upon receiving the second distress signal, the PV-VSI unit at the P9 area starts supplying its reactive power. It can be seen from the voltage profiles from Fig. 3.23 that the control mode E outperforms the control mode D for this PV penetration scenario. With minimum communication between DG units, control mode E can certainly provide much better voltage-profile improvement with the existing resources.

A significant point of the proposed-power sharing method is the reduction in the decentralised support requirement from the D-STATCOM/BES unit, as can be seen from the reduced VAR consumption in Fig. 3.22. The effect of power-sharing from the P9 test point on test point P1 is also shown in the plots. As the P1 point voltage remains within the allowable voltage limit, power-sharing control is not applied for P1 and the main focus is given to the P2.

To achieve 100% renewable energy integration into residential power-system networks, power-sharing among installed DG units is the most economical and optimum solution for future grid networks. The applied control selection methodology helps proper investment decisions to be made as well as robust dynamic performance improvement in a highly DG penetrated LV network.

3.4.7 PV penetration higher than 75% during winter

From case study 3.4.4, it can be seen that only the P2 area exhibits voltage constraints during the winter season with PV penetration higher than 60%. According to the proposed hierarchical method, control modes C and D would be sufficient to stabilise the voltage constraint issues in this particular PV penetration situation. From 0.60 – 1.0 s, the system operates mainly at mode D, as the PCC voltage remains within the + 3% to + 6% range. As highlighted in OP2 and OP3 in Fig. 3.24, the power-sharing option from control mode E can also be utilised to reduce the output power oscillations resulting from the stochastic irradiance and BES charging operations at the PV units. From Fig. 3.24, it is evident that the voltage constraints, even with higher PV penetration during winter, are not as severe as during summer. However, the same control selection method can be applied during winter not only for voltage regulation but also for improving power quality. The proposed methodology minimises the power-sharing complexity in a multiple-loop LV network and indicates superior voltage regulation with minimum device requirements even for a highly PV-penetrated LV network.

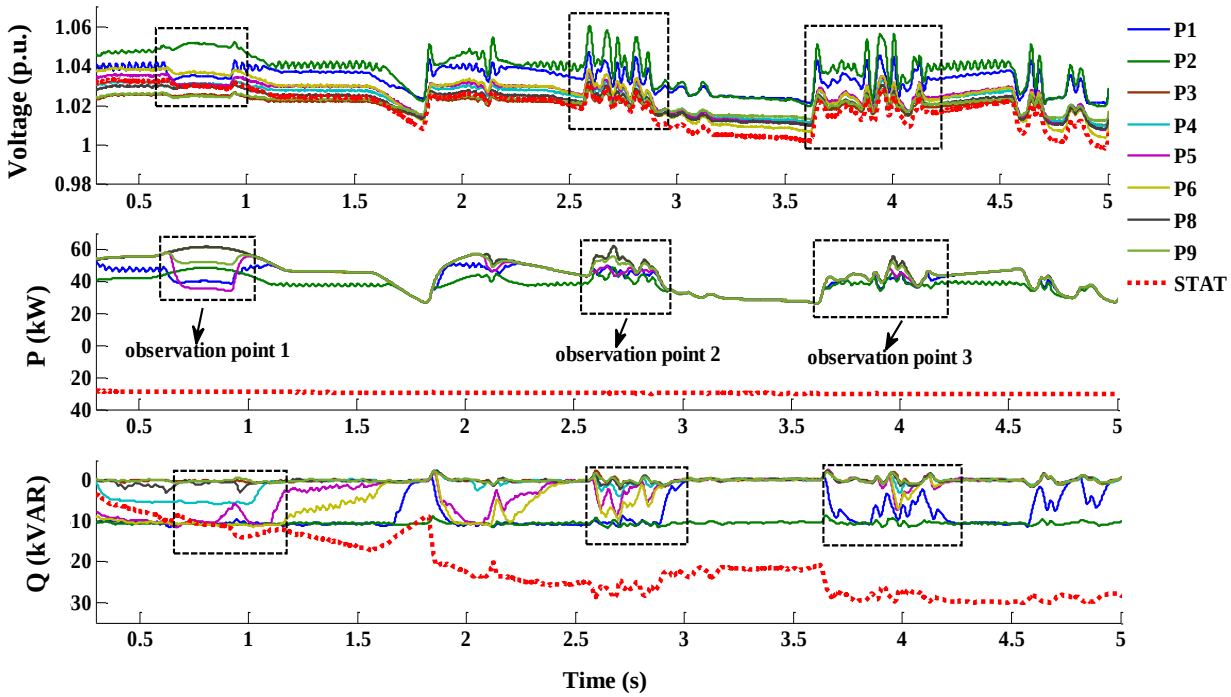

Figure 3.24. LV network with $PV_{pen.}$ >75% during winter

3.5 Economical Implications of the Developed Methodology

In conjunction with the policies enacted by federal governments in Australia, a solar PV cost reduction from 12 A$ to 2 A$ per watt contributed significantly to the number of PV installations [116]. Following this scenario, the installation numbers can be anticipated to increase more significantly in future years. For a control methodology to be effective in real-life applications, it needs to be robust in performance, as well as cost effective when compared with existing methodologies. A simplistic comparative cost analysis has been conducted for the proposed hierarchical control selection method. The standard pricing for the VAR requirement is assumed to be 50-55 US$/ kVAR and a BES unit, such as a zinc-bromide (ZnBr) flow battery is 400 US$ / kWh [111], [117]. For control modes A and B, the D-STATCOM (30 kVA) and the BES (30 kWh) total price would be around 13,500 US$. If the decentralised controls were applied from the PV penetration higher than 30%, it would require smart VSI and BES to be installed at the 6 test points, except for P3 and P4 because they are close to the distribution transformer and do not indicate much voltage sensitivity with increasing PV penetration. At a PV penetration higher than 50%, each cluster point would require at least 20 kVAR or 15 kWh BES charging-operation local support to regulate the terminal voltage at each test point. For one cluster point, the smart-VSI

total cost would be around 1000 US$ and for the BES installation 6000 US$. Assuming 6 test points, the total installation cost would be 6000 US$ for the smart VSIs and 36,000 US$ for the BES alone. With the proposed hierarchical control selection methodology, control mode C ($PV_{pen.}$ > 50%) requires local regulation at critical points only after the STATCOM/BES compensation operation, resulting in fewer device installation requirements. Moreover, as the proposed method assumes both DNOs' (D-STATCOM/BES) and customers' support, the overall cost is expected to be much less than any individual regulation. From the test results and cost analysis, it can be concluded that the proposed methodology provides a robust dynamic voltage improvement, as well as a more cost-effective solution than any individual centralised or other decentralised methods.

3.6 Chapter Summary

In this chapter, a hierarchical control-selection method is presented for mitigating voltage-rise problems associated with incremental PV penetration into LV networks. From the initial investigation, it is discovered that, when the PV penetration level exceeds a certain level, for example in this research study more than 30%, the LV network exhibits voltage constraints (± 6%), especially at the farthest customer points (P1, P2, P5, P6) from the distribution transformer. When the proposed control selection method is applied, the voltage constraint issues from different PV penetration levels can be easily resolved when the different DER units' operations are coordinated. The economical and technical justification of the proposed control method is also analysed. Rather than installing dynamic compensation devices at all the test points, voltage compensation devices, at critical points alone can provide stable and economical operation in any LV network. Before analysing the effect of transmission-system unbalances, it is important to understand the effect of RES penetration into a particular network. Therefore, in this research study, the R/X ratio is assumed to be unity and the LV network a balanced three-phase three-wire system. However, LV networks consist of both three- and single-phase loads, making the distribution system a three-phase four-wire system where an unbalance scenario is a common phenomenon. Due to unbalanced load distribution in a four-wire network, severe neutral current can be generated from loads, which can cause phase unbalance and overheating of the neutral conductor.

In the next chapter, a novel neutral current compensation method is presented with the effects from transmission line R/X ratios and improved PCC voltage regulation considered.

Table 3.3 Component specifications

Components	Specifications
PV modules	
50% penetration	No of series module = 10 No of parallel module = 6 Current limit = + 70A
> 65% penetration	No of series module = 10 No of parallel module = 8 Current limit = + 100A
> 85% penetration	No of series module = 10 No of parallel module = 12 Current limit = + 130A
DC voltage	600 - 800V
DC link capacitor	2000 μF
Switching frequency and time step	3 kHz and 5 ms
DC voltage regulator	Kp =5, Ti=0.008
Internal current controller	Kp= 8, Ti=0.003
LCL filter	$L_{inverter}$ =4 mH ; C_{filter}= 10 μF; L_{grid}= 1 mH; Rd=1 mΩ
D-STATCOM	
DC voltage regulator	Active Current limiter ± 60A
PI gain values	Kp=2, Ti=0.8
PCC voltage regulator	Reactive current limiter = ± 60 A
PI gain values	Kp=2, Ti=0.8
LC filter	L= 4mH ; C= 20μF; Rd= 3mΩ
Switching frequency	3 kHz
BES (Lithium ion)	
Nominal voltage	320 V
Initial SOC	70%
Rated capacity	6.5 Ah
Nominal discharge current	20%
Fully charged voltage	1. 15 p.u.
Resistive drop	0.005 p.u.
LV Grid	
Grid voltage	415 V/240 V
Distribution transformer rating	11kV/ 415 V, 750 KVA, leakage reactance .04 p.u.
No of customers	150
Total area length	Approx. 2 km

Chapter 4
Multifunctional Operations with Three-Phase Four-Leg PV-SVSI

Three-phase (3P) four-wire (4W) low-voltage (LV) distribution networks are widely used in many countries to supply both single- and three-phase loads connected to residential, commercial and office buildings. The additional fourth wire is provided from the grounding point of the delta/wye distribution transformer (DT) and used as the return path for the single-phase load connections. Practically, the LV networks exhibit unbalanced characteristics due to unbalanced single-phase loading and nonlinear loads, such as nonlinear rectifiers, computers, adjustable speed drives in small air conditioners, automatic office machines, and lighting ballasts. Nonlinear rectifier type loads generate the triple harmonic current which is regarded as the zero sequence current component and zero sequence currents in each phase add up and flow via the neutral conductor [119]. Additionally, unbalanced single-phase load distributions generate the fundamental zero sequence component of the unbalanced currents, which also flow through the neutral conductor, and can result in overloading the neutral conductor of the transmission lines [120].

Considering the load-generated neutral current, a novel neutral current compensation method is applied to the smart voltage source inverter (SVSI) in this chapter. The variable zero sequence R/X ratios (R_0/X_0) of transmission line conductors are considered in the neutral compensation mechanism and higher stability margin with better compensated and phase balancing performance is presented with an Australian LV residential power network.

This chapter is organised with seven sections as follows. Section 4.1 presents the introduction of neutral current generation and different neutral compensation methods, while the designed system configuration is described in Section 4.2. In Section 4.3 the stability analysis of the designed current controller using frequency and circuitry analysis are presented, and Section 4.4 is conducted with the network description with the considered test points. Extensive case studies are presented in Section 4.5. Finally, the chapter summary is included in Section 4.6, highlighting

the findings derived from the novel neutral compensation methods concerning the designed four-leg inverter. It also describes the requirements for higher capacity neutral compensation operation with unbalanced loads distribution.

4.1 Introduction

Uneven distribution of loads is a common phenomenon in LV networks. Even with a balanced utility supply, non-uniform single-phase load distributions can generate severely unbalanced currents [16]. Initially, the neutral conductor of a three-phase four-wire system was designed as a non-current carrying conductor (i.e. only to carry asymmetry currents during faults for a short period of time); however, with unbalanced loads in recent times, excessive unbalanced current can flow through the neutral conductor and can easily exceed its rated capacity. Excessive neutral current can cause overloading of the neutral conductors, mal-operation of sensitive electronic equipment, over-heating of the DT, raise electrical safety concerns because of increased ground voltage, and even cause a fire in some severe cases [18]. In 1990, a survey in the United States reported that 22.6% of computer sites carried more neutral current than the maximum full load phase-current capacity [14].

To capture realistic characteristics of LV networks with unbalanced loading in addition to a renewable energy source (RES), such as a photovoltaic (PV) system, it is imperative to analyse the neutral compensation and load balancing methods with actual customer load and network profiles. The transmission conductors in 3P-4W LV networks consist of both positive and zero sequence line parameters, which need to be accounted for while performing neutral compensation operations. Additionally, the grounding systems utilised in residential areas are designed basically for carrying transient fault currents, and cannot neutralise the leakage currents generated from non-uniform and nonlinear load distributions [24]. Therefore, different neutral current compensation and phase balancing techniques have been proposed by researchers, such as resizing the neutral conductor [14], installation of zigzag transformer (ZT) [118], delta-wye transformer [120], passive filter installation [121], and application of series [41] and shunt active power filters [122], hybrid power conditioners [123] etc. Resizing the neutral conductor, however, will incur significant cost and time. The passive harmonic filter introduces additional resonance problems with the network as well as interference with the communication link commonly installed close to the neutral line [23]. Of the passive compensation techniques, ZT is advantageous due to less complexity in

control operation and lower capacity requirements than other transformer configurations [124]. It provides a path for the zero sequence current while behaving as an open circuit to other sequence components. It is commonly used to reduce load unbalance and grid-side neutral current. However, with unbalance voltage cases, ZT causes additional neutral currents and thus it needs to be installed close to the user premises, which makes the system bulkier. Authors in [125] propose the utilisation of an additional leg with a three-leg voltage source inverter (VSI), (i.e. fourth leg), for better control flexibility and unbalanced load compensation.

Active power filters mainly employ the four-leg VSI configuration in different connections, such as series and shunt. A combination of both active and passive filters (i.e. hybrid filters) can provide better performance, but this suffers from low-voltage drop due to DC voltage reduction. Additionally, it would require more than one installation of the compensation device for optimised performance in actual LV networks. Higher capacity requirements, additional switches, and switching losses are the main impediments to the widespread installation of active power filters. With regard to economy, passive compensation provides a better investment deal due to its lower capacity requirement; however, it lacks full control over neutral currents due to its dependence on grid-side impedance.

The application of four-leg VSI can be made more attractive for customers if it is incorporated with popular RES installations, such as PV systems. Despite the popularity of PV installations, different peak periods of solar generation (day time) and residential customer load demands (night time), as well as reduction in feed-in tariff (FIT) offers [126], sometimes cause customers to rethink their initial investment in PV installations, or alternatively they may need to install storage devices, such as battery systems, with additional costs. Since the VSI is installed as an essential part of the PV system, mainly for active power and in some cases reactive power regulations with the grid [59], introducing an additional load balancing function via neutral current compensation from a four-leg SVSI can increase customers' interest in PV installations. This particularly refers to them looking for better quality of power, and lower electricity bills from the installation unit. The incorporation of a four-leg inverter with a PV source is proposed with multifunction operations, such as active power regulation, reactive power compensation, harmonic reduction, and load neutral compensation in [60]. However, in [60], stability analysis with network transmission line parameters is missing. Authors in [127] present an adaptive droop control technique with PV smart VSI and additional battery energy storage to reduce voltage-sag and swell

cases with the variation of transmission line positive sequence R/X ratios in the LV network. However, analysis with network unbalance cases is not presented in [127]. Authors in [17] propose the installation of additional battery sources for neutral to ground voltage reduction caused by unbalanced rooftop PV installations in a multi-grounded Australian LV network, which would incur an additional cost regarding customer installation units. None of the previously mentioned papers, however, has considered the effect of variable transmission line zero sequence parameters for neutral compensation and, additionally, no results are presented for PV systems' active to inactive transitions and transient fault effects for a full-day operation period.

Therefore, in this chapter, a multi-functional four-leg PV-SVSI is designed for full-day operation functionality with PV active power export, dynamic PCC voltage regulation, and active neutral current compensation controls in a 3P-4W LV residential network located in Brisbane, Australia. The network model and load data of customers are collected from the local distribution network operator)DNO(Energex as noted in the previous chapter. This chapter concentrates on the following:

(i) Developing the relationship between the load-generated neutral current and transmission lines zero sequence R_0/X_0 ratios;

(ii) Proposing a new active neutral compensation method using the load-generated neutral and zero sequence currents as direct references for the neutral and zero sequence current PI controllers; and

(iii) Designing a PCC voltage regulator with dynamically, capacity allocated current limiters in both PV active and inactive periods.

The unbalanced loads generated neutral current can be sensed using a smart residential meter, such as the SATEC smart meter]128[. The effect of positive sequence R_+/X_+ ratio of the transmission lines is mostly noted during active and reactive power-sharing operations. However, the unbalanced or harmonic currents mainly flow via the zero sequence impedance of the transmission lines, therefore, stabilised operation with variations in the zero sequence R_0/X_0 ratios of the transmission conductors needs to be ensured. Initially, the robustness and stability of the designed SVSI controller are verified by the bode-plot and circuitry model analyses from the zero sequence network. Finally, the optimised performance of the designed controller is verified by installing the PV- SVSI with real customer loads in the LV network model at remote locations with different R_+/X_+ and R_0/X_0 ratios.

Different transient faults, such as symmetrical)three-phase to ground(and asymmetrical)double-phase to ground, and single-phase to ground(, are also examined at the furthest location from the DT with lowest R_0/X_0 ratio. The subsequent results are compared with a passive ZT neutral compensator, a combination of ZT and traditional three-leg PV-VSI, and a traditional active neutral compensator which considers the neutral current controller reference as zero [129].

4.2 System Configuration with Four-Leg PV-SVSI

The configuration of the designed four-leg PV-SVSI system with the controller blocks, LCL filter, residential customer loads, and the LV network is shown in Fig. 4.1. The four-leg inverter is designed following a single-stage transformerless configuration for a 24-hour PV operation as described in Chapter 2. The additional fourth leg controller is designed independently to follow a specific reference within the inverter maximum current limits. The third-order LCL filter is designed to achieve better quality power outputs both during day and night operation. Constant DC voltage regulation on the DC side of the VSI is ensured for both PV active and inactive periods. During daytime, the PV system will export maximum power to connected loads and the remaining power after load compensation can be transferred to the grid or can be used to charge storage mediums, if available. A fixed neutral current limit is utilised for the load neutral compensation. The single-phase customer loads are designed using variable R-L loads with grounding resistor R_{GND} whose data is collected from the local DNO. The PV-VSI configuration as shown in Fig. 4.1 is utilised in different remote areas in the test power system network with different R_+/X_+ and R_0/X_0 ratios. It verifies the robustness of the designed neutral compensation due to unbalanced single-phase load distributions.

4.3 Analysis of the Designed Four-Leg SVSI

Two different analytical methods, namely frequency analysis and zero sequence circuitry analysis, are performed to verify the robustness and wide stability margins provided by the designed controllers of the four-leg PV-SVSI system.

4.3.1 Frequency analysis

The transfer functions of the designed controllers are derived from the small-signal model by applying a perturbation method around the DC operating point. The transfer functions are derived

by sensing the grid-side current that provides a faster reference following operation than sensing the current from the inverter-side.

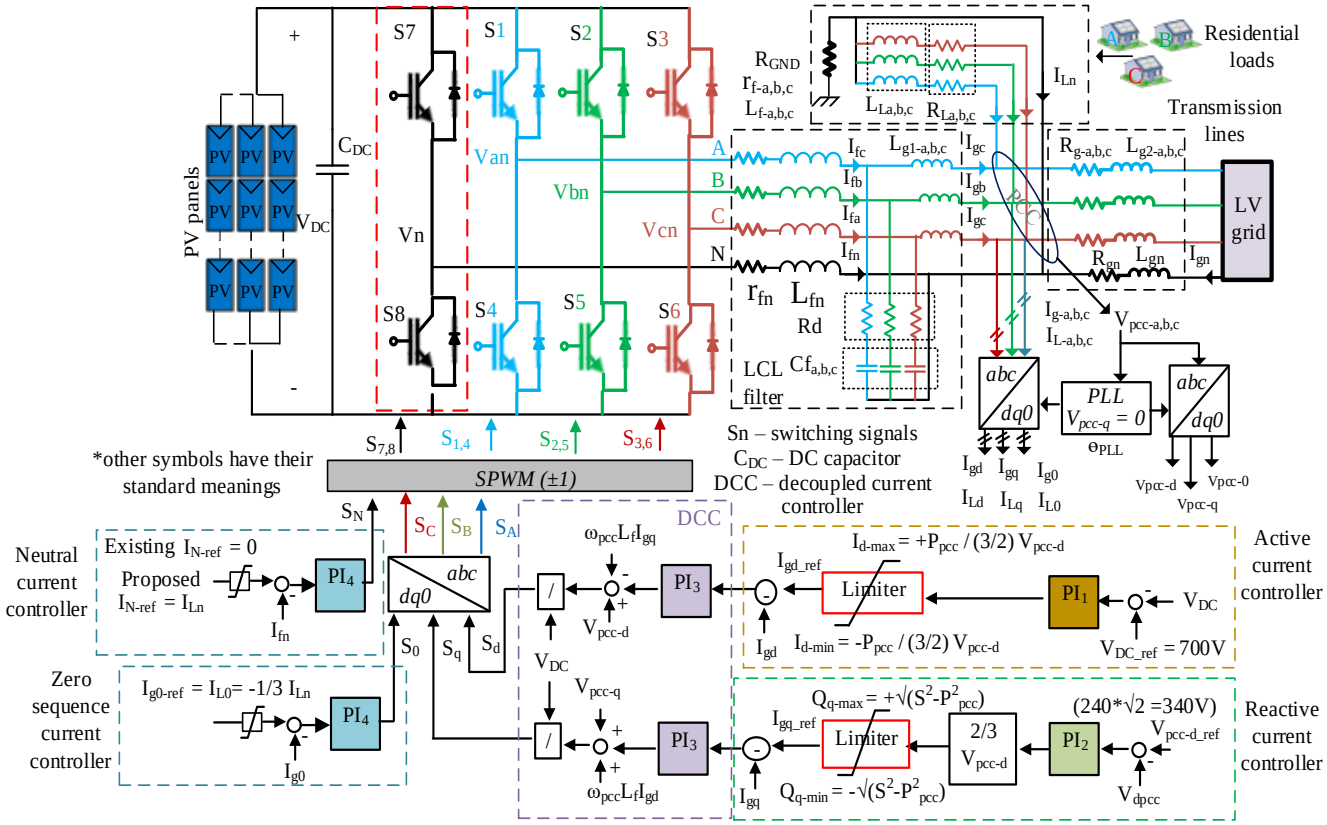

Figure 4.1. Designed four-leg PV smart VSI connection and control diagram

A digital time delay function is considered for the PWM switching following the second-order Pade approximation which can be expressed as [60];

$$G_{SPWM}(s) = e^{-sTdel} \approx \frac{1 - 0.5sT_{del} + 0.083(sT_{del})^2}{1 + 0.5sT_{del} + 0.083(sT_{del})^2} \tag{4.1}$$

where T_{del} is the switching period.

The decoupled *d* and *q* current controllers, and the zero and neutral current controllers show similar bode characteristics. Hence, only an open loop bode analysis of the *d* and zero sequence current controllers is performed by varying the R_+/X_+ and R_0/X_0 ratios in the expressions (4.2) and (4.3), and the results are shown in Fig. 4.2.

$$\frac{I_{gd}}{K_d} = V_{DC} \frac{SC_f R_d + 1}{H_1(s)} \tag{4.2}$$

$$\frac{I_{g0}}{K_0} = V_{DC}\frac{SC_fR_d + 1}{H_2(s)} \tag{4.3}$$

where $H_1(s) = S^3C_fL_gL_f + S^2C_f\left(L_f(R_g + R_d\right) + L_g(r_f + R_d)) + +S[C_f(R_gr_f + R_gR_d + R_dr_f) + \left(L_f + L_g\right)] + \left(R_g + r_f\right)$,

$H_2(s) = S^3C_fL'_gL'_f + S^2C_f\left(L'_f(R'_g + R_d\right) + L_g'(r_f' + R_d)) + S[C_fR_T + \left(L'_f + L'_g\right)] + \left(R'_g + r'_f\right)$,

$L_f' = L_f + 3L_{fn}$, $r_f' = r_f + 3r_{fn}$, $L_g = L_{g1} + L_{g2}$, $L_g' = L_g + 3L_{gn}$, $R_g' = R_g + 3R_{gn}$, and $R_T = R'_gr'_f + R'_gR_d + R_dr'_f$.

The gain values of proportional-integral (PI) controllers are tuned using the Zigler-Nichols method [129] and shown in Table 4.1 at the end of this chapter. The phase and neutral transmission line characteristics are added as new terms in the transfer function, and the values used are from different transmission conductors as shown in Table A.2 in the Appendix.

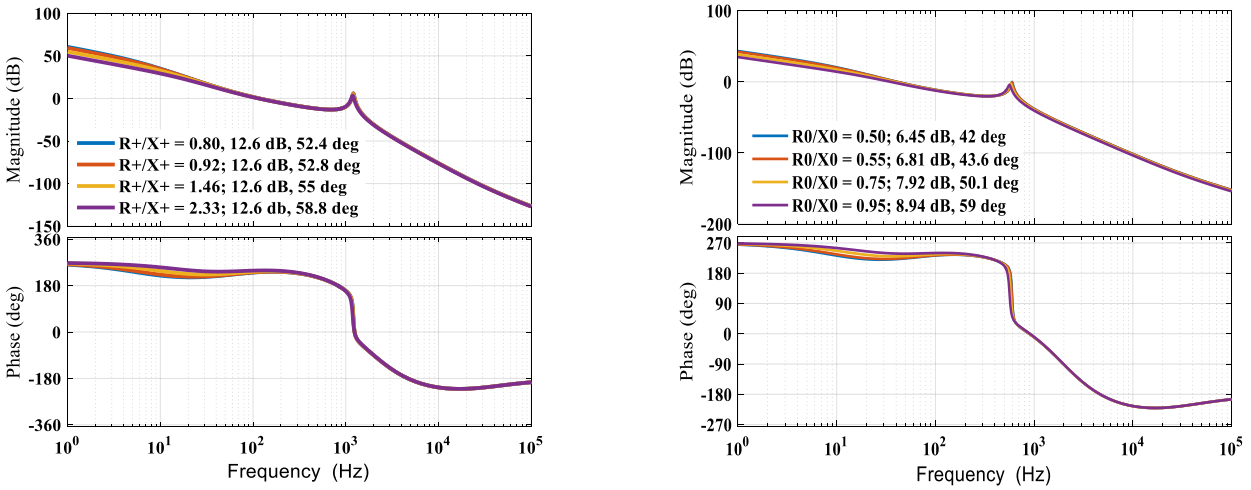

(a) (b)

Figure 4.2. Open loop bode plot of (a) I_d, and (b) I_0 current controllers

From the open loop bode analysis as depicted in Figs. 4.2 (a) and (b), it is evident that, even with the lowest R_+/X_+ (0.80) and R_0/X_0 (0.50) ratios, both the active and zero sequence current controllers have sufficient gains, of 12.6 dB, 6.45 dB, and phase margins, of 52.4 and 42 degrees, respectively. Similarly, high stability margins are recorded for higher R_+/X_+ (2.33) and R_0/X_0 (0.95) ratios with the gain margins 12 dB and 8.94 dB, and the phase margins 58.8 and 59 degrees, respectively. The other R/X ratio values indicate similar stabilised results from the designed *d* and

zero sequence current controllers. The robustness of the designed controller is ensured by keeping the same PI gain values with variable network parameters.

The bode analysis results from Figs. 4.2 (a) and (b) prove the wide margins range for network stability even with diverse LV network parameters. In the case of rural distribution networks with higher R_+/X_+ ratios (sometimes > 10) [108], only the PI gain values need to be changed with the same designed PV-SVSI system to achieve similar stable and robust performance. However, the application of four-leg VSI with a rural distribution network is not considered in this research.

4.3.2 Sequence network analysis

A zero sequence network is designed including the phase and neutral conductor zero sequence impedances with the inverter, grid, and load-side components. Three-phase load-generated zero sequence currents flow through the zero sequence impedance of the neutral conductor. Therefore, the impedance of the neutral conductor (Z_{fn0}, Z_{gn0}, and Z_{Ln0}) is three times the phase zero sequence impedance values as shown in Fig. 4.3 [123]. To analyse the effect of the load-generated zero sequence current on the utility-side zero sequence current (i.e. neutral current respectively) the superposition theorem is applied to the sequence network as shown in Fig. 4.3, where the active contributing sources are the load-generated zero sequence current, PCC zero sequence voltage, and inverter-side active zero sequence voltage.

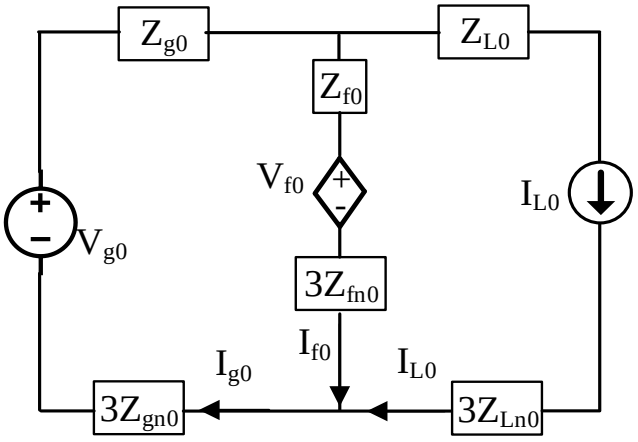

Figure 4.3. Zero sequence network of the designed system

Initially, the effect of the load-generated zero sequence current (i.e. I_{L0}) is considered as shown in Fig. 4.4, and the effect on the utility-side zero sequence current is expressed in (4.3).

$$I'_{g0} = \frac{(Z_{f0} + 3Z_{fn0})}{(Z_{f0} + 3Z_{fn0}) + (Z_{g0} + 3Z_{gn0})} I_{L0} \tag{4.3}$$

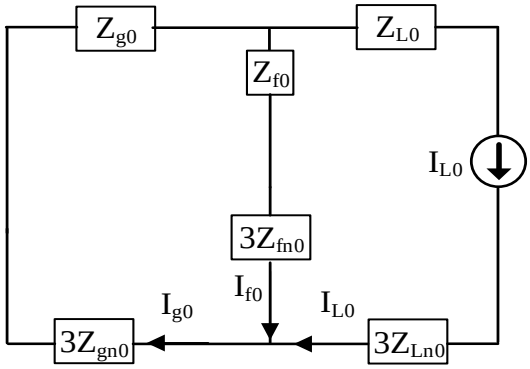

Figure 4.4. Load-generated neutral current effect on utility-side zero sequence current

In this step, the PCC voltage unbalanced effect (V_{g0}) on the grid-side zero sequence current is considered as shown in Fig. 4.5, and the mathematical expression can be written as:

$$I''_{g0} = \frac{V_{g0}}{Z_{f0} + 3Z_{fn0} + Z_{g0} + 3Z_{gn0}} \tag{4.4}$$

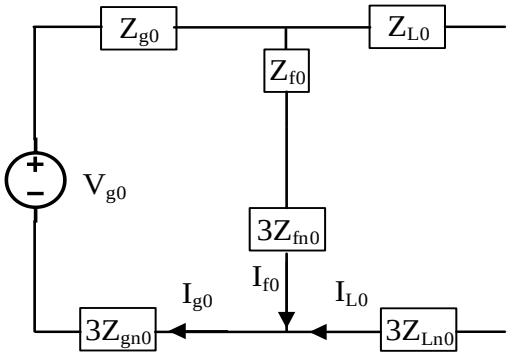

Figure 4.5. Utility-side voltage unbalance effect on grid-side zero sequence current

Lastly, the effect of the proposed active neutral compensation with controlled zero sequence voltage source (V_{f0}) is analysed as shown in Fig. 4.6, and the grid-side zero sequence current is:

$$I'''_{g0} = \frac{V_{f0}}{Z_{f0} + 3Z_{fn0} + Z_{g0} + 3Z_{gn0}} \tag{4.5}$$

Combining (4.3) to (4.5) results:

$$I_{g0} = I'_{g0} + I''_{g0} \pm I'''_{g0}$$
$$= \frac{(Z_{f0}+3Z_{fn0})}{(Z_{f0}+3Z_{fn0})+(Z_{g0}+3Z_{gn0})} I_{L0} + \frac{V_{g0}}{Z_{f0}+3Z_{fn0}+Z_{g0}+3Z_{gn0}} \pm \frac{V_{f0}}{Z_{f0}+3Z_{fn0}+Z_{g0}+3Z_{gn0}} \tag{4.6}$$

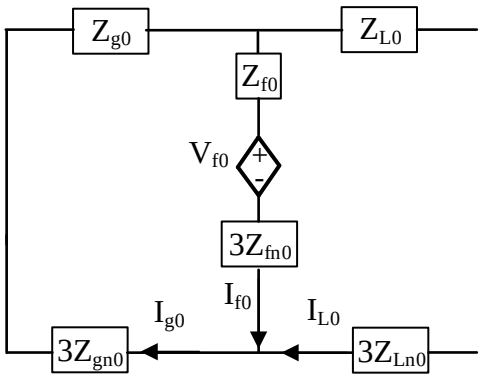

Figure 4.6. V_{f0} compensation effect on utility-side zero sequence current

From (4.6), only the inverter-side zero sequence voltage source, $V_{f0,}$ can be controlled, therefore the '±' sign is utilised. The load-side and grid-side sources present inherent values and depend on the load characteristics and network balancing condition. Therefore, from (4.6), it is evident that by controlling V_{f0}, the overall performance of the grid-side zero sequence current, due to load unbalance and PCC voltage distortion, can be actively compensated. The V_{f0} source is a neutral current dependent voltage source; therefore, controlling the zero sequence current from the four-leg SVSI can actively control the grid-side zero sequence and neutral currents. Additionally, it is evident from (4.3) – (4.6) that the grid-side impedance plays a vital role in the neutral current compensation at a particular connection point. The effects of the proposed compensation with variable R_0/X_0 ratios are shown in Fig. 4.7.

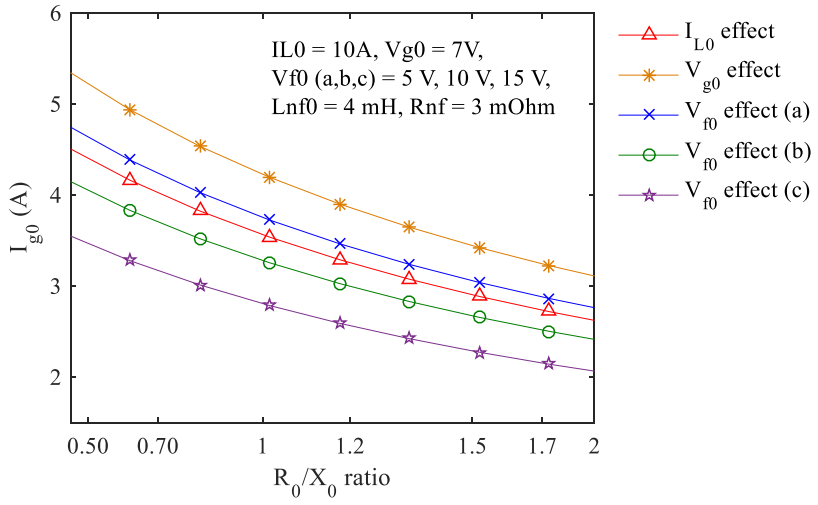

Figure 4.7. Zero sequence current compensation effect with variable R_0/X_0 ratio

It can be seen from Fig. 4.7 that the lower R_0/X_0 ratio results in a higher neutral current requirement, and the opposite happens with a higher R_0/X_0 ratio, i.e. lower neutral current. Considering linear region operation, the duty ratios of the VSI are considered as unity, and different V_{f0} values are considered. It is evident in Fig. 4.7 that the utility-side zero sequence voltage can make the grid-side zero sequence current have a worse effect with variable R_0/X_0 ratios. Conversely, by controlling the V_{f0} as much as 1 A zero sequence current can be actively compensated with the considered parameters. This also demonstrates that the same system can have different utility-side zero sequence (I_{g0}) current with different values of R_0/X_0 ratios at the customer connection points.

4.4 Description of LV Network and Test Points

The performance of the designed four-leg PV-SVSI is analysed in the 3P-4W LV distribution network described in Chapter 2. In the previous chapter, the hierarchical control selection method is applied with an LV feeder base load condition, and it is found that the furthest test points from the DT exhibit the most voltage-sensitive characteristics. Therefore, in this chapter the designed four-leg PV-SVI system is installed at the remote locations only considering voltage-sensitivity effects. An aggregated 20 kVA three-phase four-leg VSI installation with dynamic PCC voltage regulator, maximum 14 kW PV generation at standard test condition (I_d - current limit ± 22 A) and fixed-capacity neutral compensation (± 10 A limit) are considered. The aggregated installation includes four customers, two from phase C and one from phases A and B, each having 5 kVA units. From customer load data provided by Energex, it is evaluated that each customer has a maximum 3.3 kW and 0.5 kVAR load connection, and the phase C load profiles are more unbalanced than the other two phases for that particular connection point, which is the main reason for generating the neutral current at that particular customer point. The LV network is designed as a 44-bus as shown in Fig. 4.8. Actual load profiles are incorporated into the network using an additional three customers on each phase in remote locations (on buses 8, 16, 25 and 39) which are denoted as P1-P4 respectively. The R/X ratio values for the test points are shown in Table 4.2 at the end of this chapter and the detailed calculation of R/X is shown in Table A.3 in the Appendix. The sun irradiance and temperature data are collected from the microgrid installation at Griffith University, Australia. The DC bus voltage is regulated at a constant 700 V for both PV active and inactive operations. The PV specifications data from Chapter 3 are utilised in this simulation

studies. Instead of evaluating performance with specific load types, such as electric heater, air conditioner, water pump etc., 24-hour customer load profiles for individual phases are exported to a variable R-L type load connected at the PCC with the PV-SVSI installations. In this way both the transient performance and sustainability of the designed system can be easily monitored. Several case scenarios are presented in the next section and the results from the designed four-leg PV-VSI are compared with traditional neutral compensation devices, such as zig-zag transformer (ZT) and the combination of ZT and three-leg VSI, to verify the efficacy of the designed four-leg PV-SVSI with the proposed neutral compensation control for a 24-hour operation period.

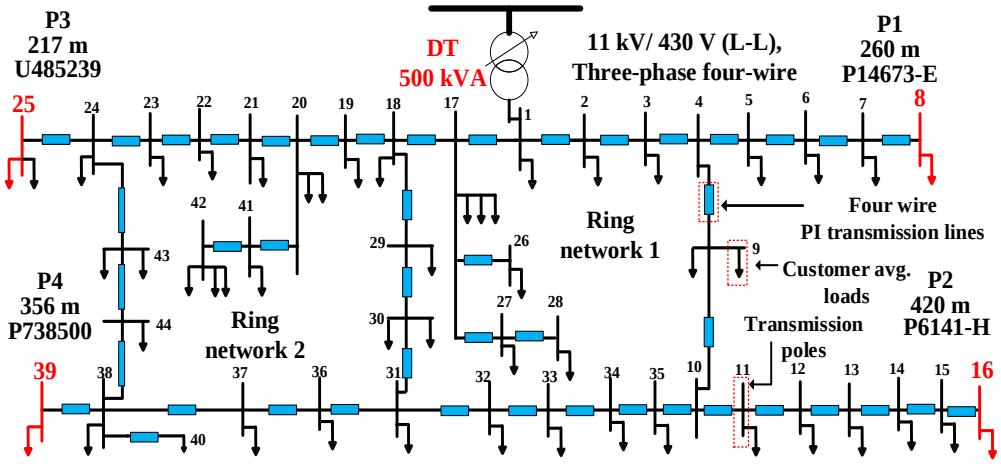

Figure 4.8. Residential 3P-4W LV network 44-bus single-line diagram

4.5 Multifunctional Four-Leg PV-SVSI Operations

4.5.1 Four-leg smart VSI performance with PV

To evaluate the 24-hour normal operation from the designed controller with the LV network, the four-leg VSI is installed at the remote customer point P2 (420 m from DT) with the customer load profiles shown in Fig. 4.9. Fig. 4.9 shows that the phase C customers consume more active power while the phase B customers consume higher reactive power. The load demands on each phase from 17:00 to 19:00 hours show the most severe unbalanced load distribution characteristics, resulting in higher load neutral current as can be seen from Fig. 4.10. As the proposed neutral compensator utilises the load-generated neutral current as a reference for the neutral controller, the significant increase in the load neutral current after 17:00 hour resulted in an increase in neutral modulating signal (S_N) as Fig. 4.11 indicates. This increase in SN ensures robust compensation for

the load-generated neutral currents at the PCC. Despite the divergent and unbalanced load profiles, both the phase and neutral modulating signals of the designed PV-SVSI operate within the linear region (± 1) as shown in Fig. 4.11.

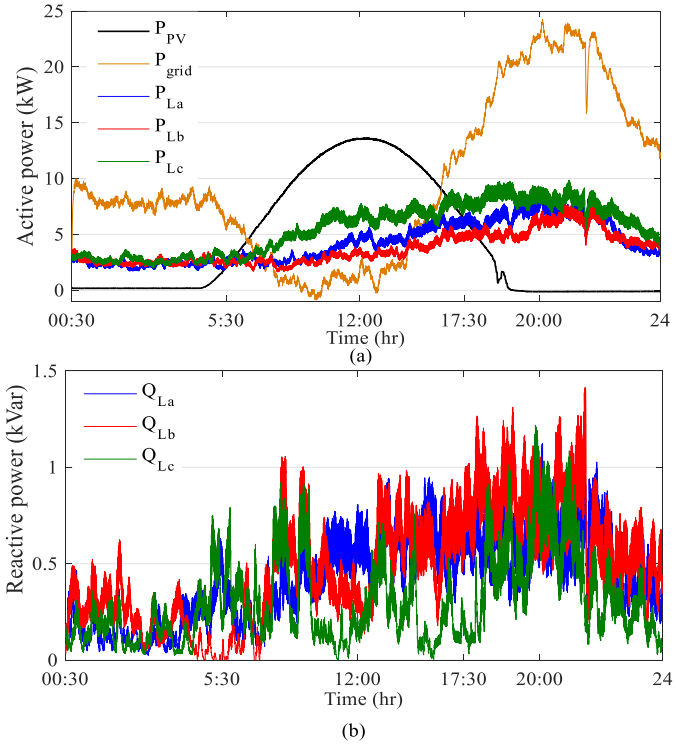

Figure 4.9. Customer profiles (a) active power, and (b) load reactive power demand

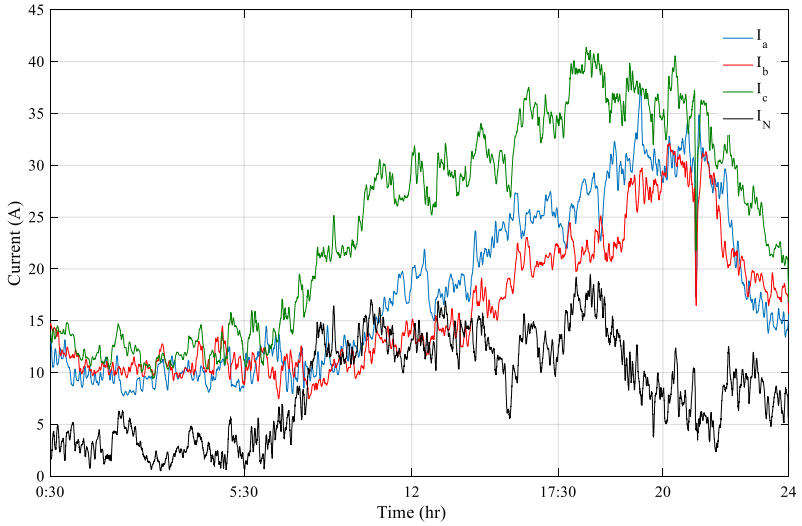

Figure 4.10. Phase and neutral currents with the customer load connection

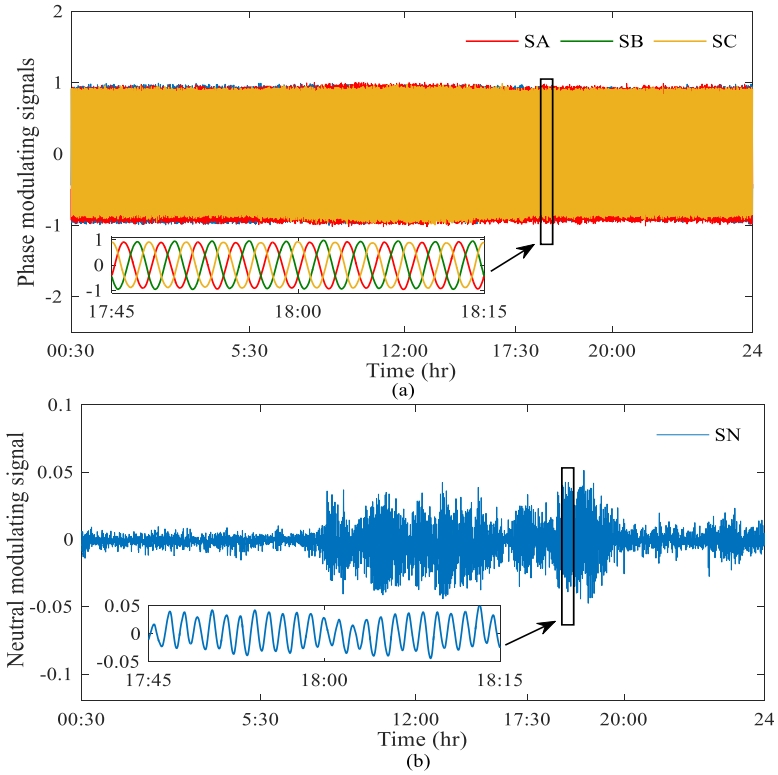

Figure 4.11. (a) Phase, and (b) neutral modulating signals of the designed four-leg VSI

Due to the linear region operation from the SPWM switching controls, negligible harmonics are generated and a seamless transition from PV active to inactive period is achieved. This is shown in the phase C voltage vs current (V-I) plot in Fig. 4.12.

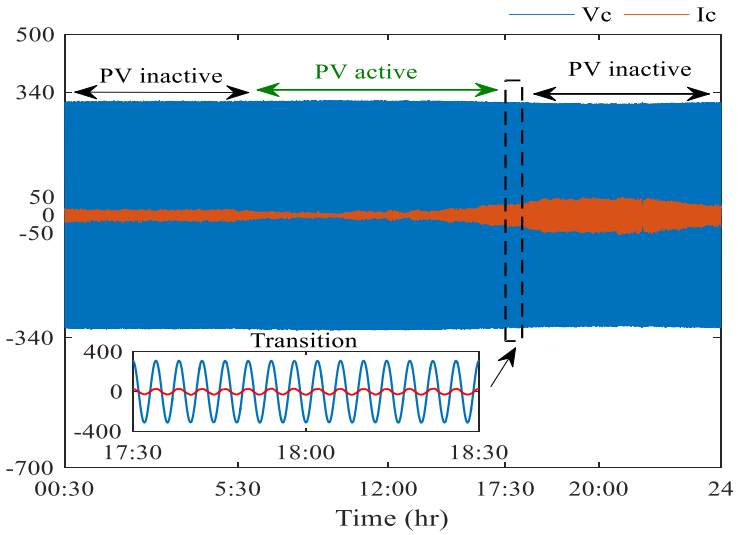

Figure 4.12. V-I plot of phase C at test point P2

It is evident from Fig. 4.12 that the voltage and current waveforms maintain a controlled phase angle even during the transition period. The seamless transition helps to operate the installed PV-VSI unit continuously despite divergent weather conditions. Even with the same PV-VSI configuration at the test points, the different load-generated neutral currents are monitored from the test system and reflect the dependence of the neutral current on the R_0/X_0 ratios of the LV network transmission conductors. This is described in more detail in the next case study.

4.5.2 Neutral compensation with variable R_+/X_+ and R_0/X_0 ratios

In this case study, the robustness of the proposed neutral current compensation with the designed four-leg SVSI is presented at different network locations (P1-P4) having different transmission-line characteristics as shown in Table 4.2. The proposed compensation considers the load-generated unbalanced current as the reference for the fourth leg control, which helps to avoid unnecessary neutral compensation resulting from inherent network unbalance, and thus more efficient operation can be achieved. The inherently unbalanced characteristics of the LV network with the base load condition for the considered test points are shown in Fig. 4.13. It is evident from Fig. 4.13 that, even with same base load condition within the LV network, the considered test points reveal quite different neutral currents and voltages. Among the test points, P1 has the highest base neutral current with the highest R_+/X_+ ratio, whereas the furthest point from DT (P2) has the highest neutral voltage with the lowest R_+/X_+ ratio.

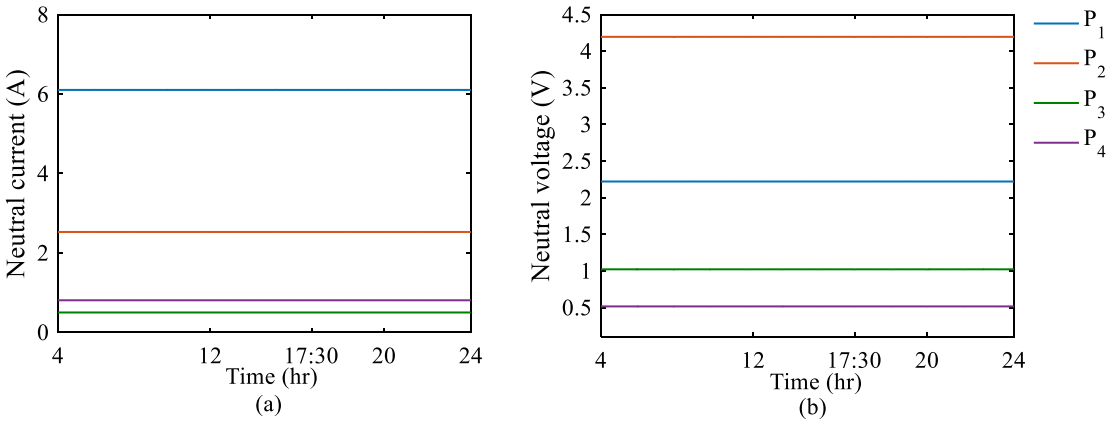

Figure 4.13. (a) Neutral current, and (b) neutral voltage of LV feeder at base load condition

The effect of zero sequence R/X ratio of the transmission-lines on the load-generated neutral current are shown in Fig. 4.14. This figure illustrates that P2 point with the lowest R_0/X_0 ratio, results in a higher value of neutral current at severe unbalance periods, and P3 with the highest

R_0/X_0 ratio results in a lower value of neutral current with the same load application. The increase in neutral current (I_N) also causes an increase in neutral voltage (V_N) as shown in Fig. 4.16 (b).

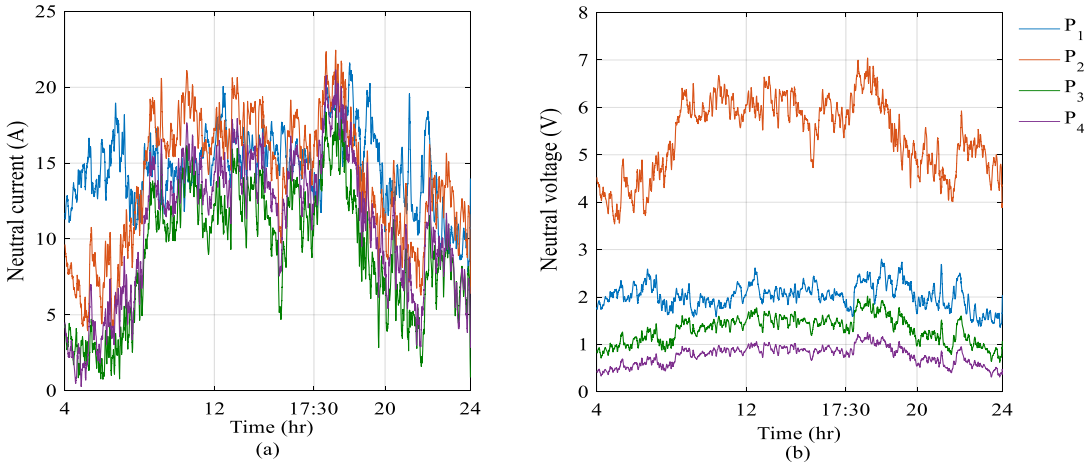

Figure 4.14. (a) I_N, and (b) V_N with same customer loads at different test points

Unlike the proposed active compensation method, passive compensation by a zigzag transformer (ZT) provides a path for the neutral current irrespective of the generating source, thus causing unnecessary overloading in the neutral conductor. The performance of neutral compensation due to unbalanced load distributions is evaluated for five cases: base LV feeder inherent characteristics, case (a) with load connection only, case (b) with load and ZT compensation, case (c) with load, ZT and traditional three-leg PV-VSI, and case (d) with the proposed four-leg PV-SVSI. The comparisons of the case conditions at different network locations from P1-P4 are shown in Fig. 4.15 (a)-(d), respectively. The same load profiles are used at all the test points (P1-P4), which is convenient to verify the load-generated neutral currents' dependence on the transmission line R_0/X_0 ratios.

It is shown in Fig. 4.7 that, a location with a lower R_0/X_0 ratio causes higher load neutral effects, and a similar trend can be observed in Fig. 4.15. The same unbalanced load connection generates a neutral current maximum of 22 A (rms) at P2 with the lowest R_0/X_0 of 0.74 in Fig. 4.15 (b), and a minimum 18 A (rms) at P3 with the highest R_0/X_0 ratio of 0.87 in Fig. 4.15 (c). The location P1 with the highest LV feeder unbalanced current (15 A) in Fig. 4.15 (a) results in a marginally high load neutral current compared to location P4 in Fig. 4.15 (d). In all the test locations, the proposed neutral compensation provides better performance than other case conditions, even with the same controller gain values. This proves the wide stability margin and robustness of the designed

controller irrespective of the PV-VSI installation locations within the LV network. The simulation results show wide stability margins even with variable R_0/X_0 ratios, similar to the bode-plot analysis in Fig. 4.4. During the 17:30-20:00 analysis period, the neutral controller exceeds the maximum fixed-capacity limit (± 10 A), which resulted in less compensated neutral operation as can be seen from Fig. 4.15. Generally, increasing the compensation capacity can further reduce the neutral current; however, in this case, even with the existing limited capacity operation, better compensated performance is achieved even during peak load unbalanced conditions.

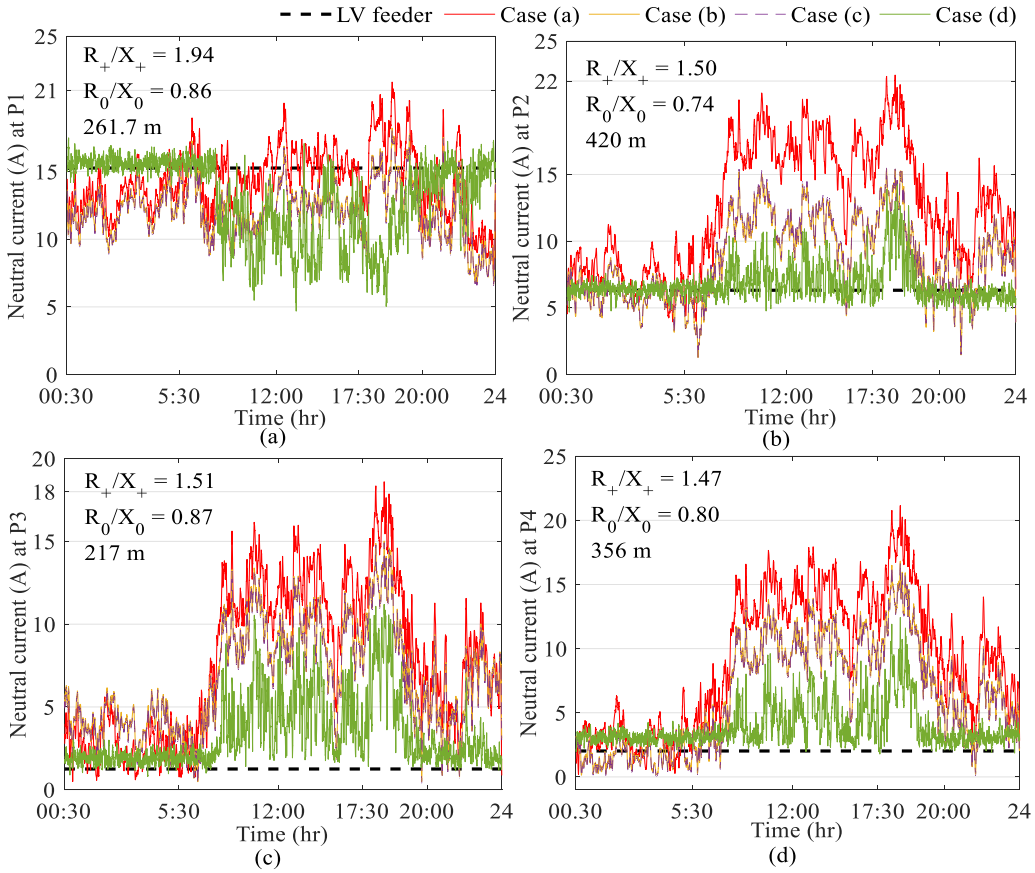

Figure 4.15. I_N compensation comparison at remote points with variable R_0/X_0 ratio

Without any additional neutral current compensation, the load-generated neutral current is generally compensated at the DT installation point. Consequently, to evaluate the effect of an increasing load-unbalance scenarios, all the loads are kept connected at the test points and the accumulated neutral current effect on the DT is shown in Fig. 4.16. It can be seen from Fig. 4.16 that the neutral current rose to max 230 A (rms) which is almost 70 A (rms) higher than the base LV requirement. With ZT compensation at all the test points, the neutral current can be reduced to

215 A (rms), whereas with the proposed active neutral compensation from the designed four-leg PV-VSI the neutral current can be reduced to as low as 170 A (rms) even at the severe load unbalance periods. Therefore, it is evident that the designed PV-VSI with divergent customer loads and network characteristics can perform robustly compared to traditional passive compensation devices.

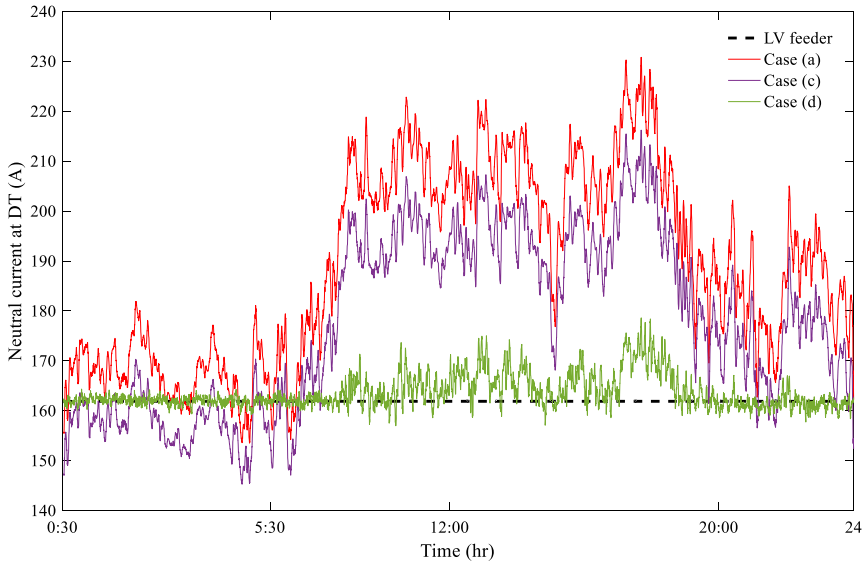

Figure 4.16. Neutral current compensation effect on DT

4.5.3 Comparison of traditional three-leg and four-leg PV-VSI operations

The contribution of the additional degree of freedom from the traditional four-leg inverter in cases with severe network unbalance case is evaluated in this case study. The neutral current controller reference is considered to be zero with the traditional four-leg PV-VSI. Severe unbalance scenarios are applied by introducing asymmetrical faults, such as a double-line to ground (2L-G) and a single-line to ground (1L-G) at the PCC of test point P2. The symmetrical fault, three-phase to ground (3L-G), is also applied at the customer installation point. The results are compared with the traditional three-leg PV-VSI system and the simulation analysis is conducted for 3.5 s periods with 20 s duration of each fault's application.

The DC-bus voltage shows a less-rippled regulated output, and similar fault recovery time with the four-leg VSI compared to three-leg VSI during the 3L-G fault from 0.80-1.0 s as shown in Fig. 4.17. However, during 1L-G and 2L-G faults, the four-leg VSI compensated the DC oscillation more robustly with lower magnitude (around 5 V) than the three-leg VSI as highlighted in Fig.

4.17. The independent neutral current forces the zero sequence current resulting from the asymmetrical faults to follow the actual zero reference resulting in improved DC voltage regulation from the four-leg VSI. From Fig. 4.17, it can be concluded that even with the traditional four-leg VSI, having the additional degree of freedom of independent control over neutral current provides better performance than the traditional three-leg PV-VSI in terms of both power quality and better DC bus voltage regulation performance.

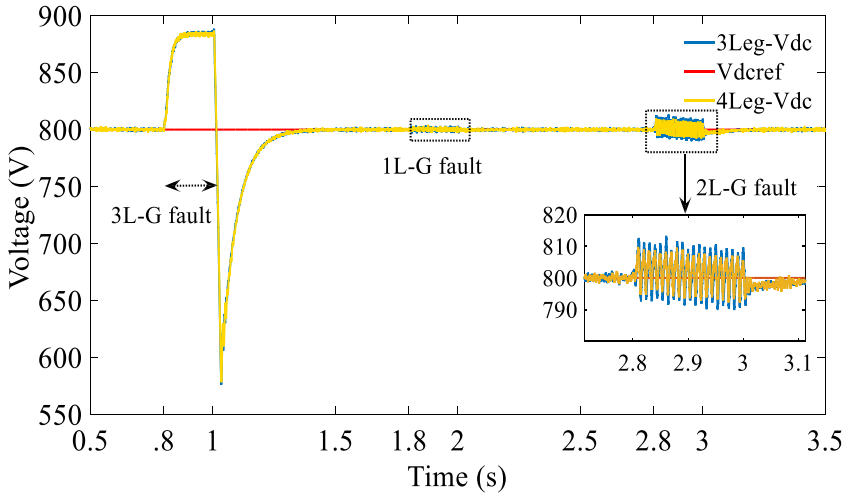

Figure 4.17. DC voltage regulation with traditional four-leg VSI during faults

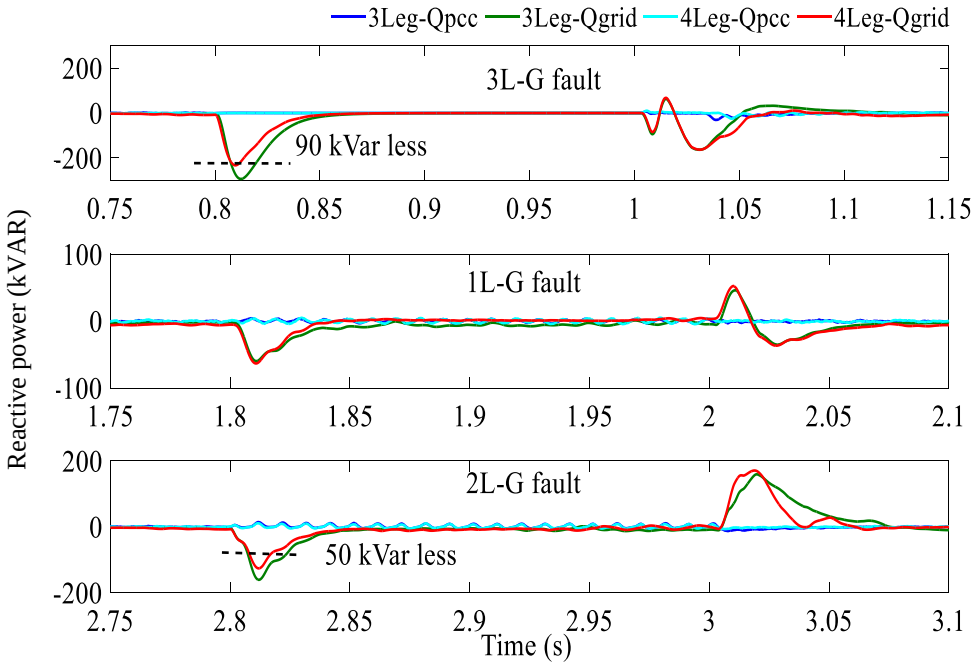

Figure 4.18. Reactive power compensation during faults

Similar improved performance can be observed from the reactive power compensation phenomenon during different faults. As unity pf operation is utilised for both three-leg and four-leg PV-VSIs, the required reactive power compensation is supplied by the grid to stabilise the unbalanced system. For a 3L-G fault from 0.80-1.0 s, the four-leg VSI requires around 90 kVAR, and for 2L-G fault from 2.80-3.0 s it requires around 50 kVAR less compensation support from the grid than for the three-leg VSI as shown in Fig. 4.18. Although the fault recovery time of the four-leg VSI indicates very little improvement (around 5 ms) compared to the three-leg VSI, in high-power and sensitive electronic device applications even this small improvement can have a robust impact on overall system stability. The active power profiles show similar characteristics for both of the VSIs during the symmetrical fault. However, four-leg VSI reduces the magnitude of the PV and grid output-power oscillations more robustly during asymmetrical faults than with three-leg VSI as shown in Fig. 4.19.

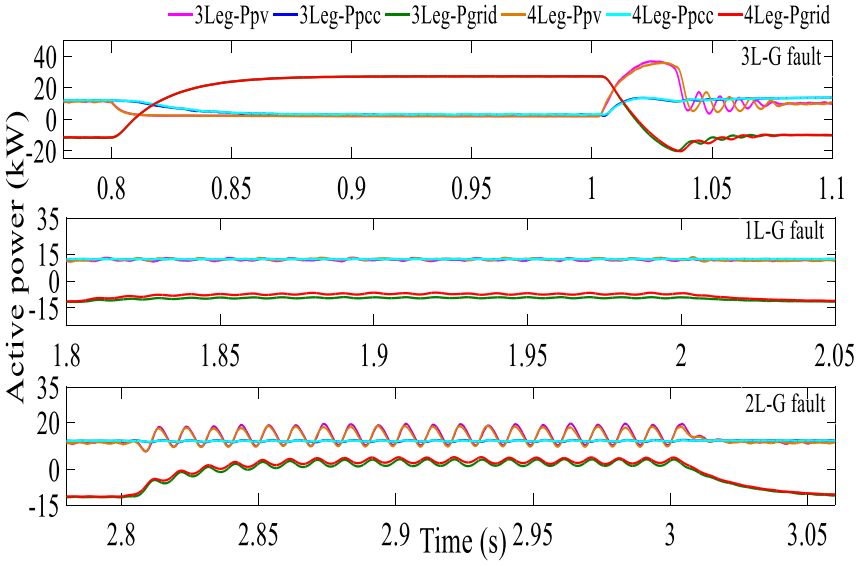

Figure 4.19. Active power profiles during faults

Another significant improvement can be observed in the magnitude reduction of the zero sequence voltage during asymmetrical faults, i.e. 1L-G (1.8-2.0 s) and 2L-G (2.80–3.0 s) as shown in Fig. 4.20. These faults cause asymmetry in the network resulting in severe voltage unbalance. With three-leg VSI, the zero sequence voltage results in approximately 200 V (peak to peak - (p-p)) oscillation, thus causing a higher fault current and this in turn may cause unnecessary tripping of the connected devices. With the same system, four-leg VSI reduces the zero sequence voltage oscillation to around 50 V (p-p), and this results in less fault current. The performance comparison

between three- and four-leg VSI is shown in Table 4.3 at the end of this chapter. Using four-quadrant operation along with zero sequence current control, the designed model can provide better fault ride-through (FRT) features. In the next case study, the independent operation of the proposed active neutral compensation is presented and the results are compared with the existing active neutral compensation operation.

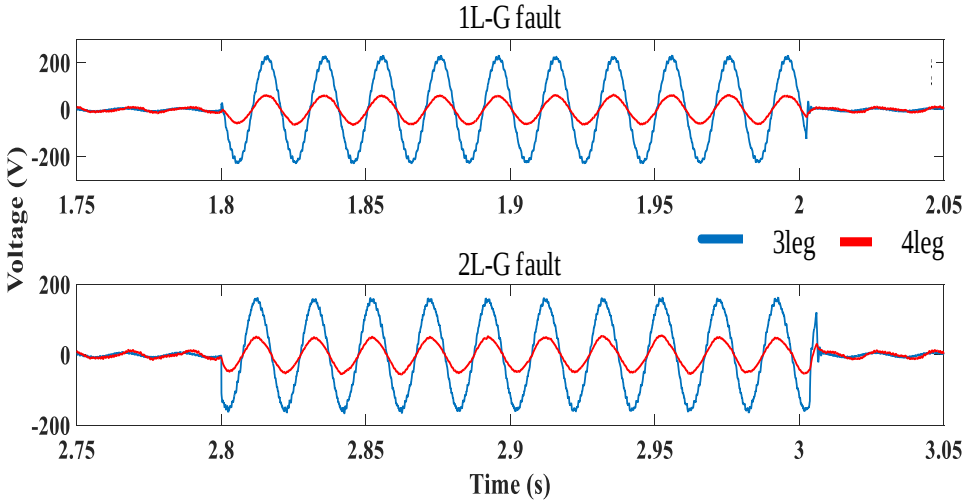

Figure 4.20. Zero sequence voltage control during asymmetrical faults

4.5.4 Active neutral compensation at a remote location (P2)

In this case study independent operation of the proposed active neutral compensation is analysed at the farthest test point, P2, with the same load profiles. The results are compared with the previously presented active neutral compensation, considering the neutral current controller reference as zero which is denoted as case condition (e) [60] [132]. For better performance evaluation, an additional case condition (f) with a traditional active compensation for the half-period (00:30-12:00) and the proposed neutral compensation for the remaining half period (12:01 – 24) is presented in Fig. 4.21.

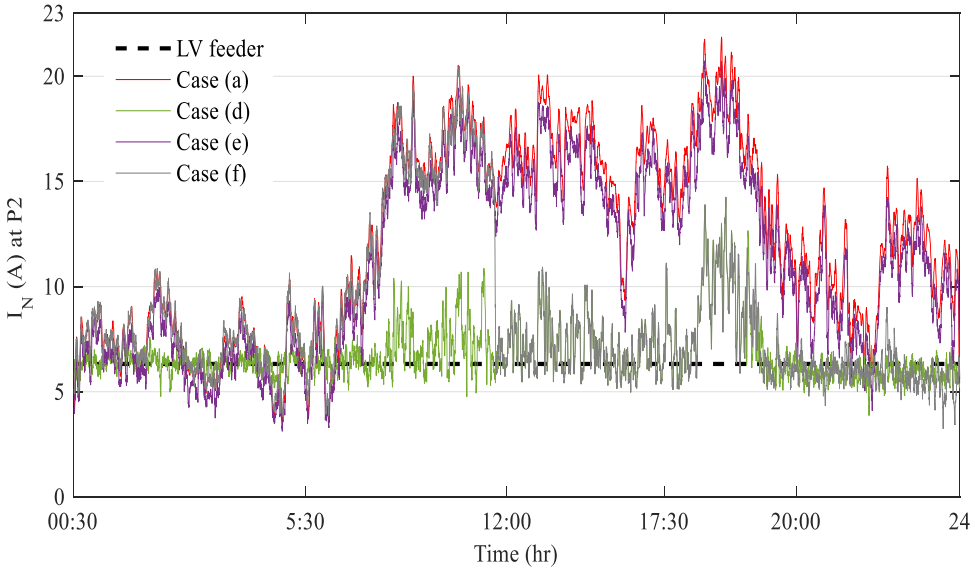

Figure 4.21. Active neutral compensation comparison

It is evident from Fig. 4.21 that the proposed neutral compensator performs better than the existing active neutral compensation method. The neutral current controller operation for case condition (f) is shown in Fig. 4.22 which clearly shows the designed neutral current controller robustly follows any given reference without any time delay. During the half-period from 00:30 to 12:00, the controller operates with zero neutral reference, and in the other half period it operates with the proposed neutral compensator, where the VSI compensates the neutral current depending on the unbalanced load-generated neutral currents.

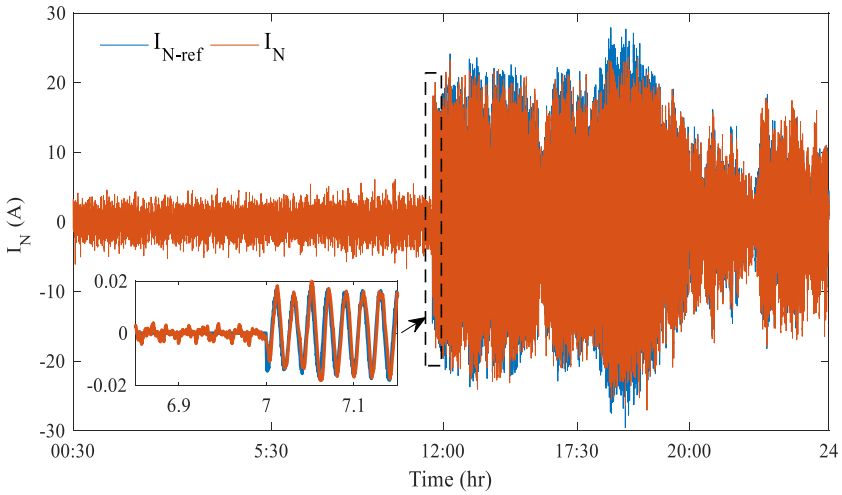

Figure 4.22. Neutral current controller reference following operation

The overall stability of the installed system can be further clarified from Fig. 4.23, where the phase modulation index remains within the linear region despite the abrupt neutral controller reference-changing operation. This verifies the proper decoupled control operation of the designed neutral current controller from the active and reactive current controllers.

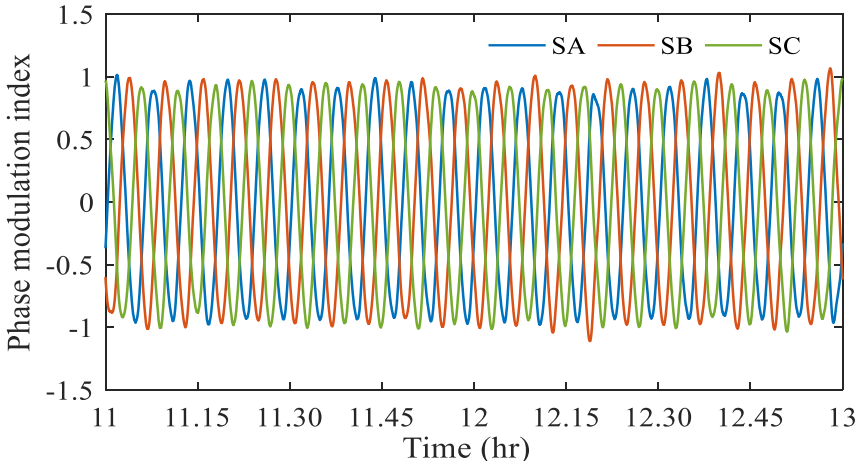

Figure 4.23. Modulation signals during neutral reference-change operation

Fig. 4.24 illustrates the DC-voltage controller performance for the whole day operation period, and it can be seen that the DC voltage remains stable despite the neutral variation operations. This demonstrates properly tuned controller characteristics and stable overall performance from the installed PV system.

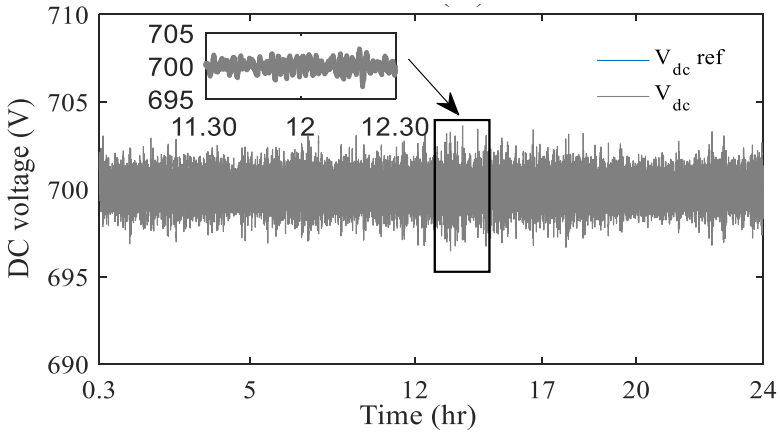

Figure 4.24. DC voltage regulator performance

The unbalanced load also increases the neutral voltage at the customer installation as depicted in Fig. 4.25 with the case condition (a). Case conditions (b) and (d) improve the neutral to ground voltage by approximately 2 V, whereas the active neural compensation with zero neutral reference

from case condition (f) does not show any significant improvement in neutral to ground voltage reduction. This is due to the fact that case condition (f) mainly considers the harmonic reduction effect at the customer installation point, not the aggregated neutral current reduction. However, the proposed neutral controller considers both the harmonic contents and the magnitude reduction of the load-generated neutral current. Therefore, it is evident from this case study that the proposed neutral compensation not only improves the neutral conductor overloading problem but also improves the customer safety issues by reducing the neutral to ground potential.

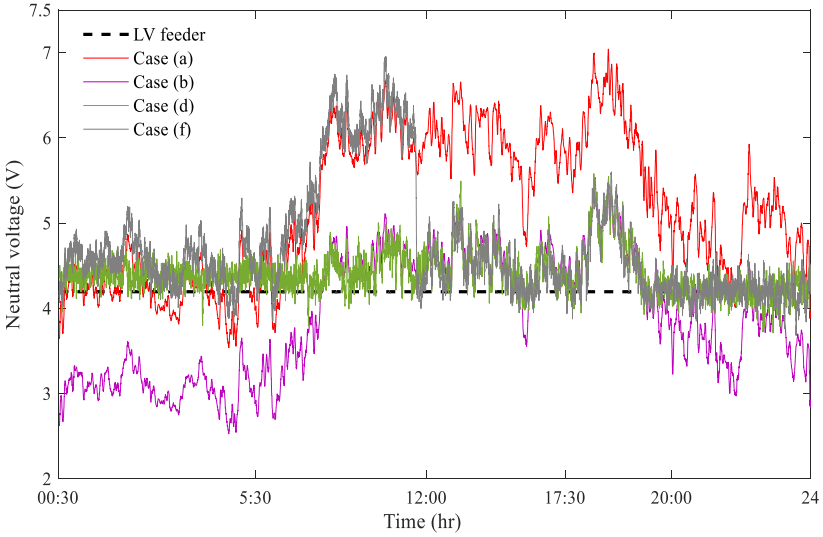

Figure 4.25. V_N comparison with reference-change operation from neutral current controller at PCC

4.5.5 Load balancing effect at a remote location (P2)

In this case study the phase balancing operation with the proposed neutral compensation is evaluated at the remotest location from the DT (420 m), P2, with the lowest R_0/X_0 ratio of 0.74. The phase balancing results are shown in Fig. 4.26 from 17:00 to 20:00 and represent both the PV active to inactive transition operation and severe load unbalance periods. The *abc* phase currents from the loads, after ZT and after the proposed active compensation, are further analysed during the high load neutral current generation period from 19:30 to 20:00 in Fig. 4.27.

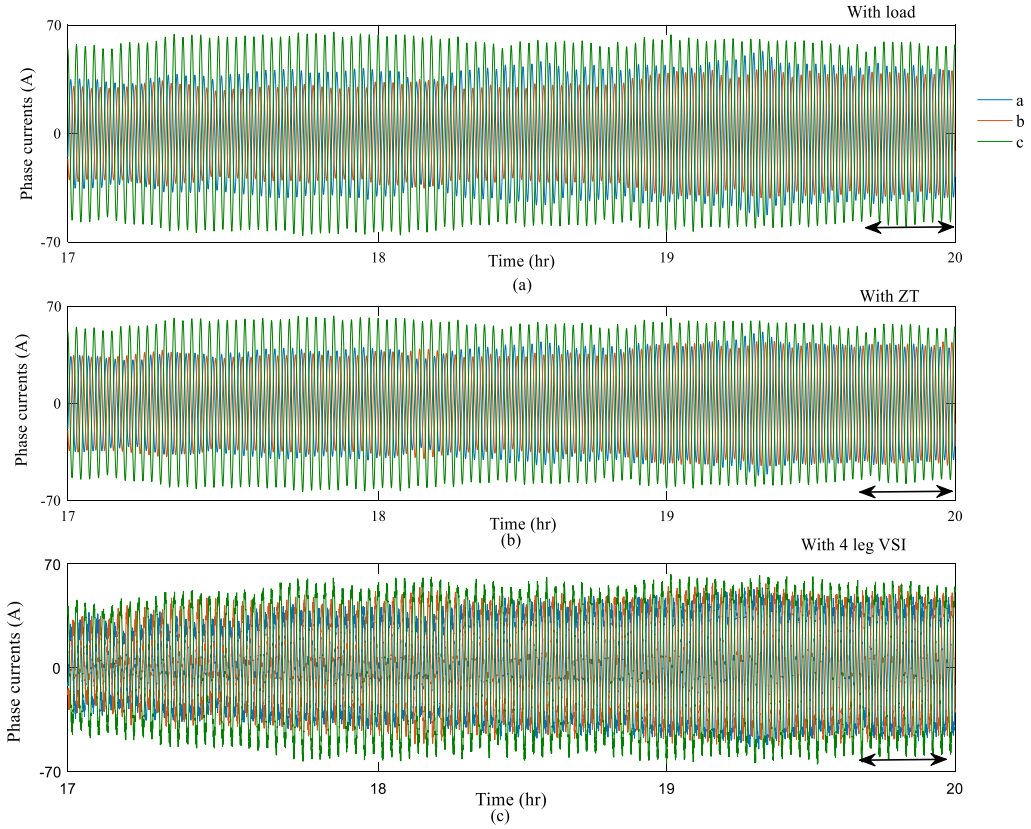

Figure 4.26. Phase currents with (a) load only, (b) ZT, and (c) 4L-SVSI

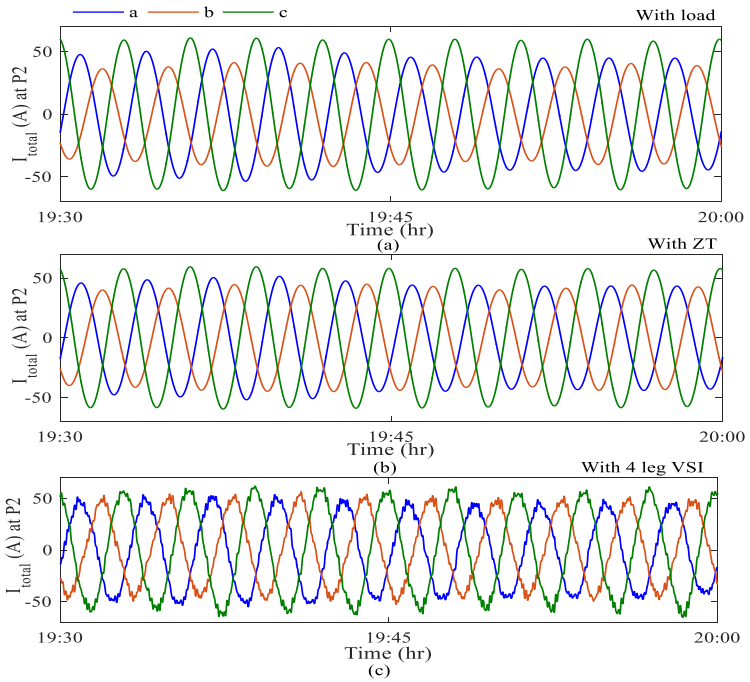

Figure 4.27. Phase currents under unbalanced load condition with (a) no compensation, (b) ZT and (c) 4L-SVSI

It is evident from Figs. 4.26 and 4.27 that the phase C current becomes more balanced with the proposed active compensation compared to a ZT in both the PV transition period and severe load unbalance cases. This is due to the better load-generated neutral current compensation operation from the designed PV-VSI system as shown in Fig. 4.28. The balancing effect can be further clarified with the voltage and current unbalance factors calculated using unbalance factor calculation from (2.2), and the results are shown in Fig. 4.29.

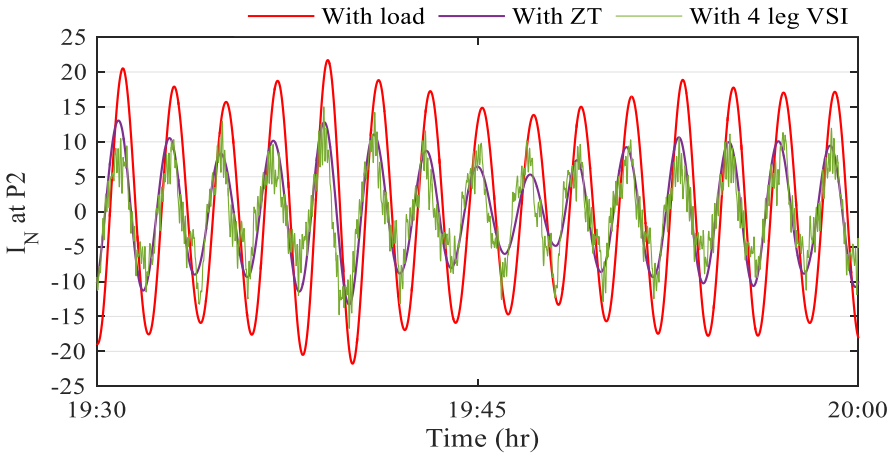

Figure 4.28. Neutral current contribution during load balancing

According to [131], the voltage negative sequence unbalance has to be less than 3% for average 10-30 minute intervals and once in 1-hour periods. Even considering the zero sequence component in both voltage and current unbalance factor (VUF/CUF) calculations, the proposed compensation using the designed four-leg VSI improves VUF significantly so that it remains less than 3%, whereas other cases violate the limit mainly during PV active periods as shown in Fig. 4.29 (a). The improved phase balancing operation can be further explained by the better current unbalance factor (CUF) results as shown in Fig. 4.29 (b) which are approximately 10% from case (a), 5% from case (b) and 3% from case (c) during 18:30-20:00 operation periods. This case study demonstrates that with the proposed neutral current compensation using the four-leg PV-VSI system, better phase balancing can be achieved at the PCC along with superior neutral current reduction performance. This can wield a significant effect on power quality improvement at the customer installation point.

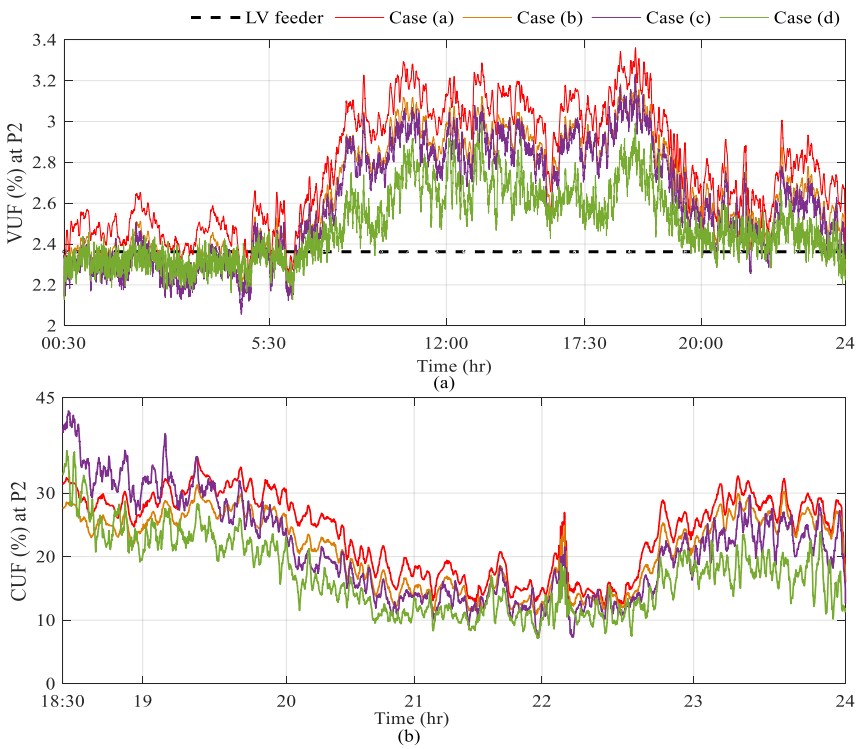

Figure 4.29. Unbalance factor improvement comparison (a) V, and (b) I

4.5.6 Different faults analysis with 4L PV-SVSI at P2

It is shown in case study 4.5.3 that, even with traditional four-leg PV-VSI, better fault-recovery characteristics can be achieved at test point P2. In this case study, different faults, such as asymmetrical (single-line to ground at 9:30 and 19:45 denoted as Fault 1) and (double-line to ground at 12:00 and 21:30 denoted as Fault 2), and symmetrical (three-phase to ground at 13:30 and 23:10 denoted as Fault 3), are applied for 20 s periods during PV active and inactive periods at bus 13 (120 m from the location P2) to analyse the effects on grid-side neutral current compensation from the four-leg PV-VSI installation with proposed neutral current compensation method. The asymmetrical faults can cause a severe neutral current for short durations of time, and the symmetrical fault can cause severe DC voltage instability and oscillation problems. The robustness of the designed controller ensures prompt following of the DC reference (within 10 ms) with minimal oscillation at post-fault operating conditions and maintaining a constant DC voltage ensuring a seamless transition from PV active to inactive periods as shown in Fig. 4.30.

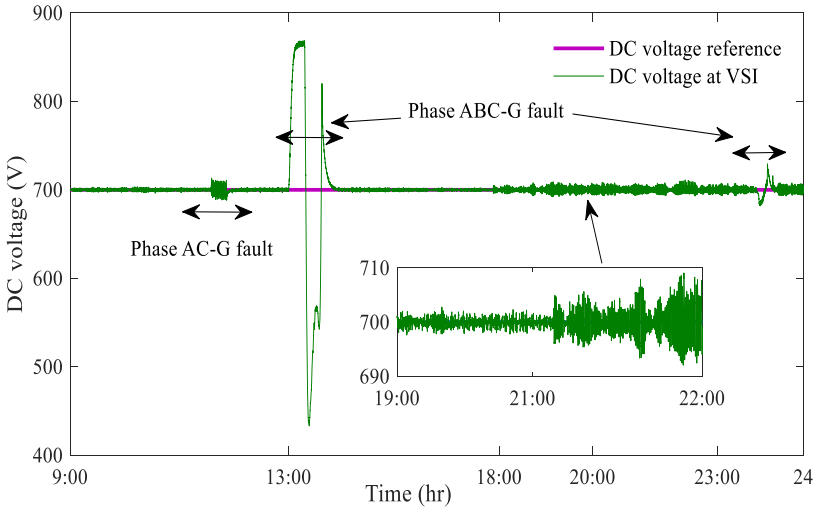

Figure 4.30. DC voltage regulation with proposed four-leg VSI under different faults

The effects of asymmetrical faults are compared similarly to the case conditions from previous case studies with an additional case condition (g) ZT with a higher kVA rating at the PCC and with the three-leg PV-VSI. The results for both PV active and inactive operations are shown in Fig. 4.31.

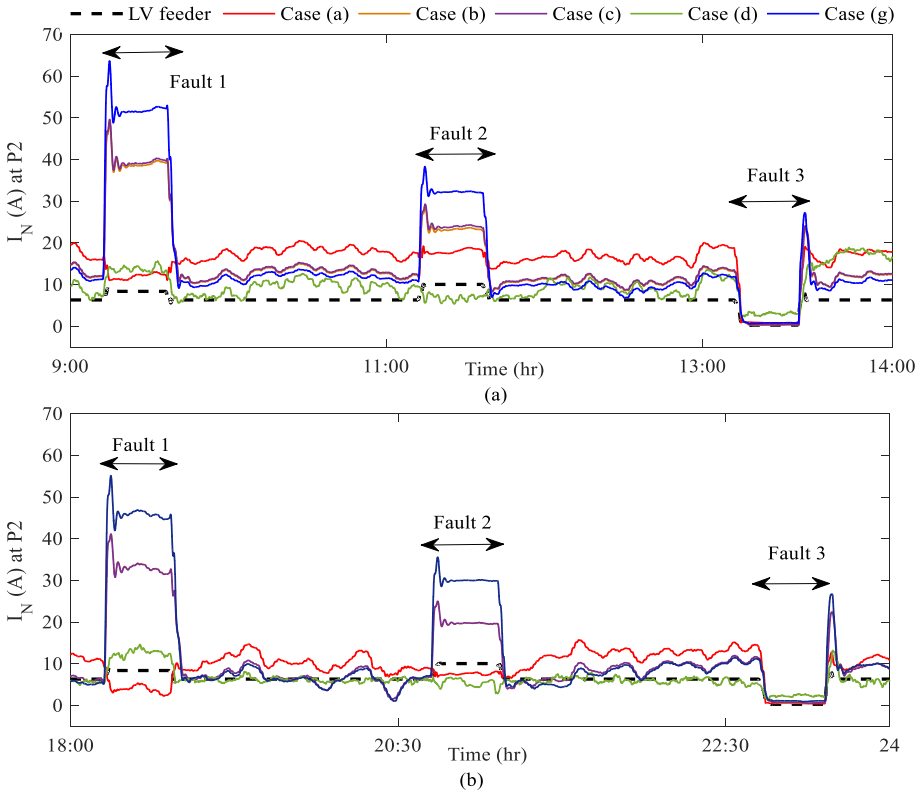

Figure 4.31. Neutral compensation with PV (a) active, and (b) inactive

From Figs. 4.31 (a) and (b), it is evident that asymmetrical faults contribute significant neutral current and the proposed neutral compensation provides improved performance compared to other case conditions for both PV active and inactive periods. The new case condition (g) with a higher capacity ZT (5 kVA each phase) increases the neutral current to approximately 18 A (rms) for Fault 1, and approximately 15 A (rms) during Fault 2 from case conditions (b) and (c), which reflects the degraded performance from the higher capacity ZT during network unbalance cases. The proposed compensation prevents the fault-generated neutral current from exceeding more than 5 A (rms) during Fault 1 and a very negligible increase during Fault 2, which shows the improved neutral compensation performance compared to other neutral compensation methods.

From this case study, it can be concluded that the designed PV-SVSI with proposed neutral current compensation method not only shows robust neutral compensation during load unbalance but can also significantly improve network stability performance even during extreme network unbalance conditions.

4.5.7 PCC voltage regulation with dynamic current limiter

In the previous case studies, the designed PV-SVSI is considered to have a unity pf, hence no reactive power operations are presented. In this case study the PCC voltage regulation with dynamic capacity allocation for reactive power controls is presented. The remaining capacity of PV-SVSI after active power has been exported during daytime and full capacity during night time is autonomously allocated for PCC voltage regulation. This dynamic reactive power capacity allocation method is embedded with a current limiter where the maximum and minimum current limits are allocated as discussed in Chapter 2 in Section 2.5.

In voltage-sag cases, such as during evening to early nighttime with high load demand, the full capacity of the PV-SVSI can be utilised for PCC voltage restoration. A new case condition (h) with a separate PCC voltage regulator in addition to active power and neutral compensation controls is introduced and the PCC voltage at the furthest test point P2 with different case conditions are shown in Fig. 4.32. It is evident from Fig. 4.32 that the dynamic saturation selector for the PCC voltage regulator in case condition (h) utilises the total-unused capacity of the PV-SVSI during PV inactive periods (from 00:30 – 5:30 and 18:00 -24). During the peak PV generation periods (from 10:00 – 14:00), the SVSI unused capacity becomes approximately zero and case condition (h) shows the same voltage profile as case condition (d), which operates with

unity pf control. The other case conditions do not indicate any voltage regulation operation, and as with the ZT there are no active voltage control options available.

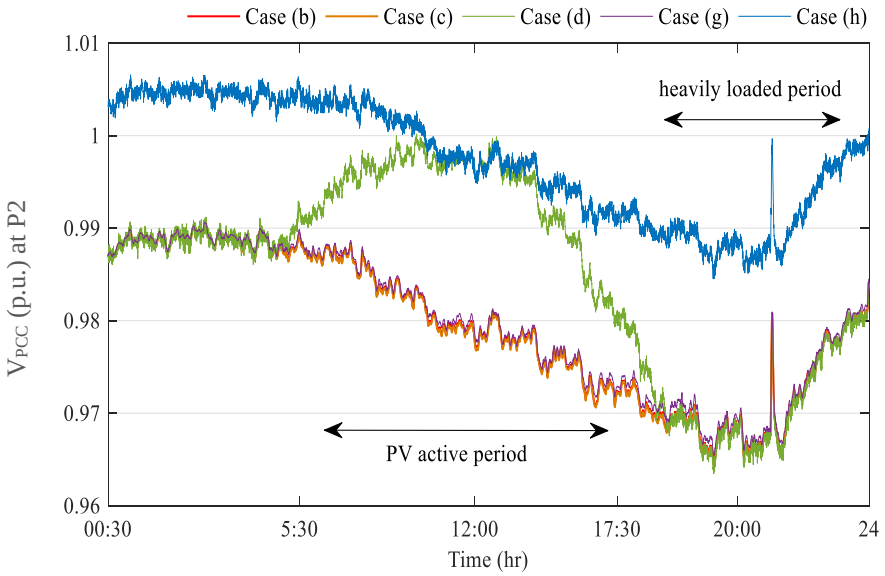

Figure 4.32. PCC voltage regulation operation

The dynamic capacity allocation of the current limiter (Q_{limit}) with the PV-SVSI generated reactive power (Q_{VSI}) and reactive power supplied to the grid (Q_{grid}) are shown in Fig. 4.33. It can be seen that during PV active periods (6:00 – 17:00) the current limiter dynamically saturates the PCC voltage regulation capacity. During PV inactive periods with a high load demand requirement around 17:00 – 22:00, the full unused VSI capacity is allocated for PCC voltage regulation which improves the PCC voltage (p.u.) profile as depicted in Fig. 4.33.

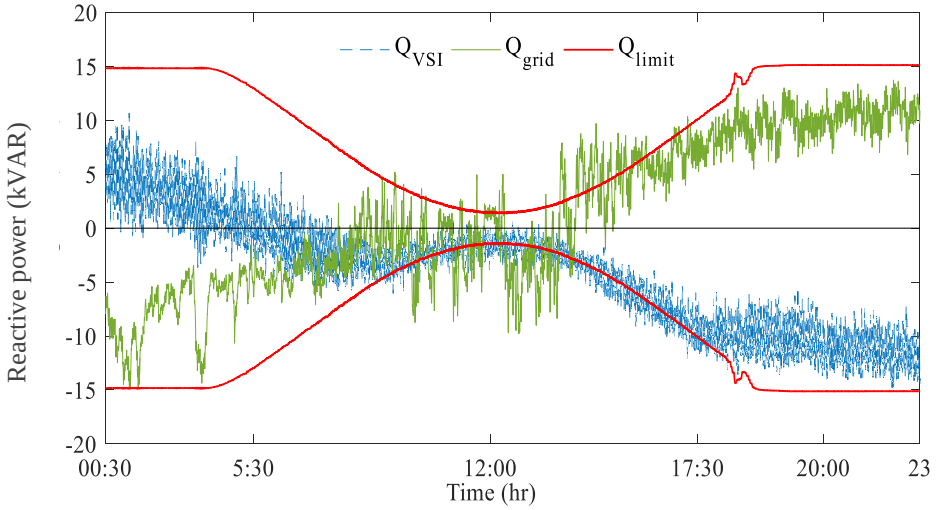

Figure 4.33. Dynamic reference allocation for PCC voltage regulator

The phase relationships between the V-I plots of phase C customers at P2 are shown in Fig. 4.34. During the PV system's peak generation period, the V-I curve shows similar characteristics to unity pf VSI due to the lack of unused capacity, whereas during night time a controlled angle shift can be observed in the V-I plot. With the additional PCC voltage regulation operation from the designed PV-SVSI, proper decentralised control over active, reactive and neutral currents can be achieved without any stability issues in any LV networks.

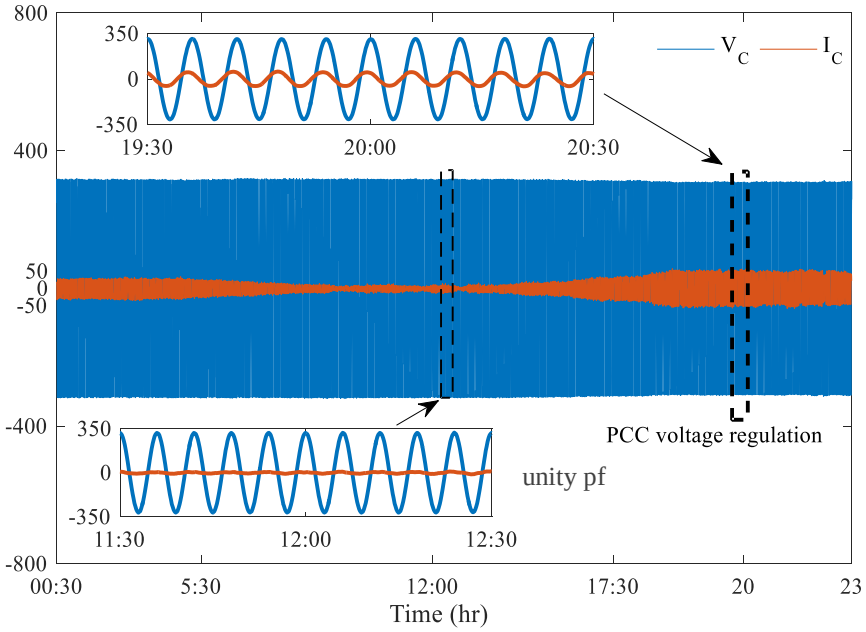

Figure 4.34. V-I relationship of phase C at PCC with voltage regulation

4.6 Chapter Summary

A four-leg PV-SVSI with improved neutral current compensation and dynamic PCC voltage regulation controls is designed and applied to an actual LV network in this chapter. The designed VSI is operated for a 24-hour period with both PV active and inactive conditions. The relationship between the zero sequence R_0/X_0 ratios of the LV network and the load-generated neutral current effects is evaluated, and a new neutral current compensation controller is proposed taking the load-generated neutral current as a direct reference. The wide range of stability margins and the robust performance of the designed controller is evaluated analytically from frequency and circuitry analysis and verified with different loads and faults. Extensive case scenarios with actual customers' unbalanced load data, transient faults and PCC voltage regulation operations are conducted for the designed PV-SVSI in different locations in the LV network with variable R_+/X_+

and R_0/X_0 ratios. Analytical and simulation results show that maximum PV power export, improved neutral current compensation, better phase balancing, seamless PV transitions and optimised PCC voltage regulations for a full-day operation period can be achieved using the designed smart VSI system. The proposed active compensation with the PV system can in many respects provide more economical option than passive compensation.

The neutral current controller in this chapter is designed with a fixed current limiting capacity, which lacks the higher capacity utilisation method. With higher compensation capacity, better phase balancing and reduction in neutral to ground voltage-rise can be achieved. A dynamic capacity distribution method is presented in the next chapter, the objective being to conduct higher capacity neutral compensation from the designed four-leg inverter.

Table 4.1 Specifications of the designed system

PV-VSI **(**3**-** and 4**-** leg**)**	DC bus voltage: 700 V, DC capacitor: 3000 μF, Fsw and time step: 3.5 kHz and 5 ms, V_{DC} regulator gains (PI_1): Kp = 2, Ti = 0.005, V_{PCC} regulator gains (PI_2): Kp= 0.5, Ti=0.03, *d-q* current controller gains (PI_3): Kp= 8, Ti=0.003, I*d* current limit ± 25A, zero and neutral controller gains (PI_4): Kp= 4, Ti=0.05, I*N* current limit ± 10A**,**
LCL filter	L_f = 4 mH ; C_f= 10 μF; L_g= 1 mH; R_d= 1 mΩ,
Zigzag Transformer	Single-phase transformer rating: 2 kVA, leakage reactance (X_L): 0.10 p.u.
LV Grid	DT rating: 11 kV/ 420 V, 500 KVA, X_L 0.04 p.u., total number of customers: 150, Customer grounding resistance (3P) R_{GND}: 10 Ω, DT grounding resistance R_DT_{GND} = 1 Ω, Total area length: 1.8 km.

Table 4.2 Specifications remote test locations

Point	Cables used	Total L (m)	R_{T+} (Ω/km)	X_{T+} (Ω/km)	R_{T0} (Ω/km)	X_{T0} (Ω/km)
P1	2, 4	260	0.188	0.096	0.278	0.325
P2	2,4,5	420	0.227	0.151	0.362	0.490
P3	2, 3, 6	217	0.088	0.058	0.182	0.21
P4	2,3,6,7	356	0.163	0.111	0.30	0.377

Table 4.3 Performance comparison index

Fault	**Q_{Grid} compensation**		**kVar (less)**	**V_0 compensation**		**V_0 p-p (less)**	**Settling time(s)**
	3-Leg kVar	4-Leg kVar		3-Leg Vp-p	4-Leg Vp-p		4-Leg (faster)
3L-G	300	220	27%	N/A	N/A		50%
1L-G	N/A	N/A		200	60	70%	50%
2L-G	160	50	69%	190	50	70%	same

Chapter 5
Capacity Improvement of Four-Leg Smart Inverter

Distribution power networks are inherently unbalanced and dynamic due to continuously changing loads. Divergent single-phase load allocation can cause a significant rise in the neutral current along with a neutral to ground voltage (NGV) increase, poor voltage regulation, harmonic pollution and phase unbalancing in three-phase (3P) four-wire (4W) multi-grounded low-voltage (LV) networks [132]. The neutral current, which is the summation of the load-generated triple-harmonic currents, flows via the neutral conductor, i.e. the fourth wire. Excessive neutral current can cause overloading of the neutral conductor and distribution transformer (DT), serious electrical safety concerns by raising the NGV, neutral shift-related problems [27], and even fire in severe cases [18]. Some sensitive electronic and computer equipment have stringent NGV limits as low as 0.5 V [133].

It is expected that the smart regulation devices to provide robust and optimised operation while following proper electricity connecting standards. Dynamic capacity distribution for a three-leg PV-VSI provides the flexibility of utilising the PV-VSI as a voltage regulator whenever VSI capacity becomes available after active power regulation. A similar concept can be applied with four-leg inverters, where the dynamic capacity is allocated for both reactive and neutral current regulations. Based on this concept, this chapter presents a novel dynamic capacity distribution method for higher capacity neutral compensation operation to achieve better phase balancing and lower NGV at the customer installation point.

This chapter is organised as follows. Section 5.1 presents different control operations from active and passive neutral compensators to facilitate the novelty of the proposed method. Section 5.2 describes the PV-VSI connection with the load and LV network. Section 5.3 describes the proposed dynamic capacity distribution method, while Section 5.4 analyses the stability of the designed system with small signal model and vector analysis. The results from different case studies are presented and discussed for both residential and commercials areas in Section 5.5. Section 5.6 looks at the economic justification of a four-leg inverter application, and the chapter summary is presented in Section 5.7.

5.1 Introduction

The increase in neutral current due to unbalanced load allocation can cause a floating neutral problem at the connection point. The increase in NGV is proportional to the increase in neutral current and can cause the voltage unbalanced factor (VUF) to increase as well. The VUF is generally specified by the local distribution network operator (DNO), such as 2-3% for Australian LV networks [134]. Traditionally, different configurations of transformers, such as zigzag, star-delta, and T-shape are installed close to the customer's installation point to provide passive neutral control. The neutral current and associated problems can also be mitigated using methods, such as oversizing the neutral conductor [135], distributed energy storage (ES) [17], community energy storage [133], load balancing with power redistribution devices [136], and four-leg active power filters [125]. The authors in [137] experimentally verified that the four-leg (4L) voltage source inverter (VSI) configuration provides better harmonic and neutral compensation than the delta-wye transformer and split DC-bus 4L-VSI for a standalone double-fed induction generator system. Similarly, it is shown in [133] and [17] that the traditional passive neutral compensation solutions cannot control the NGV within a 0.5 V limit with unbalanced PV and load allocations, and the application of community energy storage [133] and distributed energy storage (ES) [17] to maintain the NGV within the limit is proposed. However, ES is still expensive and requires an additional inverter to connect to the grid. The active power filter combinations can have resonance problems and can create interference with the grid communication links. The authors in [59] utilised the 4L inverter with PV installation, however, no results are presented for network interaction analysis with different loads. Considering only the LV network R_+/X_+ ratios, the authors in [127] proposed adaptive droop control to improve the power sharing for point of common coupling (PCC) voltage regulation, however, unbalanced scenarios are not considered.

Considering the control flexibility, superior performance in neutral compensation and easy installation with renewable energy sources (RES), such as PV, in this chapter a 3P-4L multifunctional smart VSI (SVSI) is designed with a novel dynamic capacity distribution method (DCD) to utilise the maximum SVSI capacity for active power supply, PCC voltage regulation and robust neutral current compensation. The DCD method estimates and utilises the available capacity of the PV-SVSI after active and reactive power operations for higher capacity neutral compensation controls. In the case of 3P three-wire balanced networks, the SVSI remaining

capacity utilisation is available for reactive power operations [138]. However, with 3P-4W unbalanced networks, the available capacity after VSI active and reactive operations can be utilised for higher capacity neutral compensation operations.

Therefore, in this chapter, a multi-functional 3P-4L PV-SVSI system is designed with the DCD method for active, reactive and neutral regulation control operations. The PCC voltage and neutral current compensation controllers are designed based on the three-leg and four-leg smart inverters from Chapters 3 and 4. The 4L-SVSI with the DCD method can increase the neutral compensation performance significantly compared to fixed-capacity 3P-4L inverters and can justify the additional cost for the additional phase leg. The SVSI is designed with the popular PV installation which can make the system more appealing to customers and DNOs. A small-signal model of the designed SVSI is developed to demonstrate the network interaction effects with variable R_+/X_+ and R_0/X_0 ratios with the PV-SVSI unit. The performance of the designed PV-SVSI with the DCD method is compared with neutral compensation with fixed-capacity operation from 3P-4L SVSI; and significant neutral current reduction, improved phase balancing, and reductions in NGV rise are achieved.

5.2 Designed System Description

The single-stage transformerless 3P-4L PV-SVSI system is designed with an LCL filter, multiple single-phase loads and grid connections as shown in Fig. 5.1.

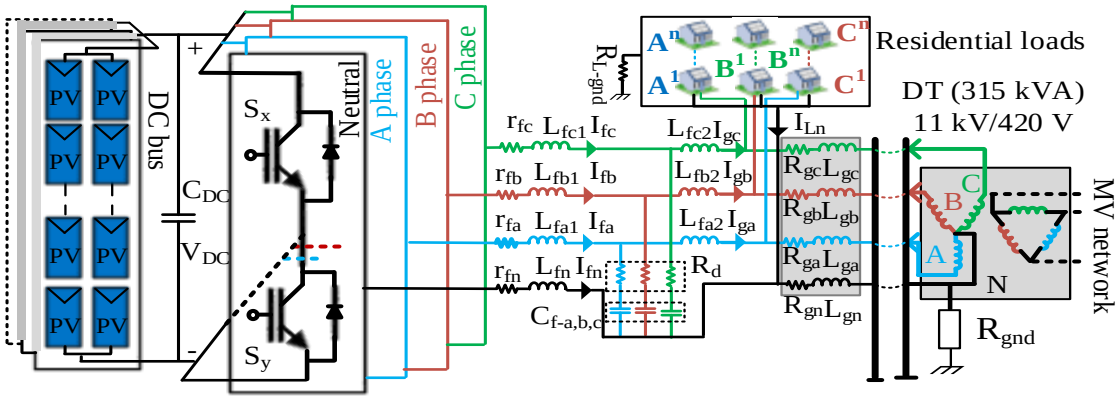

Figure 5.1. PV-SVSI connection with loads and LV network

A DC-link capacitor is used to maintain constant DC-bus voltage, and each VSI leg is connected with corresponding phase wires to control the phase currents as shown in the above figure. The SVSI operation is divided into two periods:

(i) PV active, and

(ii) PV inactive.

During PV active periods, the SVSI total capacity is mainly utilised to supply maximum PV power to the PCC point, and the amount of remaining VSI capacity is low. On the other hand, during PV inactive periods, the whole VSI capacity remains available. Therefore, the PV-SVSI controllers are designed to use the remaining capacity after PV active power operation both during PV active and inactive periods for two tasks:

(i) PCC voltage regulation, and

(ii) PCC neutral compensation.

The *SRF* transformed quantities are utilised to design the decoupled current controller (DCC) for the active (I*d*) and reactive (I*q*) current components. The DC-bus voltage is regulated at a constant 700 V and it generates the Id_{ref} signal for daylong PV-SVSI operations. The constant DC bus voltage ensures a seamless control transition from PV active to inactive operations. The three-phase PCC voltage regulator is designed to generate the Iq_{ref} signal and utilise the remaining capacity of the SVSI after active power operation for voltage regulation. With the 3P-4L VSI, four controllable modulating signals are required to optimally utilise the VSI capacity. Therefore, individual current controllers are designed for the zero sequence and neutral currents. The load-generated zero sequence current is considered the reference to the zero sequence current controller, $I_{g0\text{-}ref}$, and the PCC neutral current as $I_{n\text{-}ref}$. Desired control operations are performed by controlling the eight IGBT switches, and the sinusoidal pulse width modulation (SPWM) method is applied to generate the 2^4 gating signals for the SVSI switches. The controllers are designed to operate in the linear region with modulation index set to ± 1 for the daylong operation period. A detailed control block diagram is shown in Fig. 5.2. The dynamic current limiters ($DL_{1\text{-}4}$) are included with all four current controllers to apply the dynamic capacity distribution method in the designed 3P-4L PV-SVSI system as discussed in Section 5.3. The PI controllers are tuned using the Zigler-Nichols method and the gain values are illustrated in Table 5.1 at the end of this chapter.

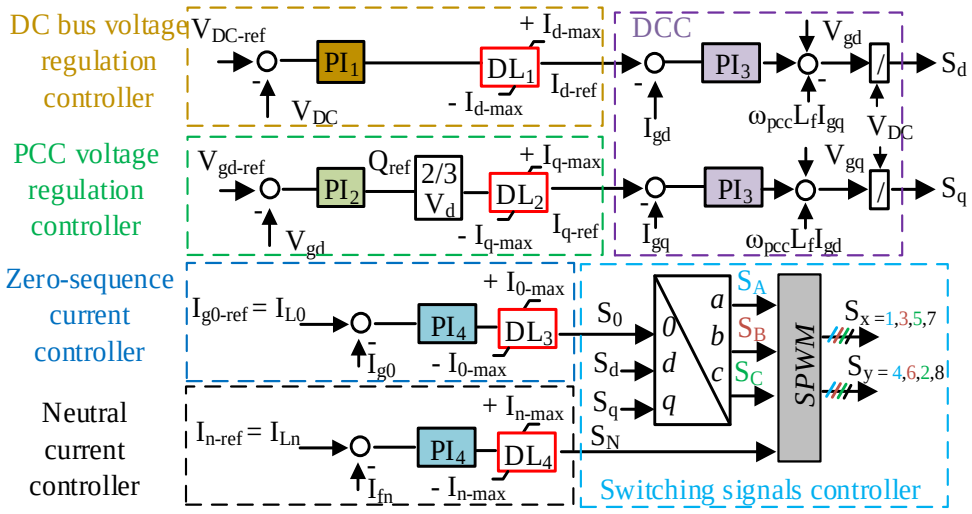

Figure 5.2. Overall control block diagram of the PV-SVSI system

5.3 Dynamic Capacity Distribution (DCD) Method

A novel dynamic capacity distribution (DCD) method is proposed to distribute the SVSI available capacity after the PV active power operation to the PCC voltage regulation and the higher capacity active neutral compensation. For balanced three-phase three-wire systems, the SVSI apparent power can be expressed as:

$$S_{VSI} = P + jQ = \frac{3}{2}(V_d I_d - V_d I_q) \tag{5.1}$$

where S, P, and Q are the apparent, active and reactive power capacities of the VSI, respectively. However, with 3P-4W DNs, the zero sequence components exist and the apparent power can be written as [139]:

$$S_{VSI} = P + jQ + 3P_0 = \frac{3}{2}(V_d I_d - V_d I_q) + 3V_0 I_0 \tag{5.2}$$

Therefore, with 3P-4W networks, the VSI capacity can be distributed for the zero sequence component operations, and this concept is applied in the dynamic current limiters ($DL_{1\text{-}4}$) with the designed controllers for the 3P-4L PV-SVSI. The DCD method can significantly improve the active neutral compensation performance due to higher capacity availability for neutral compensation, and can outperform fixed-capacity neutral inverters even with the same SVSI

nameplate ratings. The DCD method is divided into four operation modes of execution as shown in detail in Fig. 5.3.

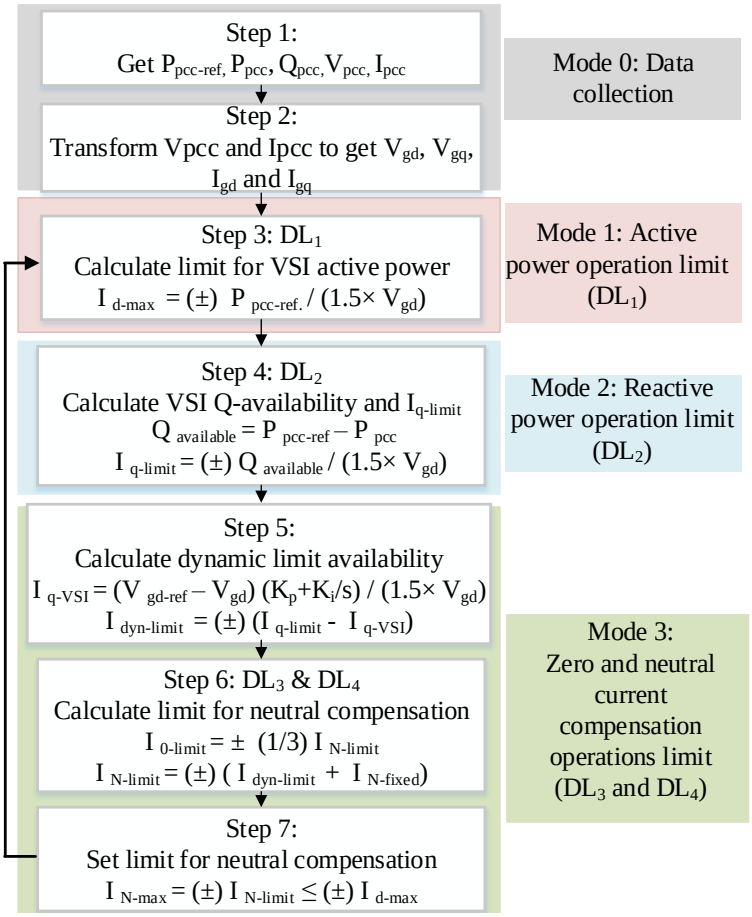

Figure 5.3. PV-SVSI dynamic capacity distribution method

5.3.1 Mode 0 (Data collection)

The initial mode includes two main steps:

(i) Collecting the nameplate ratings of the VSI powers, PCC voltages, and currents; and

(ii) Transforming the collected quantities from *abcn* to *dq0n* components and using the SRF transformed quantities to select the current limit for the PV active power operations.

5.3.2 Mode 1 (Active power operation)

The main objective of this mode is to utilise the VSI maximum capacity to extract maximum power from the PV installation. Using the collected data from mode 0, the active power controller maximum limit is calculated as shown in step 3 in Fig. 5.3. For a 14.5 kVA unit with 240 V (L-N), the maximum current limit $I_{d\text{-}max}$ is set to ± 29 A in DL_1. As the DC-voltage controller regulates the DC-bus voltage at a constant value, with variation in sun irradiance only the active current reference ($I_{d\text{-}ref}$) varies and the designed DCC controller ensures that the VSI active power component (I_d) follows the reference promptly to export maximum PV power to the PCC.

5.3.3 Mode 2 (Reactive power operation)

The VSI capacity availability is calculated in each simulation period using the expression from step 4 in Fig. 5.4. The maximum limit of the SVSI reactive power operation is set dynamically (± $I_{q\text{-}limit}$) with the current limiter -DL_2 as shown in the control block diagram in Fig. 5.3. For instance, the 14.5 kVA PV-SVSI installation can utilise the whole 29 A limit for reactive power operations during night time and cloudy situations. It will, however, have a zero operation limit during the full PV generation period. The PCC voltage regulator is controlled to maintain the PCC voltage within ± 6% limit [134].

5.3.4 Mode 3 (Neutral current compensation operation)

The remaining dynamic current limit ($I_{dyn\text{-}lim}$) is evaluated using the expressions in step 5 from Fig. 5.3, where the limit will be zero if the active and reactive power operations utilise the full SVSI capacity. Therefore, for daylong operation, a fixed neutral compensation capacity is allocated with the additional phase leg (half bridge) in addition to the dynamic current limit from step 6. To avoid SVSI over-capacity operation, the maximum neutral current limit (± $I_{N\text{-}max}$) is checked in step 7 to ensure that it remains lower than the SVSI total capacity.

For instance, during full-capacity PV generation, $I_{dyn\text{-}limit}$ will be zero and the neutral compensator will operate with $I_{N\text{-}fixed}$ limit capacity. In the case where the PCC voltage controller requires less than $I_{q\text{-}limit}$ to keep the PCC voltage within ± 6%, $I_{dyn\text{-}limit}$ will have some capacity available which will be included with the $I_{N\text{-}fixed}$ limit and it will be utilised for higher capacity neutral compensation operation. The PV-SVSI with the DCD method can provide superior neutral current compensation in several instances in a daylong operational period as shown in Section 5.5.

5.4 Problem Formulation of Four-leg PV-VSI in 3P-4W LV Network

5.4.1 Small-signal analysis at different network locations

It is important to understand how the network interacts with the installed PV-SVSI system at different network locations having different transmission line R/X ratios. It is shown in Chapter 4 that with variation in transmission line zero sequence R/X ratios at different network locations, the same load profile generates different amounts of neutral current at PCC. Therefore, the small-signal model of the designed PV-SVSI system is analysed to evaluate the stability of the PV-VSI system. The model can be expressed as [129]:

$$\dot{X} = AX + BU \qquad (5.3)$$
$$Y = CX + DU$$

where $Y = [\hat{\imath}_{gd} \quad \hat{\imath}_{gq} \quad \hat{\imath}_{g0} \quad \hat{v}_{DC}]^T$; $U = \left[\hat{d}_d \quad \hat{d}_q \quad \hat{d}_0 \quad \hat{v}_{gd} \quad \hat{v}_{gq} \quad \hat{v}_{g0}\right]^T$;

$X = [\hat{\imath}_{fd} \quad \hat{\imath}_{fq} \quad \hat{\imath}_{f0} \quad \hat{\imath}_{gd} \quad \hat{\imath}_{gq} \quad \hat{\imath}_{g0} \quad \hat{v}_{cfd} \quad \hat{v}_{cfq} \quad \hat{v}_{cf0} \quad \hat{v}_{DC}]^T$

$\mathrm{A} = \mathrm{A}_{10\times10};\ \mathrm{A}_{11} = -\frac{\mathrm{r_f}+\mathrm{R_d}}{\mathrm{L_f}}, \mathrm{A}_{12} = \omega, \mathrm{A}_{14} = \frac{\mathrm{R_d}}{\mathrm{L_f}}, \mathrm{A}_{17} = \frac{-1}{\mathrm{L_f}}, \mathrm{A}_{110} = \frac{\mathrm{d_d}}{\mathrm{L_f}},$

$\mathrm{A}_{21} = -\omega, \mathrm{A}_{22} = -\frac{\mathrm{r_f}+\mathrm{R_d}}{\mathrm{L_f}}, \mathrm{A}_{25} = \frac{\mathrm{R_d}}{\mathrm{L_f}}, \mathrm{A}_{28} = \frac{-1}{\mathrm{L_f}}, \mathrm{A}_{210} = \frac{\mathrm{d_q}}{\mathrm{L_f}},$

$\mathrm{A}_{33} = -\frac{(\mathrm{r_f}+3\mathrm{r_{fn}})+\mathrm{R_d}}{\mathrm{L_f}+3\mathrm{L_{fn}}}, \mathrm{A}_{36} = \frac{\mathrm{R_d}}{\mathrm{L_f}+3\mathrm{L_{fn}}}, \mathrm{A}_{39} = \frac{-1}{\mathrm{L_f}+3\mathrm{L_{fn}}}, \mathrm{A}_{310} = \frac{\mathrm{d_0}}{\mathrm{L_f}+3\mathrm{L_{fn}}},$

$\mathrm{A}_{41} = \frac{\mathrm{R_d}}{\mathrm{L_g}}, \mathrm{A}_{44} = -\frac{\mathrm{R_g}+\mathrm{R_d}}{\mathrm{L_g}}, \mathrm{A}_{45} = \omega, \mathrm{A}_{47} = \frac{1}{\mathrm{L_g}},$

$\mathrm{A}_{52} = \frac{\mathrm{R_d}}{\mathrm{L_g}}, \mathrm{A}_{54} = -\omega, \mathrm{A}_{55} = -\frac{\mathrm{R_g}+\mathrm{R_d}}{\mathrm{L_g}}, \mathrm{A}_{58} = \frac{1}{\mathrm{L_g}},$

$\mathrm{A}_{63} = \frac{\mathrm{R_d}}{\mathrm{L_g}+3\mathrm{L_{gn}}}, \mathrm{A}_{66} = -\frac{(\mathrm{R_g}+3\mathrm{R_{gn}})+\mathrm{R_d}}{\mathrm{L_g}+3\mathrm{L_{gn}}}, \mathrm{A}_{69} = \frac{1}{\mathrm{L_g}+3\mathrm{L_{gn}}},$

$\mathrm{A}_{71} = \frac{1}{\mathrm{C_f}}, \mathrm{A}_{74} = \frac{-1}{\mathrm{C_f}}, \mathrm{A}_{78} = \omega, \mathrm{A}_{82} = \frac{1}{\mathrm{C_f}}, \mathrm{A}_{85} = \frac{-1}{\mathrm{C_f}}, \mathrm{A}_{87} = -\omega,$

$\mathrm{A}_{93} = \frac{1}{\mathrm{C_f}}, \mathrm{A}_{96} = \frac{-1}{\mathrm{C_f}}, \mathrm{A}_{101} = \frac{-\mathrm{d_d}}{\mathrm{C_{DC}}}, \mathrm{A}_{102} = \frac{-\mathrm{d_q}}{\mathrm{C_{DC}}}, \mathrm{A}_{103} = \frac{-\mathrm{d_0}}{\mathrm{C_{DC}}}$

$B = B_{6\times10}; B_{11} = \frac{V_{DC}}{L_f}, B_{22} = \frac{V_{DC}}{L_f}, B_{33} = \frac{V_{DC}}{L_f+3L_{fn}}, B_{44} = \frac{-1}{L_g}, B_{55} = \frac{-1}{L_g}, B_{66} = \frac{-1}{L_g+3L_{gn}},$

$B_{101} = -\frac{I_{fd}}{C_{DC}}, B_{102} = -\frac{I_{fq}}{C_{DC}}, B_{103} = -\frac{I_{f0}}{C_{DC}}$

$C = C_{10\times4}; C_{14} = C_{25} = C_{36} = C_{410} = 1; D = 0$

The equivalent small-signal average circuit model is shown in Fig. 5.4. Each PV-SVSI unit with neutral current control is modelled as a tenth-order system [129]. Therefore, a total of 50 eigenvalues are derived from the five PV-SVSI units as shown in Fig. 5.5, considering four PV installations at different network locations with the addition of transmission-line parameters ($L_{g(a,b,c,n)}$ and $R_{g(a,b,c,n)}$), and one PV-VSI without considering those parameters. The eigenvalues are determined without the interaction of the current controllers and load connection effects.

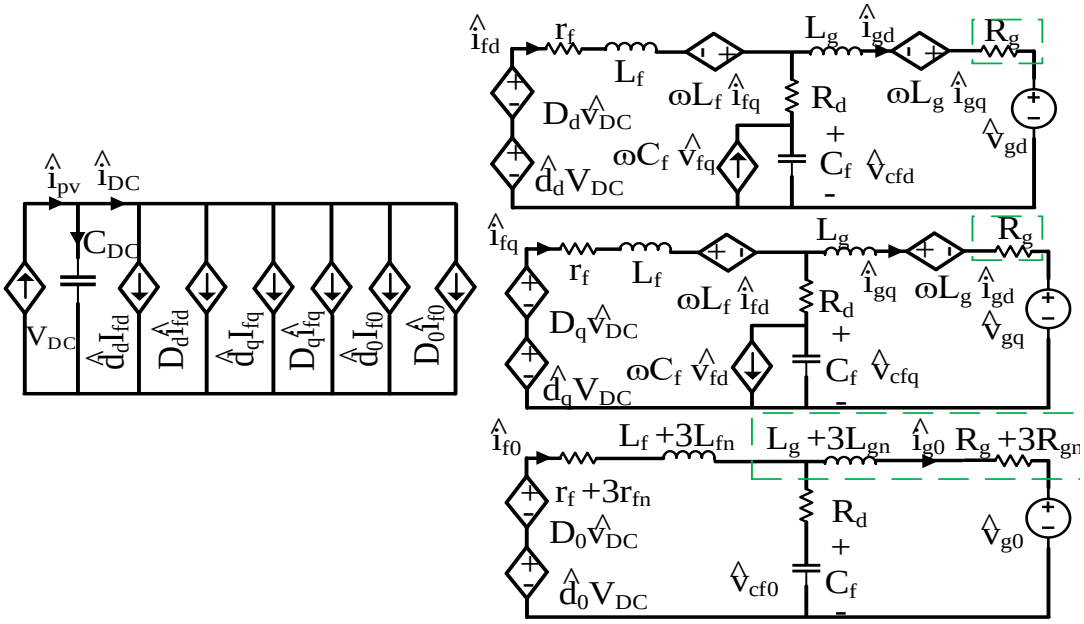

Figure 5.4. Average equivalent small-signal circuit model

It is therefore possible to investigate the inherent stability of the PV-SVSI in the case of network contingencies. Generally, the poles close to the real-axis zero point are considered as dominant poles (DP). The DP, -0.2 ± 0.0924i, from conventional PV-SVSI design (without R/X effect consideration), do not show any network interaction effects and remain very close to the real-axis zero point. The conclusion can be made that the PV-VSI system inherently requires an additional controller to keep the system stable, and the dynamics of this kind of PV-SVSI are not applicable to practical situations.

Two small-signal models are designed so that the system can be applied in practice, and the DP movements are presented for the PV-SVSI with: (i) varying only R_+/X_+ ratios (DP_p); and (ii) varying both the R_+/X_+ and R_0/X_0 ratios (DP_{pz}) in Fig. 5.6. The details of the transmission-line conductors and R/X ratios for the considered points in the LV network are shown in Table 5.1 at the end of this chapter. The decrease in the R_+/X_+ ratio of a particular network location means that

the point has more inductive characteristics, and based on this, the active and reactive power regulation related operations are generally selected. It can be seen from Fig. 5.5 that the more inductive the network characteristics are, the more unstable the PV-SVSI system tends to become (i.e. the dominant poles move closer to the right-hand plane).

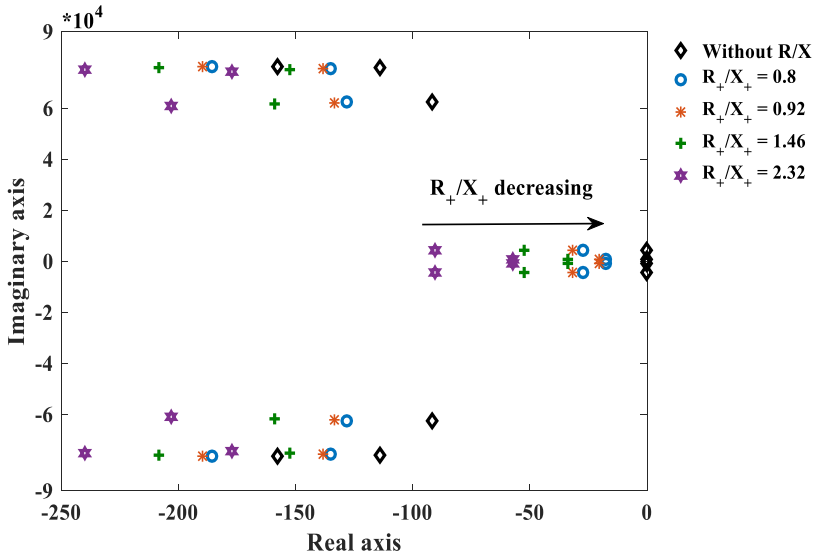

Figure 5.5. Total 50 poles from five PV-SVSI units

With 3P-4W networks, both the R_+/X_+ and R_0/X_0 ratio variations are considered in this chapter, and it can be seen from Fig. 5.6 that the DPs are moving more towards the 0-real axis (towards the right-hand plane) with the decrease in the R/X ratios (both R_+/X_+ and R_0/X_0). Therefore, the SVSI controllers need to be designed and verified so that the designated operations can be provided even with different network contingencies.

The small signal analysis makes it possible to conclude that the PV-VSI system does show movements of dominant poles with variations in the R/X ratios of a particular LV network. With the decrease in the positive sequence R/X ratios, the network tends to become more unstable due to the more inductive characteristics, which may cause unbalance in that particular connection point. Power system networks in rural areas are generally more resistive and have higher R/X ratios, where the customer installation points are quite far from the distribution transformer. In any voltage constraint issues with this kind of network, active-power operation provides better regulation than reactive power controllers. With variations in the zero sequence transmission-line parameters, the dominant poles move closer to the zero real axis point, thus making the system more prone to unstable characteristics as shown in Fig. 5.6. When an unbalanced distribution of

the loads is added, the stability issue can become more severe, and the compensation device connected at that particular point needs to be capable of maintaining the system stability despite the network and load contingencies. Therefore active neutral compensation with the four-leg inverter is designed in this chapter.

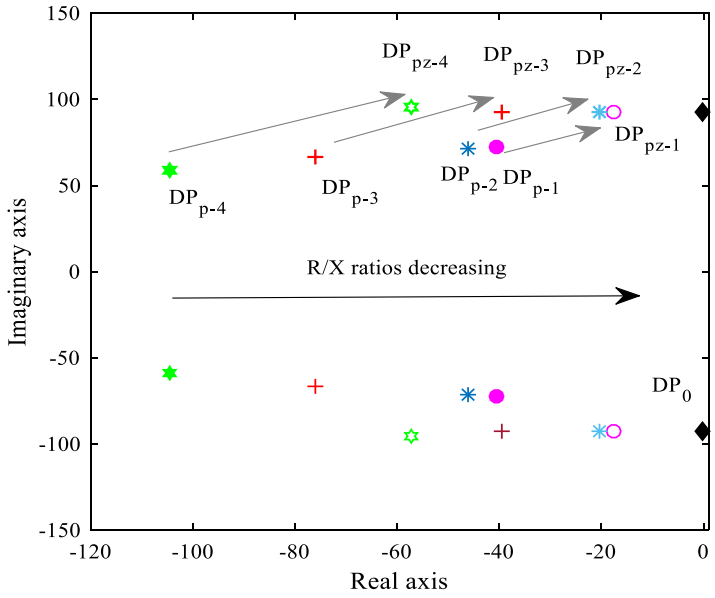

Figure 5.6. Dominant poles movement with LV network parameter variations

5.4.2 Load unbalance effects at PCC

The difference in network impedances, unequal numbers of customer load connections and unequal power consumption from each phase are the main causes of unbalance at a particular customer connection point. Intentional or unintentional load connection or disconnection occurs frequently due to system maintenance or different faults, which can cause significant neutral current, NGV rise and increase in the UF. In actual DNs, a fixed amount of voltage unbalanced factor (VUF) is permitted; for example, according to the National Electricity Rules, Australia (S5.1a.7), negative sequence VUF must be between 2-3% in different time intervals. The maximum current in any active phase conductors should be not more than 25 A from any other service conductors [134]. The load changing effect on each phase current and the corresponding neutral current generation schematic is shown in Fig. 5.7 at one of the network locations. Two types of load connection and disconnection effects are evaluated with the vector plot analysis for each phase currents and corresponding phasors of the neutral currents as shown in Figs. 5.8 and 5.9.

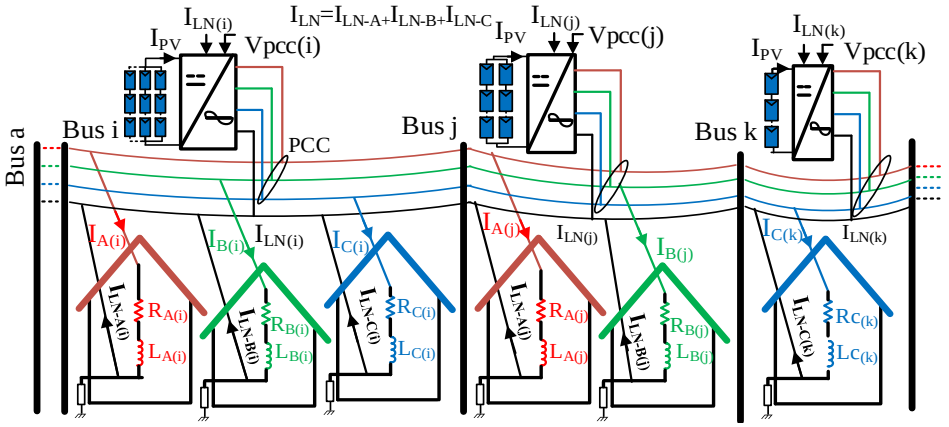

Figure 5.7. Different customer loads connections with the four-leg inverter

Initially, it is considered that the test point consists all the three single-phase load connections, and at a particular time, initially a single-phase (phase C) and after a certain period of time the double-phase (A and B) loads are disconnected from the network location. The vector representation of the three-phase loads is shown in Fig. 5.8 (a). The two-phase load disconnection scenarios cause severe unbalance in that particular network location resulting in higher neutral current generation compared to single-load disconnection as can be seen with the increase in the vector magnitude of I_{n4} from Figs. 5.8 (b) and (c). Increasing the neutral current significantly changes the CUF from 18% to 136% which is more than 100% unbalance generation in that particular network location.

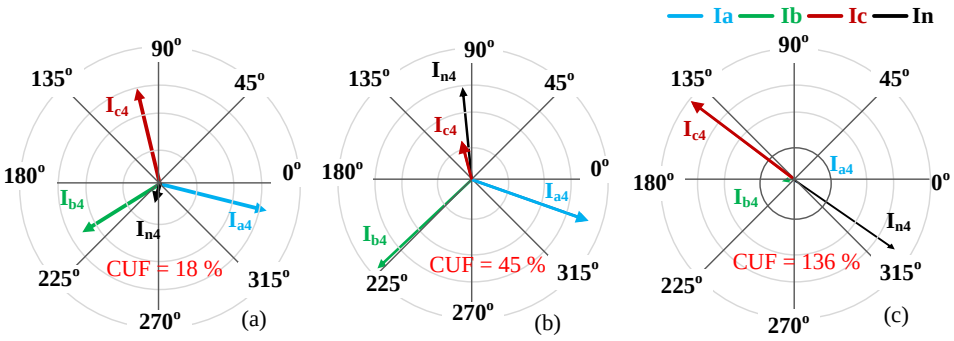

Figure 5.8. Phasor diagram: (a) No load, (b) single- and (c) double-phase load disconnection

Similar unbalance generation characteristics can be seen with increases in the phase loads. Increasing double-phase loads will generate higher neutral current than the load increment in three- and single-phase connections as shown in Fig. 5.9. Increasing loads abruptly in three phases do not cause any severe unbalance in the network, hence does not generate significant neutral current.

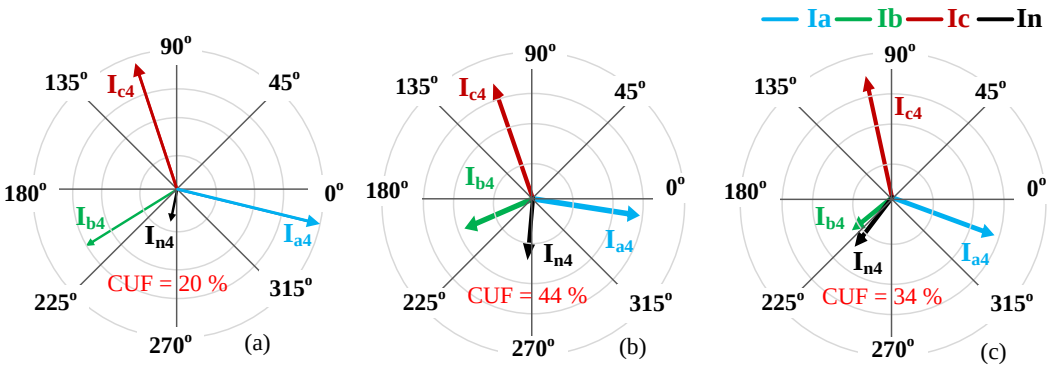

Figure 5.9. Phasor diagram: (a) Three-, (b) double- and (c) single-phase load addition

The CUF also increases marginally from 18% to 20% as can be seen from Figs. 5.8 (a) and 5.9 (a). The addition of double-phase loads increases the current unbalance factor more than the single-phase load addition. This is due to the fact that the single-phase load addition causes unbalance in one phase whereas double-phase load addition in two phases results in a higher neutral current generation.With the uneven distribution of loads, it is possible to get a neutral current few times higher than the phase current ratings at a particular point. Therefore, it is necessary to maintain a proper neutral current limit with load changing scenarios, and having higher neutral capacity can help to maintain the output of the PV-VSI within proper current limits.

5.5 Performance Evaluation in an Australian LV Network

The low-voltage Australian distribution network presented in Chapter 2 is considered in this chapter for evaluation pf performance. Different network locations are considered in the network to assess different R/X ratio effects. The considered test points for different case studies in the 3P-4W residential 44-bus Australian LV network are shown in Fig. 5.10. The solar PV data was collected on 1st February 2016 from the Griffith University microgrid installation, and additional customer load data was collected from the local DNO, Energex. Four test points ($P_{1\text{-}4}$) are considered in the network having divergent customer load characteristics and PV-SVSI units as shown in Table 5.2 at the end of this chapter. Four different load characteristics with three single-phase loads are considered in this chapter, whereas in Chapter 4 a single load characteristics are utilised to evaluate the neutral compensation performance with wide stability margin.

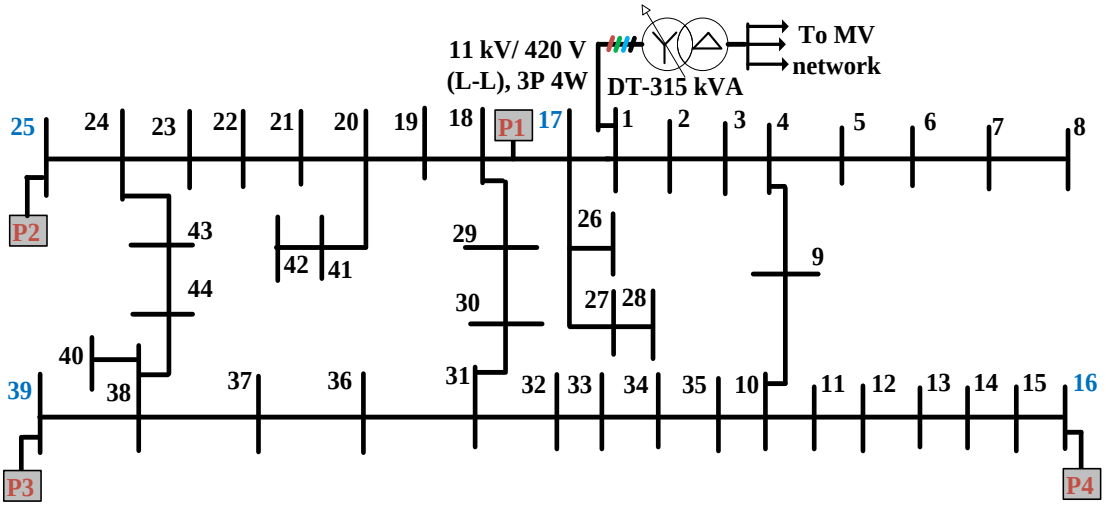

Figure 5.10. 44-bus 3P-4W LV network single-line diagram

Test point P1 is the closest one to the DT with the lowest R_+/X_+ and R_0/X_0 ratios, and the farthest test point from the DT is P4. The 3P-4L PV-SVSI is designed as a 15 kVA aggregated unit from at least four customer installations. A constant 700 V DC bus voltage is maintained with maximum SVSI current limit as ± 29 A for a rated 14.5 kW PV system. The fourth leg is constructed to operate with the fixed current limit at ± 10 A in addition to the dynamic capacity limit operation described in Section 5.3. The LV network neutral conductor is considered to have the same current carrying capacity as the phase conductors. At a standard test condition, the PV installation unit generates around 14.5 kW and the detailed specifications of the PV panels are described in Chapter 3. The customer load and solar data are collected at 1 min intervals and, with a 5 ms simulation time step, the total simulation run time is 14.4 s for a daylong operational period (24 hrs) which can represent the actual diversity and characteristics of an unbalanced network. The neutral compensation performance with the DCD method is compared with the zig-zag transformer (ZT) and the fixed-capacity (± 10 A) 3P-4L neutral compensation method designed in Chapter 4. The detailed specifications of the designed system are shown in Table 5.3 and included at the end of this chapter. Energex has restricted the PV penetration limit to 20% for the considered network, and no additional active and reactive supports, such as D-STATCOM, BES etc. are available in the residential area. Several case studies are undertaken to evaluate the performance of the designed four-leg PV-VSI with DCD method, and these scenarios are described in the following sections.

5.5.1 PV-SVSI operation with different customer loads

The designed PV-SVSI is operated in the STC condition with the stochastic sun irradiance and temperature data as shown in Fig. 5.11. The PV active period is roughly from 6.30 am to 5 pm peaking at around 11 am -1 pm. Different customer load characteristics are shown in Figs. 5.12 and 5.13. The customer loads at each test point are presented as aggregated customer loads for each phase; for example at P1, phases A and B have two loads and phase C has a single customer connection resulting in a total maximum load demand at phase A of around 6 kW and 2 kVAR.

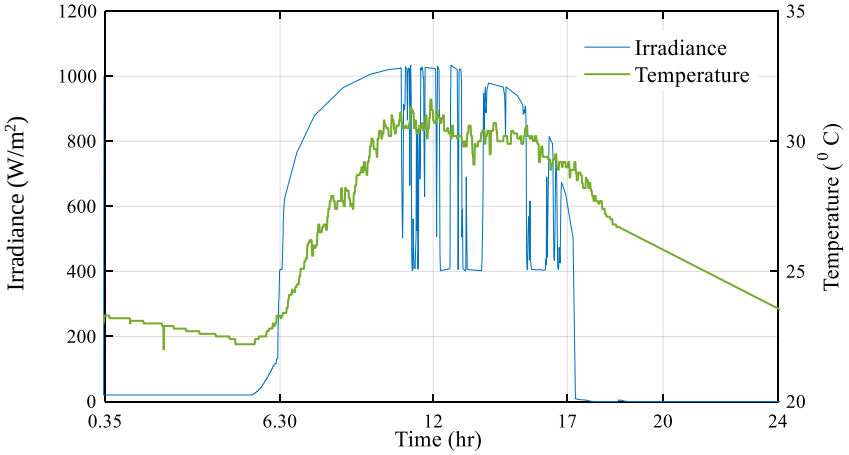

Figure 5.11. Sun irradiance and temperature data on 1st February 2016

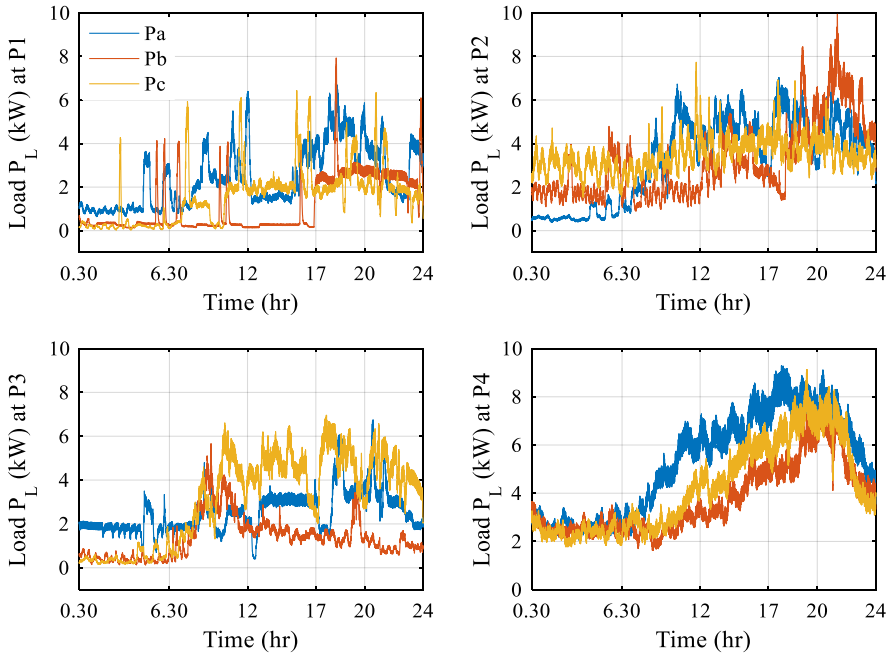

Figure 5.12. Different customer load active power profiles: (a) P_1 (b) P_2 (c) P_3 and (d) P_4

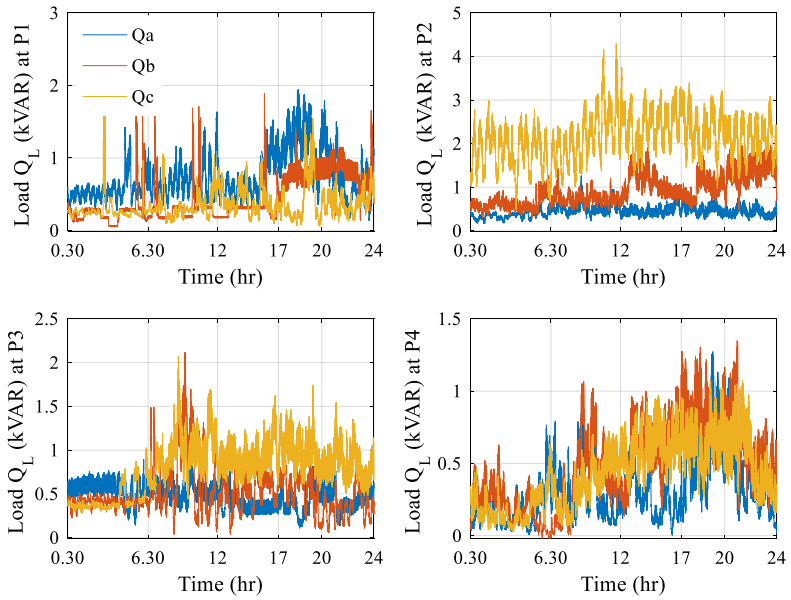

Figure 5.13. Different customer load reactive power profiles: (a) P_1 (b) P_2 (c) P_3 and (d) P_4

The unbalanced load allocations are evident from the load profiles, where the maximum load demand occurs after 5 pm (17 hr in plots) which is a common scenario in residential areas. The remaining PV active power after load compensation is exported to the grid which improves the PCC voltage. The three-phase PCC voltage profiles at the four test points are shown in Fig. 5.14, where case (a) represents an LV feeder with base load connection, case (b) additional customer load connection without PV-VSI, case (c) with unity power-factor PV-VSI and case (d) with PV-SVSI with the dynamic PCC voltage regulator.

At the test points from P_1-P_3 the three-phase PCC voltage remains stable within ± 2% variation, however, at P_4 it drops to - 4% from 5 pm to 10 pm in cases (b) and (c) due to customers' higher load consumption. In case (d), the PCC voltage improves to around 0.98 p.u. making the connection more stable than without the PV-SVSI. With the considered load connections, the PCC voltage remains within the ± 6% limit for the 24-hour operation period. The PCC voltage for each phase at test point P4 is shown in Fig. 5.15, where a new case condition (h) is introduced to show the effect of PV power export to the grid with the LV network base load connection, i.e. high power generation and low consumer demand. It can be seen from Fig. 5.15 that the phase C voltage drops to the – 6% limit during heavy load conditions from 5 pm – 10 pm while the other phases remain within the – 2% range. Consequently, with the three-phase dynamic PCC voltage regulation operation, the Phase C voltage improves by around 2% and remains within the safe operation

region. The voltage profile improvement from the PV export power to the grid can be seen from cases (c), (d) and (h).

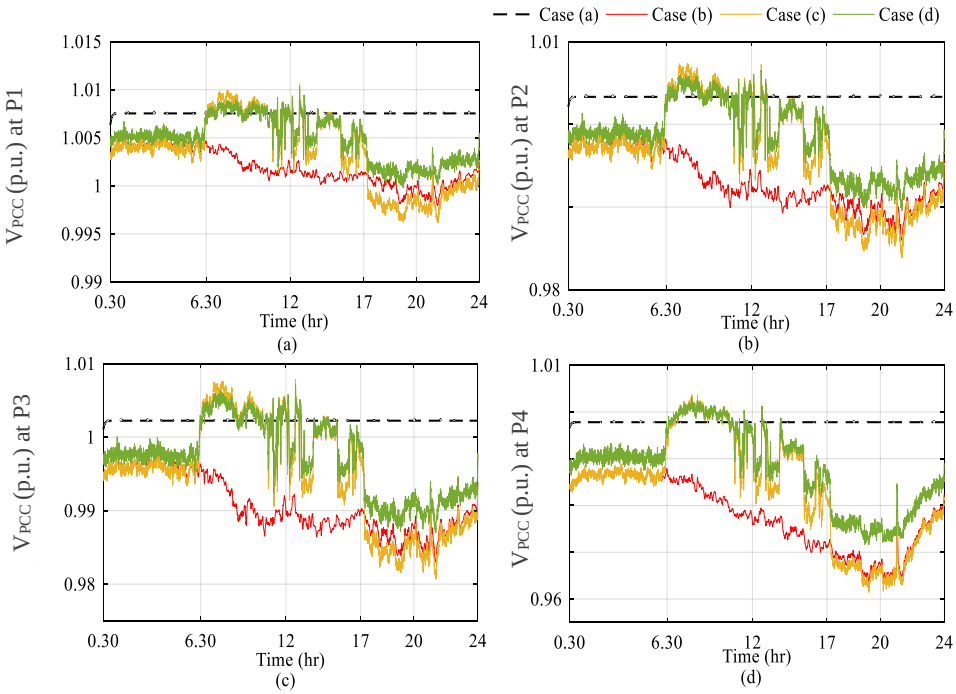

Figure 5.14. V_{PCC} at (a) P1, (b) P2, (c) P3, and (d) P4

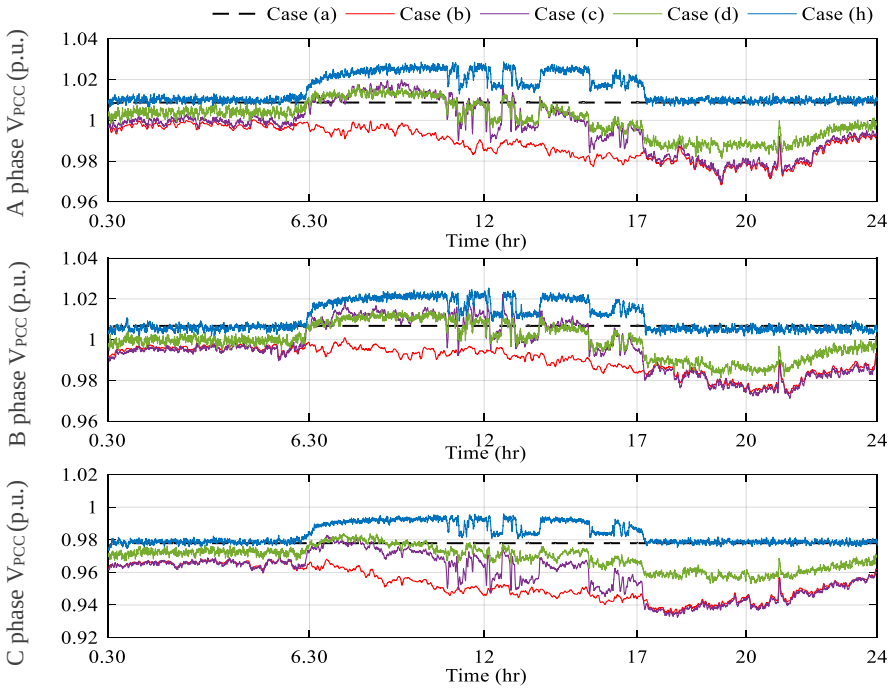

Figure 5.15. V_{PCC} at P4 for phases A, B, and C

The uneven load distributions at each phase from P_1-P_4 cause a significant neutral current at the PCC as shown in Fig. 5.16 in case (b). Different neutral compensation methods, such as ZT with 3 kVA/phase in case (e), four-leg PV-SVSI with active neutral compensation having fixed $I_{N\text{-limit}}$ = 10 A in case (f) and $I_{N\text{-limit}}$ = 20 A in case (g) are applied at the four test points. The compensation performance from the different applied methods is shown in Fig. 5.16. It is discussed in Chapter 4 that the considered LV network with base load condition inherently exhibits unbalanced characteristics. For this reason the main consideration is given to the customer load-generated neutral current compensation performance. Among the neutral compensators, the ZT outperforms the PV-SVSI at P1 which is close to the DT (63.4 m), and in all other test points from P_2-P_4, the four-leg PV-SVSI performs better neutral compensation than ZT, even with a lower neutral compensation capacity limit, i.e. case (f). The customers close to the distribution transformer are not expected to install any auxiliary devices for voltage or neutral compensation, since it is expected that the DT should have a sufficient regulation effect on them. However, the customers situated far from the DT are expected to face both lower PCC voltage and higher neutral currents.

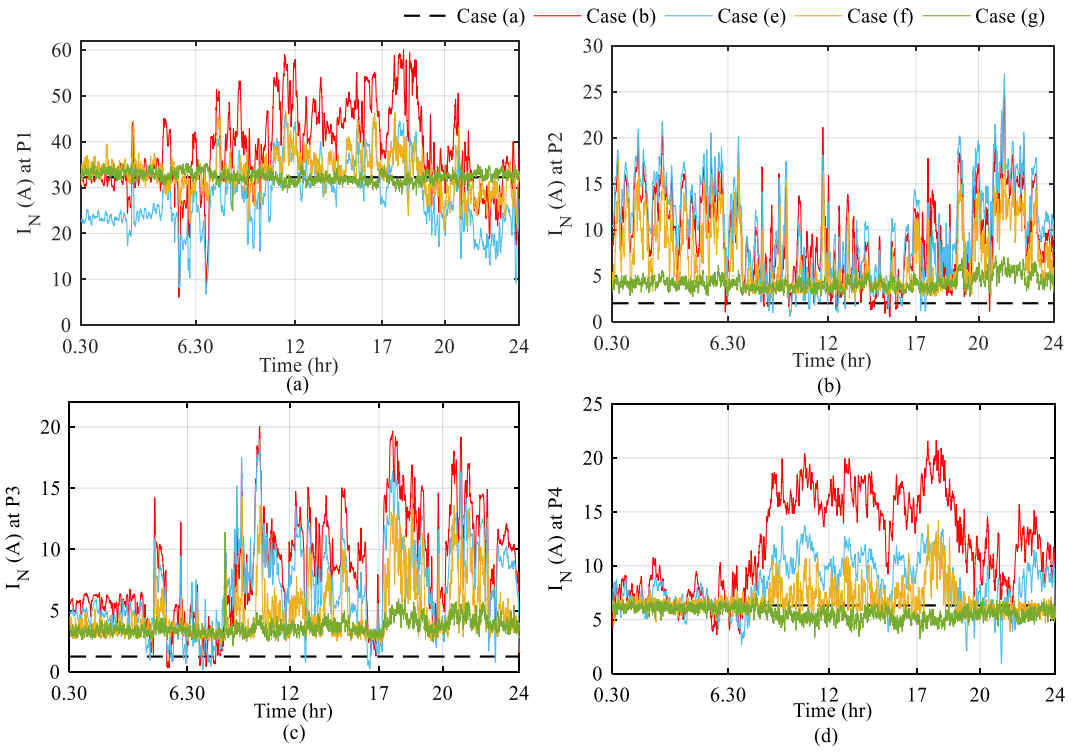

Figure 5.16. PCC neutral current at (a) P1, (b) P2, (c) P3, and (d) P4

It can be seen from Fig. 5.16 that the neutral compensation performance with higher capacity operation from case (g) outperforms all the other auxiliary devices and the load-generated neutral

current can be completely compensated at the PCC for all four test points. This demonstrates the requirement of higher capacity neutral compensation operation at most of the customer installation points situated far from the DT and having dynamic load characteristics.

5.5.2 PV-SVSI capacity management

As shown in the previous case study, only P4 faces a lower PCC voltage during the heavy load period than the other test points. In fact, P4 requires more reactive power support (capacitive effect) compared to other test points. The PV-generated active power and the requirement of reactive power for the PCC voltage regulation at all four test points are shown in Fig. 5.17. From Fig. 5.17, it can be seen that the designed controller robustly distributes the remaining VSI capacity for reactive power operations, and the test points $P_{1\text{-}3}$ require less than 5 kVA reactive power support to maintain V_{PCC} within ± 2% from their PV-SVSI installations. However, test point P4 requires nearly 10 kVA to maintain the V_{PCC} within the ± 6% limit during the heavily loaded condition, and the remaining VSI capacity from a 15 kVA aggregated installation, i.e. approx. 5 kVA, can be utilised to increase the capacity for neutral compensation controller.

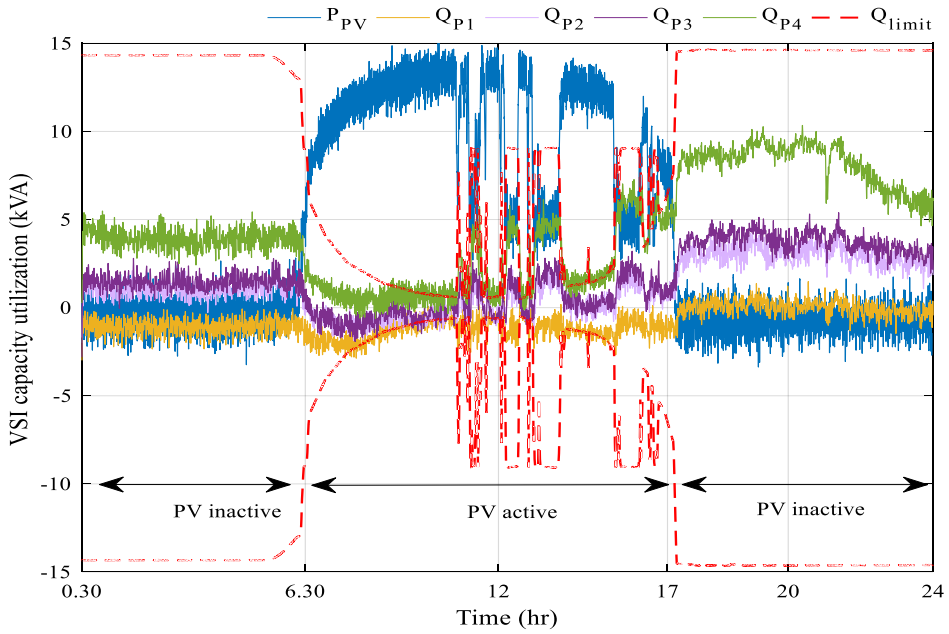

Figure 5.17. SVSI capacity utilisation for active and reactive operations

The dynamic reactive power distribution operation is controlled using a dynamic current limiter as discussed in Section 5.3. The $Q_{capacity}$ limit is shown in Fig. 5.17 to demonstrate the capacity

availability of the VSI after the PCC voltage regulation, which can be used for higher capacity neutral current compensation.

It can be seen from Fig. 5.16 (d) that the loads at P4 generate an average 12 A (rms) neutral current (after deducting the network unbalance effects) around the peak load demand conditions from 5 pm to 10 pm. The maximum neutral current occurs at around 5-7 pm and is approximately 16 A (rms). This higher neutral current can also cause the PCC neutral to ground voltage (NVG) to rise and cause electrical safety concerns for customers. The effects of independent neutral current compensation with different neutral current limiters are shown in Fig. 5.18. In Fig. 5.18, only the neutral current controller capacity is changed by varying the current limit ($I_{N\text{-}limit}$) on the dynamic current limiters DL_3 (1/3 $I_{N\text{-}limit}$) and DL_4 at P4. An NGV rise of 2 V can be seen in Fig. 5.18 (b) during the peak load condition. It is also evident from Figs. 5.18 (a) and (b) that to maintain the NGV at less than 1 V, $I_{N\text{-}limit}$ equal to at least 10 A is required, and with 20 A the load-generated neutral current and NGV rise can be fully compensated. With the increase in neutral capacity, the 3P-4L SVSI capacity and associated costs will also rise. Therefore, the DCD method is proposed with the 3P-4L PV-SVSI to utilise the remaining VSI capacity after reactive power regulation for higher capacity neutral compensation operation. The higher capacity neutral compensation operation can be employed in several instances in a daylong operation period without increasing the total SVSI installation capacity.

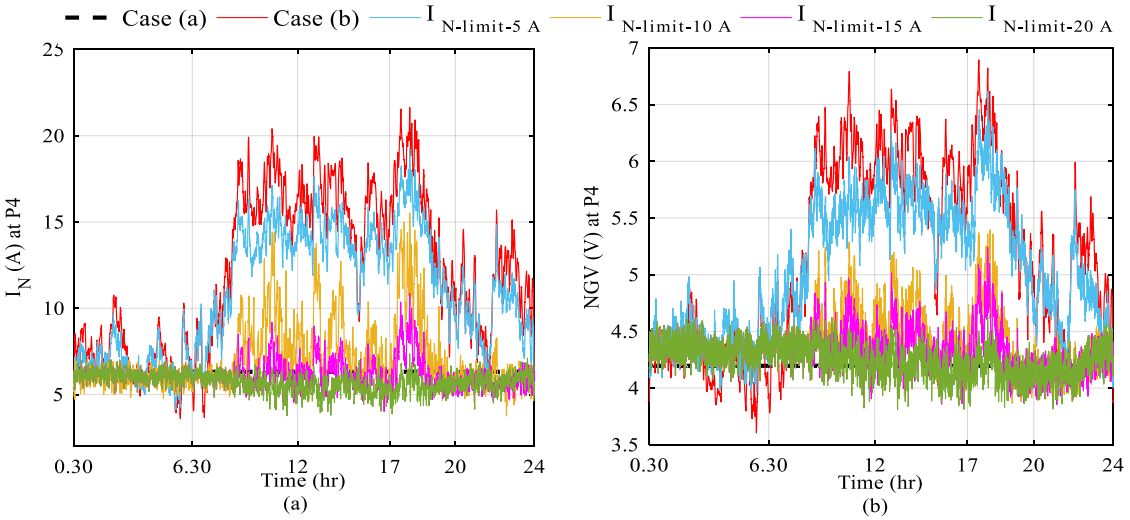

Figure 5.18. (a) I_N and (b) NGV with different neutral compensation capacities

5.5.3 PV-SVSI with dynamic capacity distribution (DCD)

The PV-SVSI with the DCD method is installed at test point P4 for a daylong operation. The neutral current and the NGV compensation operations are compared with fixed-capacity neutral compensation, i.e. $I_{N\text{-}limit}$ of ± 10 A (case f) as shown in Fig. 5.19. During the PV active period, the PCC voltage remains close to 1 (p.u.), therefore the PCC voltage regulator utilises little capacity and the remaining capacity is utilised for a higher capacity neutral compensation operation. With the higher capacity neutral compensation operation, the NGV voltage is reduced to less than 1 V from 2.4 V in case (b). The main performance improvement with the DCD method can be seen during peak load periods from 5 – 8 pm where the four-leg PV-VSI with DCD reduces the NGV by 1.2 V and 2.5 V, respectively, compared to cases (b) and (f). Similarly, compared to case (f), the system with the DCD executes better neutral current compensation, and nearly 5 A of neutral current improvement can be observed in Fig. 5.19 (b).

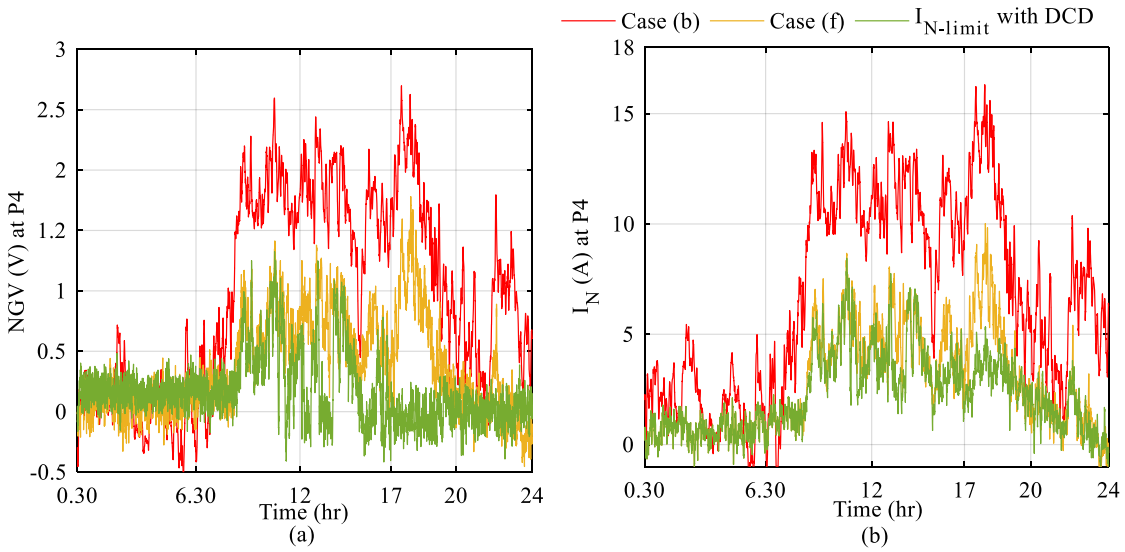

Figure 5.19. (a) NGV and (b) I_N at P4

The four-leg VSI with DCD also provides better phase balancing than fixed-capacity neutral compensation even with the same PV-SVSI configuration and capacity, especially during PV inactive periods as shown in Figs. 5.20 (b) and (c). Fig. 5.20 makes it evident that the DCD method improves the CUF, VUF, neutral current and NGV rise significantly. From 5.30 pm to 6 pm more than 10.5 A and 3.5 A neutral compensated performance is achieved compared to cases (b) and (f). Similarly, the CUF improved by around 18% and 6% compared to case (b) and case (f) as

shown in Figs. 5.20 (a) and (b), respectively. The NGV rise is also improved with the proposed method and the electrical safety concerns with load alone can be mitigated by applying the designed SVSI installation.

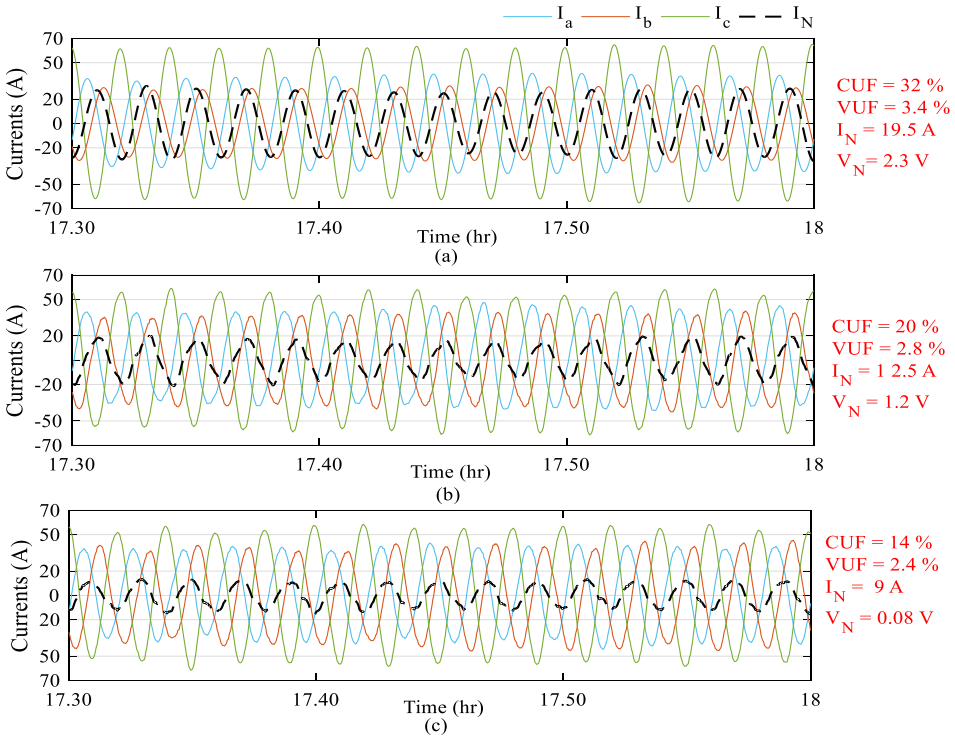

Figure 5.20. LV network with loads: (a) no compensation, (b) fixed neutral capacity PV-SVSI, and (c) DCD integrated PV-SVSI

When any unbalance occurs in a network, it mainly shifts the zero neutral point for the voltage and current quantities of a balanced system and results in a floating neutral issue. Therefore, shifting the floating neutral close to the original zero mainly signifies better phase balancing and unbalance improvement at that particular connection point as shown in Fig. 5.21. It can be seen from Fig. 5.21 that the VUF at the customer point is 0.4% less and the neutral point is much closer to the origin for the PV-SVSI system with DCD compared to the fixed-capacity neutral compensation operation. As the LV feeder is inherently unbalanced, additional load unbalance shifts the neutral further from the origin but is improved with the higher capacity neutral compensation with the four-leg PV-SVSI.

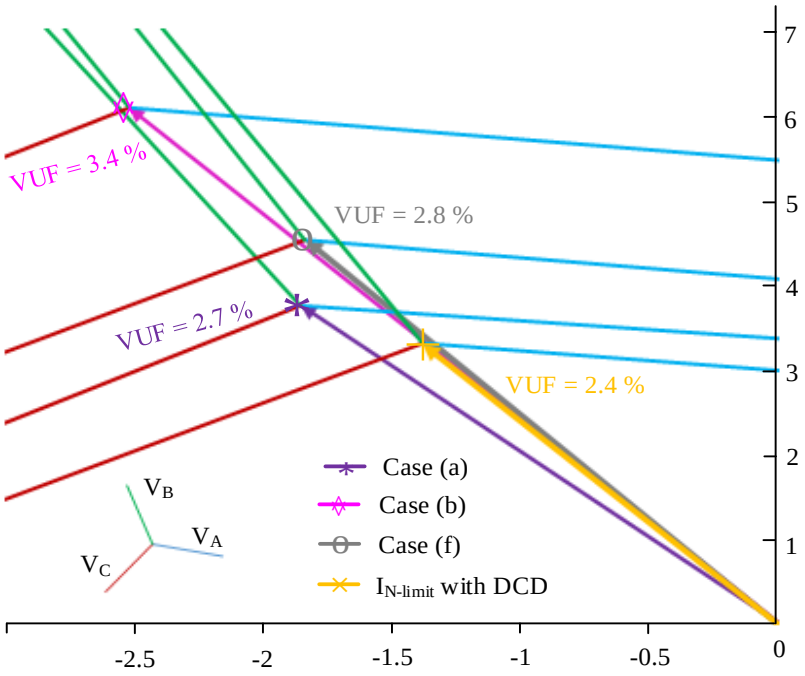

Figure 5.21. V_{PCC} neutral shift effects at P4

It can be seen from Fig. 5.22 (a) that the considered customer loads from all four test points can increase the neutral current by more than 40 A at DT from 5 – 8 pm, which can overload the DT and in turn reduce its life cycle. In the worst case scenario, a connection failure can also occur with high neutral current at the DT. The neutral current compensation performance is evaluated with a ZT having 3 kVA/phase and 5 kVA/phase capacities, represented as cases (e) and (e*), and compared with case (f). Although case (e*) provides better neutral compensation including both load and network unbalance, the PV-SVSI with the DCD provides stable neutral compensation as it does not include the unbalance from the LV network. Case (f) also improves the CUF compared to other methods for a daylong operation as shown in Fig. 5.22 (b). It is evident from Fig. 5.22 (a) that the proposed method can eliminate more than 90% of the load-generated neutral current at the DT terminal where the fixed-capacity method eliminates around 80%. The improvement in CUF at DT is also around 1% which is quite significant considering the high capacity rating of the DT.

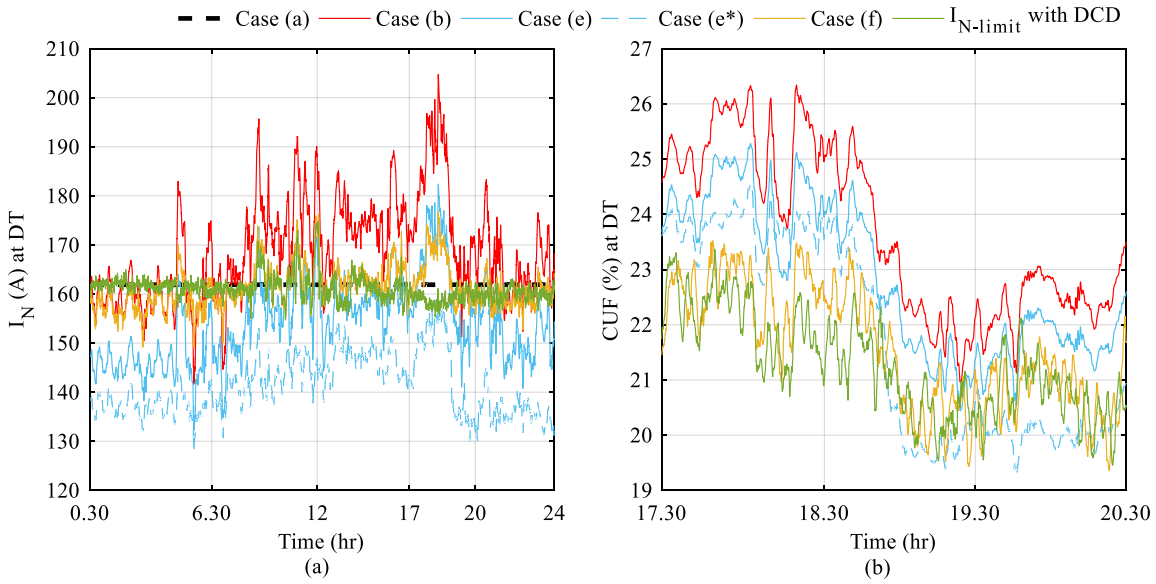

Figure 5.22. (a) I_N, and (b) CUF at DT terminal

5.5.4 Load changing effect with DCD method

The load changing effects are demonstrated at test point P4 with two scenarios considered here:

(i) Sudden load connection, and

(ii) Sudden load disconnection.

The sudden load connection case is further divided into:

(a) Three single-phase load connections (from 7.30 – 8.30 pm) - which is a balanced condition and will cause a severe voltage drop, and

(b) Single- and double- phase load connections – which is an unbalanced condition and will cause a severe neutral current.

The phase C and A loads are increased from 7.30 – 8.00 pm and 7.50 – 8.20 pm, and double-phase loads (phases C and A) are increased from 7.50 – 8.00 pm. The load at phase B is kept unchanged. The DCD method interaction with both balanced and unbalanced load changing is demonstrated in Fig. 5.23. From 0.30 – 6.30 am, the required reactive power for the PCC voltage regulation utilises less than 10 A of current capacity from the total capacity of 29 A (15 kVA system), and the remaining capacity is added to $I_{N\text{-limit}}$ ±10 A for higher capacity neutral compensation. During single-phase load addition in all three phases, the PCC voltage at P4 drops significantly due to the overloading. Fig. 5.23 (a) shows that the reactive power current component ($I_{q\text{-}VSI}$) reaches the maximum VSI capacity limit resulting in zero dynamic capacity availability for

neutral compensation. However, due to the loads' changing in a balanced way, i.e. adding load in all three phases, no significant neutral current rise occurs at P4 and the PV-SVSI neutral controller operates with the fixed neutral current limit (± 10 A) as shown in Fig. 5.23 (c) and (e). However, with unbalanced load addition, the required reactive power for the PCC voltage regulation is lower than the available capacity and the remaining available capacity is utilised for higher neutral compensation with the DCD method as shown in Figs. 5.23 (b), (d) and (f). It can be seen from Figs. 5.23 (c) and (d) that the unbalanced load addition causes more neutral current generation and the balanced load addition causes a higher voltage drop resulting in different amounts of SVSI capacity being available.

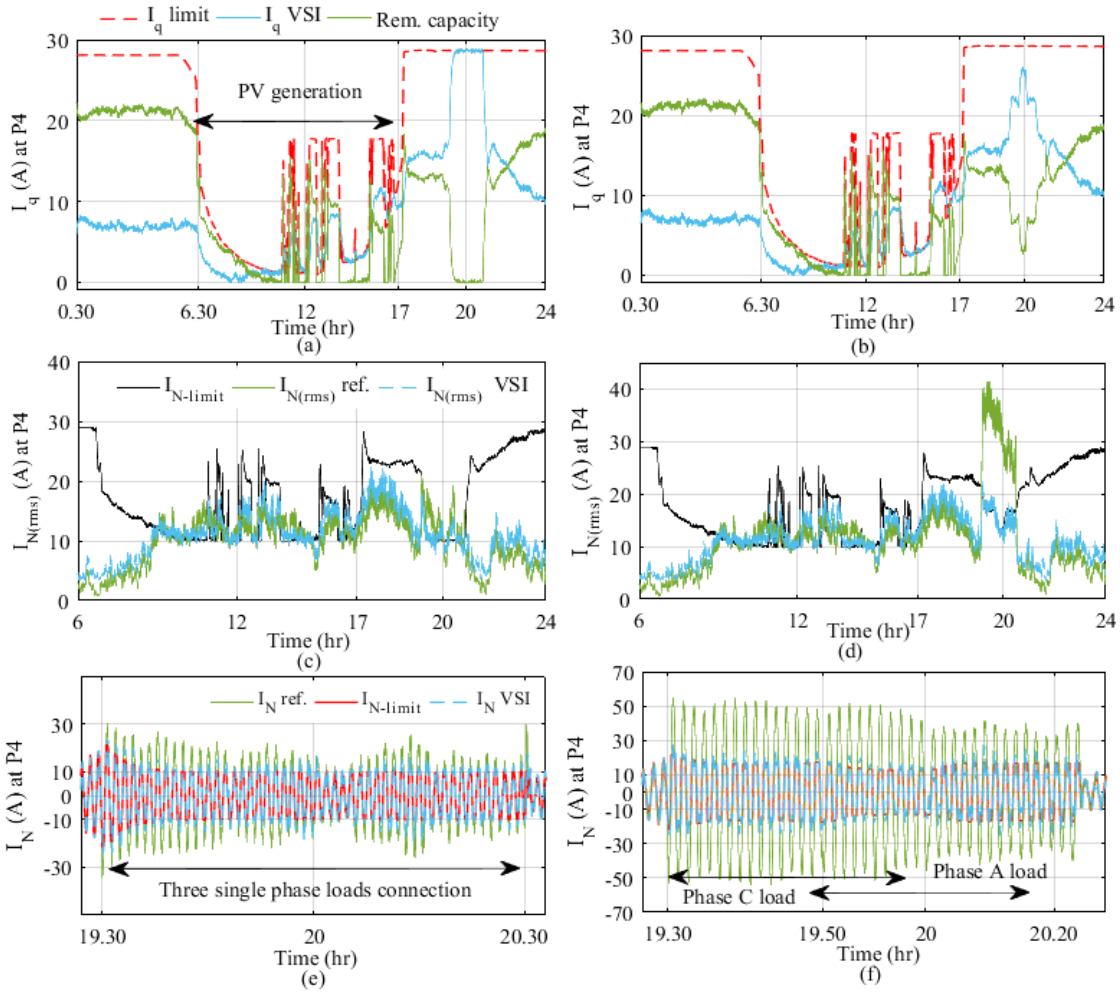

Figure 5.23. Iq_{VSI} for (a) balanced, (b) unbalanced; neutral controller $I_{N\text{-}VSI}$ (rms) for (c) balanced, (d) unbalanced, and IN-VSI (e) balanced, (f) unbalanced loads addition

The PV-SVSI performance with the DCD method to regulate PCC voltage regulation and for neutral current compensation is shown in Fig. 5.24. Here, the cases (b-1) and (b-2) represent balanced and unbalanced load increase cases, and case conditions (i) and (j) indicate the PV-SVSI performance with corresponding loads from cases (b-1) and (b-2). With case (b-1), the PCC voltage drops to 0.94 p.u. due to an overload condition and I_N increases to around 5 A, however, those components are compensated significantly with the PV-SVSI system in case (i). With case (i), the case (b-1) PCC voltage and neutral current reduce to approximately 0.96 p.u. and less than 10 A as depicted in Figs. 5.24 (a) and (c). This also improves the VUF and CUF by 1.5% and 10% compared to the case (b-1) as shown in Figs. 5.24 (b) and (d). Case (b-2) generates a significant neutral current, and with the proposed method it can be seen in case (j) in Figs. 5.24 (c) and (d) that around 12 A of neutral current, around 10% CUF, and around 1% VUF improvements are achieved.

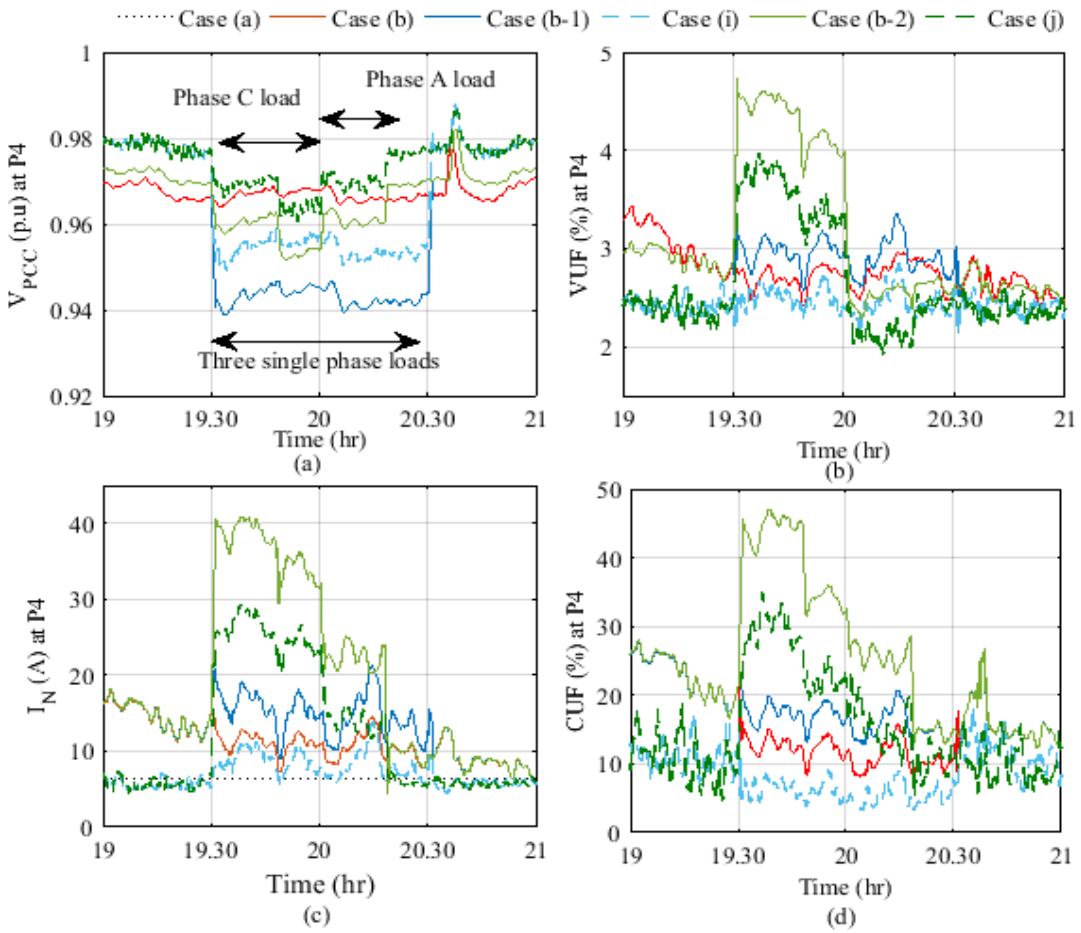

Figure 5.24. Load connection: (a) V_{PCC}, (b) VUF, (c) I_N and (d) CUF at P4

The sudden load disconnection effect is shown as case (b3) in Fig. 5.25, where initially the single-phase (C) load from 8.00 – 8.20 pm and later double-phase (A and B) loads from 9.40 -10 pm remain disconnected while keeping the other phases live. In both disconnected conditions, the PCC voltage increases due to the low load demand compared to the base LV feeder load, and results in more SVSI capacity availability for neutral compensation as shown in Fig. 5.25 (a) and (b). The double-phase load disconnections cause more neutral current (10 A) and SVSI capacity availability (~ 4 kVA) than the single-phase load disconnection case as shown in Fig. 5.25 (b). The performance of the PV-SVSI with the DCD method for neutral current compensation is compared with case (e) and case (f), and the results are shown in Fig. 5.25 (d).

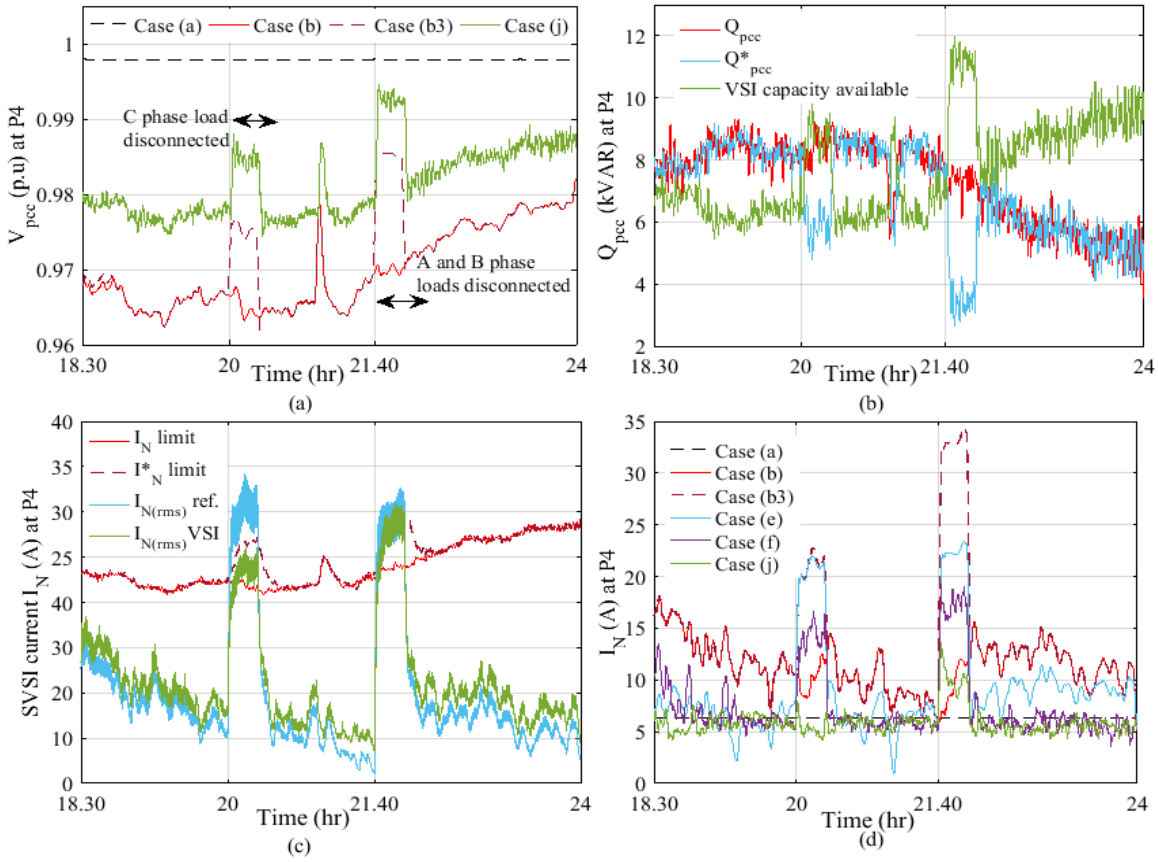

Figure 5.25. Load disconnection: (a) V_{PCC}, (b) Q_{PCC}, (c) I_N controller and (d) I_N

The double-phase load disconnections cause around 12 A more neutral current than the single-phase one, and with the additional neutral capacity, the proposed neutral compensator outperforms case (e) and (f) significantly. Due to higher capacity availability at 9.40 pm, the designed SVSI compensates for around 20 A of neutral current, whereas the fixed-capacity neutral controller

compensates for around 8 A ($I_{N\text{-limit max}}$ = ± 10 A (rms)) and the ZT around 6 A only. The reference-following operation from the neutral current controller with increased capacity can be seen in Fig. 5.25 (c). Higher neutral current is generated, around 30 A (rms), at 8 pm and at the same instant the V_{PCC} becomes nearly 0.98 p.u. which makes around 10 A capacity available. It can be seen that the designed PV-VSI with DCD method robustly utilises the available capacity for higher neutral current compensation. A similar improvement in neutral capacity can be observed at 9.40 pm in Fig. 5.25 (c).

From this case study, it is evident that higher capacity neutral compensation with the proposed DCD method can improve the traditional fixed-capacity 3P-4L PV-SVSI performance significantly in the neutral compensation and phase balancing operations at the customer installation point with divergent load connection and disconnection, and even with different contingencies in the LV network.

5.5.5 Performance with nonlinear loads

The performance of the designed 4L PV-VSI with nonlinear loads is evaluated in this case study. Three single-phase loads are connected with a full bridge rectifier circuit at the PCC point as shown in Fig. 5.26. Phase A is designed with an R-C load from 1.50 – 1.80 s, phase B with an R-L load from 1.90 to 2.20 s and phase C with a resistive load from 1.70 to 2.0 s.

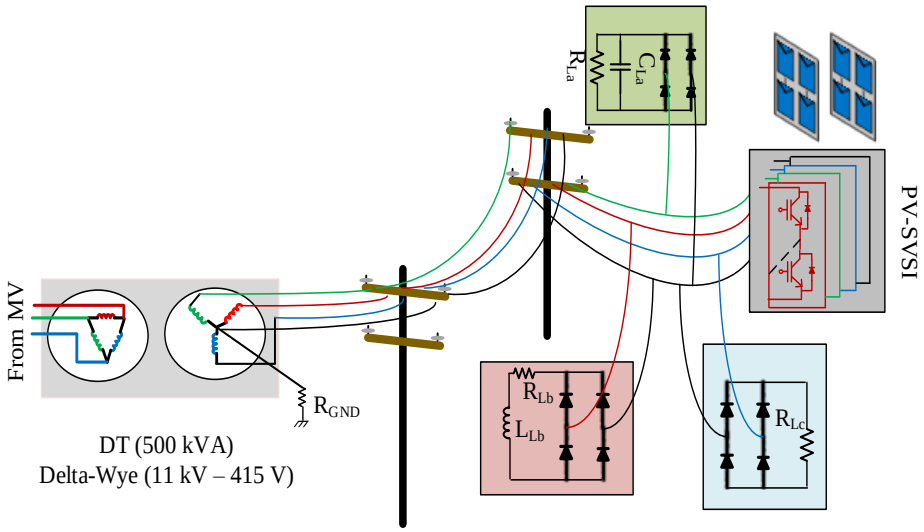

Figure 5.26. Nonlinear load connection at customer installation

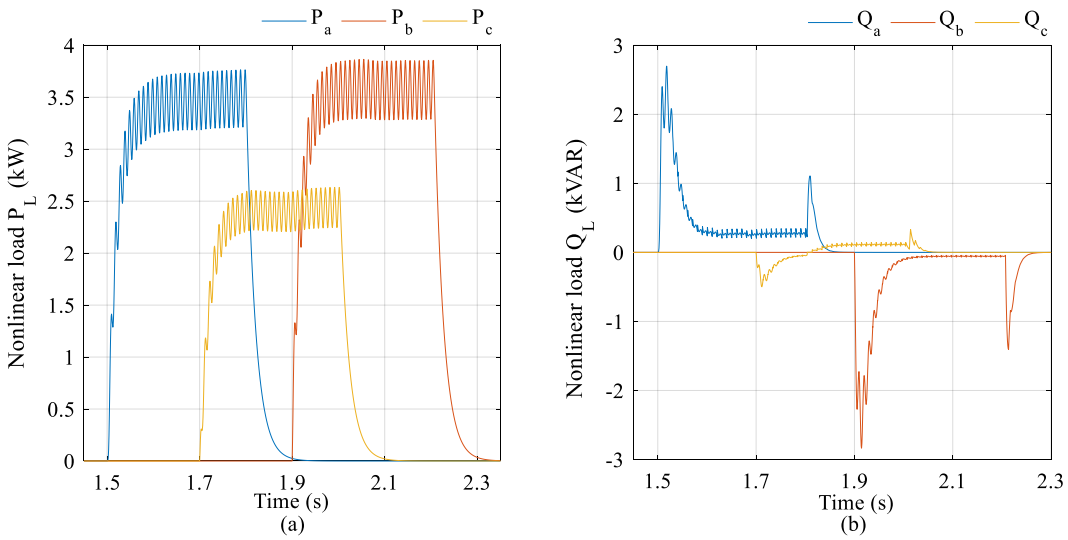

Figure 5.27. Nonlinear load profiles: (a) active, and (b) reactive power

The load profiles of the designed nonlinear loads are shown in Fig. 5.27. The simulation study is evaluated for a 3 second period (5 hr equivalent) in addition to the load profiles from case (b). It can be seen from Fig. 5.27 that phases A and B consume around 3.5 kW active power, with the same reactive power value but in opposite polarity due to the capacitive and inductive characteristics of the loads; and phase C is purely a resistive type.

The neutral current generation and corresponding operation of the designed neutral current controller are shown in Fig. 5.28 (a). As the proposed neutral current controller considers compensation operation from the load-generated neutral only, except for the load connection period from 1.50 – 2.20 sec, there is no significant operation from the neutral controller. However, even in normal operation, the designed controller improves the current unbalance factor significantly as shown in Fig. 5.28 (b). During the load connection, the designed system reduces the CUF by almost 20% from 1.80 – 2.00 s. The high unbalance factor occurs due to the transients from all the three single-phase loads and the system interacts robustly to mitigate the unbalance significantly.

The neutral compensation operation with nonlinear loads and the corresponding phase balancing operation from each phase are shown in Fig. 5.29. Significant neutral current generation (approx. I_N 20 $A_{p\text{-}p}$) can be seen from 1.80 – 2.0 s in Fig. 5.29 (a), and the robust neutral compensation operation (approx. I_N 5 $A_{p\text{-}p}$) with better phase balancing can be seen in Fig. 5.29 (b). The phase

unbalancing mainly occurs due to neutral shift problem as discussed in the case study 5.5.3, and is improved significantly with the proposed four-leg PV-VSI system.

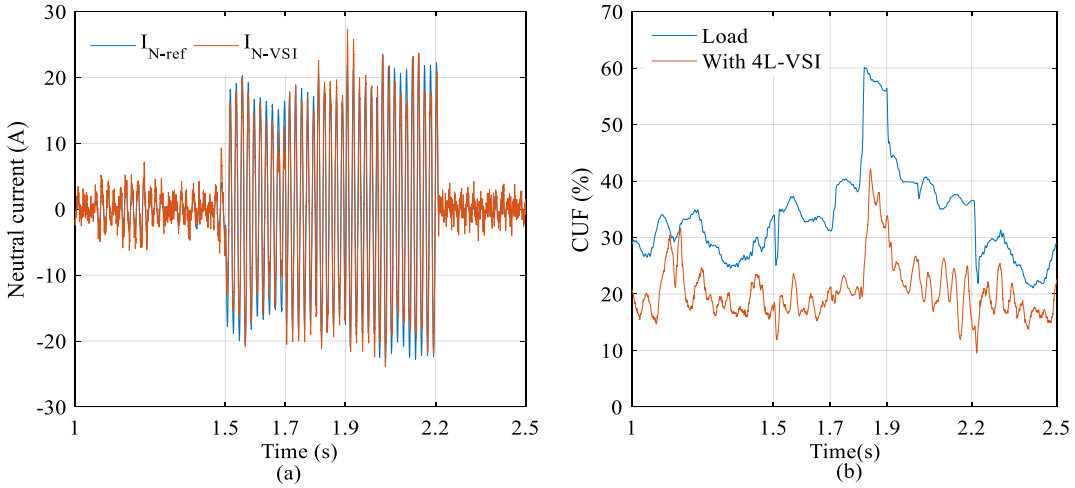

Figure 5.28. (a) Neutral controller operation, and (b) CUF at PCC

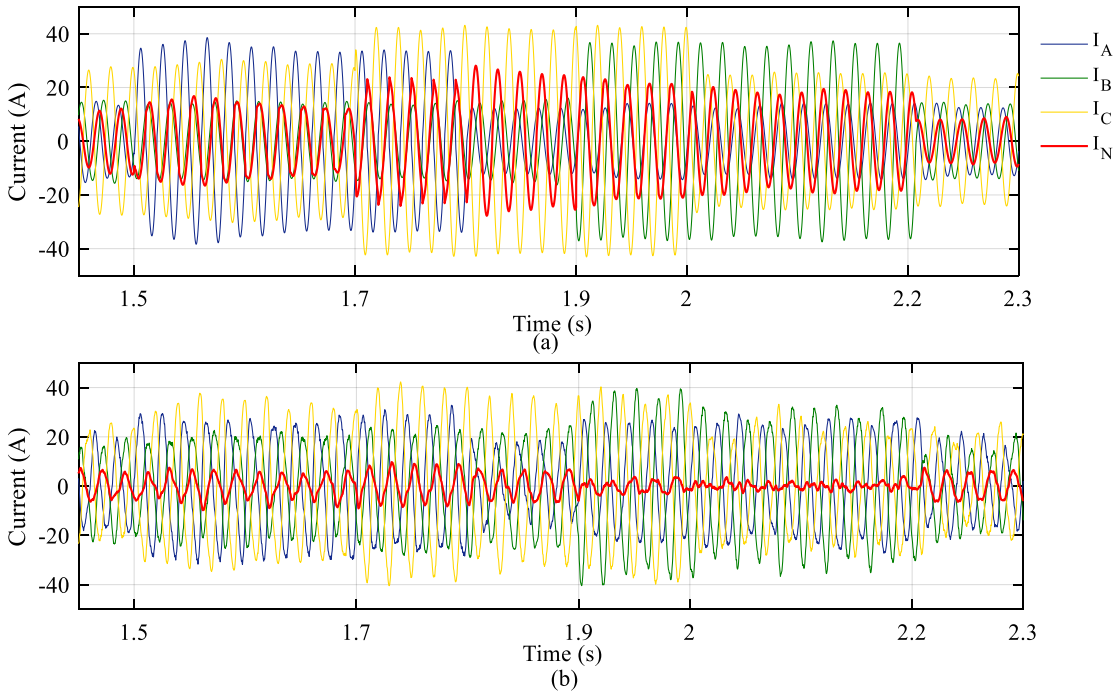

Figure 5.29. Phase currents (a) with load, and (b) with 4L PV-VSI

5.5.6 Performance with commercial loads

Different commercial loads, such as those required for university buildings, shopping malls etc., are generally connected to the low-voltage distribution network with their own substation

installation. In this case study, the load profiles of a university building are considered as the commercial load. The load variation of a commercial unit is quite different from a residential unit, as the peak load of a university (commercial load) occurs around midday when the PV is active, whereas the residential peak load occurs during the early evening period when the PV is inactive. Therefore, the available VSI capacity utilisation is different in these two cases. Most of the PV-generated power is consumed by the commercial load itself due to similar peak demand and generation schedules. Thus the voltage-rise due to excessive PV power export rarely occurs and as the main activities in any university area occur during daytime, the voltage sag is not prominent during the night time. On top of that, due to the shorter distance of the commercial unit from the distribution transformer/substation, any voltage constraints are regulated by the transformer itself. The connection of a commercial building with the DT is shown in Fig. 5.30.

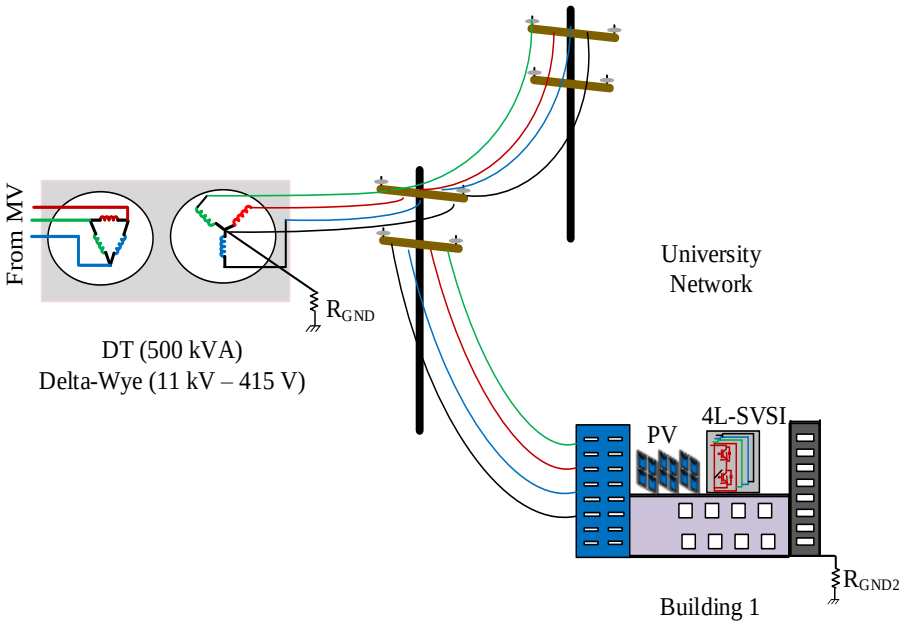

Figure 5.30. University building (commercial load) connection with DT

The four-leg PV-SVSI with reference to the residential area is also considered with a similar control configuration to the commercial load to evaluate the significance of the PV-SVSI unit with the commercial network. Two days of consumption data from two different months (May'16 and September'16) are collected from the N44 building in Griffith University, Brisbane. The building is about 200 m from the distribution transformer. Sun irradiance data for two days is considered in the simulation analysis and is shown in Fig. 5.31. Two days of load profiles are chosen to show

the variation between weekend and weekday consumption. Also, two different months are considered to evaluate the load for winter and summer periods.

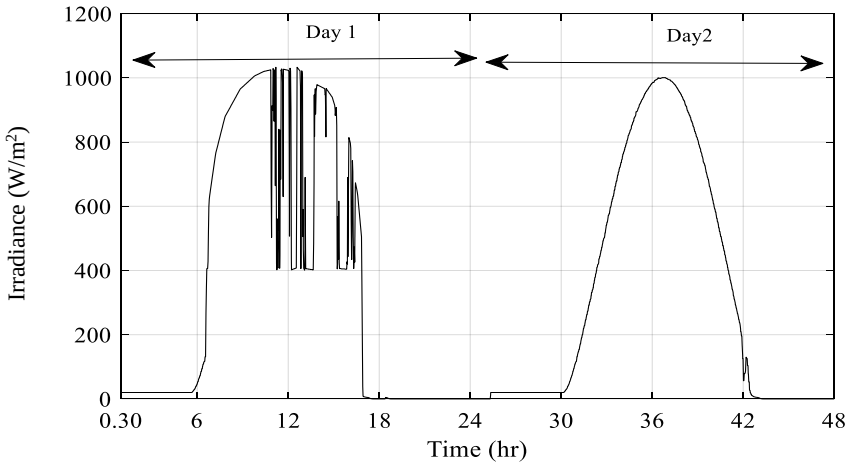

Figure 5.31. Sun irradiance profile for continuous 2 days

The load profiles are shown in Fig. 5.32 and it can be seen that the load profiles in both months present similar power consumption trends. However, the load consumption during September is higher than in May due to the status (middle of the semester) of the university classes and the weather conditions (beginning of summer). The unbalanced load distribution among the different phases is evident, but is not as significant compared to residential areas.

The load consumption difference is quite evident from the weekend and weekday load profiles. The system is expected to show different characteristics with the variations in load profiles. This is also reflected in the PCC voltage as shown in Fig. 5.33, where the main voltage dip occurs during weekdays, but it is within the range of ± 2% of the PCC voltage. The voltage regulation operation from the designed PV-SVSI is also compared and shown in Fig. 5.33. It can be seen that, even with the small PV-VSI installation unit compared to total load consumption, the voltage profile can be regulated closer to 1 p.u. The operation of the PCC voltage regulator to generate the reactive power reference is shown in Fig. 5.34. During the PV peak generation time, the VSI available capacity becomes quite low, resulting in almost zero voltage regulation operation. However, during night time, the controller utilises the full VSI capacity and follows the reactive power reference promptly as shown in Figs. 5.34 (b) and (c).

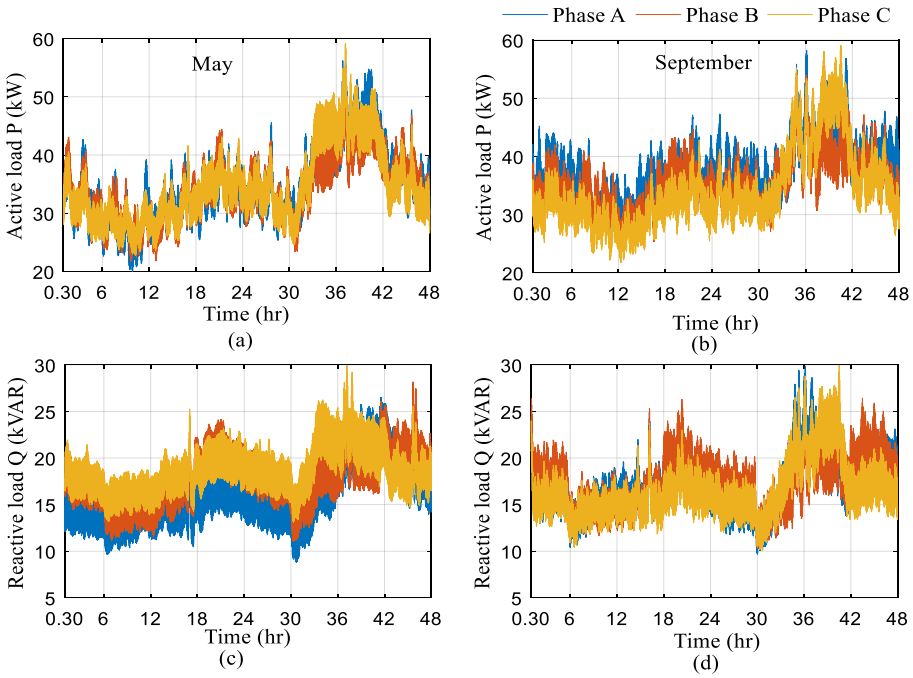

Figure 5.32. Load profiles: (a) P_{May}, (b) $P_{Sep.}$ (c) Q_{May}, and (d) $Q_{Sep.}$

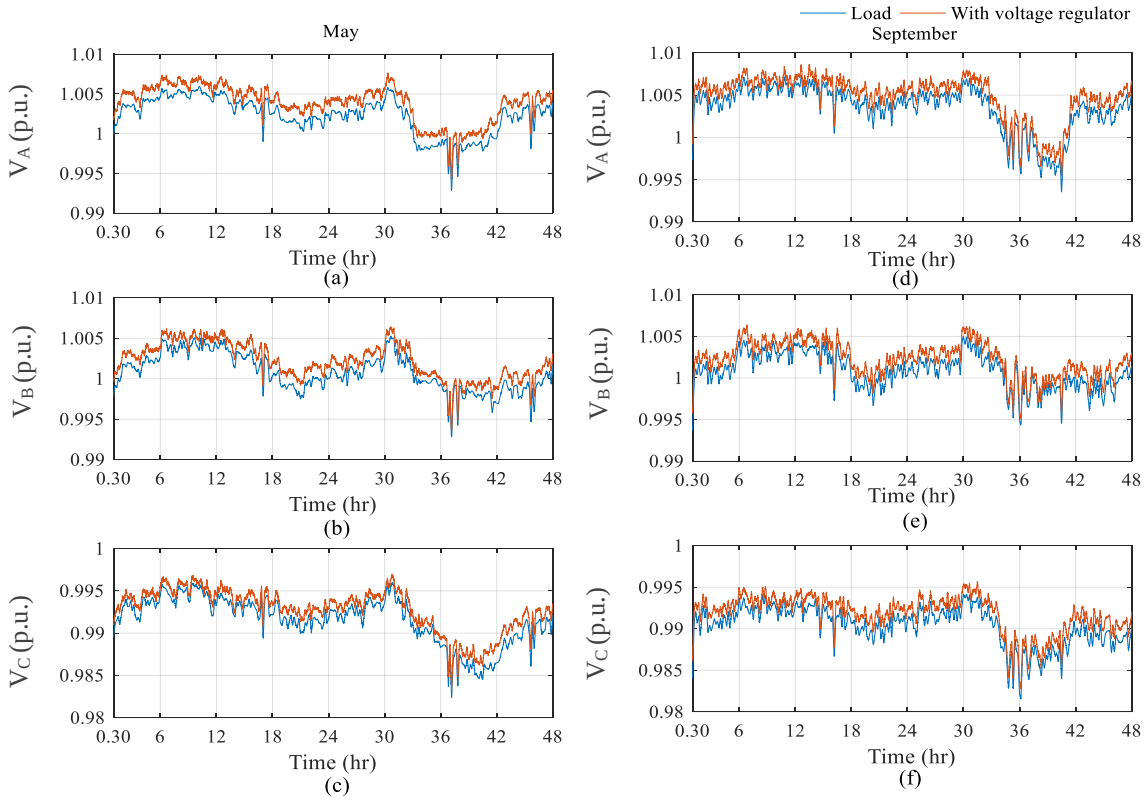

Figure 5.33. V_{PCC} in May for phase (a) A, (b) B, (c) C, and in September for phase (d) A, (e) B, and (f) C

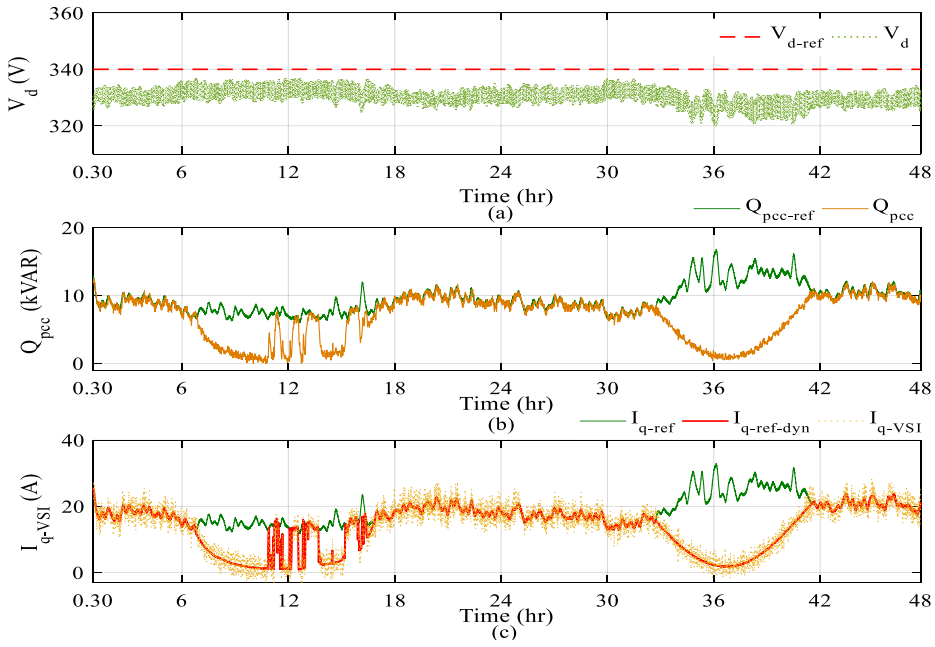

Figure 5.34. PCC voltage regulation: (a) Vd, (b) Q_{PCC}, and (c) Iq-$_{VSI}$

As the PCC voltage remains within the ± 2% range, utilising the 10 kVA capacity from the PV-SVSI unit the remaining SVSI capacity is utilised for higher neutral compensation following the proposed DCD method. The load-generated neutral current is shown in Fig. 5.35, and it can be seen that higher neutral current is generated during weekdays in September'16. The difference in the load-generated neutral current is significant (approx. 20 A (rms)) from 36 – 42 (hr). Therefore, the main consideration is given to the commercial load profiles from September'16, and the capacity utilisation for higher neutral compensation is shown in Fig. 5.36.

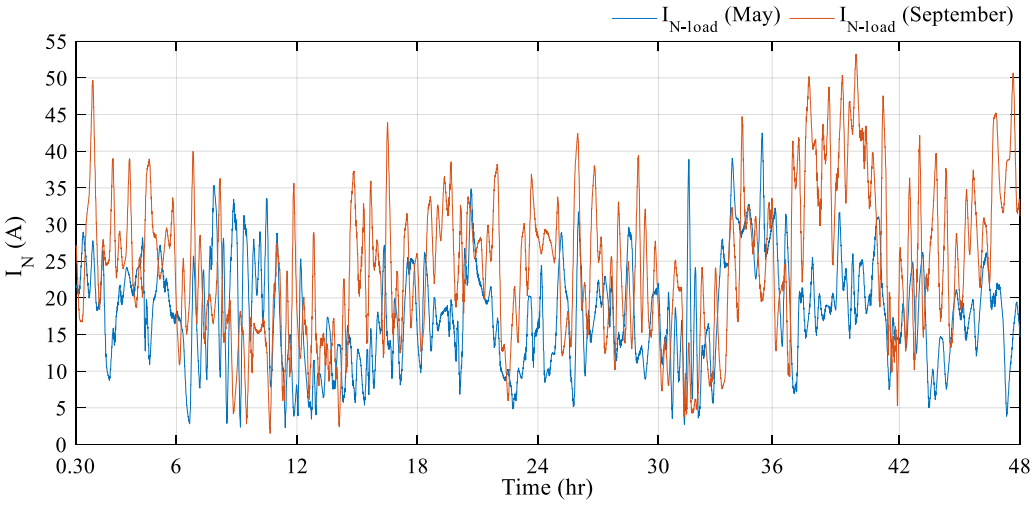

Figure 5.35. Load-generated neutral current at N44 building

Four new case conditions are included in this case analysis: case (k) with no reactive power operation, i.e. the remaining VSI capacity after active power operation is used for neutral compensation alone; case (l) neutral compensation without any fixed $I_{N\text{-limit}}$ capacity, i.e. the neutral controller will only operate if any capacity remains available after active and reactive power operations; case (m) and (m*) with $I_{N\text{-limit}}$ 10 A (p-p) and with the DCD method; and case (n) and (n*) with $I_{N\text{-limit}}$ 20 A (p-p) and with the DCD method, respectively.

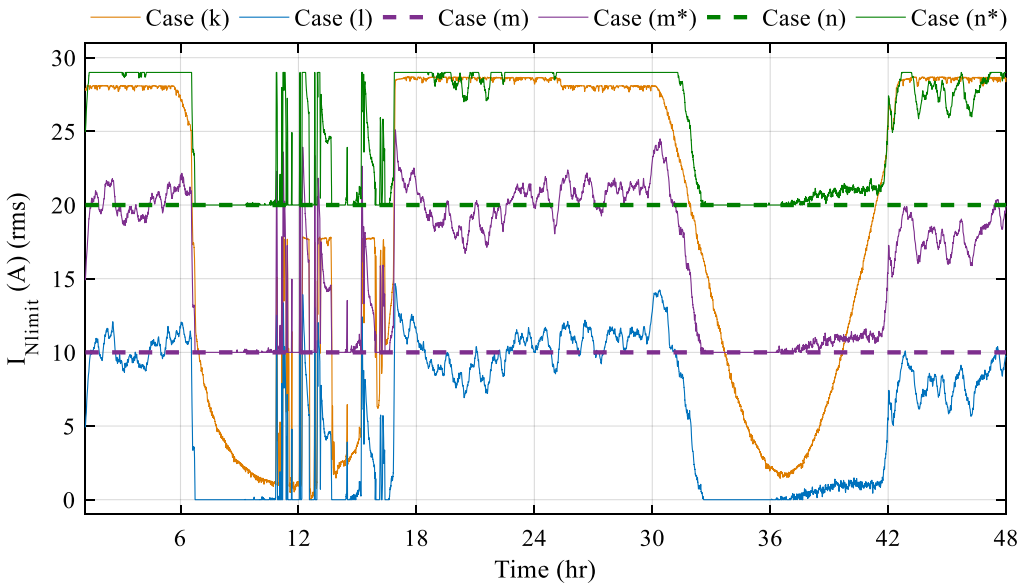

Figure 5.36. Available capacity estimation from the four-leg PV-VSI

The available capacity estimation can be easily understood from Fig. 5.36. As the total capacity of the considered PV-SVSI unit is 29 A, for case (k) full capacity during night time can be utilised for either reactive or neutral compensation. For case (l), as the PCC voltage regulator utilises around 19 A as shown in Fig. 5.34 (c), the remaining capacity of around 10 A is used for neutral compensation with the DCD method. For cases (m) and (n), additional fixed neutral current controller capacity is allocated. Any available SVSI capacity will be added as an extra to the fixed neutral current capacity as shown with cases (m*) and (n*).

A comparison of the compensated neutral current among the different case conditions is shown in Fig. 5.37. One additional case condition is included in Fig. 5.37 as a case (O) where the neutral current controller reference is considered as zero rather than considering the load-generated neutral current. It can be seen from Fig. 5.37 that cases (m), (m*), (n) and (n*) compensate more neutral current (15 A (rms)) during the peak PV generation period especially from 32 – 42 (hr). This is

expected due to the availability of additional fixed-capacity allocation for the neutral compensation controller. Case (k) shows a similar performance to cases (n) and (n*) during night time periods even without any additional capacity allocation specifically for the neutral current controller. Case (l) also compensates around 8 A (rms) of neutral current during the night time which is comparable to case (m).

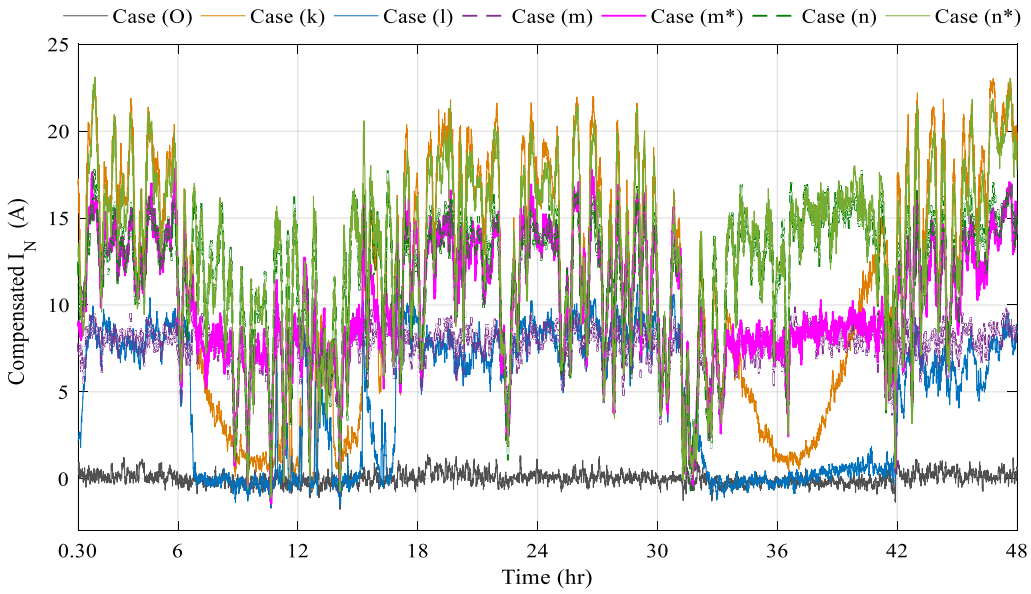

Figure 5.37. Compensated neutral current comparison

It can therefore be concluded from this case study that the PV-VSI with the proposed DCD method not only provides better neutral compensation performance but also gives the customer the flexibility to incorporate their intended auxiliary regulation operations. The variation in load characteristics between commercial and residential loads is easily noticeable, and the designed system with the same configuration can perform robustly to provide high PV power export, dynamic PCC voltage regulation, and higher neutral current compensation.

5.6 Economic Implications of the Four-leg SVSI

The proposed 4L SVSI with the DCD method can be used for large-scale RES integration, PCC voltage regulation, and superior neutral compensation. However, it requires additional cost for one phase leg – 39 US$ (Semikron SKM75GB176D), gate driver – 78 US$ (Semikron SKHI 22B), and sensors- 5-10 US$ (Hall Effect sensors) [137], [140], [141]. To achieve a similar multi-functional performance with the presented load diversities, each test point would require a three-phase smart VSI for renewable energy integration and PCC voltage regulation. Additionally, for neutral compensation, it would require installing either a zig-zag transformer or a four-leg active power filter or community storage which would require a high kWh capacity, for example, 100 kWh for 30 customers [133]. The designed PV-SVSI would not be an economical choice if only individual operations are considered, however, it can certainly be one with multifunctional operations.

5.7 Chapter Summary

The three-phase four-leg PV-SVSI with the proposed dynamic capacity distribution method provides superior neutral compensation to fixed-capacity four-leg PV-SVSI and zig-zag transformers. It is also evident that RES installation and PCC voltage regulation operations can be performed with the PV-SVSI with different load connection types at different network locations. The designed system can maintain proper NGV limits while improving the phase balance of different phase currents at variable R/X ratios. Although the designed 3P-4L PV-SVSI model is applied to an Australian LV network, it could be connected to any 3P-4W LV network. The same control configuration can also be utilised to obtain similar superior multifunctional performance for any kind of commercial load.

The experimental verification of the proposed neutral current compensation along with multifunctional controls from the three-phase three-leg and four-leg inverters are discussed in detail in the next chapter.

Table 5.1 Dominant poles for different R/X ratios of transmission cables

DP	R+/X+	R0/X0	Cables
0	0	0	No cable
1	0.80	0.50	MOON 7/4.75AAC
2	0.92	0.55	WASP-7/.173 AAC
3	1.46	0.75	FLY - 7/.134 AAC
4	2.32	0.95	7/.080 - Cu (7/14)

Table 5.2 No. of customers and connected network locations

Phases	No. of customers			
	P1 (63.7 m) R_+/X_+= 0.92 R_0/X_0 =0.55	P2 (217 m) R_+/X_+=1.52 R_0/X_0 = 0.86	P3 (356 m) R_+/X_+=1.47 R_0/X_0=0.80	P4 (420 m) R_+/X_+=1.50 R_0/X_0 = 0.74
A	2	2	2	3
B	2	3	1	2
C	1	2	2	3

Table 5.3 Specifications of the designed system

PV-SVSI (4-leg)	V_{DC}: 700V, C_{DC}: 3000 μF, Fsw: 3.5 kHz, time step: 5 ms, PI controller gains: $Kp_{1\text{-}VDC}$ = 2, $T_{i1\text{-}VDC}$ = 0.005, $K_{p2\text{-}Vd}$ = 2, $T_{i2\text{-}Vd}$ = 0.5, $K_{p3\text{-}Idq}$= 8, $T_{i3\text{-}Idq}$=0.003, $K_{p4\text{-}0N}$= 15, $T_{i4\text{-}0N}$=0.5, $I_{N\text{-}fix}$ limit ± 10A,
LCL filter	$L_{f(a,b,c,n)}$=4 mH; C_f =10 μF; $L_{g(a,b,c)}$ =1 mH; $r_{(a,b,c,n)}$= 1 mΩ, R_d =3 mΩ,
Nonlinear loads	Phase A (R = 15 Ω , C = 10 μF), Phase B (R = 15 Ω, L = 10 mH), and Phase C (R = 15 Ω);
LV Grid	Upstream 33 kV/ 11 kV (1.5 km), 11 kV/ 420 V (1.8 km), 150 customers, DT rating: 500 KVA, X_L .04 p.u., grounding resistance (3P) R_{GND}: 10 Ω, $R_{DT\text{-}GND}$ = 1 Ω.

Chapter 6

Experimental Setup and Results Analysis with SVSI

6.1 Introduction

This chapter describes the construction procedure of the four-leg inverter, experimental setup steps with the smart voltage source inverter (SVSI) and results from the hardware setup. The platform utilises the switchgear controller unit based on Texas Instruments Delfino F28335 microcontroller unit (MCU) for real-time control application provided by Denkinetic Pty Ltd [142]. The simulation results reported in Chapters 3-5 are collected from the PSCAD/EMTDC software environment. However, for the hardware implementation, a separate code is written in the Code Composer Studio (CCS) v. 6.20 for the MCU real-time control operation of the four-leg inverter. One of the main contributions to the hardware implementation is the Semikron Electronic teaching system being modified to the four-leg inverter by replacing the chopper leg from the three-leg inverter system [143]. The details concerning the hardware modification are described in Section 6.2. Fig. 6.1 depicts the modified block diagram from the simulation studies, and the corresponding experimental setup is shown in Fig. 6.2. A summary list of the components used for the experimental setup is provided in Table 6.1.

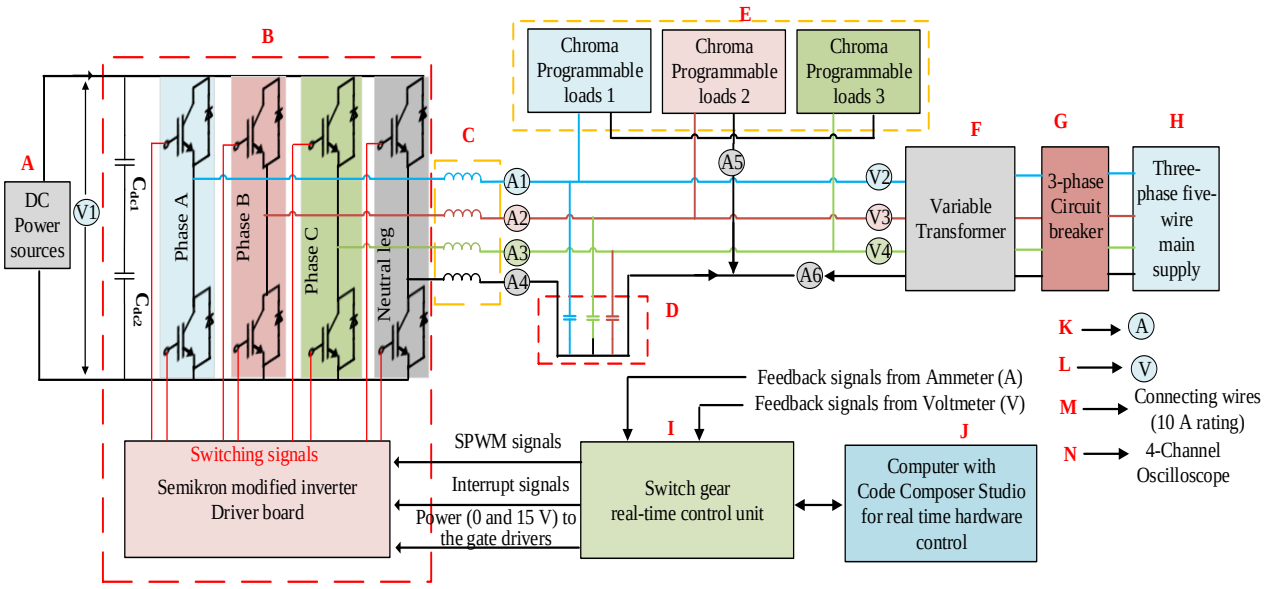

Figure 6.1. Control block diagram of the experimental platform configuration

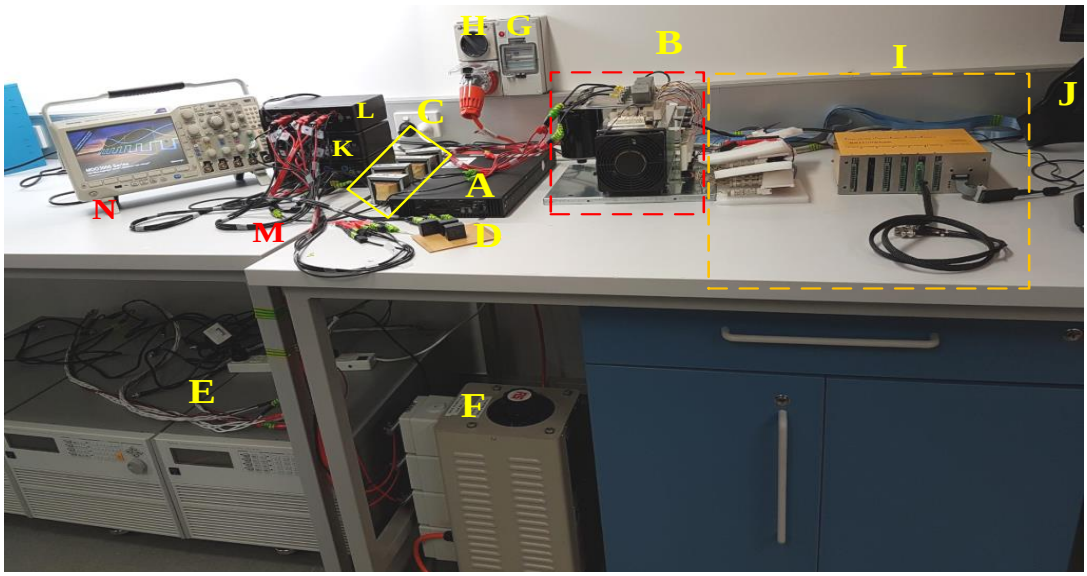

Figure 6.2. Experimental setup at the high-voltage lab in Macquarie University

Table 6.1 Components list for the experimental setup

Hardware caption	Component name	Specifications
A	DC voltage source	0-300 V, 2.8 A, 850 W
B	Semikron modified inverter	750 V_{DC}, 400 V_{AC}, 30 A, 50 Hz
C	Power inductors (inverter side)	2.5 mH, 10 A, 0.044 ohm, ± 15%
D	Filter capacitors	Film capacitor, 10 µF, 500 V_{DC}
E	Single-phase electronic loads	3.6 kW, 36 A, 350 V_{AC}
F	3-phase variable transformer	8.14 kVA, 415 V, 10 A/phase
G	Three-phase circuit breaker	40 A, and residual current of 30 mA
H	Three-phase five pin out sockets	500 V_{AC}, 20 A
I	Switchgear controller unit	Texas Instruments Delfino F28335 Control Card
J	Operating desktop computer with Code Composer Studio running	Core i7 – 3.2 GHz, 8 GB DDR3 Ram
K	Ammeter (AC) sensor board	± 30 A
L	Voltmeter sensor board	+ 1000 V
M	Connecting wires Banana-Banana and Banana–Alligator clips	± 10 A
N	Four-channel Oscilloscope	Tektronix, MDO3104 1 GHz, 4-Ch Mixed Domain

6.2 Experimental Hardware Description

6.2.1 DC power supply (A)

A programmable DC power supply is utilised to provide 0-300 V and 2.8 A DC current to the DC bus as shown in Figs. 6.1 and 6.2. A DC power supply from Sorensen XG series having 850 W maximum DC power rating is utilised in this experimental study [144]. The power supply provides DC power with soft switching technology, high power density, comprehensive digital and analogue interface options, multi-unit design, and high reliability. Fig. 6.3 shows the user access panel of the DC power supply.

Figure 6.3. DC power supply (850 W)

6.2.2 Four-leg inverter (B)

The Semikron Semiteach power electronic teaching system (SPETS) is modified in the high-voltage lab at Macquarie University to make it work as a four-leg inverter. The default Semiteach package consists of a three-phase rectifier module, three IGBT half-bridge modules that function as a three-leg inverter and one IGBT chopper module working as a DC-to-DC converter. Two DC link capacitors are connected in series to maintain a stable DC bus voltage, and two bleed resistors are installed in parallel with the DC-link capacitors to discharge the stored energy when the inverter is turned off. Snubber capacitors are also connected with the IGBT modules to reduce the parasitic inductance caused by a continuous switching operation of IGBT switches. Fig. 6.4 shows the default package of the Semiteach system while details for the Semiteach inverter are shown in Table 6.2.

Table 6.2 Semiteach power electronic teaching system

Model	Semiteach B6U+E1CIF+B6CI
DC voltage	600 V_{DC}
AC voltage and current output	400 Vac, 30 A
IGBT modules	SKM 50 GB 123 D (50 A, 1200 V)
IGBT driver board	SKHI 22 A-R

DC link capacitor	Two 2200 µF in series
Bleed resistors	22 kΩ
Snubber capacitor	0.22 µF
Power supply	+ 15 V

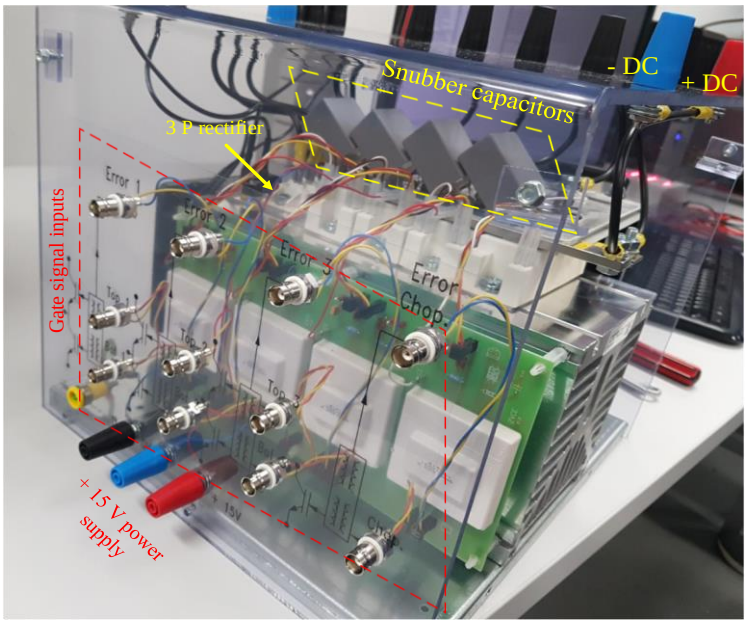

Figure 6.4. Semiteach power electronic teaching system (before modification)

The chopper module from the Semiteach system is removed from the default package as shown in Figs. 6.5 (a) and (b). An additional IGBT half-bridge module is installed at the location of the removed chopper module while keeping other component connections the same as the default configuration as shown in Figs. 6.6 (a) and (b). Although the additional IGBT module (SKM 75GB176D) has a different power rating (1200 V, 70 A) than the existing IGBT half-bridge modules (SKM 50GB123D), the overall four-leg construction works without any issues because of the similar synchronous switching characteristics of the half-bridge modules. As the IGBT driver board in the Semiteach system already has four SKHI-22 A-R drivers installed, with the addition of the fourth leg only a few additional components, such as R_{ON}, R_{OFF}, R_{CE} and $C_{CE,}$ are installed to operate the installed half-bridge module independently. The driver board assembly with the additional component installation area (rectangle marked) is shown in Fig. 6.7. The control input signals for the top switches are received via the BNC connectors and are denoted as $T_{1\text{-}4}$, for the bottom switches as $B_{1\text{-}4}$ and for the error signals as $E_{1\text{-}4.}$ The additional passive components for the fourth leg switching controls are installed in the 'N' driver board following a similar construction to the 'A', 'B', and 'C' driver boards and the component values are shown in Table 6.3. The detailed connection block diagram of the fourth leg IGBT module and the SKHI driver board is shown in Figs. 6.8 (a) and (b). The hardware-implemented diagram of the four-leg inverter is indicated in Fig. 6.9.

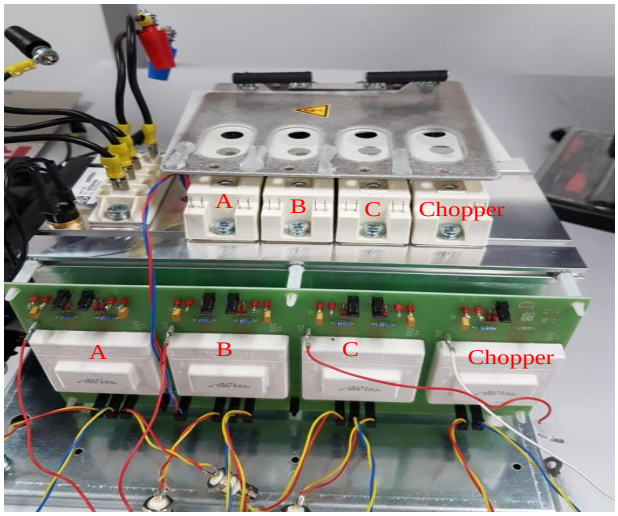

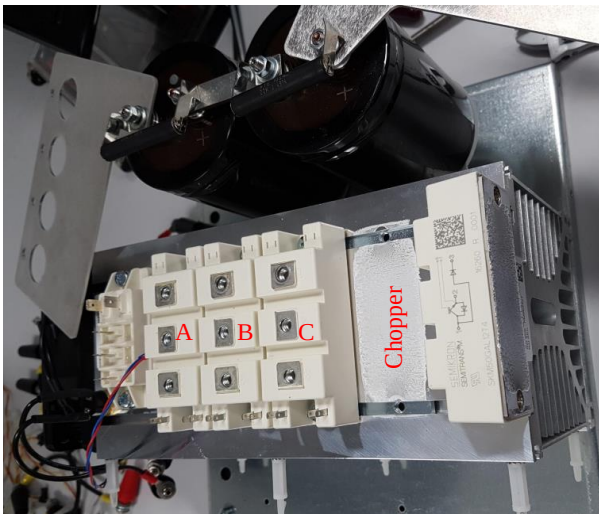

(a) (b)

Figure 6.5. SPETS with (a) default package, and (b) chopper removed

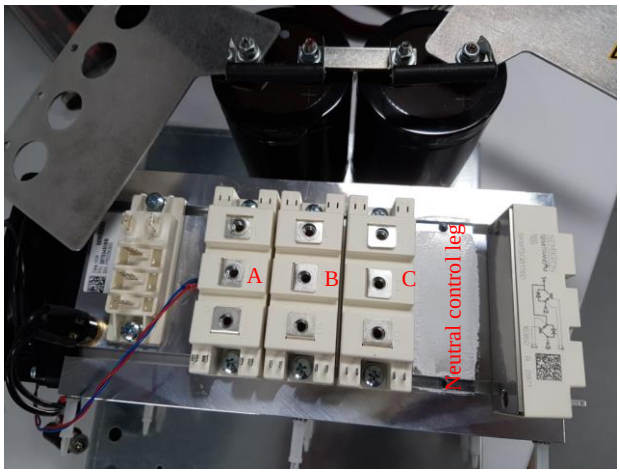

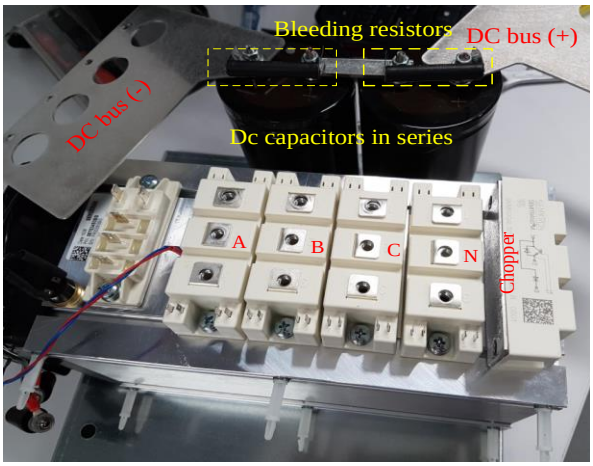

(a) (b)

Figure 6.6. SPETS with (a) additional IGBT module, and (b) four-leg configuration

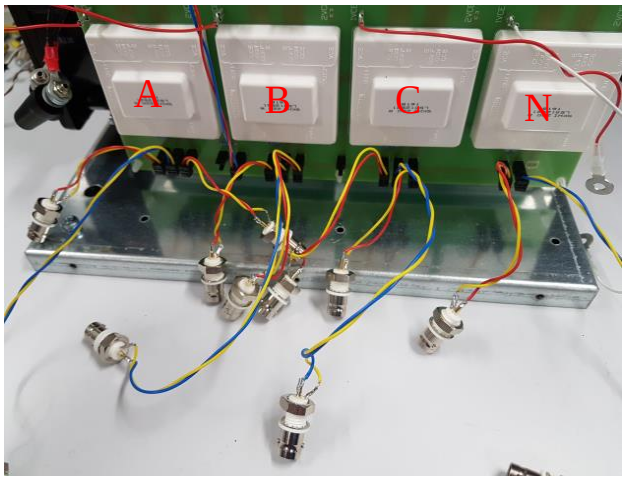

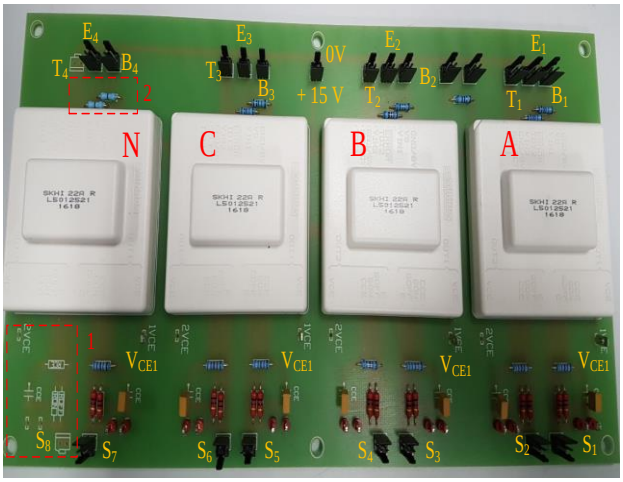

(a) (b)

Figure 6.7. IGBT module driver board with (a) BNC inputs, and (b) four-leg modification

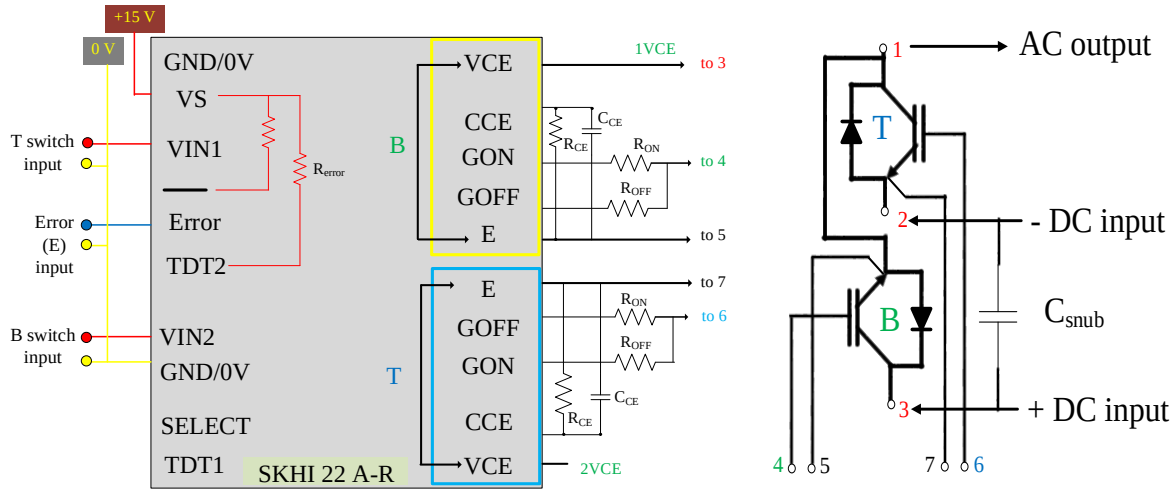

(a) (b)

Figure 6.8. Fourth leg connection with (a) SKHI 22 A-R driver board, and (b) IGBT module pin

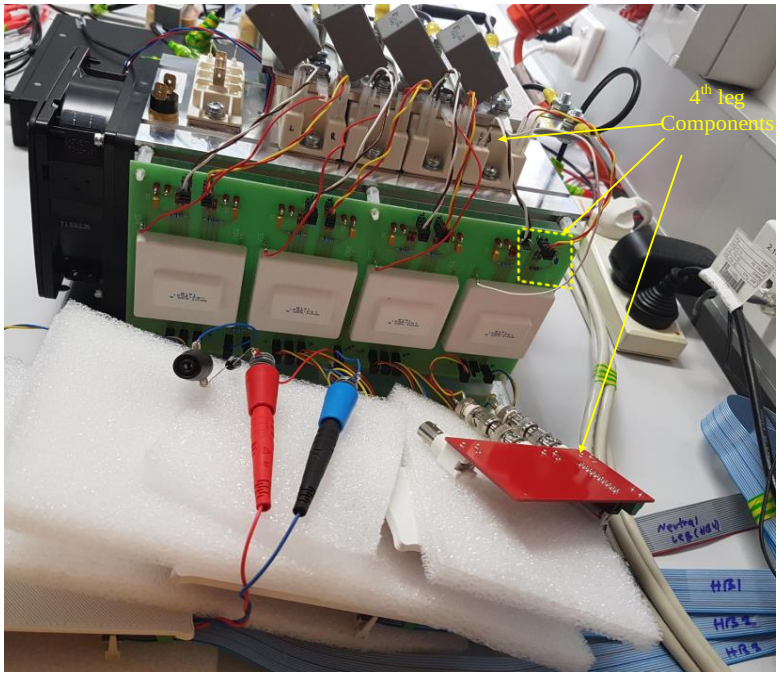

Figure 6.9. Four-leg inverter modified at Macquarie University

Table 6.3 Components list of inverter driver board for IGBT switch

Fourth leg components	
IGBT module	SKM 75GB176D, 1200 V, 70 A
R_{ON}	20 Ω
R_{OFF}	20 Ω
R_{CE}	12.1 kΩ
C_{CE}	680 pF
R_{error}	10 kΩ
Power supply	+ 15 V

6.2.3 Filter, sensor boards and connecting wires (C, D, L, M, N)

The modified four-leg inverter is connected to the grid via an LC filter and different hall-effect sensor circuits, such as current and voltage sensors. Theoretically, the inverter can be considered as a voltage source, therefore, connecting directly to the grid, which is another voltage source, will cause severe damage to the hardware components unless an interim energy-dissipating passive component, such as an inductor, is connected between them. This is considered as the L filter configuration, however, it does not provide better harmonic attenuation performance. For this reason a third-order LCL filter combination is generally utilised. The LC filter combination, which is a second-order filter, is utilised in this experimental setup as shown in Fig. 6.9 (a). In future, the LCL filter combination will be utilised and the details regarding the filter parameter values are documented in Table 6.5.

Two types of current sensors are used in this experiment: (i) Hioki on-leak current sensor clamps as shown in Fig. 6.9 (a); and (ii) current sensor modules (one quad-current sensor module and one double-sensor module) designed by Denkinetic Pty Ltd as shown in Fig. 6.9 (b). The current sensors from Denkinetic Pty Ltd are mainly utilised to sense the actual signal from the experimental setup, and transferred to the host MCU to generate the gating signals for the four-leg inverter control operations. The current clamp sensors are mainly utilised to monitor the three-phase currents from the grid-side supply via the four-channel oscilloscope as shown in Fig. 6.10 (a).

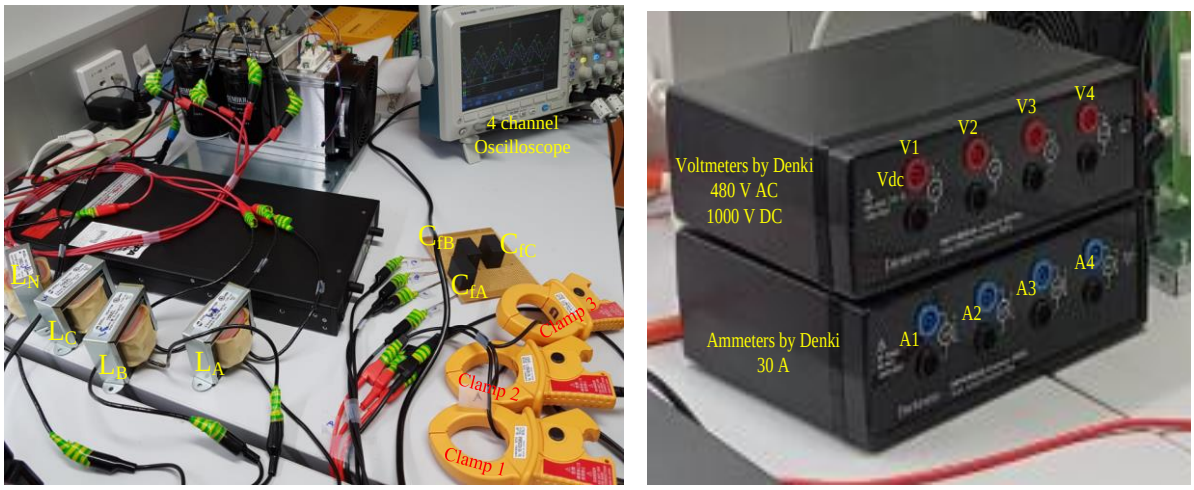

(a) (b)

Figure 6.10. (a) Filter circuit and current clamps, and (b) voltage and current sensors by Denkinetic

Four voltage sensors are also used in this experimental setup as Figs. 6.1 and 6.10 show. The voltage sensor board is provided by Denkinetic Pty Ltd as well and the modules are depicted in Fig. 6.10 (b). The current and voltage sensor modules are directly connected with the switchgear controller unit, and the host MCU receives the actual sensed signal via a serial peripheral interface (SPI). The specification of the additional components is shown in Table 6.4.

Table 6.4 Additional components list for the experimental setup

Components	Specifications	Quantity
Inverter side inductors (L_{1-4})	Surface-mount power inductor, HAMMOND 159ZL, 2.5 mH, 10 A, 0.044 ohm, ± 15% tolerance both inductance & resistance	4
Filter capacitor (C_{fa-c})	Metallised Polypropylene Film Capacitor, 10 µF, 500 V_{DC}	3
Current sensor modules by Denkinetic	Closed-loop Hall-effect current sensors, ±50 A_{pk}, 30 A_{rms}, frequency response DC to 200 kHz, gain accuracy 0.9%	6
Current clamps by Hioki	Model 9675 clamp on-leak sensor, 10 A (AC)	3
Voltage sensor module by Denkinetic	± 1000 V_{DC}, ± 400 Vac, frequency response DC to 20 kHz, gain accuracy 0.4%, high-impedance floating inputs, internally shielded to reduce noise	4
Four-channel Oscilloscope	Tektronix MDO3104, 1GHz, 4-channel, Mixed-domain oscilloscope	1

6.2.4 Programmable single-phase AC loads (E)

Three single-phase programmable AC loads are utilised in this experimental setup to generate unbalance at the point of common coupling (PCC). The Chroma programmable loads (63803) can be connected to both AC and DC systems, and can also be configured to run in different load configurations, such as constant-current, constant-impedance, constant-power etc. Each load is connected directly to the point of common coupling (PCC), and the neutral terminals from the loads are configured in wye connection to obtain a single neutral return connection as indicated in Fig. 6.11. The load neutral connection is passed via the 5^{th} current sensor as shown in Fig. 6.1, and utilised to generate the reference signal for the neutral current controller. The load connections are evident in Fig. 6.11, and it can be seen that the programmable loads include five user access sections as denoted in the figure. The function description of each user access section is shown in Table 6.5. Different AC load configurations are utilised in this experimental work as discussed in Section 6.4. The Chroma programmable load requires two types of supply: (i) AC single-phase connection (load power plugs), and (ii) external AC or DC source connection via the load connection terminals (red and black) which is used to make the load active at the PCC. The desired load type, load demand current, and maximum allowable current need to be set manually before turning the load on.

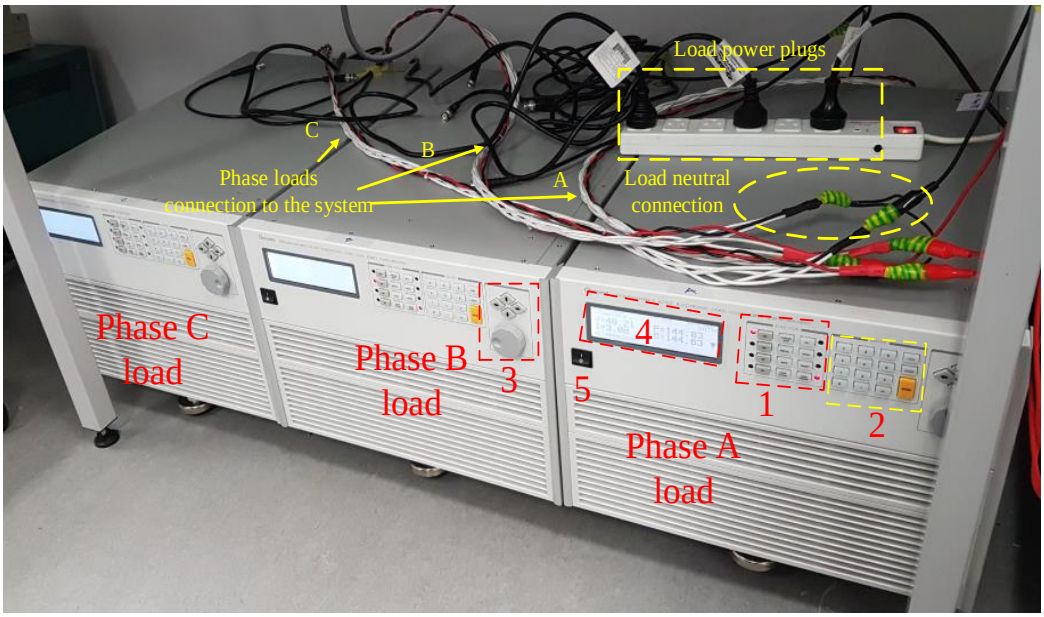

Figure 6.11. Three single-phase Chroma electronic load connections at the PCC

Table 6.5 Chroma 63803 programmable AC and DC load functions

Load sections	Function
1	Load type selection. There are six configurations available: (i) Constant-current (CC) (ii) Constant-impedance (CZ) (iii) Constant-power (CP) (iv) Constant-voltage (CV) (v) RLC nonlinear load (vi) Programmable load function which requires external connection to a host computer This section also includes the load type (AC or DC) and load on/off button.
2	Number pad for load value selection
3	Fine tuning knob and cursor pad. The cursor pad helps to move the load selection pointer to configure different settings.
4	Display panel shows V, P, I, pf, Q, S, THD etc. The top display lines of this unit give access to the users to set load current consumption and maximum current values.
5	Programmable load on/off switch
Load power plugs	AC power supply to the electronic load

6.2.5 *Variable transformer (AC source) (F)*

The variable AC transformer is utilised as the AC grid system for the experimental work. For electrical safety reasons, the developed four-leg system is connected with the lower AC voltage (< 100 V_{AC}/ phase) side from the variac outputs. The output connections of the variable transformer are shown in Fig. 6.12.

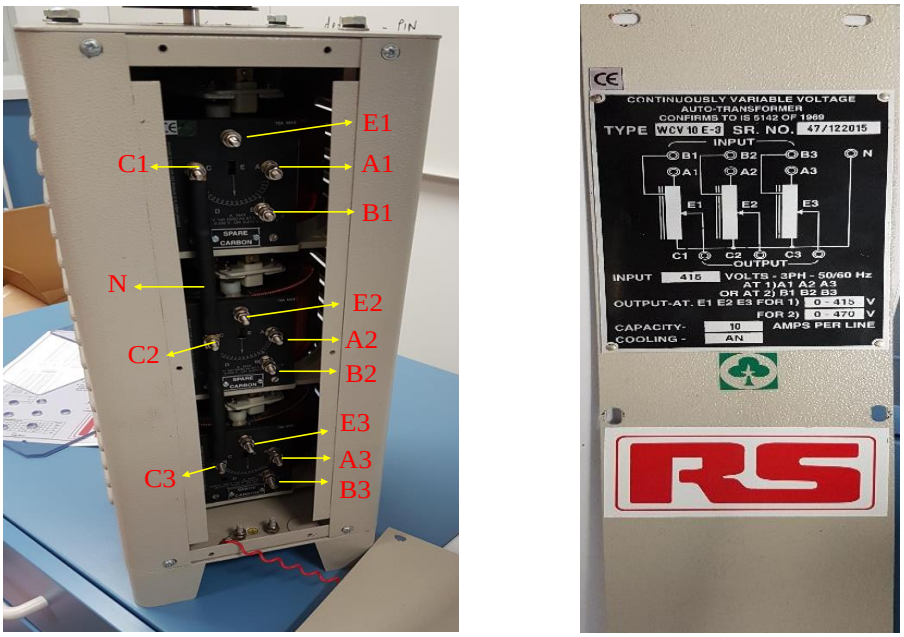

(a) (b)

Figure 6.12. Variable transformer by RS: (a) output terminals, and (b) output configuration

The input of the transformer can be connected to the terminals from $B_{1\text{-}3}$ or $A_{1\text{-}3}$. Depending on the input connection terminals, the output voltage can be varied from 0-470 V and 0 to-415 V as shown in Fig. 6.12 (b). The output terminals ($E_{1\text{-}3}$) are directly connected to the external rotating knob of the variac. The output voltage can be changed based on the knob position which is labeled as percentage of the main input voltage. The three-phase terminals are connected in wye configuration ($C_{1\text{-}3}$) in the variac, and the neutral point (N) is collected from the wye common point to create the fourth wire required for the single-phase load connections. The maximum power rating of the RS transformer is 8.4 kVA and each output phase line can have a maximum 10 A current output.

6.2.6 *Three-phase circuit breaker and grid supply pinouts (G and H)*

The main grid supply is connected to the inputs of the variable transformer via a three-phase four-pole residual current circuit breaker (RCCB) from Hager as shown in Fig. 6.2. The RCCB has a maximum 40 A current rating with a residual current rating of 30 mA as depicted in Fig. 6.13. The main grid supply is accessed via the five-round-pin socket from Clipsal as also shown in Fig. 6.13. The five-pin connection provides three-phase lines, one neutral line and one earth return line. The

maximum voltage and current rating of the pin outlet of the main grid are 500 V and 20 A at 50 Hz. Both components are IP 66 certified and the CB has a high thermal protection scheme to provide electrical hazard security in the lab.

Figure 6.13. RCCB and main grid supply-pin outlet connections

6.2.7 Switchgear controller unit

The switchgear controller unit is built up with interface modules suitable for power converter applications. Unlike some other controller units, the switchgear module used in this experiment does not require any external signal conditioning circuit. The input signals to the IGBT modules from the Semiteach inverter is ± 15 V logic, and the input/output to/from the DSpace type controller is ± 10 V. Therefore, an additional signal conditioning circuit is required as the interfacing unit between the DSpace and the Semiteach systems. In addition, the gate drivers and different sensor board circuits, such as hall-effect current and voltage meters, require multiple DC power supplies with different ratings. Additionally, the output from the different sensor circuits, such as LV 25-P and LA 55–P, need to be designed and scaled properly to ensure the controller unit can utilise the feedback signals for real-time controller application. With the switchgear controller unit designed and developed by Denkinetic Pty Ltd, no additional signal conditioning stage is required, and also the controller unit can supply power to the gate drivers and sensor circuits via a single 24 V DC supply input to the controller unit. The voltmeter and ammeter modules also provide a better noise cancelling operation due to an additional shielding layer between the primary and secondary sides of the sensor circuits. They also have multiple scaling options to utilise the feedback signals. The base structure of the switchgear controller unit is shown in Fig. 6.14. The base module of the controller unit has twelve module input slots, a host microcontroller control-card slot, a 14-pin joint test action group (JTAG) pin out and a single 24 V DC power supply connection.

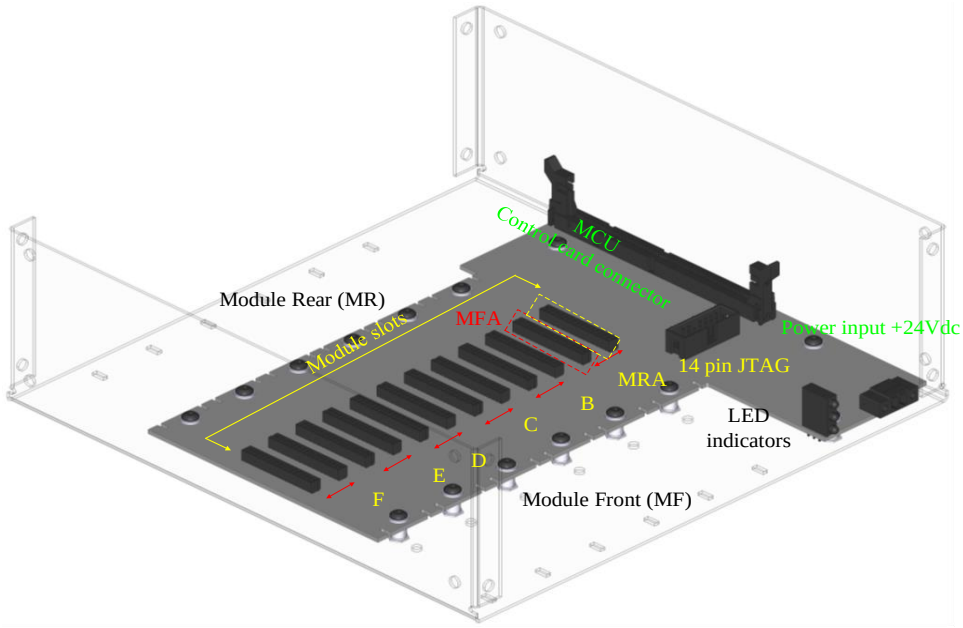

Figure 6.14. Switchgear base unit CAD diagram collected from Denkinetic manuals

The embedded microcontroller unit (MCU) has a 100-pin dual-in-line memory module (DIMM) slot to accept control cards from Texas Instrument (TI) that can provide 47 digital I/O and up to 16 analogue input signals. Different MCUs, such as Piccolo^{TM}, Delfino^{TM,} and Concerto^{TM}, can be utilised with the controller unit. The Delfino^{TM} MCU is utilised in this research project. Details of the host MCU are provided in Table 6.6.

Table 6.6 Host MCU specifications

Host real-time MCU	
Connector	DIMM 100-pin
Pin out	Texas Instruments Control CARD 100-pin
MCU module	CC100_F28335, 32-bit CPU, up to 150 MHz, up to 18 PWM outputs, 12-bit 16 ADC channels etc.
Description	Texas Instruments Delfino F28335 Control Card
Field bus	CAN, RS-485, RS-232

The TI code composer studio IDE V.6.2 is used to execute the coding for the MCU real-time control operation. The Simulink embedded code generator can also be used to generate the code to work with the switchgear controller unit. The 100-pin outlet of the host MCU slot is shown in Fig. A.1 in the Appendix. The connection layout of the switchgear controller unit with the host computer is revealed in Fig. 6.15. Details of each hardware interface module are also shown in Table 6.7.

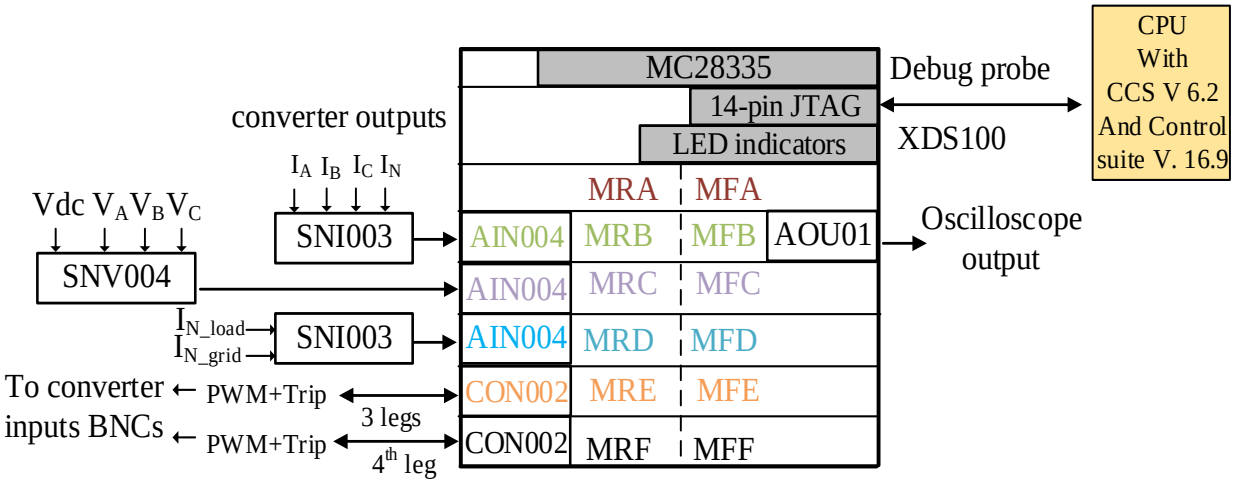

Figure 6.15. Configuration block diagram of real-time switchgear controller

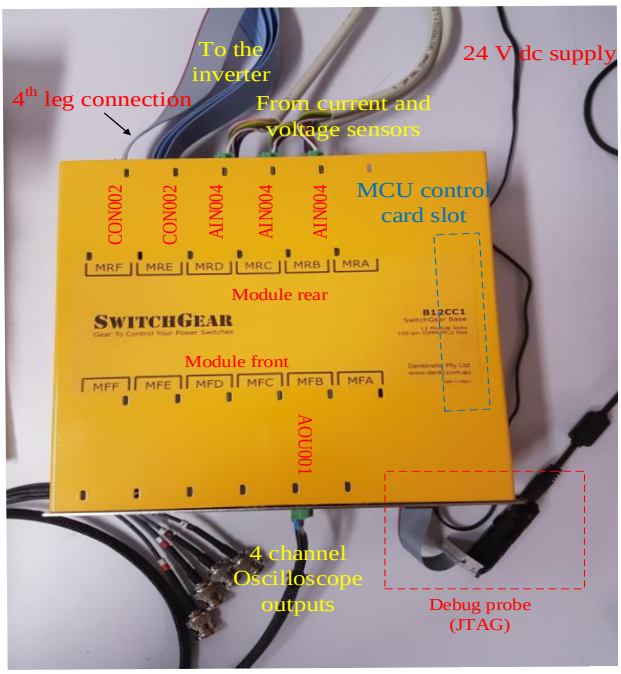

Figure 6.16. Switchgear controller connection from the experimental setup

As shown in Fig. 6.15, two current sensor modules (SNI003) and one voltage sensor module (SNV004) are used to feedback the real-time sensed signals from the experimental setup to the host MCU controller via the modular rear ports (MRB-D). The converter control codes are debugged via the TI CCS software environment and the control commands for the inverter switching modules are interacted in real-time via the debug probe to the host MCU (28335). The switching signals (PWM and trip signals) for the three-leg inverter IGBT modules are sent via the hardware interface module CON002 connected in MRE slot and for the fourth leg in the MRF slot. The fourth leg is designed as an independent half-bridge switching module; therefore it is possible to control the modified converter system for both 3- and 4-leg configurations. A separate half-bridge control command is initiated in the controller code and this enables and disables the fourth leg half-bridge in real-time application. The

connections of the switchgear controller unit with the modular interfaces units and external devices are shown in Fig. 6.16.

Although the fourth leg half-bridge module can be controlled to operate as single-phase active power factor (APF), it is not considered in this experimental setup, however, it is possible to operate all four IGBT switching modules as a single half-bridge configuration with individual PWM and interrupt signals. The PWM signals for the fourth leg are synchronised to follow the three-leg PWM configuration, i.e. a single carrier-frequency signal (triangular wave) is used to generate the switching signals for all eight switches. This way the four IGBT modules can function as an aggregated four-leg configuration, which ensures that no unintentional dead time delay occurs in the fourth leg operation. Any control variables from the designed four-leg current controller can be observed in real-time via the AOU01 module outputs connected in the MFB slot to the external oscilloscope (max. 4 outputs at a time). This helps to observe the reference-following operation and corresponding transient effects in the output currents from the current controllers.

Table 6.7 Hardware interface module descriptions for the switchgear controller unit [142]

	Hardware interface Modules		
	AIN004	CON002	AOU01
Description	4-channel analogue input for sensors with current output	3-phase half-bridge interface	4-channel analogue output Isolated industrial signalling
Typical usage	Closed-loop Hall-effect current sensors. Voltage sensors	Connect to half-bridge gate drivers from power integrations using ribbon cable	Real-time output of internal control variables via oscilloscope
System Connector	12-way pluggable screw terminal	Three 10×2 pin headers	12-way pluggable screw terminal
MCU peripherals & signals	ADC, TripZone/GPIO	PWM, TripZone	DAC
Digital inputs and outputs		3× trip inputs 6× gate outputs	
Analogue inputs and outputs	±20 to ± 200 mA in 12 ranges inputs only		Voltage output ranges include ±10 V, 0 to 10 V, ±5 V, 0 to 5 V Current output ranges include 4 to 20 mA, ±20 mA
Supply output	± 12 V_{DC}	+15 V_{DC}	

6.3 Technical Explanations of the Experimental Setup

A three-phase five-round-pin outlet is used to connect the designed inverter system to the main grid via a variac and a circuit breaker. Additional care has been taken during the experiment to make sure that the neutral compensation with the four-leg inverter does not cause any unnecessary tripping while performing active and reactive current control operations. The filter inductor used in this experiment is not the optimal one and therefore, cannot provide a better quality output current. However, the total harmonic distortion is monitored from the output current and is ensured to be less than 5% while supplying current to the loads, following the IEEE-1547 standard. The switching frequency (F_{sw}) is chosen as 5 kHz and varied to 9 kHz during the experiment with different load combinations in order to evaluate the effects of a different switching frequency on the performance of the system. The LC filter combination is used in this experiment and the resonance frequency (F_{res}) is calculated as 1.03 kHz which satisfies the filter design condition, i.e. $10\times F_{grid}$ (grid frequency) < F_{res} <0.5 F_{sw}. A double-rate pulse width modulation (PWM) technique, which compares a triangular carrier-frequency signal with the demanded modulating signals for both positive and negative half-cycles, is utilised so that the current controllers perform better. The experimental outputs are collected from a Tektronix four-channel oscilloscope with 100 k sample rate (samples per second), and the current clamp meters (10 A) from Hioki are utilised to monitor the grid-side and load-side phase currents. Special attention is given to the scale matching between the sensor circuits and outputs collected from the oscilloscope. The detailed specifications of the experimental analysis are given in Table 6.8.

Table 6.8 Detailed specifications of the experimental setup

Parameter name	Parameter value
DC voltage	110–170 V
AC voltage	30-50 V
DC current	2.8 A max.
Reactive current	± 3 A max.
Neutral current	± 3 A max.
Switching frequency	5 – 9 kHz
Time steps	1 ms
Inductor	2.4 mH
Capacitor	10 µF
DC capacitor	1100 µF
Bleed resistors	22 kΩ
Chroma single-phase load	5 A (AC) max.

6.4 Experimental Results and Discussion

The four-leg inverter system is built, modifying the Semiteach electronic teaching module as discussed in the previous section. An additional fourth leg is connected as a half-bridge module and is controlled independently. As the microcontroller unit can support up to 18 PWM outputs, an additional half-bridge control code is included with the three-leg controller code. The PWM signals are properly synchronised between the three- and four-leg inverter configurations. A control command is developed to provide flexibility of turning on/off the neutral half-bridge while keeping the three-leg inverter operation active. This way, the experiment with three-leg and four-leg inverter configurations are evaluated with different load conditions. The reference input to the neutral current controller can be received either from user defined constant values or from the load-generated neutral current. The current controller (PI) gain values are given in Table 6.9 at the end of this chapter. The performance of the proposed neutral compensation method is compared with the existing method, utilising the control flexibility of selecting different reference values while the system is active. Different single-phase loads are utilised, such as constant-current (CC), constant-impedance (CZ) and constant-power (CP). Intentional unbalance is created in the system by setting uneven load demand in programmable loads. With unequal load distribution the neutral current as high as the load demand current is monitored. Even with equal load distribution, comparatively high neutral current and phase unbalance (mainly magnitude) is observed with the different single-phase loads. With the proposed neutral compensation method from the four-leg inverter, better neutral performance and phase balancing is achieved while implementing the active and reactive current control operations. The current supplied from the inverter to the grid is considered as positive current quantity and Kirchhoff's current law is applied at the PCC neutral connection to demonstrate the neutral generation and mitigation operation.

6.4.1 Grid synchronisation with phase locked loop (PLL)

The most important step in the experiment with the synchronous reference frame (SRF) current and voltage controllers is to make sure; firstly, the signals are properly synchronised; and secondly, the PLL angle is locked with the grid voltage. To ensure safe operation, a condition is set in the controller code to ensure that the PLL angle will only lock to the grid voltage if the V_{rms} is higher than 10 V. The PLL angle with the grid voltages is shown in Fig. 6.17. Utilising the PLL angle, the feedback current and voltage components are transformed to a synchronous reference frame (*abc-dq0*) that are utilised in the decoupled current controllers. The SRF transformed V_d and V_q components of the grid voltage ($V_{a,b,c}$) are shown in Fig. 6.17 (b). The grid voltage is set to 50 V_{rms} (L-N) and the synchronising operation by the PLL forces V_q to follow 0 V and V_d to follow 70.7 V ($50\times\sqrt{2}$) as shown in Fig. 6.17

(b). These quantities are used as an external noise input in the decoupled current controller as demonstrated in the simulation studies in Chapters 3-5.

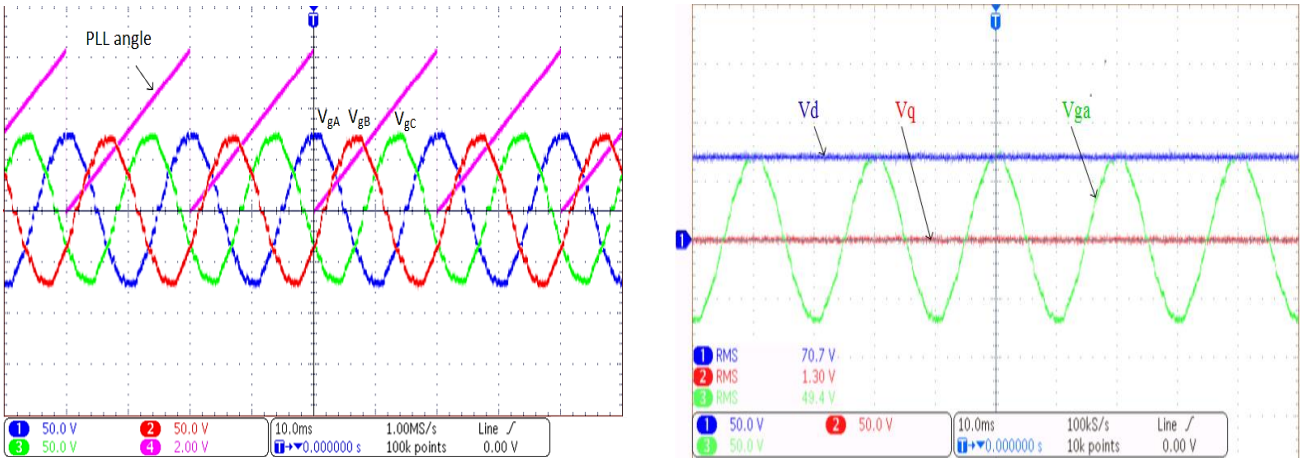

(a) (b)

Figure 6.17. (a) PLL operation with grid voltage, and (b) SRF transformed voltage quantities

It is evident from the results from Fig. 6.17 that the SRF PLL is properly locked with the grid voltage, and the V_d and V_q components show the expected results from the initial analysis. The same SRF PLL angle is utilised to transform the inverter phase currents from the natural *abc* frame to the SRF frame (*dq0*) for independent current control operations.

6.4.2 Active and reactive current control operations

This case study presents active and reactive current control operations from the three-leg (3L) VSI. Initially, no load is connected to the PCC and the active current is changed manually to delivered the desired current to the grid. The DC power source used in this experiment can supply a maximum 2.8 A DC current. The supply of the DC current is controlled by changing I_{dref} manually from 0 to + 2.8 A. The decoupled current controller (DCC) ensures a robust reference-following operation from the developed system. The reference-following operation from the active (I_d) current controller is shown in Fig. 6.18, where the reference is manually changed from +2 A to 0 A while keeping I_{qref} to 0A. The step-changing operation is shown with the help of the triggering function from the oscilloscope. The trigger point is set at 400 mA for both rising- and falling-edge changing of the I_{dref} value.

An unity power factor (pf) relation is evident from the grid voltage and the inverter output current (phase A). The inverter generates an output current in the same phase as the grid voltage (I_{qref} is 0 A) and the magnitude of the generated current depends on the value of I_{dref}. With I_{dref} equal to + 2 A, the inverter generates output current ($I_{Inv\text{-}a}$) with 4 A (p-p). When the reference is changed to 0 A, $I_{Inv\text{-}a}$ instantly follows the zero reference as can be seen from Fig. 6.18. The output current with the 0 A reference is the current required by the DC link capacitor to keep the DC voltage stable at around 150

V. It is demonstrated in the simulation studies that the designed PV-VSI operates both in PV active and inactive conditions. Therefore, the manual reference-following result from this case study verifies that the designed real inverter system can operate even with 0 A active current reference, which resembles the PV inactive operation mode.

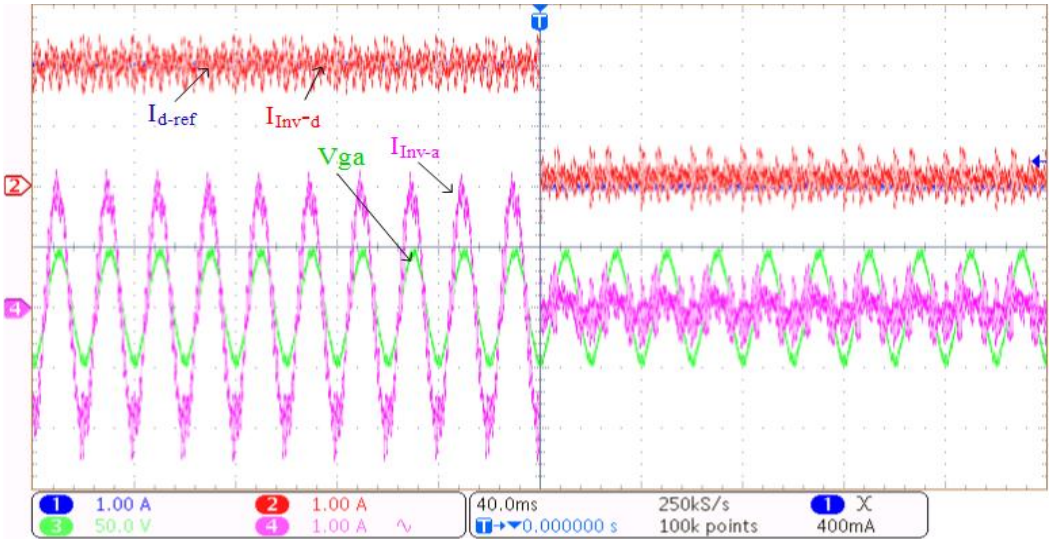

Figure 6.18. I_{dref} control operation from +2 A to 0 A

The unity pf operation of the designed controller is shown in Fig. 6.19 (a) where the reactive current component, $I_{Inv\text{-}q}$ is controlled to 0 A and I_{dref} to 1 A. The Iq_{ref} is manually changed to + 1 A (inductive mode) and -1 A (capacitive mode) to show the phase lagging and leading operation of the inverter-generated current with the grid voltage (phase A) as shown in Figs. 6.19 (b) and (c). It is evident from these figures that the phase angle of the inverter-generated current can be independently controlled while keeping its magnitude close to ± 1A. This verifies the decoupled control operation of the designed three-leg inverter. In Fig. 6.19 (d), the step-change operation is shown for I_{qref} from +1 A to – 1 A, and robust phase changing can be monitored from the inverter output current.

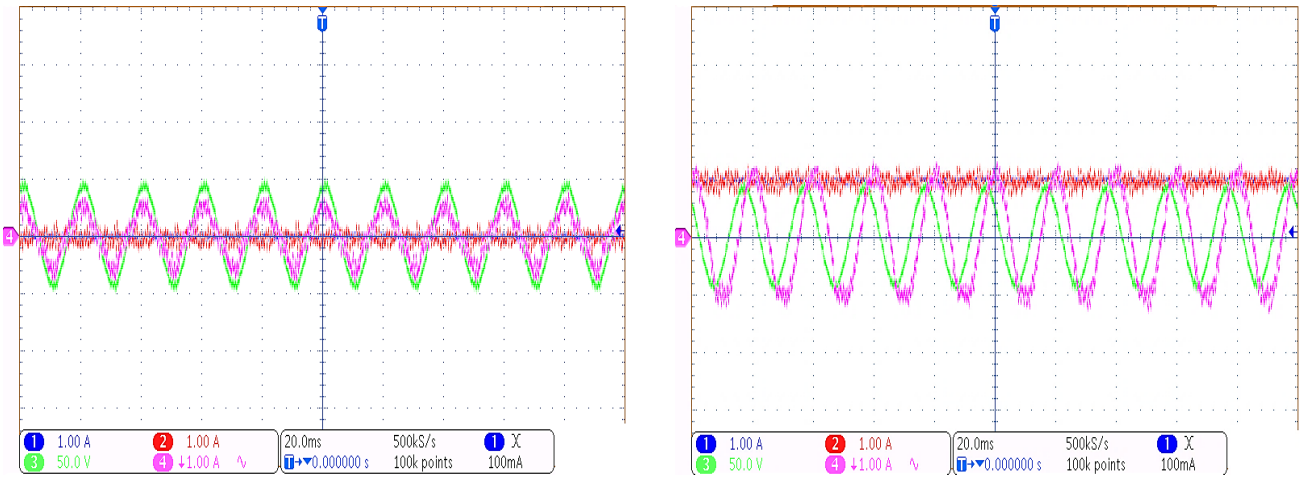

(a) (b)

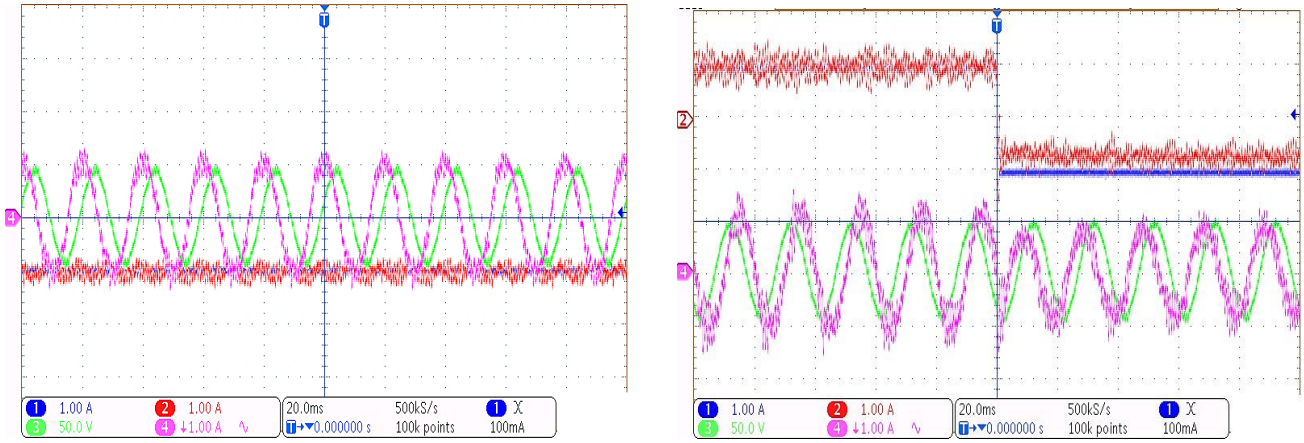

(c) (d)

Figure 6.19. I_q current control with (a) unity pf, (b) lagging pf, (c) leading pf, and (d) step-change

The '+' reference in the I_q current control commands the inverter to operate in inductive current control mode which can be used to regulate the PCC voltage in voltage-rise conditions. Conversely, the '-' reference commands the inverter to operate in capacitive current control mode which can be used to improve the PCC voltage during voltage-sag cases.

A step-changing operation for the I_d and I_q components of the inverter-generated currents are shown in Figs. 6.20 (a) and (b). The load-generated neutral current is also shown with the inverter-generated output currents. From Figs. 6.20 (b) and (d), it is evident that the three-phase current injection to the grid does not degrade the load-side neutral current. The I_{dref} and I_{qref} are manually changed from 0 to + 2 A and 0 to – 1 A respectively, and during this operation, the opposite components reference is set to 0 A, i.e. I_{qref} is 0 A in Fig. 6.20 (a) and I_{dref} is 0 A as shown in Fig. 6.20 (b). Three-phase current outputs, before and after the initiation of the current controller reference changing commands, are illustrated in Figs. 6.21 (a) and (b). The inverter-generated output currents show proper phase alignment, and it is shown in the next case studies that, with the 4L-VSI, the load-generated neutral current can be robustly compensated while generating the desired output currents from the inverter.

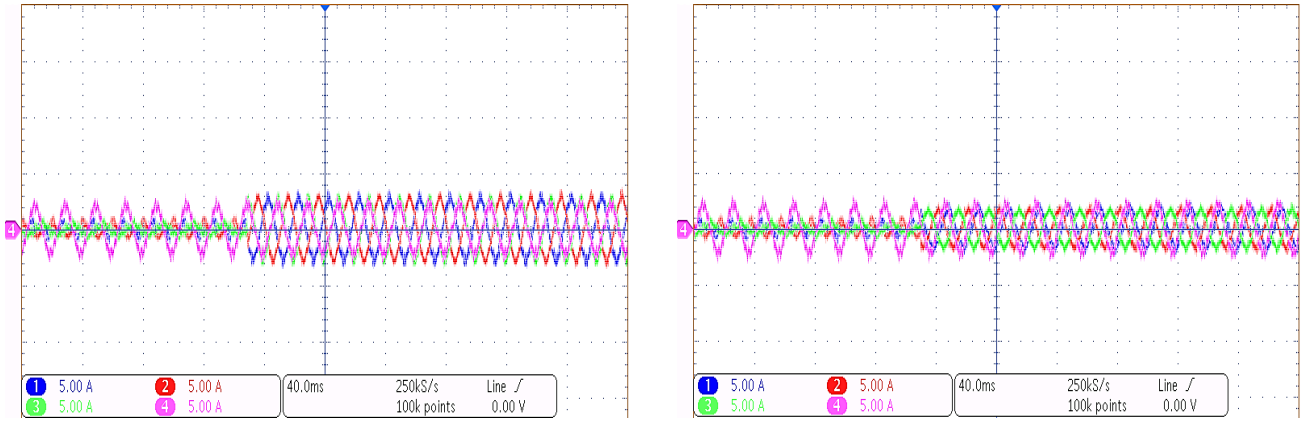

(a) (b)

Figure 6.20. (a) I_{dref} change, and (b) I_{qref} change operation with 3L-SVSI

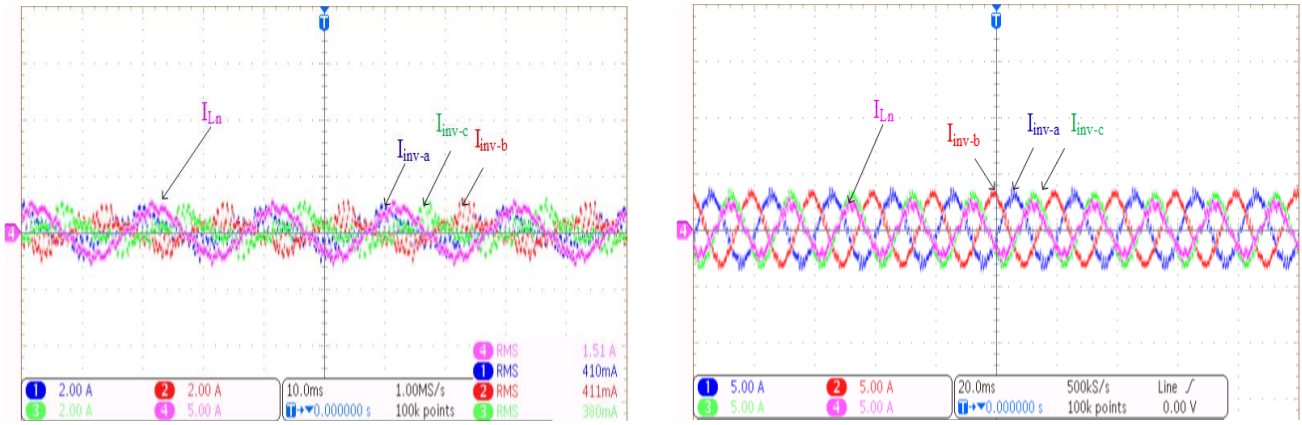

(a) (b)

Figure 6.21. 3L-SVSI operation with (a) no current control, and (b) I_{dref} (2 A) and I_{qref} (- 1 A)

6.4.3 DC bus voltage regulation

In this case study, the DC bus voltage regulation with the I_d current controller is demonstrated. As discussed in previous chapters, an external voltage control loop is designed to regulate the DC bus voltage to generate the $I_{dref.}$ The DC bus voltage controller performance is evaluated in two cases: (i) with the DC power source (PV-SVSI mode); and (ii) without the DC power source (D-STATCOM mode). With active current sources, such as a PV system, the DC bus voltage regulator maintains the DC voltage at a constant value while supplying the PV generated current to the grid. Similar characteristics can be monitored from the experimental results with the DC power source connection as shown in Figs. 6.22 (a) and (b). The DC bus voltage reference is set to 150 V, higher than the required DC voltage, which is around 130-140 V.

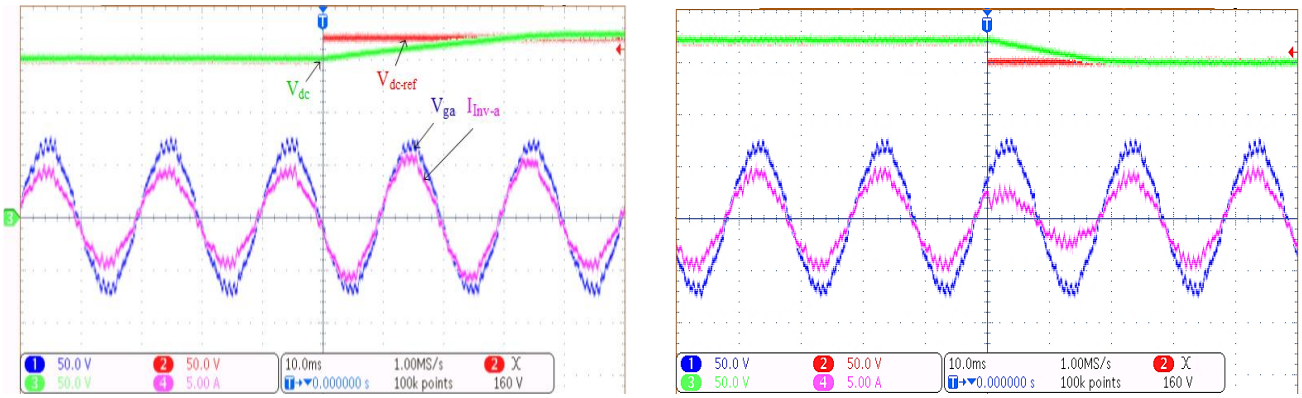

(a) (b)

Figure 6.22. DC voltage regulation from (a) 150 to 170 V, and (b) 170 to 150 V

The trigger point is set to 160 V, and it can be seen from Fig. 6.22 that the voltage controller robustly regulates the DC bus voltage within 20 ms. The DC voltage regulator, with the 170 V step-change, increases the supply current from the inverter. This happens to raise the DC bus voltage at that instant by consuming more DC current from the DC power source. Similarly, when the reference is changed

from 170 V to 150 V, the inverter-generated transient current becomes lower than the previous step; however, the controller follows the reference within 20 ms.

For the distributed static compensator (D-STATCOM) mode analysis, the DC power source is disconnected from the system and the DC bus voltage is regulated utilising the grid supply voltage rectification from the anti-parallel diodes from the IGBT modules. In this case, the grid voltage is reduced to 30 Vrms from 50 Vrms to reduce the demand voltage at the DC bus. The DC bus voltage regulation operation in D-STATCOM mode is shown in Fig. 6.23. The DC bus voltage is set to 100 V and the trigger point is selected as 110 V. Since the current is primarily supplied by the grid, the inverter-side phase current has a 180^0 phase difference with the grid supply voltage due to the opposite sign convention of currents. Similarly to the PV-SVSI operation, changing the DC bus voltage to a higher reference value requires a larger supply of grid current compared to a downward step-change operation as shown in Fig. 6.23 (b). The developed DC voltage regulator and decoupled current controllers can robustly stabilise the DC bus voltage reference within 20 ms. This ensures proper DC bus voltage regulator performance in both daytime (PV-SVSI mode) and nighttime (D-STATCOM) scenarios.

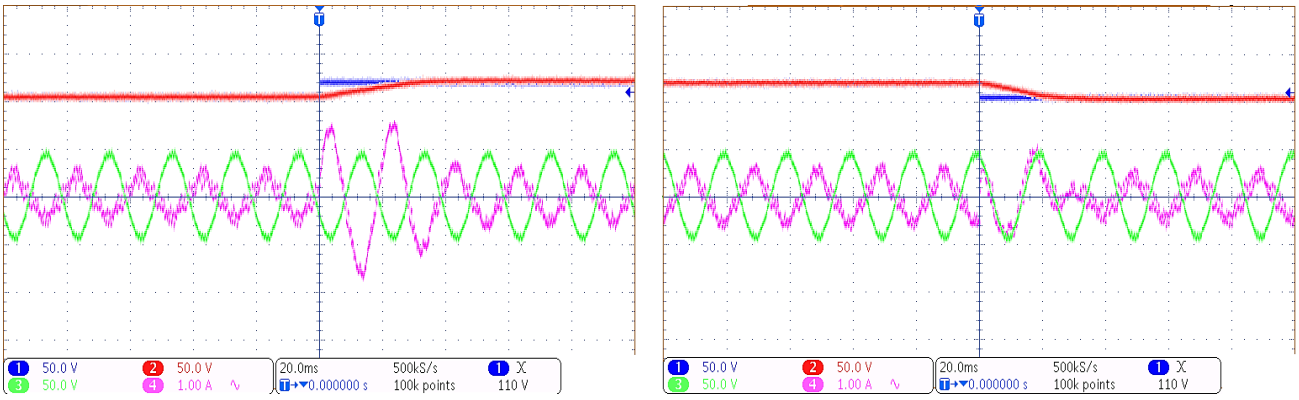

(a) (b)

Figure 6.23. V_{DC} regulation in D-STATCOM mode from (a) 100 to 120 V and (b) 120 to 100 V

6.4.4 Current control with four-leg inverter

In the previous case studies, the active and reactive currents are controlled utilising the 3L-VSI configuration. In this particular case study, the same decoupled current controller is applied to the 4L-VSI with an additional neutral current controller for the fourth leg half-bridge switching module. Due to the poor filtering performance from the DC choke filter utilised with the inverter out current, the noise from the switching frequency is evident on the inverter output current. Despite the switching noise in the output current, the designed four-leg inverter delivers properly controlled outputs following the given reference to the controller. Initially, no loads are connected at the PCC and the four-leg inverter outputs from individual current controllers are shown in Fig. 6.24 from (b) to (f). Fig.

6.24 (a) shows the inverter-generated current before connecting the inverter with the system. Initially, only I_{dref} is changed to + 1 A while keeping I_{qref} and I_{nref} to 0 A, and the results are shown in Fig. 6.24 (c). Similarly, I_{qref} is changed to + 1 A (lagging pf) while keeping I_{dref} and I_{nref} to 0 A as shown in Fig. 6.24 (d). In Fig. 6.24 (e), both I_{dref} and I_{qref} are set to + 1 A and + 500 mA while keeping I_{nref} to 0 A. Figs. 6.24 (c) to (e) reveal that the inverter generates the required current properly following the I_{dref} and I_{qref}. As the magnitude of current generated from the inverter is quite low, the system noise becomes more prominent in the inverter output currents because the system cannot compensate the additional losses. This includes, for example, switching and line losses which require being compensated utilising the active current components of the inverter system.

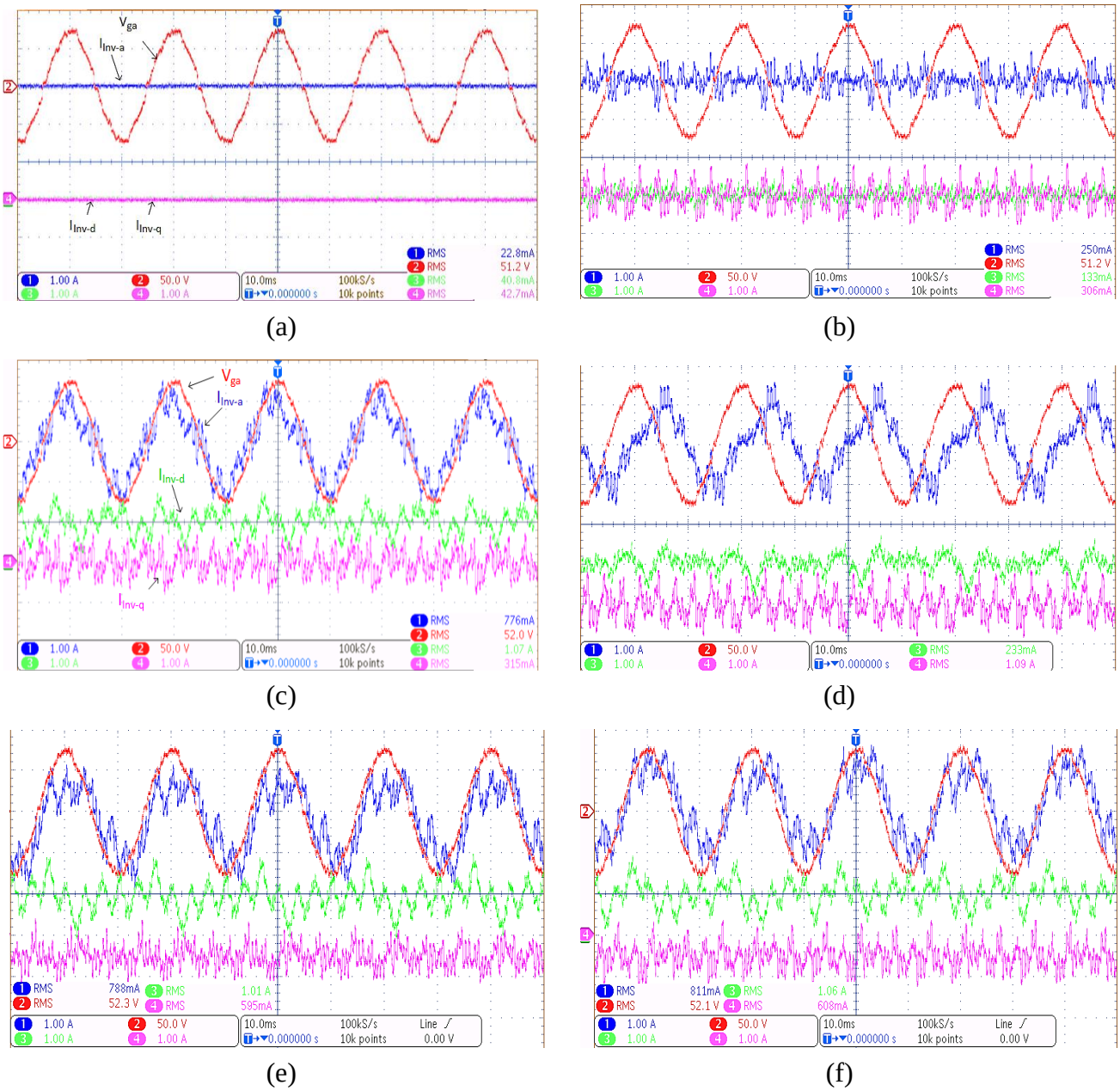

Figure 6.24. Four-leg SVSI operation: (a) before connection, (b) after connection, control of: (c) I_d, (d) I_q, (e) I_d and I_q, and (f) I_d, I_q, and I_n

In Fig. 6.24 (f), I_{nref} is manually changed to + 1 A while commanding I_{dref} and I_{qref} to follow +1 A and + 500 mA. Due to the neutral current controller operation, it is evident that the centre point of the output current shifts upward compared to Fig. 6.24 (e). Therefore in existing neutral current compensation methods, I_{nref} is set to 0 A to make sure that the neutral point of the phase currents remains at 0 irrespective of system unbalance conditions. This is mainly related to the neutral shift theory as discussed in Chapter 5. The modulation index of the four-leg inverter with the I_{dref} and I_{qref} changing operation is shown in Fig. 6.25 (a). The neutral current controller demanded modulation signal for +1 to 0 A reference-change operation is shown in Fig. 6.25 (b).

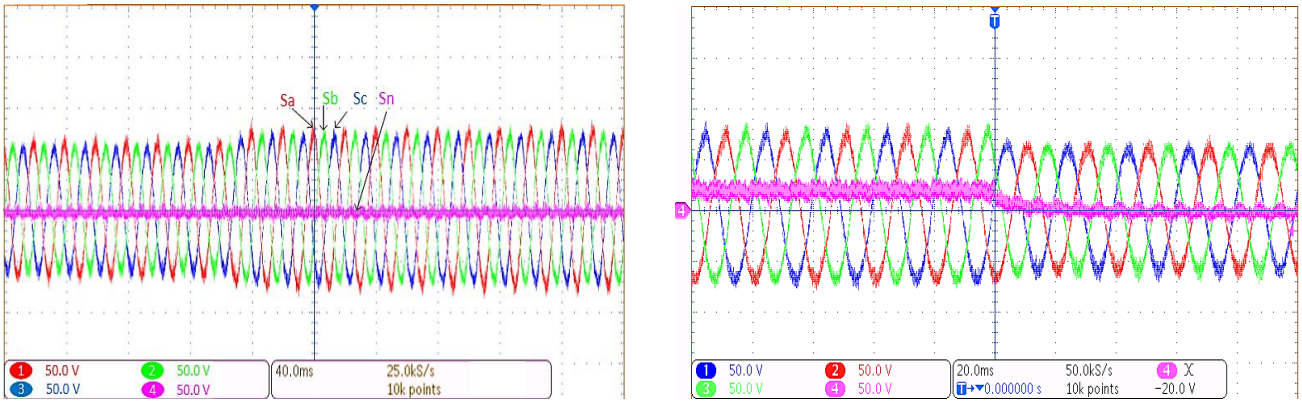

(a) (b)

Figure 6.25. Four-leg SVSI modulation index: (a) I_d and I_q control, and (b) I_d, I_q and I_n control

The limit for the modulation signal is set to ± V_{DC}. It can be seen from Fig. 6.24 that the modulating signals (Sa, Sb, Sc, and Sn) show variation in the phase and magnitude, and thus in the PWM output duty ratio, in correspondence with the step-changing operations from the current controllers. With the reference-changing operation from the neutral current controller, the neutral point of the inverter output phase currents also shifts accordingly. The neutral current generation due to unequal load distribution and different active neutral mitigation methods are presented in the next section.

6.4.5 Neutral current compensation with different loads

In this case study, the proposed neutral compensation method is applied on a four-leg smart VSI and results are presented with different load configurations. The neutral current compensation performance is presented in conjunction with the active and reactive current control operations. The performance of the four-leg inverter is investigated with and without the DC power source to show a 24-hour operation compatibility with the PV system for both day and night operation. Three different load types are connected at the PCC: (i) constant-current (CC), (ii) constant-impedance (CZ), and (iii) constant-power (CP). System unbalance is introduced in two ways: unequal loads (i) connection, and (ii) disconnection while the other phase loads are active. The simulation results of similar load-

unbalance scenarios are reported in Chapter 5 with the application of the dynamic capacity distribution method. However, in this chapter, the fixed-capacity neutral compensation operation is applied and the DC bus voltage is regulated at constant 140 V without the DC source connection (D-STATCOM).

The phase currents before connecting the loads at the PCC are shown in Fig. 6.26 (a) and it can be seen that the system has an inherent neutral current which can contribute to degraded power quality. The neutral current generation from different load demand values and the corresponding effect on the grid-side neutral current with the CC load distribution are shown in Figs. 6.26 from (b) – (f).

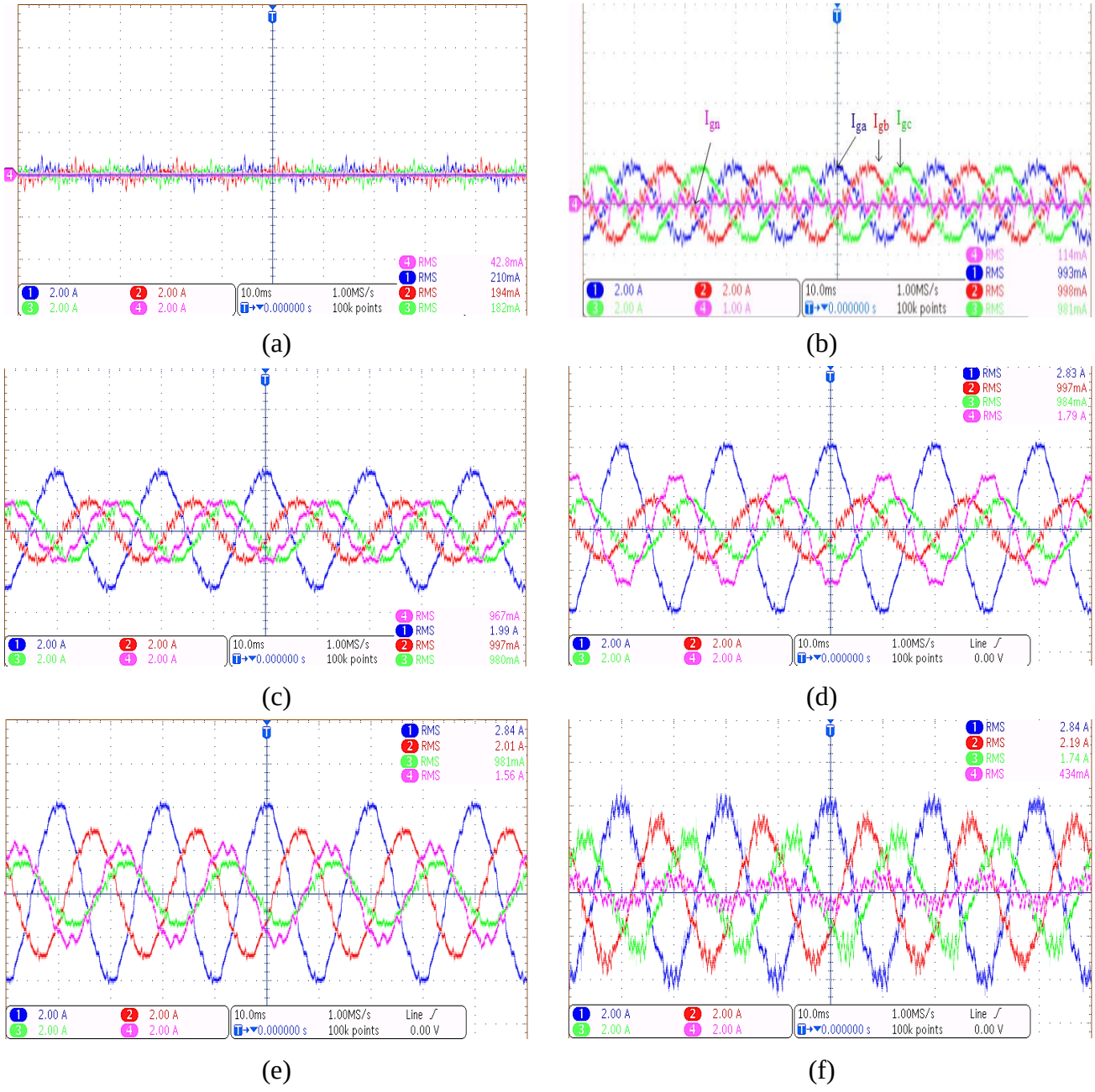

Figure 6.26. CC type load (a) before connection, with I_{Lb}=1 A, I_{Lc}=1 A, and I_{La} (b) 1 A, (c) 2 A, (d) 3 A, and I_{La}=3 A, I_{Lb}=2 A, I_{Lc}=1 A (e) without-, and (f) with- 4L-SVSI

The load-generated neutral current becomes significant with the increase in unbalanced load distribution in the system that can be seen from the higher neutral current at the grid-side. It is evident from Figs. 6.26 (b) to (d) that increasing only the single-phase load can certainly increase the grid-side neutral requirement more than the case of increasing loads in two phases as indicated in Fig. 6.26 (e). The grid-side neutral current requirement is compensated by more than 1 A with the application of the four-leg SVSI as illustrated in Fig. 6.26 (f). It also improves the phase unbalances as is evident from the increased current of approximately 1 A in phase C. Comparison of the grid-side phase and neutral currents are shown in a comparison bar chart in Fig. 6.27. It is evident from the experimental results that the developed 4L system with the proposed neutral compensation method can certainly improve the grid-side neutral compensation as well as improve the phase unbalances at the PCC with different load unbalance scenarios, such as increasing load demand in a single phase and in two phases.

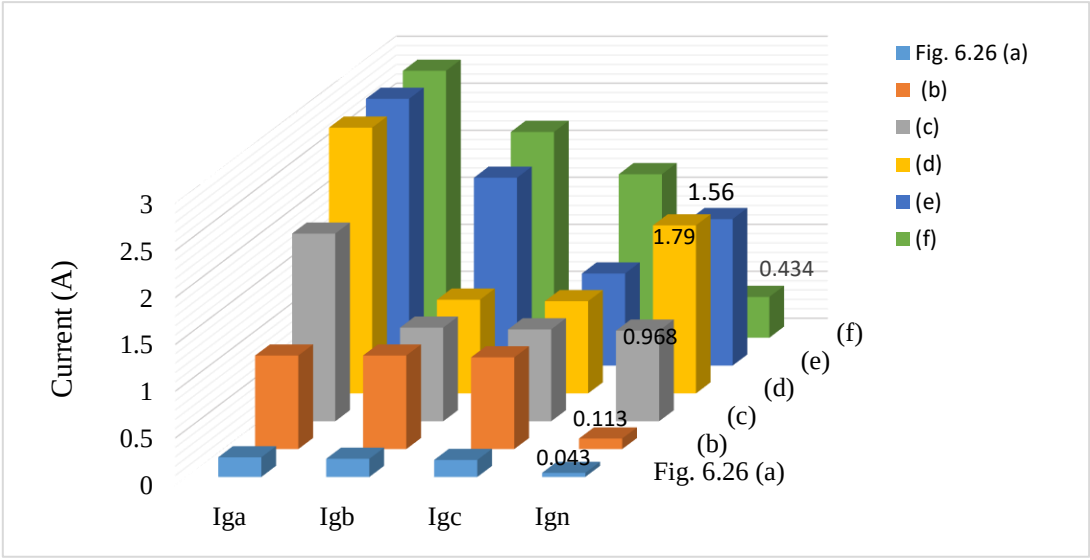

Figure 6.27. Grid-side phase currents (I_{ga}, I_{gb}, and I_{gc}) and I_{gn} comparison bar chart from Fig. 6.26

The four-leg inverter is designed to control active, reactive and neutral current components at the same time. The four-leg inverter is operated in the D-STATCOM mode which controls the required I_{dref} generation using the DC voltage regulator. Therefore, the reactive and neutral current components are controlled manually with the CC load distribution of I_{La} = 3 A, I_{Lb} = 2 A, and I_{Lc} = 1 A, and the results are shown in Fig. 6.28. Initially, I_{qref} is manually changed to + 1 A and -1 A to show the lagging and leading pf controlled operation from the 4L-SVSI while keeping the neutral controller following 0 A reference. The results with the DC voltage regulator and I_{qref} changing operations are shown in Figs. 6.28 (b) and (c). It can be seen from Figs. 6.28 (b) and (c) that the grid-side phase currents show controlled phase-shifting while the I_q current control from the 4L-SVSI and the grid neutral current remain the same even with the existing active neutral control, i.e. I_{nref} is set to 0 A. The proposed neutral compensation method is applied within the VSI and the results are shown in Fig. 6.28 (d). The

controlled neutral current supplied by the fourth leg of the inverter helps to improve the phase unbalance of the grid-side currents significantly. This phase balancing mainly occurs due to the neutral shifting and current redistribution operations to compensate the unbalance effects. The neutral compensation performance comparison from Fig. 6.28 is presented in a bar chart in Fig. 6.29.

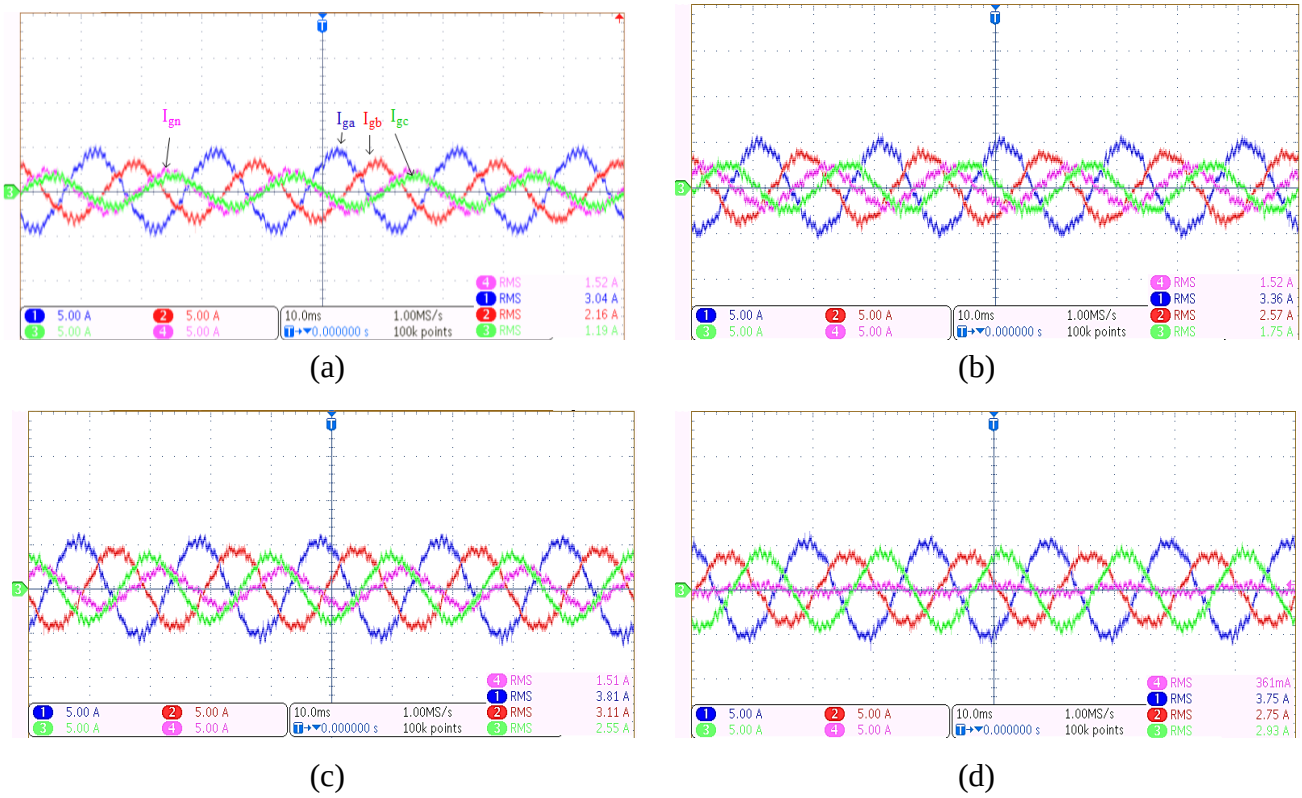

Figure 6.28. (a) Load demands supply, 4L-SVSI control operation, with (b) I_{qref} = + 1 A, (c) I_{qref} = - 1 A, and (d) I_{qref} = - 1 A and proposed I_n compensation

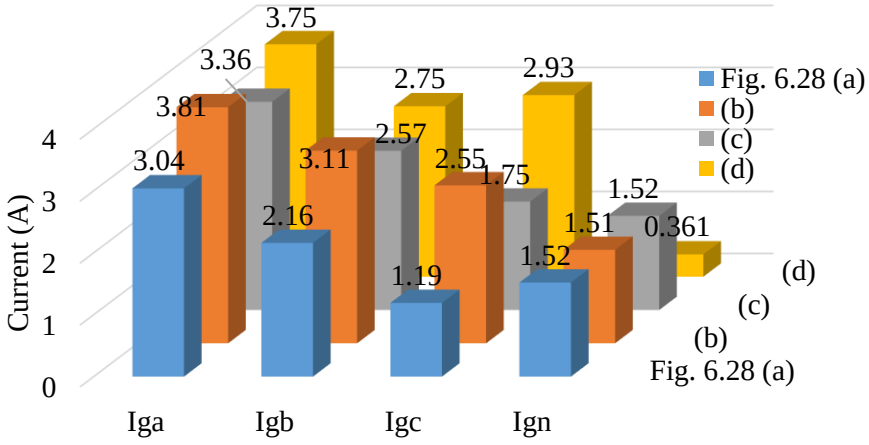

Figure 6.29. Four-leg SVSI operation comparison with unbalanced load distribution

The proposed neutral current compensation method with the four-leg VSI utilises the load-generated neutral current as a reference for the fourth leg half-bridge and compensates the neutral current at the

grid. This operation is demonstrated in Fig. 6.30. It can be seen from Fig. 6.30 (a) that the grid-side neutral current represents the same magnitude with 180^0 phase shift as the load-generated neutral current when the 4L-VSI is inactive. The PCC neutral connection for the experimental system can be represented as:

$$I_{gn} + I_{Ln} + I_{Inv-n} = 0 \tag{6.1}$$

Therefore, when $I_{Inv-n} = 0$, the relation becomes:

$$I_{gn} = -I_{Ln} \tag{6.2}$$

Similar phase characteristics can be seen from the experimental results in Fig. 6. 30 (a). With the 4L-VSI, the inverter fourth leg is controlled to generate a neutral current having the same magnitude of the load side neutral current but with opposite phase, i.e. to cancel the effect of load-generated neutral current at the PCC. Therefore, with the proposed 4L-VSI, (6.1) can be written as:

$$I_{Inv-n} = -I_{Ln}; I_{gn} = 0 \tag{6.3}$$

The results with the 4L-VSI are shown in Fig. 6.30 (b) and it is evident that the grid-side neutral current is significantly reduced, from 1.70 A to 490 mA, with the application of the four-leg VSI which generates 1.67 A neutral current in opposite phase to the load side neutral current. As the four-leg VSI redistributes the grid-side phase currents to reduce the neutral current effect, the voltage at PCC also improves respectively as can be seen from channel (1) in Fig. 6.30.

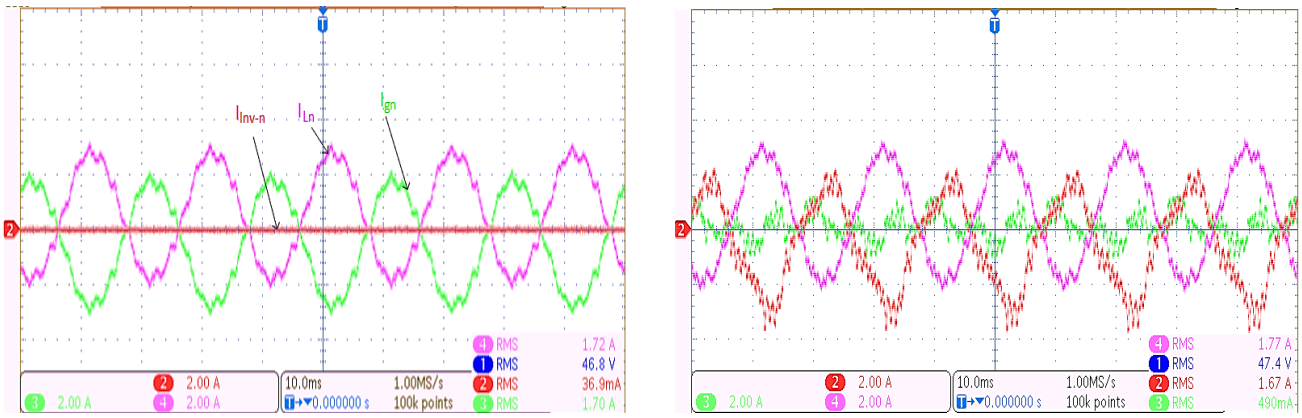

(a) (b)

Figure 6.30. (a) Without and (b) with the four-leg SVSI system

To demonstrate the PV-SVSI operation of the designed four-leg hardware, I_{dref} is manually changed and the effect on the grid-side currents due to the inverter current supply is shown in Fig. 6.31. It can be seen from Fig. 6.31 that when I_{dref} is changed from 0 to 2 A, and 2 to 0 A, the grid-side supply current is changed by 2 A (p-p) in all the three-phase currents. This demonstrates that the designed four-leg VSI system can be operated with any active current sources to compensate for the load demands and reduce the consumption from the main grid, i.e. can reduce electricity bills.

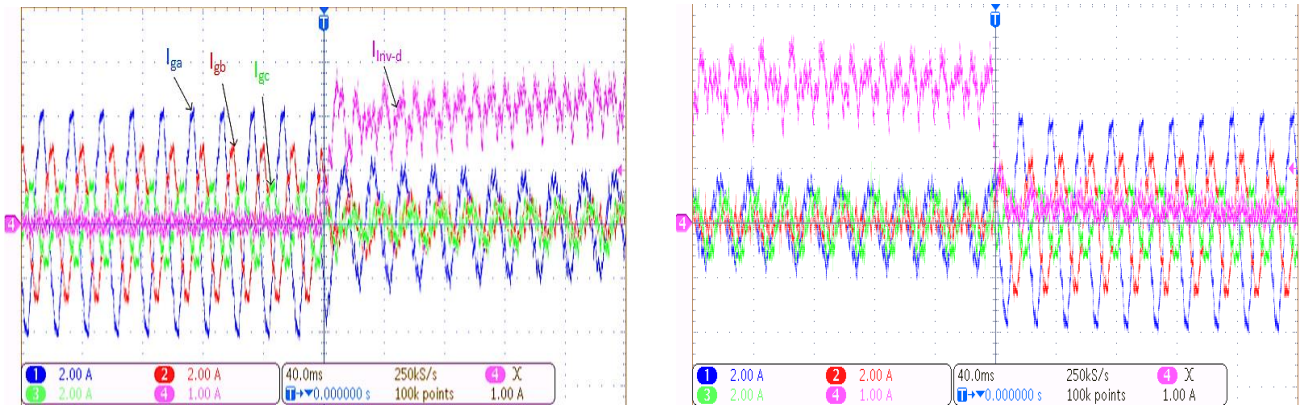

(a) (b)

Figure 6.31. I_{dref} step-change and corresponding effects on grid currents for (a) 0 to +2 A and (b) +2 to 0 A

The 4L-VSI is operated with individual current control modes and the inverter-generated current (AC) and the grid-side voltage relationship for the A phase are shown in Fig. 6.32.

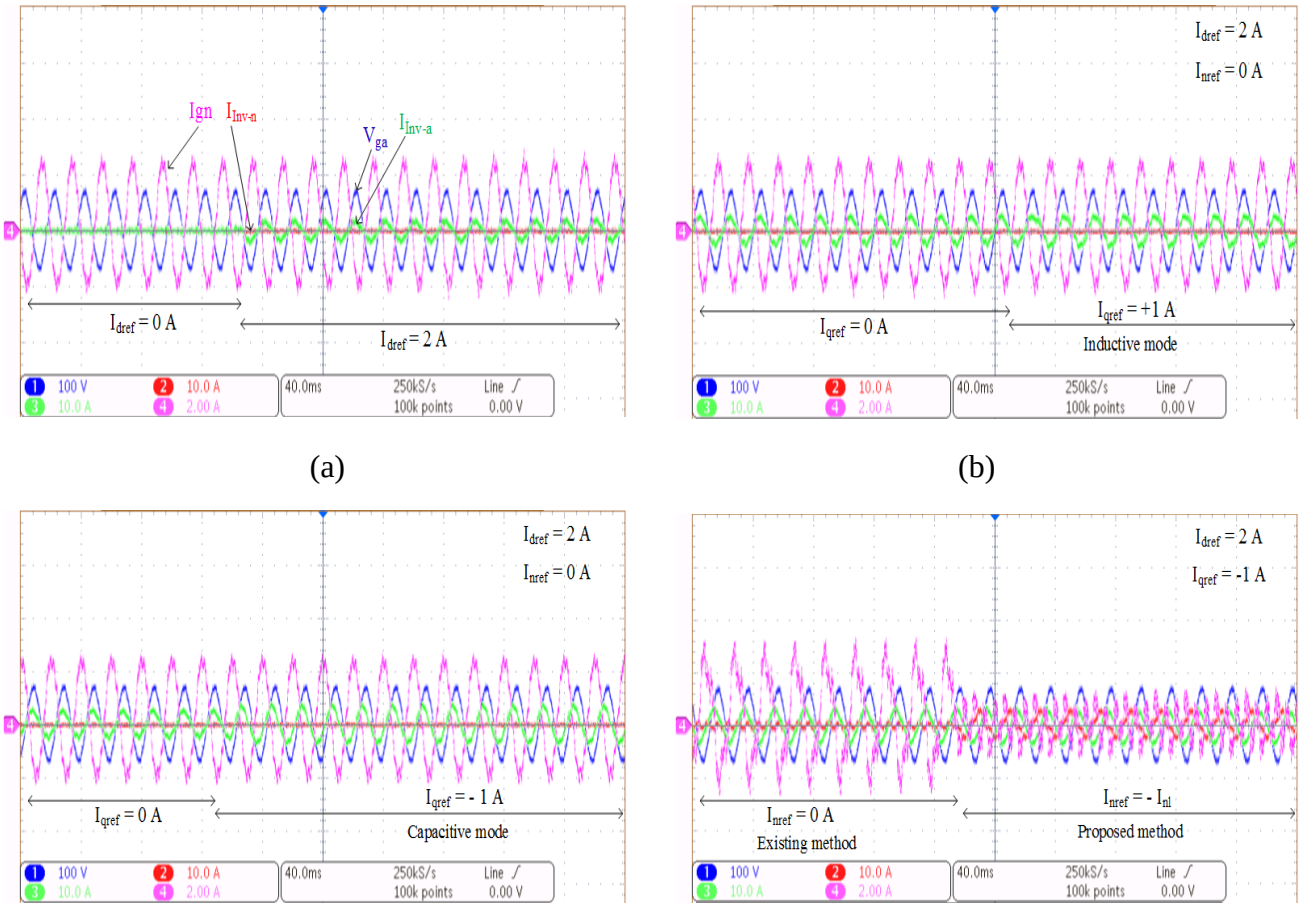

(a) (b)

(c) (d)

Figure 6.32. Four-leg SVSI controller reference-changing operation with- (a) I_{dref}, (b) + I_{qref}, (c) - I_{qref}, and (d) I_{nref}

Fig. 6.32 (a) shows that the inverter generates the same phase current with the grid-side voltage during the I_{dref} change (I_{qref} = 0 which is unity pf). Keeping I_{dref} following 2 A, I_{qref} is changed manually

to + 1 A and - 1 A to show the lagging and leading pf control operation from the 4L-SVSI in Figs. 6.32 (b) and (c). Fig. 6.32 (d) shows the results of controlling all three current components, i.e. active, reactive and neutral, from the experimental system, and it is evident from these results that the grid-side neutral current can be compensated significantly with the four-leg inverter without hampering the other current controller operations. This demonstrates the independent and decoupled current control of the designed four-leg inverter.

6.4.6 Four-leg VSI operation with load disconnections

This case study presents the neutral current generation due to a sudden load disconnection and the mitigation operation from the four-leg smart voltage source inverter (4L-SVSI). Three types of loads are considered to represent the load-disconnection effects. The switching frequency of the inverter is changed to 9 kHz from 5 kHz to indicate the robustness of the designed 4L-SVSI. The inverter is operated in D-STATCOM mode and the DC voltage regulator is applied to regulate the DC bus voltage. The I_q current controller reference is also set to 0 A. Therefore, only the neutral current controller is utilised to compensate for the load-generated neutral current. The performance of the designed fourth-leg current controller with different load-generated neutral currents is presented in the next sections.

6.4.6.1 Constant-current (CC) loads

The aim of this case study is to explain the transient effects on the PCC neutral current from sudden disconnection of CC loads. The four-leg inverter is utilised to mitigate the PCC neutral current from the sudden load disconnection. The neutral current generation with the unequal distribution of constant-current loads in all the three phases is shown in Fig. 6.33 (d), where the loads are set to consume maximum 3 A, 1 A and 1 A current from phases A, B, and C, respectively. The unequal load distribution in all three phases generates around 1.79 A neutral current, however, the neutral current increases significantly to 2.41 A and 2.76 A with the sudden disconnection of single- (phase B) (1P) and double- (phases B and C) phase (2P) loads respectively as shown in Figs. 6.33 (a) and (b). It is evident that the sudden load disconnection causes more neutral current than the unbalanced load connection cases mentioned earlier. The grid-side neutral current is compensated by more than 2 A with the application of the four-leg VSI in cases with the single- and double-phase load disconnections shown in Figs. 6.33 (c) and (d). The results make evident that the proposed neutral compensation method with the four-leg inverter can operate even with higher neutral current compensation. The load-side phase currents and the corresponding neutral currents are shown in the comparison bar chart in Fig. 6.34. Here is shown the sudden load disconnection that can cause a significant amount of neutral

current, and the four-leg inverter system is able to mitigate the grid-side neutral current by more than 2 A without causing any interruption in the load-demand phase currents.

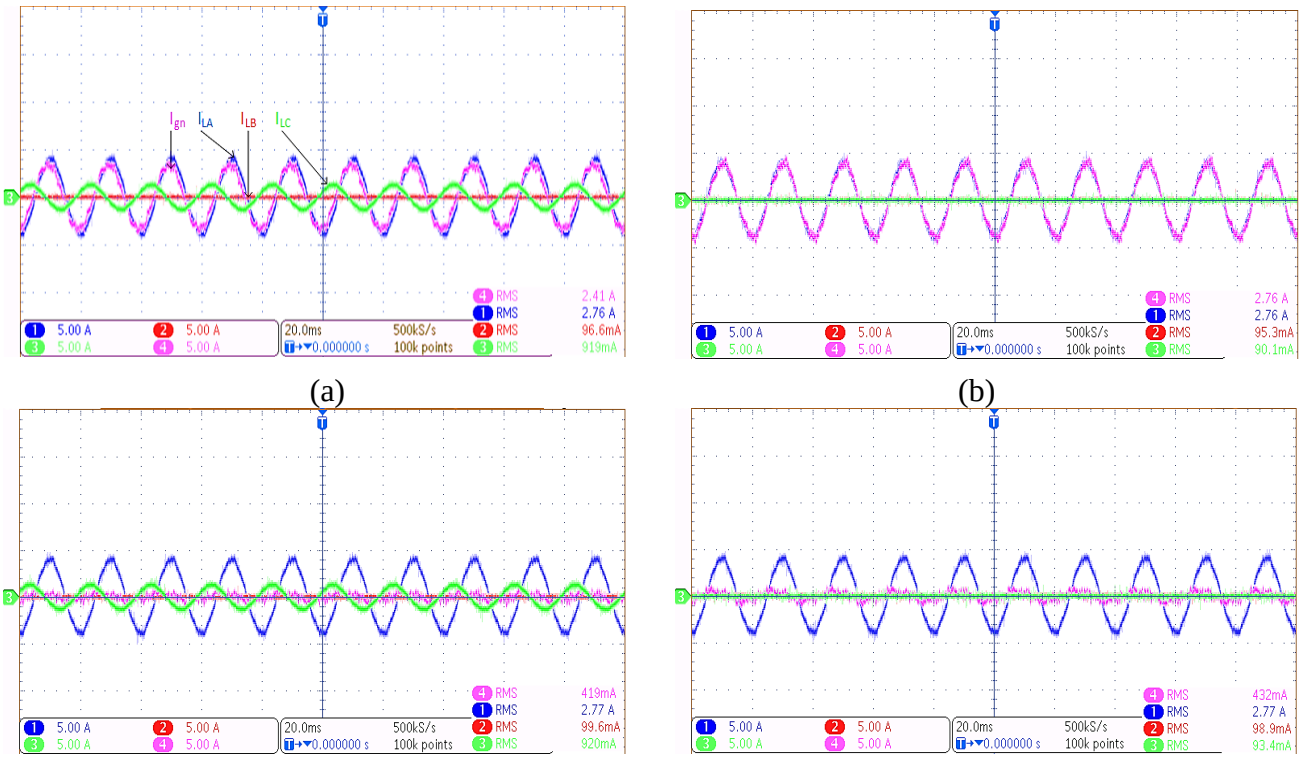

Figure 6.33. Load disconnection (a) 1P, (b) 2P, and corresponding operation with 4L-VSI (c) 1P, and (d) 2P

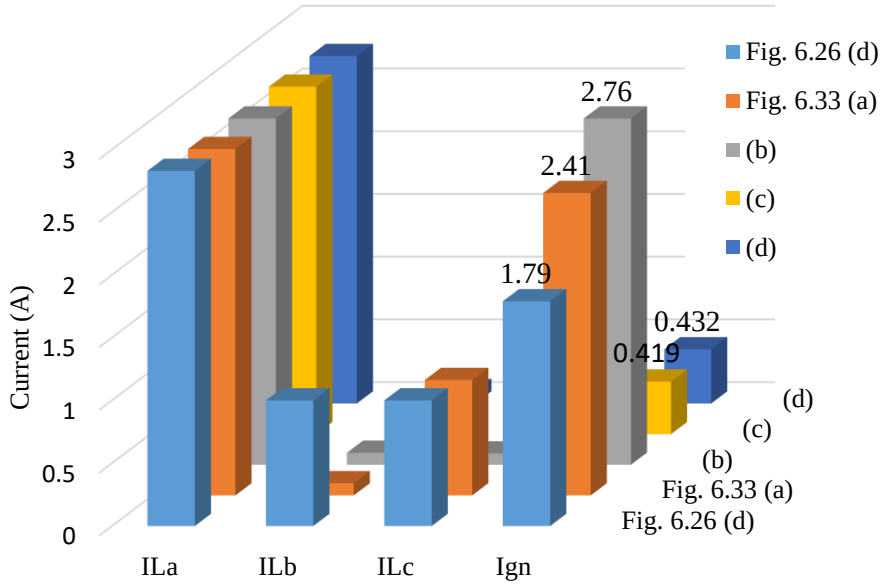

Figure 6.34. CC load disconnections and operation with 4L-SVSI comparison bar chart

6.4.6.2 Constant-impedance (CZ) loads

In this case study, constant-impedance (CZ) loads are applied at the PCC and the load disconnection effects are evaluated with the four-leg inverter system. With the fixed supply voltage (50 Vrms), different resistor values are set for the load to consume different currents from the grid, for example, the A, B, and C phase loads are set to 50, 25 and 16.7 Ω to consume a maximum 1, 2 and 3 A current from the grid. Even with equal load distribution (each load is set to consume 2 A current), the CZ load generates around 800 mA neutral current as shown in Fig. 6.35 (a). The single- and double-phase load disconnections cause a similar amount of neutral current generation (2.14 A) which is different from the previous case where the double-phase load disconnection caused more neutral current than the single-phase load disconnection. This is the consequence of equal load distribution in each phase which is set to consume 2 A current. However, in the previous case, the A, B, and C phases are set to consume unequal load currents of 3, 1 and 1 A respectively. The load disconnection results are illustrated in Figs. 6.35 (c) and (e). The 4L-SVSI with the active neutral current control robustly compensates the grid-side neutral current for the three load configurations as shown in Figs. 6.35 (b), (d), and (f). This proves that the proposed neutral compensation method works robustly with different types of loads and connection conditions as shown in the comparison bar chart in Fig. 6.36.

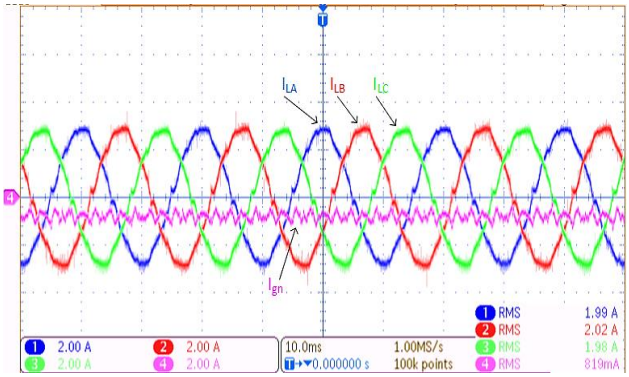

(a)

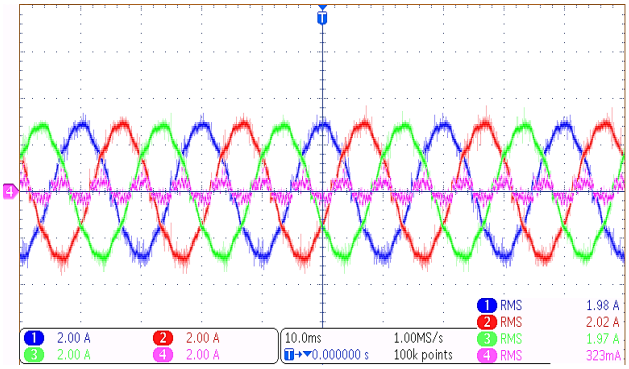

(b)

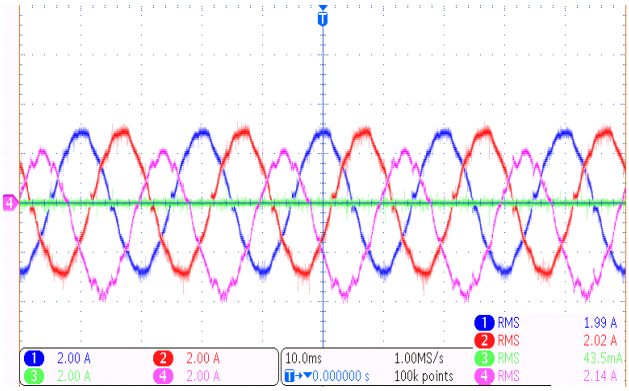

(c)

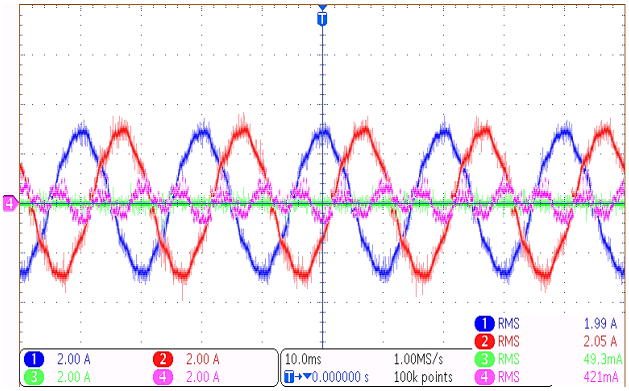

(d)

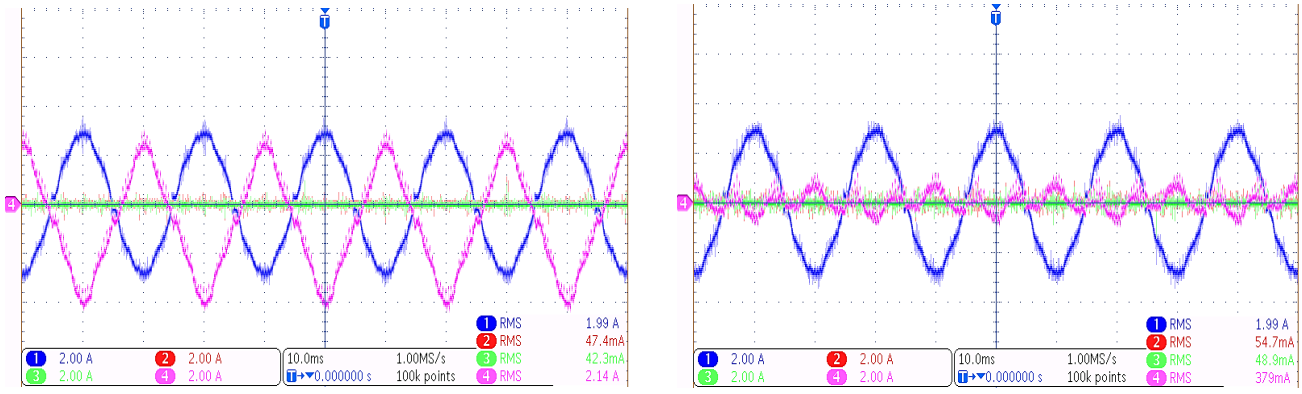

(e) (f)

Figure 6.35. (a) 3P-load, (b) 3P-load with 4L-SVSI, (c) 2P-load, (d) 2P-load with 4L-SVSI, (e) 1P-load, and (f) 1P-load with 4L-SVSI

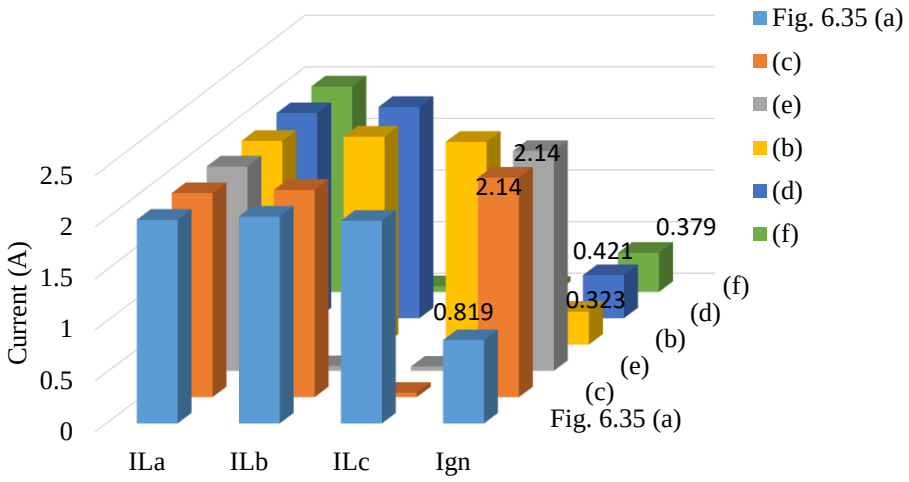

Figure 6.36. Constant-impedance loads performance comparison with 4L-SVSI

6.4.6.3 Constant-power (CP) loads

Similar to the previous case studies with CC and CZ loads, in this case study the load disconnection effects with constant-power (CP) loads are evaluated. The CP loads are configured based on the fixed amount of watt ratings in the loads. For example, with the 50 V grid supply, 50, 100 and 150 W CP loads will consume a maximum 1, 2, and 3 A currents from the PCC. The single- and double-phase load-disconnection effects are the main consideration of this case study, while the CP loads and their neutral current generation effects on the grid-side neutral current are shown in Fig. 6.37 (a) and (b). Similar to the CZ loads, the CP loads are also configured to consume maximum 2 A current from each phase, and the 1P and 2P load disconnections cause approximately the same amount of neutral current generation of 1.96 A. It is evident from Fig. 6.37 (c) and (d) that the neutral compensation operation with the designed four-leg smart VSI performs similarly to the CC and CZ loads and compensates

more than 1.5 A of grid-side neutral current. This demonstrates the wide range of compatible performance of the designed 4L-VSI with different load types and different operating conditions.

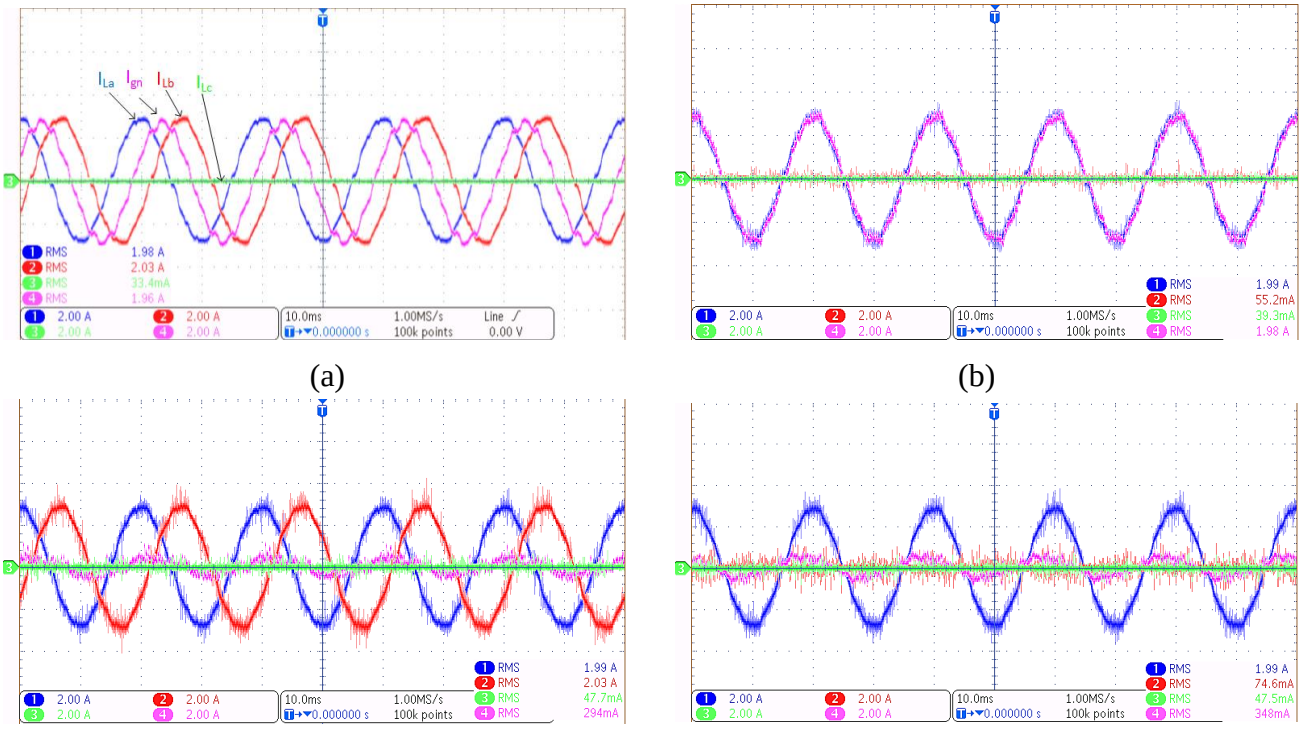

(a) (b)

(c) (d)

Figure 6.37. CP type (a) 2P- load, (b) 2P- load with 4L-SVSI, (c) 1P-load, and (d)1P-load with 4L-SVSI

6.4.7 Different load (CC, CZ and CP) connections

In this case study, the constant-current, constant-impedance, and constant-power loads are connected with phases A, B, and C at the PCC. They are configured to draw 3 A each and it can be seen from Fig. 6.38 (a) that, even with equal distribution of loads, more than 1 A grid-side neutral current exists. The introductions of Chapters 4 and 5 discussed the contention that PCC can have significant neutral current even with balanced load distribution if the load types are different. This is evident from the experimental results as well as shown in Fig. 6.38 (a). Single- and double-phase load disconnection effects are shown in Figs. 6.38 (c) and (e) where the grid-side neutral current is close to the phase current rating of 3 A. Therefore, it is desirable to set the grid-side neutral conductor to have the same capacity as the phase conductors or even higher to reduce the hazardous effects of the sudden high neutral current. Alternatively, with the proposed neutral compensation method integrated with the 4L-SVSI, the neutral current can be effectively compensated and redistributed among the grid-side phases as shown in the case with single- and double-phase load disconnection effects in Figs. 6.38 (d) and (f). It is evident from Figs. 6.38 (d) and (f) that the compensated neutral current helps to balance the unequally distributed phases quite significantly. The double-phase load disconnections from Figs.

6.38 (e) and (f) show that the grid-side A and B phase currents are redistributed by more than approximately 500 mA with the 4L-SVSI. Concurrently, more than 1 A of phase C current on the grid-side is reduced in Fig. 6.38 (f) compared to Fig. 6.38 (e) with the proposed compensation of the 4L-SVSI which is utilised in the current redistribution operation.

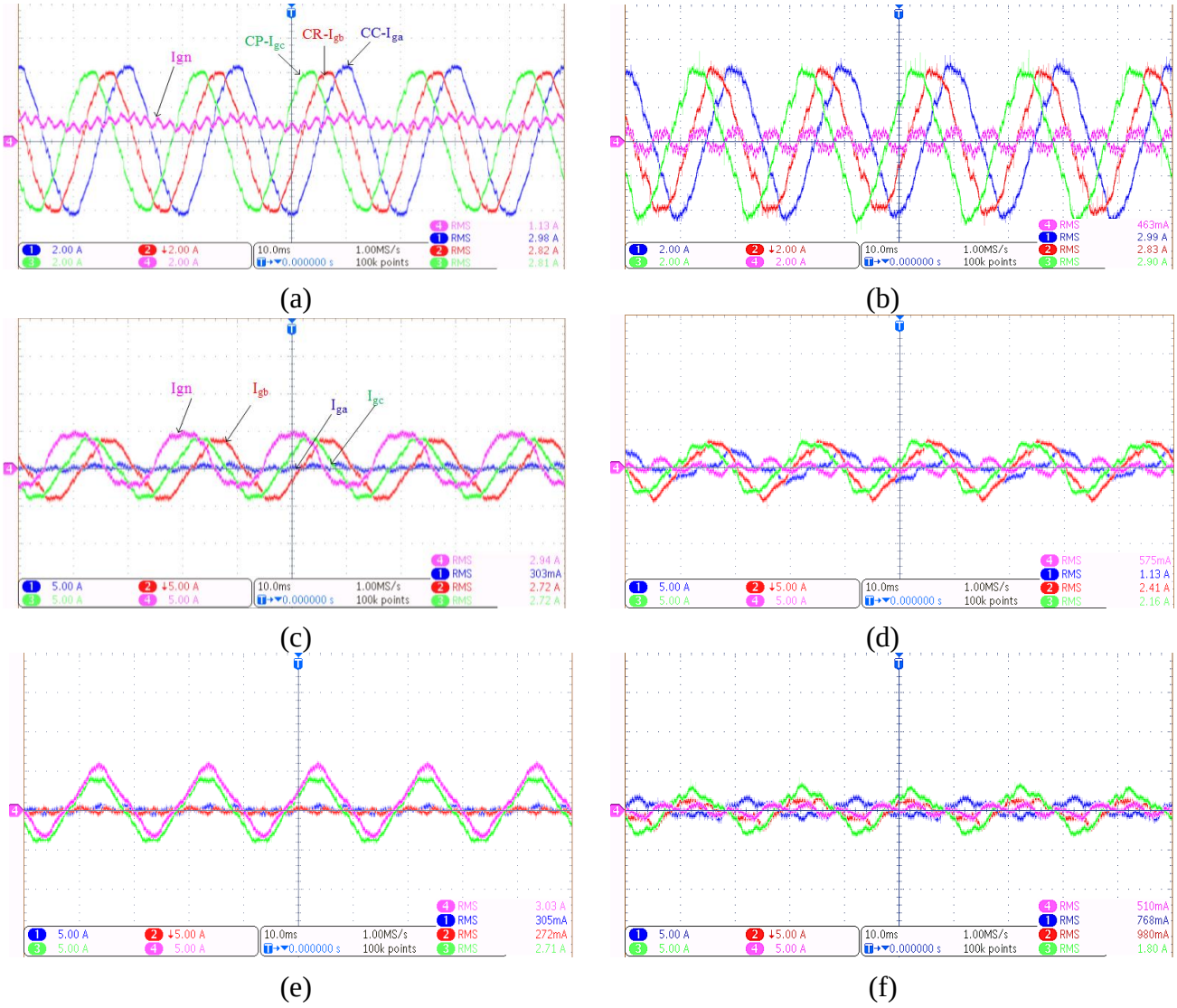

Figure 6.38. (a) Three 1P loads, (b) three 1P loads with SVSI, (c) two 1P loads, (d) two 1P loads with SVSI, (e) 1P load, and (f) 1P load with SVSI

Theoretically, while it is not possible to completely balance an unbalanced system without any additional current supply to each phase, with the proposed neutral compensation a significant amount of unbalance phase current can be reduced as demonstrated in this case study. The three types of load configurations and the neutral compensation effects with the 4L-SVSI are shown in the comparison bar chart in Fig. 6.39. It is evident from all presented case studies that the proposed system performs significantly for the grid-side neutral current compensation and phase balancing at PCC despite different load types and configurations.

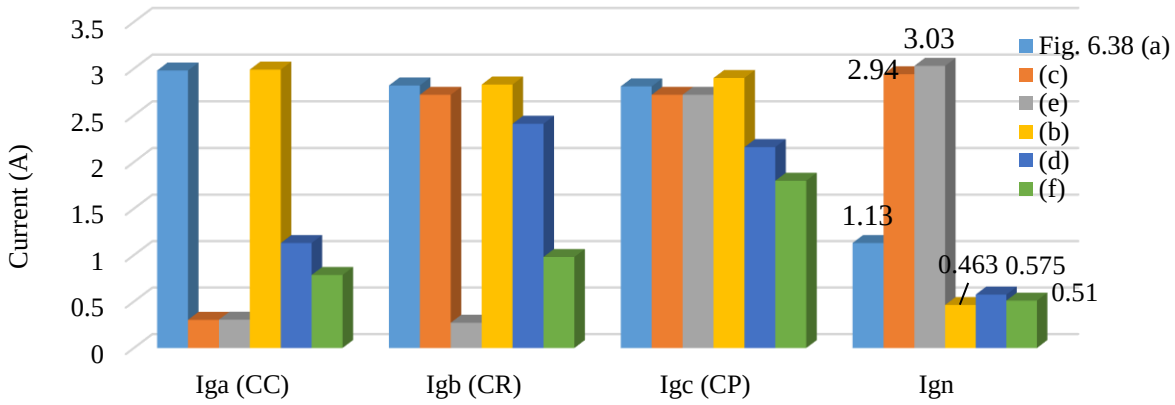

Figure 6.39. Bar chart for three different load conditions and results with the 4L-SVSI

6.4.8 SVSI operation with constrained limits

This case study demonstrates the experiment using the designed four-leg SVSI to test limit-constrained operation. It has been discussed in Chapters 4 and 5 that each current controller is set with a current limiter which restricts the inverter from generating more current than the maximum limiter value. As the IGBT switching modules used in the four-leg hardware configuration can have a maximum 50 A current-carrying capacity, it is necessary to constrain the current controllers with fixed current limits. Considering the maximum current rating from the current limiters, the inverter maximum VA rating can also be defined. For example, with ± 3 A maximum allocated current for the active and reactive current operations, and an additional ± 2 A for the neutral compensation operation, the SVSI require a total ± 5 A current capacity operation. Then the inverter's total capacity (with the losses considered) can be calculated following the instantaneous power theory as 550 VA for a 50 V_{rms} grid system. To demonstrate the controller operation with the current limiter, the DC bus voltage reference is changed to 170 V and then to 135 V, which is lower than the demanded value from the DC bus voltage regulator. The subsequent results are shown in Fig. 6.40.

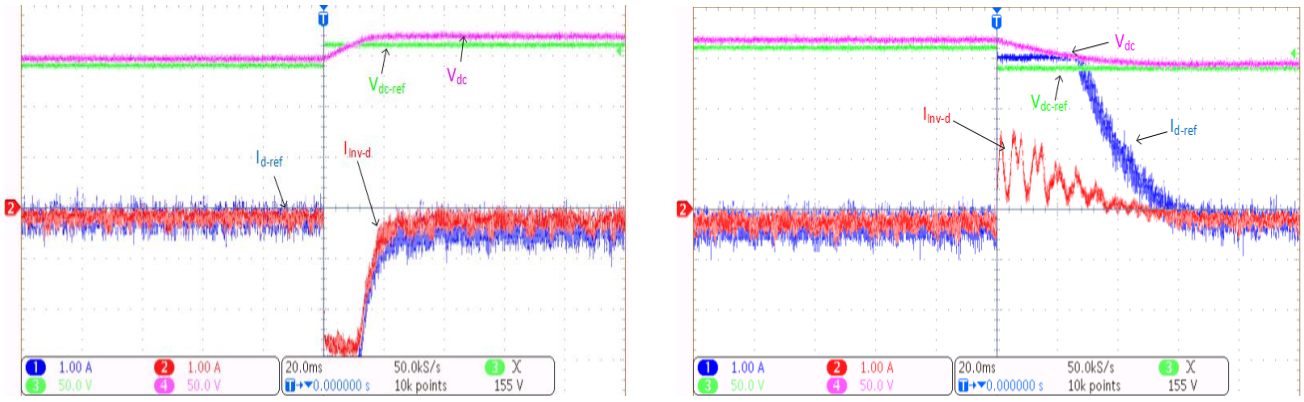

(a) (b)

Figure 6.40. Limit-constrained operation from the DC voltage regulator: (a) 150 to 170 V and (b) 170 to 135 V

The system is operated in D-STACOM mode with the 50 V grid supply voltage and the trigger point set to 155 V. It can be seen from Fig. 6.40 (a) that, during normal operation, the DC voltage regulator generates a negative reference for the I_d current controller (approx. -200 mA), i.e. current is delivered from grid to the DC link capacitor of the inverter via the rectification operation. When the DC bus reference is changed from 150 to 170 V, the DC link capacitor consumes more current from the grid and the DC voltage controller takes around 20 ms to stabilise the DC voltage at 170 V. During the step-changing operation, the I_{dref} hits the maximum – 3 A current limit and consumes more current from the grid to maintain the 170 Vdc voltage (I_{dref} approx. -500 mA) as shown in Fig. 6.40 (a).

When the DC bus voltage is changed from 170 V to a value less than 140 V, the regulator fails to follow the DC bus voltage reference within the 20 ms time due to the limit-constrained operation as well as the lack of an external current supply source. During the voltage-changing transients, I_{dref} hits the maximum set limit of + 3 A, and due to the unavailability of an external active current source at the DC side, the DC link capacitor tries to supply the required current from the stored energy as can be seen from the positive I_d current in Fig. 6.40 (b). After 60 ms operation time (3 times the normal operation), the regulator stabilises the system utilising the proportional-integral (PI) controller, and the I_d current controller operates to follow the I_{dref} value (-50 mA) generated by the DC bus voltage regulator to regulate the DC bus voltage at 140 V.

This case study verifies that the inverter output current can be controlled using the current-limiter operation. Therefore, the proposed dynamic current distribution method from Chapter 5 can be integrated with the three current controllers using dynamic current limiters instead of a fixed one as discussed in this chapter.

6.5 Chapter Summary

This chapter presents the experimental setup and results from the designed four-leg inverter with active, reactive and neutral current controller operations using three-leg and four-leg inverter configurations. Results show that both the inverter configurations can robustly control the active and reactive current components to operate in both PV-SVSI and D-STATCOM modes. Different load types in variable load configurations are used to cause the system unbalance phenomena and generate neutral current at the PCC. The experimental results show improved neutral current compensation performance from the proposed neutral compensation method compared to the existing method. The quality of the inverter output current can be further improved with the application of an AC filter with inductors and LCL filter combination. The dynamic capacity distribution method can also be incorporated with the current limiters to achieve higher neutral compensation operations from the

experimental platform. The experimental results from the designed four-leg smart inverter confirm the previous chapters' mathematical assumptions and simulation results. It is therefore concluded that the four-leg PV-SVSI system can be installed in any real network with a three-phase four-wire network, such as residential and commercial areas, to perform active current supply, PCC voltage regulation by controlling the I_q current and active neutral compensation operations.

Table 6.9 Current controller gain values

PI Controllers	Kp	Ki
DC voltage controller	0.5	1
Decoupled current controller	5	10
I_n current controller	30	2000

Chapter 7
Conclusion and Future Work

In this research, the primary focus is on to the design and application of a smart voltage source inverter, utilised with photovoltaic (PV) installations, in different configurations, such as three-phase (3P) three-leg and four-leg, to provide optimised voltage regulation and better neutral current and voltage unbalance compensation in an Australian low-voltage (LV) distribution network. This work is relevant and applicable to any power grids worldwide with a three-phase four-wire electricity distribution systems.

The results presented in this thesis are based on the development and application of new control methodologies with smart voltage source inverters installed with PV systems to provide improved voltage regulation and unbalance compensation. However, before applying the proposed methodologies in simulation and hardware models, an extensive overview of existing controllers, power management topologies, and electricity connection standards is provided for various operating conditions to compare the performance and practical applicability of the proposed methods with renewable energy systems (RESs).

To develop the hierarchical control selection methodology for voltage-rise mitigation with increasing PV penetration level, the feasibility of its practical implementation and the associated costs are considered. The coordinated control selection method demonstrates better voltage-rise mitigation with minimum resource utilisation even with high PV penetration levels (~100%). Some assumptions, such as a reactive power control operation from PV-VSI, the availability of residential battery energy storage systems, and minimum communication among neighbouring RES units, are considered during the development and application of the controls in the Australian LV network. They are already being applied in top PV installation countries such as Germany, Italy, the United States, Japan etc.

The design and development of the smart inverter topologies with PV systems are verified with mathematical analysis and hardware implementations in the research laboratory. Neutral current generation and system-unbalance scenarios from real load consumption data of residential and

commercial customers are utilised with the developed system and with the proposed control methodologies to provide the practical implications of this research study. Independent active, reactive and neutral compensation operations are provided from the designed PV-VSI (voltage source inverter), and a new method of utilising the VSI capacity is implemented with a four-leg (4L) inverter to achieve better neutral current and unbalance compensation under divergent network conditions. The relationship of network inherent contingencies to load-generated neutral current is developed to ensure that the designed system can provide stabilised operation despite variations in uncontrollable parameters from the distribution system. Improvements in the controller (proportional-integral) are achieved by increasing the span of the stability region and finding proper gain values which can withstand different divergent conditions, such as intermittency in PV generation, customer load variations, different symmetrical and asymmetrical faults and network contingencies. The new neutral current control method, with a three-phase four-leg inverter, provides improved unbalance compensation compared to existing solutions from the zig-zag transformer (ZT), a combination of ZT and three-leg D-STATCOM (distribution static synchronous compensator) configurations, and four-leg inverter application with different neutral current control methods.

To overcome the drawback of a higher capacity requirement from fixed-capacity four-leg inverters, a new capacity utilisation method is proposed and implemented in the 3P-4L PV-SVSI (smart voltage source inverter) system. In addition to the neutral current compensation performance, the neutral to ground voltage rise, the neutral shift of voltage and current phase unbalance scenarios are also presented for the developed four-leg inverter. To verify the applicability of the designed system in real life, three-leg and four-leg inverter topologies with the proposed neutral current compensation method are applied on the hardware platform with different load combinations. Both the simulation and hardware results prove the robustness and enhanced performance from both topologies of the smart inverter installed with the PV system.

From this research work, the following conclusions can be drawn:

- an increasing amount of PV penetration into the low voltage distribution network can cause voltage instability and unnecessary tripping of customer connections;

- customers situated farther from the distribution transformer (DT) are more vulnerable to the PV penetration effects, i.e. voltage-rise beyond +6%, compared to customers closer to the DT;
- application of dynamic voltage regulation from emerging renewable source technologies, such as smart voltage source inverters, battery energy storage installations, and power-sharing among neighbours' units, is required after exceeding a certain level of RES penetration, such as higher than 30% for the considered LV network in this research;
- an unbalanced distribution of residential and commercial loads can cause high neutral current to flow via the neutral conductor, resulting in a rise in neutral to ground voltage, neutral shift of voltages, current magnitude unbalance, and increase in voltage and current unbalance factors;
- three-phase four-leg inverters can be designed to independently control the load-generated neutral current to improve the overall system's unbalanced performance;
- different neutral conductors have different zero-sequence R/X ratios and can cause different neutral current generation from the same load configuration at different network locations;
- neutral current compensation using the four-leg inverter with the proposed method of utilising the load-generated neutral current as a direct reference to the fourth-leg controller provides robust performance irrespective of load combinations and network locations;
- increasing the capacity of the neutral current controller provides better neutral current compensation, however, it increases the associated cost of the four-leg inverter. Dynamic capacity utilisation of the 4L-VSI can provide improved neutral compensation without increasing the inverter capacity. It can provide better magnitude balancing for the line currents, reductions in voltage and current unbalance factors, improvement in neutral shifts of voltage and lower neutral to ground voltage;
- the three-leg Semiteach power electronic teaching module can be modified and constructed to operate as both three-phase three-leg and three-phase four-leg configurations to perform SVSI control operations for independent active, reactive and neutral current components; and

- with the proposed control methodologies, any DC power source can be utilised to get the benefit of reduced electricity bills by supplying active and reactive power to the loads and better power quality by reducing the neutral current and balancing the phase currents.

7.1 Directions for Future work

The renewable energy sector continuous to grow, as do the associated challenges. The future research directions of this thesis are:

- hardware implementation of the dynamic capacity allocation method for better neutral current compensation from the 4L-SVSI; only fixed-capacity neutral compensation is presented in this thesis;
- harmonic compensation with nonlinear loads;
- integration of cost-benefit analysis, such as the Transactive energy system, with the 4L PV-SVSI for residential and commercial loads;
- application of nonlinear controllers, such as zero dynamic, model predictive etc., for unbalance compensation in simulation and the hardware prototypes. Since RESs exhibit nonlinear characteristics, a nonlinear controller operates better than the traditional PI controller in robust fault recovery and harmonics reduction;
- islanded control operations from the 4L-SVSI with multiple PV and BES units;
- utilisation of various communication protocols, such as RS485, Zigbee, Wi-Fi etc. to communicate multiple smart inverter units integrated with proposed methodologies to regulate active, reactive and neutral currents in a smartgrid/ microgrid system; and
- utilisation of actual PV panels or PV simulators along with dynamic loads, such as induction motors, to show how well the hardware prototype performs in transient situations with variable parameters.

APPENDIX

Table A.1 Overhead cable specifications for the LV network

Cable no.	Cable Material/ code name	Specifications	Total cable installed length
1	Moon	Overall diameter (OD) –14.3 Strands No./Dia-7/4.75, Line impedance 0.232 Ω/km	Upstream network (UN)-850 m LV network -130 m
2	Hard drawn bare copper (HDBC) 1	(OD)- 6.1 mm Strands No./Dia-7/.080; Line impedance 0.816 Ω/km	UN -620 m
3	Wasp	OD 13.18 mm Strands No./Dia.7/0.173, Line impedance 0.27Ω/km	LV - 360 m
4	Fly	CSA- 64mm^2, OD 10.21 mm, Strands No./Dia. 7/.134, Line impedance-0.45 Ω/km	LV -170m
5	Mars	CSA-77.31mm^{2,} OD-11.3mm, Strands No./Dia-7/3.75; Line impedance 0.37Ω/km	LV - 60m
7	HDBC cable 2	Conductor size 7/0.104 OD- 7.92mm, DC resistance- 0.45/km	LV -340 m
8	HDBC cable 3	OD-6.1 mm, Conductor size -7/.080; Line impedance .816 Ω/km	LV -490 m
9	HDBC cable 4	OD - 10.54 mm, Conductor size -19/0.083 Line impedance 0.278/km	LV -130 m
10	HDBC cable 5	OD- 8.2 mm Conductor size 19/0.064 Line impedance 0.466/km	LV -50 m

Table A.2 Transmission cables R/X ratios

No.	Cable names	R+ (Ω/km)	X+ (Ω/km)	R0 (Ω/km)	X0 (Ω/km)
1	MOON 7/4.75AAC	0.265	0.33	0.50	1.01
2	WASP-7/.173 AAC	0.31	0.34	0.57	1.04
3	FLY - 7/.134 AAC	0.51	0.35	0.86	1.15
4	7/.080 - Cu (7/14)	0.89	0.38	1.28	1.34
5	7/.104 - Cu (7/12)	0.53	0.37	0.87	1.18
6	MARS 7/3.75 AAC	0.39	0.085	1.12	0.66
7	19/.064 - Cu	0.52	0.36	0.86	1.17

Table A.3 R/X calculations of test points (P1-P4)

P1									
Cable	L (m)	R+ (Ω/km)	X+ (Ω/km)	R0 (Ω/km)	X0 (Ω/km)	R_T+ (Ω/km)	X_T+ (Ω/km)	R_T0 (Ω/km)	X_T0 (Ω/km)
2	79.1	0.3091	0.336	0.5725	1.0352	0.02444	0.02657	0.04528	0.0818
4	182.6	0.8956	0.3852	1.2767	1.3403	0.1635	0.0703	0.2331	0.2447
Total (261.7 m)						0.188	0.096	0.278	0.325
R/X						R_{T+}/X_{T+} = 1.94		R_{T0}/X_{T0} = 0.86	

P2									
Cable	L (m)	R+ (Ω/km)	X+ (Ω/km)	R0 (Ω/km)	X0 (Ω/km)	R_T+ (Ω/km)	X_T+ (Ω/km)	R_T0 (Ω/km)	X_T0 (Ω/km)
2	169.8	0.3091	0.336	0.5725	1.0352	0.05248	0.05705	0.09721	0.1757
4	113.4	0.8956	0.3852	1.2767	1.3403	0.101561	0.04368	0.14477	0.152
5	136.4	0.5335	0.3683	0.8744	1.1805	0.07276	0.05023	0.11926	0.1610
Total (~ 420 m)						0.227	0.151	0.362	0.49
						R_{T+}/X_{T+} = 1.50		R_{T0}/X_{T0} = 0.74	

P3									
Cable	L (m)	R+ (Ω/km)	X+ (Ω/km)	R0 (Ω/km)	X0 (Ω/km)	R_T+ (Ω/km)	X_T+ (Ω/km)	R_T0 (Ω/km)	X_T0 (Ω/km)
2	76	0.3091	0.336	0.5725	1.0352	0.0234	0.0254	.0435	.0786
3	77	0.5146	0.3524	0.8574	1.1516	0.03977	.0271	.0662	.089
6	64	0.3912	0.0853	1.1246	0.6577	0.0254	4.88e-3	.0723	.0423
Total length = 217 m						0.088	0.058	0.182	0.21
						R_{T+}/X_{T+} = 1.51		R_{T0}/X_{T0} = 0.87	

P4									
Cable	L (m)	R+ (Ω/km)	X+ (Ω/km)	R0 (Ω/km)	X0 (Ω/km)	R_T+ (Ω/km)	X_T+ (Ω/km)	R_T0 (Ω/km)	X_T0 (Ω/km)
2	76	0.3091	0.336	0.5725	1.0352	0.0234	0.0255	.0435	.0786
3	77.3	0.5146	0.3524	0.8574	1.1516	.03977	0.0272	.0662	.089
6	57.3	0.3912	0.0853	1.1246	0.6577	.0224	4.88e-3	.0644	.0376
4	118.9	0.5335	0.3683	0.8744	1.1805	.0634	0.0438	.1039	.140
7	25.9	0.5193	0.3643	0.858	1.169	.0134	9.435e-3	.022	.0302
Total length = 356 m						0.163	0.111	0.30	0.37
						R_{T+}/X_{T+} = 1.47		R_{T0}/X_{T0} = 0.80	

Figure A.1: MCU 100-pin configurations

Signal Type	Pin		Signal Type
-	1	51	-
-	2	52	-
-	3	53	-
-	4	54	-
-	5	55	-
-	6	56	-
ADCIN	7	57	ADCIN
GND	8	58	GND
ADCIN	9	59	ADCIN
GND	10	60	GND
ADCIN	11	61	ADCIN
GND	12	62	GND
ADCIN	13	63	ADCIN
GND	14	64	GND
ADCIN	15	65	ADCIN
GND	16	66	+3V
ADCIN	17	67	ADCIN
GPIO	18	68	GPIO
ADCIN	19	69	ADCIN
GPIO	20	70	GPIO
ADCIN	21	71	ADCIN
GPIO	22	72	GPIO

Continued ...

Signal Type	Pin		Signal Type
GPIO	23	73	GPIO
GPIO	24	74	GPIO
GPIO	25	75	GPIO
GPIO	26	76	GPIO
GND	27	77	+5V
GPIO	28	78	GPIO
GPIO	29	79	GPIO
GPIO	30	80	GPIO
GPIO	31	81	GPIO
GPIO	32	82	+5V
GPIO	33	83	GPIO
GPIO	34	84	GPIO
GPIO	35	85	GPIO
GPIO	36	86	GPIO
GND	37	87	+5V
GPIO	38	88	GPIO
GPIO	39	89	GPIO
GPIO	40	90	GPIO
GPIO	41	91	GPIO
GPIO	42	92	+5V
GPIO	43	93	GPIO
GPIO	44	94	GPIO
GPIO	45	95	GPIO
GPIO	46	96	+5V
GND	47	97	JTAG
JTAG	48	98	JTAG
JTAG	49	99	JTAG
JTAG	50	100	JTAG

References

1. "Solar Photovoltaics: Status, Costs, and Trends," Electric Power Research Institute, 2009.
2. REN21, “Renewables 2016: Global Status Report,” 2016.
3. REN21, “Renewables 2014 global status report,” 2014.
4. The Clean Energy Regulator, “Administrative Report and Annual Statement,” 2015.
5. Energex, “Energex Distribution Annual Planning Report 2015” Web-link: https://www.energex.com.au/__data/assets/pdf_file/0006/283677/2015-DAPR-Volume-1.pdf.
6. P. Kundur, “Power System Stability and Control,” New York: McGraw-Hill, 1994.
7. S. Jashfar and S. Esmaeili, “Volt/var/THD control in distribution networks considering reactive power capability of solar energy conversion,” *Int. J. Electr. Power Energy Syst.*, vol. 60, pp. 221–233, 2014.
8. C. L. Masters, “Voltage rise: the big issue when connecting embedded generation to long 11 kV overhead lines,” *Power Eng. J.*, vol. 16, no. 1, pp. 5, 2002.
9. E. L. Ratnam, S. R. Weller, and C. M. Kellett, “Scheduling residential battery storage with solar PV: Assessing the benefits of net metering,” *Appl. Energy*, vol. 155, pp. 881–891, 2015.
10. R. Tonkoski, L. a C. Lopes, and T. H. M. El-Fouly, “Coordinated active power curtailment of grid connected PV inverters for overvoltage prevention,” *IEEE Trans. Sustain. Energy*, vol. 2, no. 2, pp. 139–147, 2011.
11. N. C. Scott, D. J. Atkinson, and J. E. Morrell, “Use of load control to regulate voltage on distribution networks with embedded generation,” *IEEE Trans. Power Syst.*, vol. 17(2), pp. 510–515, 2002.
12. J. Ji, Y. Wang, W. Yuan, W. Sun, W. He, C. Guo, “Experimental comparison of two PV direct-coupled solar water heating systems with the traditional system,” *Appl. Energy*, vol. 136, pp.110–8, 2014.
13. I. T. Papaioannou, A. Purvins, and E. Tzimas, “Demand shifting analysis at high penetration of distributed generation in low voltage grids,” *Int. J. Electr. Power Energy Syst.*, vol. 44, no. 1, pp. 540–546, 2013.
14. A. C. Liew, “Excessive neutral currents in three-phase fluorescent lighting circuits,” *IEEE Trans. Ind. Appl.*, vol. 25, no. 4. pp. 776–782, 1989.

15. R. Arthur and R. Shanahan, “Neutral currents in three phase wye systems,” *Power System Engineering Data*, Square D, Oshkosh, Wisconsin, 1996.
16. A. V. Jouanne and B. Banerjee, “Closure on ‘assessment of voltage unbalance,’” *IEEE Trans. Power Deliv.*, vol. 17, no. 4, pp. 1176–1177, 2002.
17. M. J. E. Alam, K. M. Muttaqi, and D. Sutanto, “Alleviation of neutral-to-ground potential rise under unbalanced allocation of rooftop PV using distributed energy storage,” *IEEE Trans. Sustain. Energy*, vol. 6, no. 3. pp. 889–898, 2015.
18. T. M. Gruz, “A survey of neutral currents in three-phase computer power systems,” *IEEE Trans. Ind. Appl.*, vol. 26, no. 4, pp. 719–725, Jul./Aug. 1990.
19. A. Hintz, U. R. Prasanna, and K. Rajashekara, “Comparative Study of the Three-Phase Grid-Connected Inverter Sharing Unbalanced Three-Phase and/or Single-Phase systems,” *IEEE Trans. Ind. Appl.*, vol. 52, no. 6, pp. 5156–5164, 2016.
20. Z. Zhang and H. Zhao, “A novel neutral current control scheme for three-phase four-wire distribution transformers,” *Australian Journal of Electrical and Electronics Engineering*, vol. 10, no. 2, pp. 191–197, 2013.
21. T. Fukami, T. Onchi, N. Naoe, and R. Hanaoka, “Compensation for neutral current harmonics in a three-phase four-wire system by a synchronous machine,” *IEEE Trans. Ind. Appl.*, vol. 38, no. 5, pp. 1232–1236, 2002.
22. P. N. Enjeti, W. Shireen, P. Packebush, and I. J. Pitel, “Analysis and Design of a New Active Power Filter to Cancel Neutral Current Harmonics in Three-Phase Four-Wire Electric Distribution Systems,” *IEEE Trans. Ind. Appl.*, vol. 30, no. 6, pp. 1565, 1994.
23. K. W. Park, H. C. Seo, C. H. Kim, C. S. Jung, Y. P. Yoo, and Y. H. Lim, “Analysis of the neutral current for two-step-type poles in distribution lines,” *IEEE Trans. Power Del.*, vol. 24, no. 3. pp. 1483–1489, 2009.
24. M. J. E. Alam, K. M. Muttaqi, and D. Sutanto, “A three-phase power flow approach for integrated 3-wire MV and 4-wire multigrounded LV networks with rooftop solar PV,” *IEEE Trans. Power Syst.*, vol. 28, no. 2. pp. 1728–1737, 2013.
25. “IEEE Recommended Practice for Grounding of Industrial and Commercial Power Systems,” IEEE Standard 142-2007, 2007.

26. R. E. Bushman, S. J. Salon, M. H. Hesse, and J. King, “Calculation of neutral voltage shift in LCI driven induction motors,” *IEEE Trans. Energy Convers.*, vol. 6, no. 3. pp. 507–513, 1991.
27. L. Degroote, B. Renders, B. Meersman, and L. Vandevelde, “Neutral-point shifting and voltage unbalance due to single-phase DG units in low voltage distribution networks,” *IEEE Bucharest Power. Tech.* pp. 1–8, 2009.
28. J. Acharya and W. Xu, “Characteristics of Voltage Swell in Multigrounded Systems,” *IEEE Trans. Power Del.*, vol. 22, no. 2. pp. 1259–1260, 2007.
29. N. Gupta, A. Swarnkar, and K. R. Niazi, “Electrical Power and Energy Systems A novel method for simultaneous phase balancing and mitigation of neutral current harmonics in secondary distribution systems,” *Int. J. Electr. Power Energy Syst.*, vol. 55, pp. 645–656, 2014.
30. M. W. Siti, D. V. Nicolae, A. A. Jimoh, and A. Ukil, “Reconfiguration and load balancing in the LV and MV distribution networks for optimal performance,” *IEEE Trans. Power Deliv.*, vol. 22, no. 4, pp. 2534–2540, 2007.
31. T. Key and J. S. Lai, “Analysis of harmonic mitigation methods for building wiring systems,” *IEEE Trans. Power Syst.*, vol. 13, no. 3, pp. 890–897, Aug. 1998.
32. G. W. Chang, H. L.Wang, G. S. Chuang, and S. Y. Chu, “Passive harmonic filter planning in a power system with considering probabilistic constraints,” *IEEE Trans. Power Del.*, vol. 24, no. 1, pp. 208–218, Jan.2009.
33. Michael Levin, "Combined phase-shifting directional zero phase sequence current filter and method for using thereof", US Patent, US5416688, 16th May 1995.
34. B. Singh, P. Jayaprakash, and D. P. Kothari, “Magnetics for neutral current compensation in three-phase four-wire distribution system,” *2010 Joint International Conference on Power Electronics, Drives and Energy Systems & 2010 Power India*, pp. 1–7, 2010.
35. B. Singh, P. Jayaprakash, and D. D. Kothari, “A T-connected transformer and three-leg VSC based DSTATCOM for power quality improvement,” *IEEE Trans. Power Electron.*, vol. 23, no. 6, pp. 2710–2718, 2008.
36. P. Jayaprakash, B. Singh, and D. P. Kothari, “DSP based implementation of a three-phase four-wire DSTATCOM for voltage regulation and power quality improvement,” *35th Annual Conference of IEEE Industrial Electronics.*, pp. 3660–3665, 2009.

37. B. Singh, P. Jayaprakash, S. Kumar, and D. P. Kothari, “Implementation of neural-network-controlled three-leg VSC and a transformer as three-phase four-wire dstatcom,” *IEEE Trans. Ind. Appl.*, vol. 47, no. 4, pp. 1892–1901, 2011.
38. S. Choi, and M. Jang, “A Reduced-Rating Hybrid Filter to Suppress Neutral Current Harmonics in Three-Phase Four-Wire Systems,” *IEEE Trans. Ind. Electron.*, vol. 51, no. 4, 2004.
39. P. N. Enjeti, W. Shireen, P. Packebush, and I. J. Pitel, “Analysis and Design of a New Active Power Filter to Cancel Neutral Current Harmonics in Three-Phase Four-Wire Electric Distribution Systems,” *IEEE Trans. Ind. Appl.*, vol. 30, no. 6, pp. 1565, 1994.
40. S. Choi and M. Jang, “Analysis and control of a single-phase-inverter-zigzag-transformer hybrid neutral-current suppressor in three-phase four-wire systems,” *IEEE Trans. Ind. Electron.*, vol. 54, no. 4, pp. 2201–2208, 2007.
41. S. Inoue, T. Shimizu, and K. Wada, “Control methods and compensation characteristics of a series active filter for a neutral conductor,” *IEEE Trans. Ind. Electron.*, vol. 54, no. 1, pp. 433–440, 2007.
42. M. Aredes, J. Hafner, and K. Heumann, “Three-phase four-wire shunt active filter control strategies,” *IEEE Trans. Power Electron.*, vol. 12, no. 2. pp. 311–318, 1997.
43. A. Mohd et al., “Control strategy and space vector modulation for three-leg four-wire voltage source inverters under unbalanced load conditions,” *IET Power Electron.*, vol. 3, no. 3. pp. 323–333, 2010.
44. M. Aredes and E. H. Watanabe, “New control algorithms for series and shunt three-phase four-wire active power filters,” *IEEE Trans. Power Deliv.*, vol. 10, no. 3, pp. 1649–1656, 1995.
45. M. Valappil, M. Kumar, and M. K. Mishra, “Three-leg inverter-based distribution static compensator topology for compensating unbalanced and non-linear loads,” *IET Power Electron.*, vol. 8, pp. 2076–2084, 2015.
46. H. L. Jou, K. D. Wu, J. C. Wu, C. H. Li, and M. S. Huang, “Novel power converter topology for three phase four-wire hybrid power filter,” *IET Power Electron.*, vol. 1, no. 1. pp. 164–173, 2008.

47. D. Chen, T. Guo, S. Xie, and B. Zhou, “Shunt active power filters applied in the aircraft power utility,” *PESC Rec. - IEEE Annu. Power Electron. Spec. Conf.*, vol. 2005, pp. 59–63, 2005.
48. S. Dasgupta, I. V Prasanna, S. K. Sahoo, and S. K. Panda, “A novel four-leg three-phase inverter control strategy to reduce the data center thermal losses: Elimination of neutral current,” *IECON 2012 - 38th Annual Conference on IEEE Industrial Electronics Society*, pp. 3358–3363, 2012.
49. C. Stancu, S. Hiti, and E. Mundt, “Mobile electric power for medium and heavy duty hybrid electric vehicles,” *PESC Rec. - IEEE Annu. Power Electron. Spec. Conf.*, vol. 1, pp. 228–234, 2004.
50. K. Matsuse, N. Kezuka, and K. Oka, “Characteristics of independent two induction motor drives fed by a four-leg inverter,” *IEEE Trans. Ind. Appl.*, vol. 47, no. 5, pp. 2125–2134, 2011.
51. F. Meinguet and J. Gyselinck, “Control strategies and reconfiguration of four-leg inverter PMSM drives in case of single-phase open-circuit faults,” *IEEE Int. Electr. Mach. Drives Conf.*, no. 2, pp. 299–304, 2009.
52. J. G. Pinto, P. Neves, D. Gonçalves, and J. L. Afonso, “Field results on developed three-phase four-wire Shunt Active Power Filters,” *35th Annual Conference of IEEE Industrial Electronics*, pp. 480–485, 2009.
53. R. R. Sawant and M. C. Chandorkar, “A multifunctional four-leg grid-connected compensator,” *IEEE Trans. Ind. Appl.*, vol. 45, no. 1, pp. 249–259, 2009.
54. A. Chebabhi, M. K. Fellah, A. Kessal, and M. F. Benkhoris, “Comparative study of reference currents and DC bus voltage control for Three-Phase Four-Wire Four-Leg SAPF to compensate harmonics and reactive power with 3D SVM,” *ISA Trans.*, vol. 57, pp. 360–372, 2015.
55. V. George and M. K. Mishra, “User-defined constant switching frequency current control strategy for a four-leg inverter,” *IET Power Electron.*, vol. 2, no. 4, pp. 335–345, 2009.
56. B. Singh, P. Jayaprakash, and D. P. Kothari, “New control approach for capacitor supported DSTATCOM in three-phase four wire distribution system under non-ideal supply voltage conditions based on synchronous reference frame theory,” *Int. J. Electr. Power Energy Syst.*, vol. 33, no. 5, pp. 1109–1115, 2011.

57. E. Ebrahimzadeh, S. Farhangi, H. Iman-Eini, F. Badrkhani Ajaei, and R. Iravani, “Improved Phasor Estimation Method for Dynamic Voltage Restorer Applications,” *IEEE Trans. Power Deliv.*, vol. 30, no. 3, pp. 1467–1477, 2015.
58. J. G. Pinto, R. Pregitzer, L. F. C. Monteiro, and J. L. Afonso, “3-Phase 4-Wire Shunt Active Power Filter with Renewable Energy Interface,” *Int. Conf. Renew. Energies Power Qual.*, no. 1, pp. 28–30, 2007.
59. M. Singh, V. Khadkikar, A. Chandra, and R. K. Varma, “Grid Interconnection of Renewable Energy Sources at the Distribution Level With Power-Quality Improvement Features,” *IEEE Trans. Power Deliv.*, vol. 26, no. 1. pp. 307–315, 2011.
60. X. Wang, F. Zhuo, J. Li, L. Wang, and S. Ni, “Modeling and control of dual-stage high-power multifunctional PV system in d-q-o-Coordinate,” *IEEE Trans. Ind. Electron.*, vol. 60, no. 4, pp. 1556–1570, 2013.
61. B. Singh, D. T. Shahani, and R. K. Verma, “Neural network controlled grid interfaced solar photovoltaic power generation,” *IET Power Electron.*, vol. 7, no. 3, pp. 614–626, 2014.
62. P. Acu, L. Mor, and M. Rivera, “Improved Active Power Filter Performance for Renewable Power Generation Systems,” *IEEE Trans. Ind. Electron.*, vol. 29, no. 2, pp. 687–694, 2014.
63. J. Philip et al., “Control and Implementation of a Standalone Solar Photovoltaic Hybrid System,” *IEEE Trans. Ind. Appl.*, vol. 52, no. 4, pp. 3472–3479, 2016.
64. X. Guo, R. He, J. Jian, Z. Lu, X. Sun, and J. M. Guerrero, “Leakage current elimination of four-leg inverter for transformerless three-phase PV systems,” *IEEE Trans. Power Electron.*, vol. 31, no. 3, pp. 1841–1846, 2016.
65. R. A. Modesto, S. A. O. da Silva, A. A. de Oliveira, and V. D. Bacon, “A Versatile Unified Power Quality Conditioner Applied to Three-Phase Four-Wire Distribution Systems Using a Dual Control Strategy,” *IEEE Trans. Power Electron.*, vol. 31, no. 8. pp. 5503–5514, 2016.
66. C. García, M. Rivera, M. López, et al., “A Simple Current Control Strategy for a Four-Leg Indirect Matrix Converter,” *IEEE Trans. Power Electron.*, vol. 30, no. 4. pp. 2275–2287, 2015.
67. X. Guo, D. Xu, and B. Wu, “Four-Leg Current-Source Inverter with a New Space Vector Modulation for Common-Mode Voltage Suppression,” *IEEE Trans. Ind. Electron.*, vol. 62, no. 10, pp. 6003–6007, 2015.

68. A. L. Julian, G. Oriti, and T. A. Lipo, “Elimination of common-mode voltage in three-phase sinusoidal power converters,” *IEEE Trans. Power Electron.*, vol. 14, no. 5, pp. 982–989, 1999.
69. Z. Liu, J. Liu, and J. Li, “Modeling, analysis, and mitigation of load neutral point voltage for three-phase four-leg inverter,” *IEEE Trans. Ind. Electron.*, vol. 60, no. 5, pp. 2010–2021, 2013.
70. C. L. Chen and C. E. Lin, “An active filter for an unbalanced three-phase system using the synchronous detection method,” *Electr. Power Syst. Res.*, vol. 36, no. 3, pp. 157–161, 1996.
71. V. Khadkikar and A. Chandra, “An independent control approach for three-phase four-wire shunt active filter based on three H-bridge topology under unbalanced load conditions,” *PESC Rec. - IEEE Annu. Power Electron. Spec. Conf.*, pp. 4643–4649, 2008.
72. V. Khadkikar, a. Chandra, and B. Singh, “Digital signal processor implementation and performance evaluation of split capacitor, four-leg and three H-bridge-based three-phase four-wire shunt active filters,” *IET Power Electron.*, vol. 4, no. 4, pp. 463, 2011.
73. A. Hintz, U. R. Prasanna, and K. Rajashekara, “Comparative Study of the Three-Phase Grid-Connected Inverter Sharing Unbalanced Three-Phase and/or Single-Phase systems,” *IEEE Trans. Ind. Appl.*, vol. 52, no. 6, pp. 5156–5164, 2016.
74. Ausgrid, “Network standard,” 2015.
75. H. Markiewicz and A. Klajn, “Voltage Disturbances Standard EN 50160,” Wroclaw University of Technology, 2004.
76. “IEC 038: IEC standard voltages”, 1999.
77. F. Ghassemi and M. Perry, “Review of Voltage Unbalance Limit in The GB Grid Code CC.6.1.5(b),” *National Grid*, October 2014.
78. B. Banerjee, “Voltage Unbalance : Power Quality Issues, Related Standards and Mitigation Techniques and Effect of Unbalanced Voltage on End Use Equipment Performance,” Tech. Rep., Electric Power Research Institute, 2008.
79. “NEMA Standards Publication MG 1-2009, Motors and Generators,” National Electrical Manufacturer Association, 2009.
    Available: https://law.resource.org/pub/us/cfr/ibr/005/nema.mg-1.2009.pdf
80. “National Electricity Code Australia, Version 61,” Australian Energy Market Commission, 2014.

81. "Americal National Standard for Electric Power Systems and Equipment-Voltage ratings (60 Hz)- ANSI C84.1-2016," National Electrical Manufacturers Association, 2016.
82. A. Yazdani, A. R. D. Fazio, H. Ghoddami, et al. Modeling guidelines and a benchmark for power system simulation studies of three-phase single-stage photovoltaic systems. *IEEE Trans Power Deliv*, vol. 26, pp. 1247–64, 2011.
83. M. J. Hossain, T. K. Saha, N. Mithulananthan, and H. R. Pota, "Robust control strategy for PV system integration in distribution systems," *Appl. Energy*, vol. 99, pp. 355–362, 2012.
84. A. Reznik, M. G. Simões, A. Al-Durra, and S. M. Muyeen, "LCL Filter design and performance analysis for grid-interconnected systems," *IEEE Trans. Ind. Appl.*, vol. 50, pp. 1225–32, 2014.
85. S. Barcellona, S. Grillo, and L. Piegari, "A simple battery model for EV range prediction: Theory and experimental validation," *International Conference on Electrical Systems for Aircraft, Railway, Ship Propulsion and Road Vehicles & International Transportation Electrification Conference*, pp. 1–7, 2016.
86. M. J. E. Alam, K. M. Muttaqi, and D. Sutanto, "Mitigation of rooftop solar PV impacts and evening peak support by managing available capacity of distributed energy storage systems," IEEE Trans. Power Syst., vol. 28, no. 4, pp. 3874–3884, 2013.
87. T. Aziz, M. J. Hossain, T. K. Saha, and N. Mithulananthan, "VAR planning with tuning of STATCOM in a DG integrated industrial system," *IEEE Trans. Power Deliv.*, vol. 28, no. 2, pp. 875–885, 2013.
88. R. P. S. Leão *et al.*, "The future of low voltage networks: Moving from passive to active," *Int. J. Electr. Power Energy Syst.*, vol. 33, pp. 1506–1512, 2011.
89. REN21, "Renewables 2013 Global Status Report," 2013.
90. "Rooftop PV information paper," Australian Energy Market Operator, 2012. Available:http://www.aemo.com.au/Electricity/~/media/Files/Other/forecasting/Rooftop_PV_Information_Paper.ashx.
91. B. Noone, "PV integration on Australian distribution networks," The Australian PV Association, September, 2013.
92. Ellis A, Nelson R, Von Engeln E, MacDowell J, Casey L, Seymour E, et al. "Reactive power performance requirements for wind and solar plants," *IEEE Power and Energy Society General Meeting*, pp. 1–8, 2012.

93. “Shaping Australia’s Energy Future: National Cost Benefit Assessment. Smart Grid Smart City” Tech. Rep., AusGrid, July 2014.
94. Recommended Practice for Establishing Methods and Procedures that Provide Supplemental Support for Implementation Strategies for Expanded Use of IEEE Standard 1547 (IEEE P1547.8).
Available: http://grouper.ieee.org/groups/scc21/1547.8/1547.8_index.html.
95. Z. Yang, C. Shen, L. Zhang, M. L. Crow, and S. Atcitty, “Integration of a StatCom and battery energy storage,” *IEEE Trans. Power Syst.*, vol. 16, no. 2, pp. 254–260, 2001.
96. J. Zhao, S. Kucuksari, E. Mazhari, and Y. J. Son, “Integrated analysis of high-penetration PV and PHEV with energy storage and demand response,” *Appl. Energy*, vol. 112, pp. 35–51, 2013.
97. M. Kolenc, I. Papič, and B. Blažič, “Coordinated reactive power control to achieve minimal operating costs,” *Int. J. Electr. Power Energy Syst.*, vol. 63, pp. 1000–1007, 2014.
98. N. C. Scott, D. J. Atkinson, and J. E. Morrell, “Use of load control to regulate voltage on distribution networks with embedded generation,” *IEEE Trans. Power Syst.*, vol. 17, no. 2, pp. 510–515, 2002.
99. J. Ji, Y. Wang, W. Yuan, W. Sun, W. He, and C. Guo, “Experimental comparison of two PV direct-coupled solar water heating systems with the traditional system,” *Appl. Energy*, vol. 136, pp. 110–118, 2014.
100. A. Cagnano and E. De Tuglie, “Centralized voltage control for distribution networks with embedded PV systems,” Renew. Energy, vol. 76, pp. 173–185, 2015.
101. K. Turitsyn, P. Šulc, S. Backhaus, and M. Chertkov, “Options for control of reactive power by distributed photovoltaic generators,” *Proc. IEEE*, vol. 99, no. 6, pp. 1063–1073, 2011.
102. M. M. Aly, M. Abdel-Akher, Z. Ziadi, and T. Senjyu, “Assessment of reactive power contribution of photovoltaic energy systems on voltage profile and stability of distribution systems,” *Int. J. Electr. Power and Energy Syst.*, vol. 61, pp. 665–672, 2014.
103. R. Yan and T. K. Saha, “Investigation of voltage stability for residential customers due to high photovoltaic penetrations,” *IEEE Trans. Power Syst.*, vol. 27, no. 2, pp. 651–662, 2012.

104. P. N. Vovos, A. E. Kiprakis, A. R. Wallace, and G. P. Harrison, “Centralized and Distributed Voltage Control: Impact on Distributed Generation Penetration,” *IEEE Trans. Power Syst.*, vol. 22, no. 1, pp. 476–483, 2007.
105. C. Ahn and H. Peng, “Decentralized voltage control to minimize distribution power loss of microgrids,” *IEEE Trans. Smart Grid*, vol. 4, no. 3, pp. 1297–1304, 2013.
106. I. T. Papaioannou, A. Purvins, and E. Tzimas, “Demand shifting analysis at high penetration of distributed generation in low voltage grids,” *Int. J. Electr. Power and Energy Syst.*, vol. 44, no. 1, pp. 540–546, 2013.
107. F. Olivier, P. Aristidou, D. Ernst, and T. Van Cutsem, “Active Management of Low-Voltage Networks for Mitigating Overvoltages Due to Photovoltaic Units,” *IEEE Trans. Smart Grid*, vol. 7, no. 2. pp. 926–936, 2016.
108. M. N. Kabir, Y. Mishra, G. Ledwich, Z. Xu, and R. C. Bansal, “Improving voltage profile of residential distribution systems using rooftop PVs and Battery Energy Storage systems,” *Appl. Energy*, vol. 134, pp. 290–300, 2014.
109. L. Collins and J. K. Ward, “Real and reactive power control of distributed PV inverters for overvoltage prevention and increased renewable generation hosting capacity,” *Renew. Energy*, vol. 81, pp. 464–471, 2015.
110. Connection Guideline Small Scale Parallel Inverter Energy Systems up to 30 kVA in Ergon Energy and Energex network. Available:https://www.energex.com.au/__data/assets/pdf_file/0007/199951/Draft Connection-Standard-Small-Scale-Invertor-Energy-Systems-v1.pdf)
111. A. A. Akhil, G. Huff, A. B. Aileen, B. C. Kaun, et. al. “DOE/EPRI Electricity Storage Handbook in Collaboration with NRECA” Tech. Rep., SANDIA, 2015.
112. P. R. Thomas, T. J. Walker, and C. A. McCarthy, “Demonstration of Community Energy Storage fleet for load leveling, reactive power compensation, and reliability improvement,” *IEEE Power and Energy Society General Meeting*, pp. 1–4, 2012.
113. “Grid connection of energy system via inverter (draft),” Clean Energy Council, Australia, 2013.
114. F. H. M. Rafi, M. J. Hossain, D. Leskarac, and J. Lu, “Reactive power management of a AC/DC microgrid system using a smart PV inverter,” *IEEE Power & Energy Society General Meeting*, pp. 1–5, 2015.

115. S. Galli, A. Scaglione, and Z. Wang, “Power Line Communications and the Smart Grid,” *First IEEE International Conference on Smart Grid Communications*, pp. 303–308, 2010.
116. B. Mountain and P. Szuster, “Solar, Solar Everywhere: Opportunities and Challenges for Australia’s Rooftop PV Systems,” *IEEE Power and Energy Magazine*, vol. 13, no. 4. pp. 53–60, 2015.
117. M. Molinas, J. A. Suul, and T. Undeland, “Low voltage ride through of wind farms with cage generators: STATCOM versus SVC,” *IEEE Trans. Power Electron.*, vol. 23, no. 3, pp. 1104–1117, 2008.
118. H.-L. Jou, J.-C. Wu, K.-D. Wu, W.-J. Chiang, and Y.-H. Chen, “Analysis of zig-zag transformer applying in the three-phase four-wire distribution power system,” *IEEE Trans. Power Del.*, vol. 20, no. 2, pp. 1168–1173, 2005.
119. B. Singh, P. Jayaprakash, T. R. Somayajulu, and D. P. Kothari, “Reduced rating VSC with a zig-zag transformer for current compensation in a three-phase four-wire distribution system,” *IEEE Trans. Power Del.*, vol. 24, no. 1. pp. 249–259, 2009.
120. B. Singh, P. Jayaprakash, and D. P. Kothari, “Three-phase four-wire dstatcom with H-bridge VSC and star/delta transformer for power quality improvement,” *2008 Annual IEEE India Conference*, vol. 2. pp. 412–417, 2008.
121. A. B. Nassif, W. Xu, and W. Freitas, “An Investigation on the selection of filter topologies for passive filter applications,” *IEEE Trans. Power Del.*, vol. 24, no. 3. pp. 1710–1718, 2009.
122. O. Vodyakho and C. C. Mi, “Three-Level inverter-based shunt active power filter in three-phase three-wire and four-wire Systems,” *IEEE Trans. Ind. Electron.*, vol. 24, no. 5. pp. 1350–1363, 2009.
123. J. C. Wu, H. L. Jou, H. H. Hsaio, and S. T. Xiao, “A new hybrid power conditioner for suppressing harmonics and neutral-line current in three-phase four-wire distribution power systems,” *IEEE Trans. Power Del.*, vol. 29, no. 4. pp. 1525–1532, 2014.
124. B. Singh, P. Jayaprakash, D. P. Kothari, A. Chandra, and K. A. Haddad, “Comprehensive study of DSTATCOM configurations,” *IEEE Trans. Ind. Informat.*, vol. 10, no. 2. pp. 854–870, 2014.

125. S. M. Ali and M. P. Kazmierkowski, "PWM voltage and current control of four-leg VSI," *Industrial Electronics, 1998. Proceedings. ISIE '98. IEEE International Symposium on*, vol. 1. pp. 196–201 vol.1, 1998.
126. Information of Australian solar Feed-in-tariffs, Available:http://www.energymatters.com.au/rebates-incentives/feedintariff/
127. M. N. Kabir, Y. Mishra, G. Ledwich, Z. Y. Dong, and K. P. Wong, "Coordinated control of grid-connected photovoltaic reactive power and battery energy storage systems to improve the voltage profile of a residential distribution feeder," *IEEE Trans. Ind. Informat.*, vol. 10, no. 2. pp. 967–977, 2014.
128. EM133-AR TOU Smart Energy Meter – NMI Approved, Available: http://satec-global.com.au/portfolio/em133-tou-smart-energy-meter
129. M. J. Hossain, M. A. Mahmud, H. R. Pota, and N. Mithulananthan, "Design of non-interacting controllers for PV systems in distribution networks," *IEEE Trans. Power Syst.*, vol. 29, no. 6, pp. 2763–2774, 2014.
130. F. H. M. Rafi, M. J. Hossain, M.S. Rahman, and J. Lu, "Impact of controlling zero sequence current in a three-phase four-wire LV network with PV units," *IEEE Power & Energy Society General Meeting*, pp. 1–5, 2016.
131. National Electricity Code, V. 1, Queensland technical derogation, 2002.
132. J. C. Balda, A. R. Oliva, D. W. McNabb, and R. D. Richardson, "Measurements of neutral currents and voltages on a distribution feeder," *IEEE Trans. Power Del.*, vol. 12, no. 4, pp. 1799–1804, Oct. 1997.
133. M. J. E. Alam, K. M. Muttaqi, and D. Sutanto, "Community Energy Storage for Neutral Voltage Rise Mitigation in Four-Wire Multigrounded LV Feeders with Unbalanced Solar PV Allocation," *IEEE Trans. Smart Grid*, vol. 6, no. 6, pp. 2845–2855, 2015.
134. Customer standard for parallel embedded generation via inverters - 30kw to 5000kw, Energex, 2016.
135. Electric Power Research Institute, Inc. Elevated Neutral-to-Earth Voltage, Urban Contact Voltage and Other Perceptibility Concerns for Humans and Animals [Online]. Available: http://strayvoltage.epri.com/results.asp

136. A. S. De Morais, F. L. Tofoli, and I. Barbi, “Modeling, digital control, and implementation of a three-phase four-wire power converter used as a power redistribution device,” *IEEE Trans. Ind. Informat.*, vol. 12, no. 3, pp. 1035–1042, 2016.
137. M. Pattnaik, and D. Kastha, “Harmonic Compensation With Zero-Sequence Load Voltage Control in a Speed-Sensorless DFIG-Based System,” *IEEE Trans. Ind. Electronics*, vol. 60, no. 12, pp. 5506–5514, 2013.
138. S. Weckx, C. Gonzalez, and J. Driesen, “Combined central and local active and reactive power control of PV inverters,” *IEEE Trans. Sustain. Energy*, vol. 5, no. 3, pp. 776–784, 2014.
139. R. A. Ramos and R. Reginatto, “On electrical power evaluation in dq coordinates under sinusoidal unbalanced conditions,” *IET Gener. Transm. Distrib.*, vol. 8, no. 5, pp. 976–982, 2014.
140. Semikron online. Available: http://shop.semikron.com/en/home/?cur=1
141. J. Philip, C. Jain, K. Kant, B. Singh et al., “Control and Implementation of a Standalone Solar Photovoltaic Hybrid System,” *IEEE Trans. Ind. Appl.*, vol. 52, no. 4, pp. 3472–3479, 2016.
142. http://www.denki.com.au/SwitchGearModule.html
143. http://shop.semikron.com/en/Products-and-Shop/Product Groups/STACKs/SEMITEACH/SEMITEACH-B6U-E1CIF-B6CI.html
144. http://www.signaltestinc.com/product-p/xg%20300-2.8.html